Modeling of Hydrodynamic Circulation and Cohesive Sediment Transport and Prediction of Shoreline Erosion in Hartwell Lake, SC/GA

A Thesis
Presented to
The Academic Faculty

by

Sebnem Seker-Elci

In Partial Fulfillment
of the Requirements for the Degree
Doctor of Philosophy in the
School of Civil and Environmental Engineering

Georgia Institute of Technology
April 2004

Modeling of Hydrodynamic Circulation and Cohesive Sediment Transport and Prediction of Shoreline Erosion in Hartwell Lake, SC/GA

Approved by:

Dr. Paul Work, Advisor

Dr. Earl Hayter

Dr. Phil Roberts

Dr. Fotis Sotiropoulos

Dr. Hermann Fritz

Date Approved ____05/20/2004___

ACKNOWLEDGEMENT

I would like to express my gratitude to Dr. Paul Work, who not only served as my advisor, but also encouraged, supported and challenged me during my study. I also want to thank him for sharing his field expertise with me. I owe special thanks to Dr. Earl Hayter, who has been always very kind and supportive, and inspired me with his work discipline and devotion. I appreciate his immediate responses to my countless modeling questions. I also would like to thank my committee members Dr. Phil Roberts, Dr. Fotis Sotiropoulos and Dr. Hermann Fritz for their guidance and valuable contributions.

Many people have been a part of my graduate education at organizations I visited during various stages of my study. I am grateful to the faculty, staff and colleagues at Clemson University and Georgia Tech – Savannah for making this journey delightful.

This study was funded by the South Carolina Water Resources Center, the Georgia Water Resources Institute and the U.S. Geological Survey. I would like to thank these organizations for their support, and Joseph Hoke of the U.S. Army Corps of Engineers Savannah District for providing me with historical bathymetric survey data.

Most of all, I would like to thank my family back in Turkey, and especially my parents, for their absolute confidence in me. I wouldn't be who I am now without their endless love and support. Finally, I wish to thank my dearest husband, Alper, for his love, encouragement and inspiration.

TABLE OF CONTENTS

Page

Table of Contents (Continued)

Page

Table of Contents (Continued)

Page

LIST OF TABLES

Page

LIST OF FIGURES

Page

SUMMARY

This dissertation addresses hydrodynamics, sediment transport and shoreline erosion within the main pool of Hartwell Lake, a U.S. Army Corps of Engineers reservoir built on the Savannah River, between Anderson, South Carolina, and Hartwell, Georgia, USA between 1959-1963. A U.S. Environmental Protection Agency (EPA) “Superfund” site is located on a tributary of Hartwell Lake because of high concentrations of polychlorinated biphenyls (PCBs) in the lake sediments. PCBs are hydrophobic and typically bond to fine-grained sediments, such as silts and clays. Others have investigated the transport of non-cohesive sediments in the upper reaches of the lake (EPA, 1991). This study focuses on the transport of cohesive sediments in the main pool of the lake. The primary goal of the study was to document, through field measurements, and model, using a 3-D numerical model of flow and sediment transport, the fate of sediments within the main pool of Hartwell Lake.

To document forty years of sedimentation within the reservoir, bathymetric survey data were collected in Hartwell Lake during the period, February 10-14, 2003. The bathymetric surveys revealed that deposition was, in places, up to two meters thickness in forty years. During the field campaign, flow velocity measurements were made primarily to provide a check on the magnitude of the velocities predicted by the numerical model used in the study. Shoreline surveys provided data for the modeling procedure for shoreline change. This in turn facilitated specification of the sediment flux into the domain via shoreline erosion.

The EFDC (Environmental Fluid Dynamics Code) model developed by Hamrick (1996) is used to describe lake hydrodynamics and sediment fate. Velocities in the main pool were simulated using the EFDC model for the weather and flow conditions that existed during the field campaign and the results were compared with the velocity measurements.

Historical records of wind and flow were used to determine frequencies of occurrence and representative conditions for prediction of long-term deposition zones for sediment transported by the flow. Sensitivity of hydrodynamic processes to model parameters was investigated, and wind, as expected, was found to be the major factor controlling the circulation. According to the model results, for lower wind speeds, sediments were deposited in the old river bed (thalweg) of the lake, regardless of the magnitudes of inflows and outflows. Higher wind speeds caused deposition zones to shift slightly in the downwind direction.

Hartwell Lake is an example of a warm monomictic lake, which is vertically mixed during the months from December to March and thermally stratified to varying degrees between April and November. Effects of stratification on model results were also investigated. In general, sediments deposited mainly in the thalweg under both thermally stratified and unstratified conditions, although the stratification allowed some of the sediments to settle before reaching the thalweg due to the reduced velocities at the bottom layer during stratified conditions.

Hartwell Lake is located near the southern terminus of the Appalachian mountain chain in the Piedmont region. Sediments contain high fractions of silt and clay. Hartwell Lake has a shoreline length of 1548 km, and erosion of lake shorelines has been a

significant problem for many homeowners. As of September 2002, there were 1123 permitted riprap installations, and 393 permitted retaining walls, for a total of 1516 erosion control structures along the lakeshores (source: USACE Hartwell Office), an indication of the magnitude of the erosion problem.

To quantify the erosion rate of the shorelines, an approach that relates erosion rates to wind wave forces was developed. A simplified representation of the shape of beach profiles was employed. Historical shoreline change rates were quantified by comparing available digital aerial photos taken in different years, and the erosion prediction model was calibrated using these computed erosion rates.

The erosion prediction methodology was applied to an eroding peninsula on the east side of the lake. The estimated erosion rates agreed well with values obtained from aerial photo analysis after calibration of the methodology. Average erosion rates were estimated to be about one meter/year. Results were compared to two other approaches for prediction of erosion rates in the literature. It was concluded that the shape of the beach profiles is an important factor, and that methods used for erosion prediction should account for the variability of the beach profile slopes.

Sediments derived from shoreline erosion were introduced to the model as an additional sediment source along the model boundary, and the fate of the eroding sediments was investigated via numerical modeling. The results suggest that the eroding sediments have a localized and small impact on overall reservoir deposition patterns.

Hydrodynamic model results indicated likely zones of sediment deposition, potentially useful for mitigation of pollution problems as well as predictions of reservoir lifetime and development of maintenance schemes. The findings of the erosion prediction

methodology can be used in the development of shoreline protection regulations, and assessment of setback requirements throughout reservoir lakeshores. Although this study focused on Hartwell Lake in specific, methods described here can be applied to other lakes/reservoirs to find “hot spots” of contaminated sediments and to predict shoreline erosion for the assessment of setback requirements along the shores.

CHAPTER 1

INTRODUCTION

Hartwell Lake, a U.S. Army Corps of Engineers (USACE) reservoir, is located on the Savannah River, between Anderson, South Carolina, and Hartwell, Georgia, USA (Figure 1). The reservoir was built between 1955 and 1963, with joint goals of flood control, power production, water supply, and recreation. General characteristics of the reservoir are given in Table 1. The terrain consists primarily of gentle rolling hills and pine forests near the southern terminus of the Appalachian mountain chain (USACE, 1996b). Sediments in the reservoir contain high fractions of silt and clay.

The dam is located approximately 480 km upstream of the mouth of the Savannah River at Savannah, Georgia, and 145 km upstream of Augusta, Georgia. Two other USACE reservoirs – J. Strom Thurmond Reservoir (formerly Clarks Hill) located near Augusta, Georgia, and Richard B. Russell Reservoir, located between Hartwell and Thurmond Reservoirs near Elberton, Georgia – join Hartwell to form a chain of lakes 193 km long.

The Hartwell power plant is a “peaking” plant – the powerplant is designed to supply dependable power during hours of peak daily demand. On average, the Hartwell powerplant produces over 468 million-kilowatt hours per year. Hydroelectric power is produced when water from Hartwell Lake flows through penstocks in the dam. The penstocks are located approximately 30 m below the surface of the reservoir. Total discharge is up to 125 m^3/s when generating.

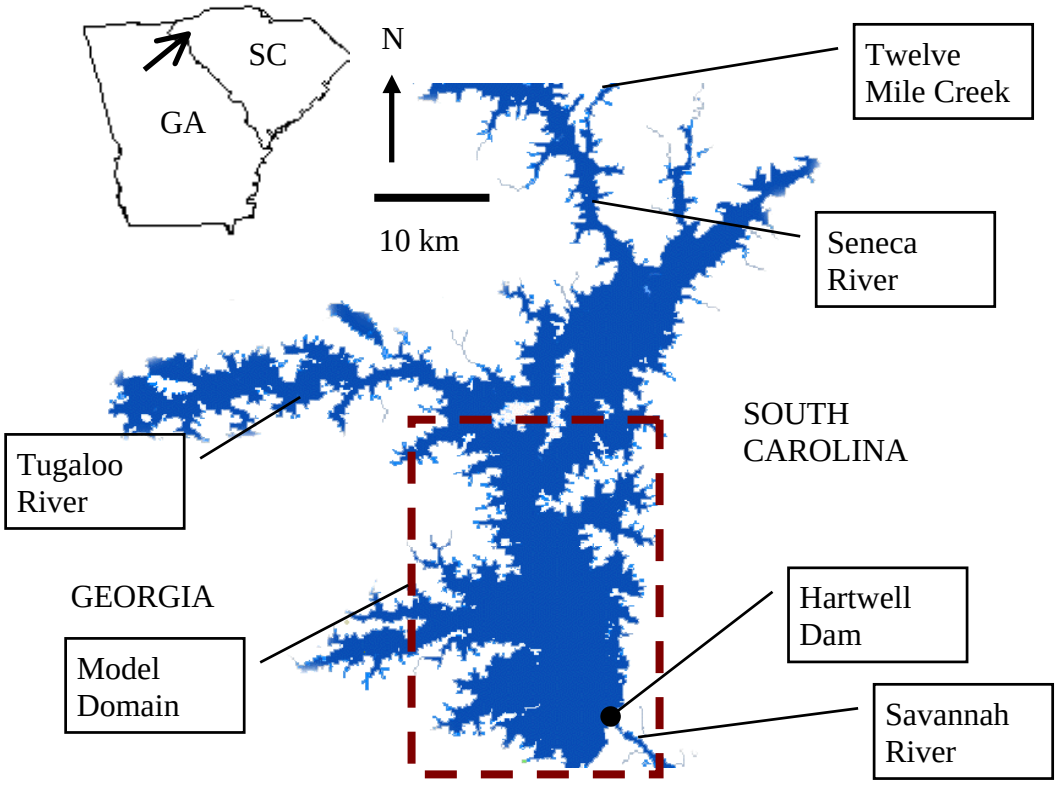

Figure 1 Map of study site: model domain shows the region within the main pool of the lake that was modeled to describe circulation, erosion, and sediment deposition patterns.

Table 1 General characteristics of Hartwell Lake (USACE, 1996b).

Parameter	Value
Mean water level (North American Datum of 1927)	201 m
Surface area	227 km^2
Drainage area	5408 km^2
Shoreline length	1548 km
Maximum depth	50 m
Average depth	20 m

High concentrations of polychlorinated biphenyls (PCBs) were found in the lake and in Twelve-Mile Creek, a major tributary of Hartwell Lake, resulting from the operation of a capacitor manufacturing facility from 1955 to 1977. In its manufacturing processes, this facility used several dielectric fluids, which contained several varieties of PCBs. Some of those were discharged with effluent into Town Creek, a tributary of Twelve Mile Creek (EPA 1991). Portions of Hartwell Lake later became a "Superfund" site. PCBs are known to cause cancer in animals and can also cause non-cancer health problems, such as reduced ability to fight infections, and low birth weights in humans (Clearwater 1997). PCBs are hydrophobic, and typically bond to sediments. They also exhibit an affinity for fine-grained sediments, such as silts and clays (EPA 1991).

The U.S. EPA performed and sponsored research on PCBs in Hartwell Lake as part of this "Superfund" program (Elzerman et al. 1994), and EPA's selected remedy was to rely on burial by natural sedimentation processes. Over time, incoming "clean" sediments should bury the contaminated sediments, providing a clean sediment cap and gradually reducing the health risks. Numerical modeling of sediment transport in Twelve-Mile Creek was performed to investigate the feasibility of this approach, focusing on non-cohesive sediments (EPA 1991). However, as the transport of (primarily) fine-grained sediments within the main pool of the lake has not been studied previously, it is addressed in this study, since the finest sediment sizes are more likely to travel from the contaminant source region to the main pool of the reservoir.

The primary objective of this study is thus to document, through field measurements, and model, using a 3-D numerical model of flow and sediment transport, the fate of sediments, those coming from the tributaries and eroding from the shorelines,

within the main pool of Hartwell Lake. The Environmental Fluid Dynamics Code (EFDC) developed by Hamrick (1996) was applied to Hartwell Lake to simulate hydrodynamic processes in the lake. This is a 3-D finite difference model, including a 3-D hydrodynamic module, as well as water quality, sediment transport and toxics modules.

In February 2003, a field trip was made to Hartwell Lake to survey the bathymetry of the lake and to quantify at selected locations 40 years of deposition since construction of the dam. During the field campaign, velocity measurements were made primarily to provide a check on the magnitude of the velocities reported by the numerical model used in the study. Shoreline surveys provided data for the modeling procedure for shoreline change.

Hartwell Lake is stratified during the months of April to November, and the effect of this stratification on reservoir circulation and depositional zones was investigated via numerical model simulations. Stratification is strong in summer and early fall, and temperature variations are as high as 14ºC over the water column. A well-defined thermocline is typically located 10 m below the surface in the early fall.

As of September 2002, there were 1123 riprap structures and 393 retaining walls that had been authorized for construction by the USACE for erosion control at Hartwell Lake (source: USACE Hartwell Office), an indication of the magnitude of the shoreline erosion problem.

To quantify the erosion rate of the shorelines, an approach that relates erosion rates to wind wave forces was applied. Predictions are based on the assumption that sediment transport rate and erosion rate are proportional to wave power at breaking,

which in turn is proportional to breaking wave height to the 5/2 power. The method described in this study accounts for the beach profile shape, water level, wind forcing and includes a calibration parameter accounting for sediment erodibility.

In addition to sediments delivered by tributaries, sediments eroding from shorelines also represent a sediment input to a reservoir. The fate of the eroding sediments quantified by the new shoreline erosion prediction methodology was investigated via numerical modeling. The results suggest that the eroding sediments have a localized and small impact on overall reservoir deposition patterns.

This dissertation focuses on the modeling of reservoir hydrodynamics and sedimentation in a deep, periodically stratified reservoir. Although others have modeled hydrodynamics and sedimentation in a reservoir before, most studies focused on shallow reservoirs and did not address the relative importance of stratification on sedimentation patterns. Also in this study, for the first time, shoreline erosion has been estimated by an improved approach that accounts for the beach shape profiles, and the potential contributions of shoreline erosion to the reservoir sediment budget has been investigated together with sediments coming from the tributaries.

This dissertation includes nine chapters. In Chapter 1, the subject is briefly introduced and the objective is stated. Previous relevant studies regarding numerical modeling of reservoir shoreline erosion and sedimentation within reservoirs are reviewed in Chapter 2. In Chapter 3, the numerical model chosen to model hydrodynamics and sediment transport is discussed, and the testing of the model is described. Field data collection strategy in Hartwell Lake and the comparison of the numerical model results with the field measurements are presented in Chapter 4. Modeling of hydrodynamics in

thermally stratified reservoirs is discussed in Chapter 5. Modeling of sediment transport is described in Chapter 6. In Chapter 7, a method for shoreline erosion prediction and modeling of eroding sediments is presented. Finally, in Chapter 8, the main results and conclusions of this research are summarized and potential improvements and issues for further study are suggested.

CHAPTER 2

LITERATURE REVIEW

This chapter gives a review of previous studies related to numerical modeling of hydrodynamics and sediment transport in reservoirs. The focus is primarily on existing numerical models and to their applications to water systems. Hydrodynamic modeling of thermally stratified reservoirs is reviewed under a separate section within this chapter, since the physical processes in reservoirs are modified when influenced by stratification. Studies related to erosion of cohesive shorelines are also reviewed in this chapter.

2.1 Numerical Modeling of Hydrodynamics and Sediment Transport in Reservoirs

Building a reservoir on a river yields environmental consequences both upstream, in the reservoir itself, and downstream because of trapping (i.e., deposition) of sediments in the artificial lake. Sedimentation can reduce the useful storage, the volume of water between the minimum pool (e.g., outlet invert elevation) and full pool (e.g., spillway crest elevation) levels, and serious problems may arise downstream as a result of erosion due to reduced sediment supply. Reservoir storage capacity impacts hydroelectric power generation and flood control operation. Many studies have investigated reservoir operation and efficiency (e.g., Arnold et al., 1987; Lo, 1994), which determine the reservoir's effective volume.

Reservoir sedimentation studies mainly involve description/investigation of the mechanism by which the sediments are transported into the reservoir, prediction of deposition rates through numerical modeling, or measurement of deposition rates via surveying (i.e. Sheng 1984; Blumberg and Mellor 1987; Blumberg et al. 1999; Jin et al.

2000; Yang et al. 2000; Rueda and Schladow 2003; Falconer et al. 1991). Modeling reservoir sedimentation requires an understanding of the hydrodynamic processes. Therefore, most studies focused on the driving forces that control circulation and thus sediment transport processes in a reservoir (e.g. Krone, 1962, Mehta et al., 1989).

The complexities of the hydrodynamic processes in a reservoir suggest the use of numerical modeling approaches to provide a description of circulation, mixing and density stratification processes that can affect the water quality and transport of pollutants within a water body. Hydrodynamic models use reservoir geometry, inflows, withdrawals, and meteorological data to simulate water levels, flow velocities, and temperatures. In a reservoir, wind-generated surface stresses, buoyancy or density forcing, turbulent momentum and mass transport are the physical processes that should be simulated by the hydrodynamic model.

In general, either a two-dimensional, vertically averaged approach or a three-dimensional approach is used to model hydrodynamics in a reservoir. Models in one-dimension or two-dimensions are formulated by integrating the full equations of motion over the appropriate dimensions, which in turn results in the loss of capability of predicting the state variables in the missing dimensions. A two-dimensional, vertically averaged approach is applied when vertical variations of velocity and temperature are not significant, which is occasionally the case for shallow water bodies. The density variations are not considered, and the vertically averaged continuity and Navier – Stokes equations are solved. In three-dimensional models, the full equations of motion are solved. For the simulation of hydrodynamic processes in Hartwell Lake, a three-dimensional approach is required due to the complex geometry and bathymetry of the

reservoir, and vertical variations of velocities and densities are potentially significant in the sediment transport modeling.

Numerous three dimensional models that describe hydrodynamics and sediment transport exist. The models listed below were recognized as widely used at a workshop held by the U.S. Geological Survey (USGS, 2000) to explore the development of a community sediment transport model.

EFDC is a public domain, curvilinear-orthogonal horizontal coordinates, stretched vertical (sigma) coordinates, coupled hydrodynamic, water-quality, and sediment transport model developed by Hamrick (1996). It is maintained by TetraTech Inc. and is currently being supported by the U. S. Environmental Protection Agency. It can simulate hydrodynamics in rivers, lakes, reservoirs, wetland systems, estuaries, and coastal oceans. The solution technique used is a finite volume – finite difference spatial discretization with a staggered C grid. The Mellor and Yamada (1982) 2-1/2 order turbulence closure model is used. This turbulence closure model relates the vertical turbulent viscosity and diffusivity to the turbulent intensity, turbulent length scale and Richardson number.

The MIKE 3 package is marketed by the Danish Hydraulic Institute (DHI, 2003). It can simulate flows in lakes, estuaries, and coastal oceans. The user can choose between a hydrostatic pressure assumption and a generalized sigma coordinate transformation; and a non-hydrostatic pressure formulation and a z-level coordinate formulation. The solution technique used is an implicit, finite difference scheme on a staggered grid and solved non-iteratively by the alternating direction implicit technique. Five turbulence closure models are available: i) a constant eddy viscosity, ii) the zero equation (Smagorinsky) model, iii) the k- one equation model, iv) the k-ε (two equation) model, v) the

combination of the Smagorinsky model for the horizontal and the k-ε model for the vertical direction.

CH3D-WES, is derived from an earlier version of the Univ. of Florida model (Sheng and Lick, 1979) and used for engineering studies by the U. S. Army Corps of Engineers (USACE, 1996). It can simulate flows in lakes, estuaries, and the coastal ocean. The solution technique used is an implicit, finite difference scheme on a staggered grid. A second-order upwind differencing scheme is used to solve the convective terms, and a third-order scheme (QUICKEST) is used to solve the advective terms. A second-order moment turbulence closure model is used. The model relates the vertical turbulent viscosity and diffusivity to the turbulent intensity, turbulent length scale and Richardson number.

ECOM-SED, is built around the Blumberg-Mellor hydrodynamic model and available as free-ware by HydroQual, Inc. and Delft Hydraulics (Blumberg-Mellor, 1987). It can simulate rivers, lakes, reservoirs, estuaries, and the coastal ocean. The solution technique used is an implicit scheme for solving the gravity wave so that the need for separate barotropic and baroclinic time steps is eliminated. As in EFDC, the Mellor and Yamada (1982) 2-1/2 order turbulence closure model is used.

Numerical models have been frequently applied to lakes, rivers and estuaries to quantify hydrodynamics and sediment transport. Sheng and Lick (1979) developed a three-dimensional model of hydrodynamics and sediment transport and applied it to Lake Erie. Sheng (1984) extended the model and applied it to the Mississippi River Sound. Sheng et al. (1991) described the development of a comprehensive fine sediment transport model and application of the model to Lake Okeechobee in Florida. In Lake

Okeechobee, suspended sediment dynamics were primarily influenced by wave induced resuspension and current-induced vertical mixing.

De Cesare et al. (2001) investigated the impact of turbidity currents on reservoir sedimentation, using both a numerical model and velocity measurements near the bottom of Lake Luzzone (reservoir) in Switzerland. They showed that the inflow, carrying sediments, plunged, and that the suspended load was carried along the reservoir bottom to the dam in the form of turbidity currents.

Podsetchine and Schernewski (1999) investigated the importance of the spatial wind irregularity on the circulation in a shallow lake (Lake Belau in Germany) using a two-dimensional vertically averaged numerical model. They illustrated that in small lakes the influence of the surrounding topography on the wind field was greater than in large lakes, and consequently the flow field changed drastically when the spatial variation of wind was considered. When the surface velocities were simulated with a constant wind, they observed that the flow followed the wind in the shallow parts of the lake and formed a return flow in the deeper parts, thus forming two horizontal gyres. However, when velocities were simulated with variable wind a single gyre was formed, the center of which was located in the middle of the lake.

Beletsky and Schwab (1998) applied the Princeton Ocean Model (POM) of Blumberg and Mellor (1987) to Lake Michigan to simulate thermal structure and circulation. The model was able to reproduce the thermal structure measured at two buoys located in the southern and northern parts of the lake. However, they observed that the model could not simulate the temperature in the thermocline area. They also observed that simulated internal waves were less pronounced than observations. They concluded

that the model generated excessive vertical diffusion that resulted in a smaller vertical temperature gradient than was measured. When zero horizontal diffusion was simulated, no improvement in the results was observed.

2.2 Thermally Stratified Reservoirs

Mixing in lakes and reservoirs is influenced by stratification, which is the layering of waters of different density, and occurs in a reservoir when colder water underlies warmer water (Figure 2). This condition can be sustained only in deeper waters because wind forcing is usually sufficient to keep shallow water bodies from stratifying. While wind influences the surface waters of all lakes, its ability to mix the entire water column in summer-stratified lakes is greatly reduced. This is because the strong density gradients within the metalimnion (transition zone between warm and cold water) act like a physical barrier between the epilimnion (warm surface layer) and hypolimnion (cold deep layer). Although not an absolute barrier, it takes strong winds to disrupt it.

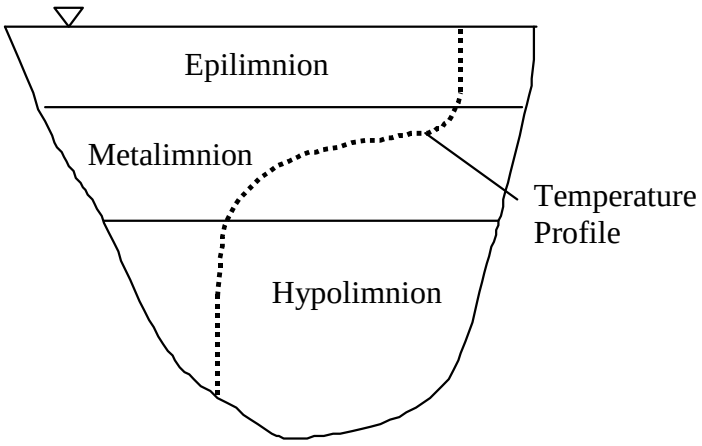

Figure 2 Layers of thermal stratification in a typical reservoir.

In the literature on modeling of thermally stratified reservoirs, generally two types of studies can be found: studies discussing the hydrodynamic processes in stratified lakes, and those describing the application of numerical hydrodynamic models to lakes and reservoirs. In this section, studies describing physical processes in stratified lakes and reservoirs, challenges encountered in modeling them, and the existing numerical models and their capabilities are emphasized.

Hodges et al. (2000) summarized the sources of energy for transport, turbulence, internal waves and mixing in stratified reservoirs as: wind, surface thermodynamics and inflow dynamics. They focused primarily on the formation and behavior of the internal waves. They explained that internal waves were initiated as a result of tilting of a thermocline as opposed to the barotropic (density is a function of pressure only) tilt resulting from downwind transport of the surface water when the wind-mixed layer was sufficiently deep. Internal waves may transfer energy to other internal waves, which dissipate eventually. As they propagate, internal waves develop an oscillating motion in the hypolimnion (cold, lower layer). The internal wave response depends on stratification, which is a result of the intensification of solar radiation penetration into the water column, and destratification due to vertical mixing.

Hodges et al. (2000) also described the challenges of numerically modeling transport processes in stratified lakes. Since wind over an entire lake is directly influenced by the surrounding topography, use of a uniform wind from one measurement station may not lead to correct simulation of circulation gyres. Instead, multiple wind stations around the lake must be monitored and data from these stations used in modeling the hydrodynamic circulation. A second problem is availability of accurate bathymetry

data representing the old riverbed (thalweg). As dense inflow enters the reservoir, it will seek the lowest path. If the thalweg is not represented correctly in the model, the model may indicate that the inflow is diluted and slowed down, when in fact cold water, transporting sediments and/or solutes could travel all the way to the reservoir outlet.

Hodges et al. (2000) also discussed the significance of the accurate representation of the depth of the wind-mixed surface layer that has an important role in the setup of internal waves. They stated that classic higher order turbulence schemes (e.g., the Mellor-Yamada model) under-predict the depth of the wind-mixed surface layer. Under-prediction of this depth leads to under-prediction of the baroclinic (density as a function of both temperature and pressure) tilt that initiates the internal waves. They proposed the use of mixed-layer models where baroclinic tilt is described as a function of wind shear velocity, depth, and reduced gravity of stratification. They also discussed the tendency of numerical models to artificially diffuse sharp temperature gradients faster than physical processes. They proposed use of a filter applied vertically to reduce the effects of numerical diffusion. Finally, they discussed the implications of the hydrostatic assumption, where dynamic pressure and vertical acceleration terms are neglected in the vertical equation of motion. They stated that problems arise in the use of the hydrostatic assumption when dealing with internal waves. In a hydrostatic model, internal waves will steepen and break, introducing a form of numerical diffusion, and will damp faster than physical processes.

Rueda and Schladow (2003) described the internal dynamics of a shallow, multibasin lake (Clear Lake in California) that mixes vertically multiple times per year (polymictic) under strong wind forcing. At the lake considered, wind acts during the

afternoon and evening hours to generate horizontal temperature gradients. Wind forcing becomes negligible at night and the baroclinic pressure gradients resulting from temperature differences drive currents. They deployed thermistor chains, acoustic Doppler current profilers and meteorological stations to collect air and water temperature, water velocity and wind data. A conceptual model of internal circulation based on field observations and previous literature was proposed. Internal dynamics of the lake were characterized by the diurnal cycles of setup and relaxation of horizontal temperature gradients formed by winds. They looked at the integrated potential energy, calculated from a temperature profile describing the stratification in a water column, and used it to trace the advection of cold or warm water. They estimated the magnitude of interface displacement due to upwelling induced by winds.

Rueda and Schladow (2003) also illustrated that the wind-driven motion moves surface water downward and deep water upward. Baroclinic currents were described as a function of temperature, gravity, thermal expansion coefficient and water depth. In a subsequent paper, Rueda et al. (2003) compared the field measurements to the results obtained using an existing hydrodynamic model called SI3D-L. SI3D-L, developed by Smith (1997), solves the continuity, Reynolds-averaged Navier–Stokes equations for momentum, a transport equation for temperature, and an equation of state relating temperature to fluid density. They examined the response of the lake to wind stress. They also looked at the vertical cross-section and observed that in a weakly stratified system, a transverse circulation forms in the wind direction, with water flowing to the right of the wind at the surface and to the opposite direction at the bottom. They found that in a weakly stratified region, the momentum in the water column is easily transferred,

whereas in a stratified flow, turbulent transfer is reduced.

Jin et al. (2000) described the application of EFDC to a large, shallow (< 5 m) lake (Lake Okeechobee in Florida) to simulate water surface elevations, velocities and temperatures. The impacts of long-wave radiation, sensible heat transfer, and latent heat transfer were modeled. They also simulated lakewide circulation patterns, and observed that surface velocities matched the dominant wind direction in the shallow regions, with reverse flows on the bottom observed.

DeGasperi et al. (2000) applied the 2-D (in horizontal) Box Exchange Transport Temperature Ecology Reservoir (BETTER) model developed by the Tennessee Valley Authority to simulate the development of temperature stratification and mixing among three branches of a reservoir in Oregon. One of the reservoir branches is affected by thermal springs and has warmer water, which tends to stay at the surface. Juvenile fish tend to follow this warmer branch, resulting in an unsuccessful migration. The seasonal response of the reservoir to structural and operational modifications was predicted using the BETTER model. The model setup divided the reservoir into different boxes, each with a specified volume, surface area and a downstream conveyance area. The model was intended to simulate heating. However, it was very much limited in terms of simulation of hydrodynamic processes, since momentum terms were not included in the flow equations, and the model did not simulate 3-D flow. In another study, this model was coupled with a 3-D hydrodynamic model (EFDC) to allow for evaluation of the effects of various flow modification structures on stratification and circulation (Yang et al., 2000).

Yang et al. (2000) applied EFDC to Lake Billy Chinook in Oregon to simulate the density driven circulation in the lake. The goal was to identify reservoir geometry

modifications suitable for the downstream passage of juvenile salmon. They also conducted Lagrangian particle tracking to investigate how the incoming river flow traveled through the reservoir. They observed that the river with colder water plunged to the bottom and was withdrawn at the downstream powerhouse intake. The bottom velocities were as strong as those in the surface layer. The surface water moved downstream in the river with warmer water, while in the river with colder water the surface water moved upstream. Also, the surface velocities were much stronger than the bottom layer velocities in the river with warm water.

Gal et al. (2002) simulated thermal dynamics of a natural lake located in Israel using a one-dimensional hydrodynamic model called DYRESM. This model was designed for predicting the vertical distributions of temperature, salinity and density in lakes and reservoirs. 3-D mixing processes were represented parametrically, but only their effect on vertical stratification was considered in the calculations. So the effect of these processes were calculated explicitly and vertical stratification was modified appropriately. Surface fluxes, including evaporation and rainfall, are computed by bulk aerodynamics formulae. Long wave radiation, sensible heat flux, and latent heat flux were assumed to operate only on the surface layer. Short wave radiation heat input decayed through the water column as described by the Beer-Lambert law. Sensitivity analysis indicated that the results were mostly sensitive to long wave radiation and wind.

Hines and Willmott (2002) developed an analytical solution of the linearized transport equation for the heat and salt fluxes for a semi-infinite ocean bounded by an eastern wall. Solutions forced by wind stress alone and by the combined effect of wind and stratification were considered. They found that the depth of penetration for

temperature (advection of warm water downwards) was very sensitive to the vertical diffusivity of heat employed in the solution.

Bonnet et al. (2000) described a different type of numerical model to simulate the thermal structure of a stratified lake in France. Their model solves the 1-D vertical heat transfer equation, which takes into account internal heat sources/sinks, advection due to inflow/outflow and molecular and eddy diffusions. Most of the numerical models discussed above are based on turbulence closure schemes, where the vertical transport rates are related to turbulent kinetic energy (i.e. EFDC, CH3D, DYRESM, ECOM, SI3D-L). The basic equation used in the process expressed time-dependent temperature as a function of vertical diffusion coefficient, vertical advective flow and a source term that represented surface-atmospheric changes. The temperature equation was solved for each vertical layer. They investigated the impact of the outlet level at different elevations at the dam on the thermal structure of the lake. They found that the vertical thermal structure depends on the outlet level, and if a lower outlet is used in summer, the thermocline moves deeper. They also observed that the advective fluxes change direction and go downwards if a deeper outlet is used. Their conclusions coincide with the fact that at high discharges, the thermocline level is lowered (drawdown) to the outlet level and radial flow will be withdrawn from all directions.

2.3 Erosion of Cohesive Shorelines

Erosion is the detachment of particles of soil and surficial sediments and rocks by hydrological processes. Bed shear stress is the primary flow-induced parameter characterizing the erosive force along shorelines. The rate of erosion depends on the bed shear stress, eroding and pore fluid compositions, and how the deposit is formed. Mehta

et al. (1989) describes erosion of cohesive sediments in three modes. 1) Surface erosion, occurring at low to moderate values of the excess shear stress, 2) mass erosion, occurring when rapidly accelerating flows cause the bed to fail along some plane below the surface and clumps of material are eroded, and 3) re-entrainment of a stationary suspension when wind-generated waves, superimposed on mean currents, act on recently formed fluid mud.

Most previous studies of shoreline change have addressed noncohesive sediments in coastal environments. Mobility of a noncohesive sediment can be predicted by knowing the grain size of the sediment, specific gravities of water and sediment, flow velocity, the slope of the bottom, and viscosity of the water, but this is not the case for cohesive soils. The erosion process in a cohesive sediment environment is different from that of a sandy shore, mainly because in a cohesive shore it is irreversible. Since the settling velocity for cohesive sediments is much less than that of sand and gravels, the cohesive sediments are easily advected away from the shore after becoming suspended in the water column. Cohesion is governed by the electrochemistry of the sediment and water, which makes prediction of erosion and mobility more complicated. Prediction of shore erosion also requires information on the shape of the beach profile, and the environmental conditions (e.g. waves, mean flows, and water levels).

Shoreline erosion studies in a cohesive environment fall into two categories: 1) studies conducted to improve the understanding of the fundamental principles of hydrodynamic processes that lead to erosion of the soil, and 2) description and application of different methods to quantify erosion. In the first category, laboratory or field experiments have been conducted to investigate the driving forces for erosion

(Arulanandan, 1975; Mehta et al., 1989; Zreik et al., 1998). Researchers have investigated the relation between the erosional resistance of cohesive soils and their physical properties, such as plasticity index, vane and unconfined shear strengths, dry density and yield stress. The effects of temperature and the physicochemical properties of the fluid on erosional behavior of soils have also been investigated (Zreik et al., 1998).

USACE (1998) summarized the fundamental principles controlling erosion of cohesive shores as follows: 1) the erosion of consolidated cohesive sediment is irreversible, 2) the long-term shoreline recession is directly related to the rate of nearshore downcutting (erosion) (Figure 3), and 3) the local rate of downcutting is proportional to the nearshore slope. Coakley et al. (1986) proposed that, outside the surf zone, the downcutting process is driven by shear stresses generated by the orbital motion under waves.

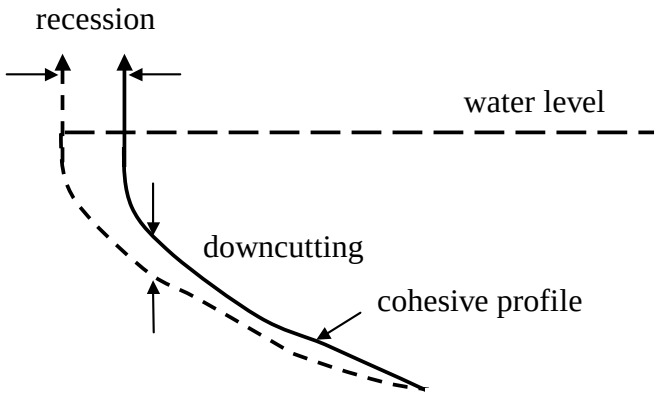

Figure 3 Shoreline recession and profile downcutting illustration (adapted from USACE, 1998).

Different methods have been developed to quantify shoreline erosion in lakes and reservoirs. One approach is to predict wave conditions at a given site from available wind time series data. Predicted deep water waves are transformed to nearshore conditions using a numerical or analytical wave transformation model. Finally, erosion rate is related to wave power at breaking. Methods developed by Kamphius (1986), Nairn et al. (1986), and Penner (1993) are examples of this approach. Kamphius (1986) considered two portions of the foreshore, on either side of the wave breakpoint. The erosion rate was related to wave power both inside and outside the breaking zone.

Nairn et al. (1986) related downcutting to the shear stress generated by orbital velocities under unbroken waves and to the rate of wave energy dissipation for broken waves. The beach profile was divided into several sections of specified depth intervals. Wave setup and wave energy were calculated for each wave condition.

Penner's (1993) method consisted of using a wave hindcast to determine the amount of wave energy that reaches a shoreline or bluff. The rate of shore recession (lateral translation) was calculated as a function of wave energy and an erodibility coefficient, *Ke* (square meters/ton). Erodibility coefficients were calibrated based on a known profile retreat rate. All of the methods used to predict the shoreline erosion in the literature require a calibration coefficient. The methods described here are based on wave conditions and do not relate erosion rate to beach profile shape.

Long-term changes in shoreline morphology are commonly quantified by comparing available topographic maps and aerial photos. Typically, shorelines are digitized and corrected to a common datum and the shoreline changes with time are determined (Leatherman, 1983; Paine and Morton, 1986). Common sources of errors are

inaccuracy of the maps, distortion of the aerial photos, and subjectivity when identifying shorelines. In order to determine the location of shorelines, usually the high water line (HWL), indicated by the change in color between the wetted and dry beach is used (Dean and Dalrymple, 2001).

As an example, Paine and Morton (1986) studied historical erosion of the Texas coast by comparing available topographic maps and aerial photos. The shoreline in the Galveston Bay system retreated an average of 0.7 m/yr over 132 years. Anglin (1986) documented that bluffs on Lake Ontario have receded approximately 30 m in 37 years with an average rate of 0.8 m/yr. Fuller (1986) studied shore and lakebed erosion in Lake Erie and estimated a recession rate of 2.3 m/yr. A study of Lake Diefenbaker in Canada by Mollard (1986) showed an average recession rate of 1-3 m/yr during the first decade of reservoir operation.

Remedial measures taken to stop erosion of cohesive shores can be summarized as follows (USACE, 1998): 1) beach nourishment to increase the sand cover volume to a level sufficient to protect the underlying cohesive shore, 2) construction of offshore breakwaters, and 3) construction of revetments. Ferguson and Overend (1998) performed an inventory of shoreline erosion problem sites on Clark's Hill/Thurmond Lake, a U.S. Army Corps of Engineers reservoir near Augusta, Georgia, on the Savannah River. Different methods to prevent bluff retreat in the lake were discussed in the paper.

Yu et al. (2000) conducted laboratory experiments to investigate the deposition behavior of fine sediments in a reservoir. They used both noncohesive (silica) and cohesive (kaolin) sediments as suspended sediment. In the upstream portion, the deposition rate was significant due to the noncohesive sediments, and the concentration

of suspended sediments near the bed was large. Toward the downstream end of the reservoir, the size of the suspended sediments became smaller, the rate of deposition decreased, and the vertical concentration profile became more uniform.

In a stratified flow, the kaolin turbidity current deposited along the flow path due to flocculation of suspended kaolin particles, and the concentration profile increased near the bed. Kaolin with a dispersing agent added did not deposit. For the stratified case, the velocity profile was dominated by the concentration distribution. Investigation of the deposition rates along the flow path indicated that the deposition rate for noncohesive sediments decayed exponentially along the path, while it increased for cohesive sediments.

Most of the studies (Blumberg et al. 1999; Jin et al. 2000; Yang et al. 2000; Rueda and Schladow 2003; Podsetchine and Schernewski 1999; Sheng et al. 1991) previously conducted and discussed here, involve modeling of hydrodynamics in a setting different from the application presented in this dissertation. Lake Okeechobee in Florida, Clear Lake in California, Lake Billy Chinook in Oregon are shallow, large lakes (depth ~ 5 m) while Hartwell Lake can be as deep as 50 m along the thalweg. In addition, Hartwell Lake is heavily stratified during the late summer, which makes the hydrodynamics even more complicated. Numerically investigating the effect of the stratification on sediment transport in such an environment is a contribution beyond that of the previous studies.

The terrain of Hartwell Lake is near the southern terminus of the Appalachian mountain chain with sediments containing high fractions of silt and clay. Although different approaches to modeling the erosion rates of cohesive shorelines are available in the literature, this study contributes as an improved approach that accounts for the beach

profile shape. Also, to date, no previous study has modeled the potential non-point source contributions from shoreline erosion to the reservoir sediment budget together with the source of sediments being supplied by the tributaries.

CHAPTER 3

THREE-DIMENSIONAL NUMERICAL HYDRODYNAMIC AND SEDIMENT TRANSPORT MODEL

For the description of the hydrodynamic processes and sediment transport in Hartwell Lake, an efficient numerical model that can simulate flow processes in all three dimensions, and a widely used and tested model with the capabilities of simulating transport of cohesive sediments was required. The Environmental Fluid Dynamics Code (EFDC) developed by Hamrick (1996) was selected for this purpose. EFDC is designed to simulate flows and transport processes in surface water systems, including rivers, lakes, estuaries, wetlands and coastal areas. The structure of the EFDC model includes four major modules: (1) a hydrodynamic model, (2) a water quality model, (3) a sediment transport model, and (4) a toxics model. EFDC is capable of simulating both cohesive and noncohesive sediment transport, near-field and far-field discharge dilution from multiple sources, eutrophication processes, and the transport and fate of toxic contaminants in the water and sediment phases. In this study, only the hydrodynamic and sediment transport modules were used.

The physical processes represented in the EFDC model and many aspects of the computational scheme are similar to those in the Blumberg-Mellor model (Blumberg and Mellor, 1987) and the U. S. Army Corps of Engineers' Chesapeake Bay model (Johnson et al., 1993). The EFDC model solves the three-dimensional, vertically hydrostatic, free surface, turbulent averaged equations of motion for a variable density fluid. EFDC uses a stretched (sigma) vertical coordinate and Cartesian or curvilinear, orthogonal horizontal coordinates. Dynamically coupled transport equations for turbulent kinetic energy,

turbulent length scale, salinity and temperature are also solved. The numerical scheme used in EFDC to solve the governing equations uses a second-order accurate spatial finite-difference scheme on a staggered or C grid. For a detailed description of EFDC, the reader is referred to Hamrick (1992), and Hamrick and Wu (1997).

3.1 Governing and Boundary Equations

In the EFDC model, for the realistic representation of horizontal boundaries, the governing equations are formulated such that the horizontal coordinates, x and y are curvilinear. To provide uniform resolution in the vertical direction, a stretching transformation is used:

$$z = \left(z^* + h\right) / \left(z_s^* + h\right) \tag{1}$$

The equations of motion and transport are turbulence-averaged, because prior to averaging, although they represent a closed set of instantaneous velocities and concentrations, they can't be solved for turbulent flows (Launder and Sandham, 2002). A statistical approach is applied, where the instantaneous values are decomposed into mean and fluctuating values to enable the solution. Additional terms are introduced to the equations for the mean flow those representing the turbulence terms. Turbulent equations of motion are formulated to utilize the Boussinesq approximation for variable density. Boussinesq approximation accounts for variations in density only in the gravity term. This assumption simplifies the governing equations significantly, but may introduce large errors when density gradients are large. The momentum equations solved in the model are obtained in the following form (Hamrick and Wu, 1997):

$$\begin{aligned}
&\partial_t\left(m_x m_y H u\right)+\partial_x\left(m_y H u u\right)+\partial_y\left(m_x H v u\right)+\partial_z\left(m_x m_y w u\right)-f_e m_x m_y H v \\
&=-m_y H\partial_x\left(p+p_{atm}+\phi\right)+m_y\left(\partial_x z_b^*+z\partial_x H\right)\partial_z p+\partial_z\left(m_x m_y \frac{A_v}{H}\partial_z u\right) \\
&\quad+\partial_x\left(\frac{m_y}{m_x} H A_H \partial_x u\right)+\partial_y\left(\frac{m_x}{m_y} H A_H \partial_y u\right)-m_x m_y c_p D_p\left(u^2+v^2\right)^{1/2} u
\end{aligned} \tag{2}$$

$$\begin{aligned}
&\partial_t\left(m_x m_y H v\right)+\partial_x\left(m_y H u v\right)+\partial_y\left(m_x H v v\right)+\partial_z\left(m_x m_y w v\right)+f_e m_x m_y H u \\
&=-m_x H\partial_y\left(p+p_{atm}+\phi\right)+m_x\left(\partial_y z_b^*+z\partial_y H\right)\partial_z p+\partial_z\left(m_x m_y \frac{A_v}{H}\partial_z v\right) \\
&\quad+\partial_x\left(\frac{m_y}{m_x} H A_H \partial_x v\right)+\partial_y\left(\frac{m_x}{m_y} H A_H \partial_y v\right)-m_x m_y c_p D_p\left(u^2+v^2\right)^{1/2} v
\end{aligned} \tag{3}$$

where

$u, v =$ horizontal velocity components in the dimensionless curvilinear-orthogonal horizontal coordinates x and y, respectively;

$w =$ vertical velocity in the stretched vertical coordinate z;

$m_x, m_y =$ scale factors of the horizontal coordinates;

$z_s^*, z_b^* =$ physical vertical coordinates of the free surface and bottom bed;

$H =$ instantaneous local water depth;

$\phi =$ free surface potential which is equal to gz_s^*,

$f_e =$ Coriolis acceleration f_e incorporates the curvature acceleration terms, with the Coriolis parameter, f as follows:

$$m_x m_y f_e = m_x m_y f - u\partial_y m_x + v\partial_x m_y \tag{4}$$

$A_H =$ horizontal turbulent viscosity (m^2/s)

A_v = vertical turbulent viscosity (m^2/s) that relates the shear stresses to vertical shear of the horizontal velocity components as:

$$\left(\tau_{xz}, \tau_{yz}\right) = A_v H^{-1} \partial_z (u, v) \tag{5}$$

p_{atm} = kinematic atmospheric pressure, referenced to (divided by) water density

$\partial_z p =$ excess hydrostatic pressure referenced to density in the water column calculated by:

$$\partial_z p = -gHb = -gH(\rho - \rho_o)\rho_o^{-1} \tag{6}$$

where

b = buoyancy;

ρ, ρ_0 = local actual and reference (density of pure water at 4° C) water densities;

The last terms in equations (2) and (3) represent vegetation resistance where

c_p = resistance coefficient;

D_p = dimensionless projected vegetation area normal to the flow per unit horizontal area;

The three-dimensional continuity equation in the stretched vertical and curvilinear-orthogonal horizontal coordinate system is:

$$\partial_t (m_x m_y H) + \partial_x (m_y H u) + \partial_y (m_x H v) + \partial_z (m_x m_y w) = Q_H \tag{7}$$

where

Q_H = volume sources and sinks including rainfall, evaporation, infiltration and lateral inflows and outflows having negligible momentum fluxes.

The continuity equation has been integrated with respect to *z* over the interval (0,1; where *z* is set to 0 at the bed and 1 at the surface) to produce the depth integrated continuity equation as follows:

$$\partial_t\left(m_x m_y H\right)+\partial_x\left(m_y H\int_0^1 u dz\right)+\partial_y\left(m_x H\int_0^1 v dz\right)=0 \tag{8}$$

The transport equation for a dissolved or suspended material having a mass per unit volume concentration *C*, is

$$\begin{aligned}&\partial_t\left(m_x m_y HC\right)+\partial_x\left(m_y HuC\right)+\partial_y\left(m_x HvC\right)+\partial_z\left(m_x m_y wC\right)-\partial_z\left(m_x m_y w_{sc}C\right)\\&\quad=\partial_x\left(\frac{m_y}{m_x}HK_H\partial_x C\right)+\partial_y\left(\frac{m_x}{m_y}HK_H\partial_y v\right)+\partial_z\left(m_x m_y\frac{K_v}{H}\partial_z C\right)+Q_c\end{aligned} \tag{9}$$

where

K_v, K_H = The vertical and horizontal turbulent diffusion coefficients;

w_{sc} = settling velocity;

C = concentration of suspended material;

Q_c = external sources and sinks and reactive internal sources and sinks.

The vertical turbulent viscosity, A_v, and the diffusivity, K_v must be specified for the solution of the momentum and the transport equations. EFDC uses the 2-1/2 turbulence closure model developed by Mellor and Yamada (1982) and modified by Galperin et al. (1988) to calculate the vertical turbulent viscosity and diffusivity.

Isotropic eddy viscosity models such as i) The zero equation (mixing length) model in which the mixing length is assumed proportional to a characteristic length scale

of the flow and obtained algebraically; ii) The one-equation model, which employs one additional partial differential equation for the velocity scale and the length scale is specified algebraically; and iii) The two-equation (k-ε) model, which employs two partial differential equations, one for the velocity scale and one for the length scale, are widely used in other hydrodynamic models. They assume that there exists an analogy between the action of viscous stresses and Reynolds stresses on mean flow; the transport of momentum by turbulent fluctuations is assumed similar to the random molecular motion in laminar flows (Sotiropoulos, 2001).

Isotropic eddy viscosity models are based on the Boussinesq approximation, and cannot reproduce the anisotropy of the Reynolds stresses. These models have been shown to fail in flows involving secondary motions such as flows in strongly curved ducts and channels (Sotiropoulos, 2001). When the fluctuations and the scale of the turbulence are not constant and the turbulence effects develop in different directions, equations for turbulent stress and mass flux are used instead of the kinetic energy equation (k). The exact equation is derived for the Reynolds stresses by subtracting the time-dependent Navier – Stokes equation from the time-averaged equation and by multiplying the resulting equation by the fluctuating velocities. The Mellor-Yamada 2-1/2 turbulence closure model used in EFDC assumes a local balance between production and dissipation of turbulent kinetic energy and use a set of assumptions that reduce the stress and flux relations to a set of algebraic equations.

The Mellor-Yamada model relates the vertical turbulent viscosity, A_v, and diffusivity, K_v, to the turbulent intensity, q, a turbulent length scale, l, and a turbulent intensity and length scale-based Richardson number, R_q.

$$A_v = \phi_A q l \tag{10}$$

where;

$$\phi_A = \frac{A_0\left(1 + R_1^{-1} R_q\right)}{\left(1 + R_2^{-1} R_q\right)\left(1 + R_3^{-1} R_q\right)}$$

$$A_0 = A_1\left(1 - 3C_1 - \frac{6A_1}{B_1}\right) = \frac{1}{B_1^{1/3}}$$

$$R_1^{-1} = 3A_2 \frac{\left(B_2 - 3A_2\right)\left(1 - \frac{6A_1}{B_1}\right) - 3C_1\left(B_2 + 6A_1\right)}{\left(1 - 3C_1 - \frac{6A_1}{B_1}\right)}$$

$$R_2^{-1} = 9A_1A_2$$

$$R_3^{-1} = 3A_2\left(6A_1 + B_2\right)$$

$$K_v = \phi_K q l \tag{11}$$

where;

$$\phi_K = \frac{K_0}{\left(1 + R_3^{-1} R_q\right)}$$

$$K_0 = A_2\left(1 - \frac{6A_1}{B_1}\right)$$

The so-called stability functions, ϕ_A and ϕ_K, account for reduced and enhanced vertical mixing or transport in stable and unstable vertically density stratified environments, respectively. Mellor and Yamada (1982) specify the constants A_1, B_1, C_1, A_2, and B_2 as 0.92, 16.6, 0.08, 0.74, and 10.1, respectively.

The turbulent intensity and the turbulent length scale are determined by a pair of transport equations:

$$\partial_t\left(m_x m_y H q^2\right)+\partial_x\left(m_y H u q^2\right)+\partial_y\left(m_x H v q^2\right)+\partial_z\left(m_x m_y w q^2\right)$$
$$=\partial_z\left(m_x m_y \frac{A_q}{H}\partial_z q^2\right)-2m_x m_y\frac{Hq^3}{B_1 l} \tag{12}$$
$$+2m_x m_y\left(\frac{A_v}{H}\left(\left(\partial_z u\right)^2+\left(\partial_z v\right)^2\right)+\eta_p c_p D_p\left(u^2+v^2\right)^{3/2}+gK_v\partial_z b\right)+Q_q$$

$$\partial_t\left(m_x m_y H q^2 l\right)+\partial_x\left(m_y H u q^2 l\right)+\partial_y\left(m_x H v q^2 l\right)+\partial_z\left(m_x m_y w q^2 l\right)$$
$$=\partial_z\left(m_x m_y \frac{A_q}{H}\partial_z\left(q^2 l\right)\right)-m_x m_y\frac{Hq^3}{B_1}\left(1+E_2\left(\frac{l}{\kappa H z}\right)^2+E_3\left(\frac{l}{\kappa H(1-z)}\right)^2\right) \tag{13}$$
$$+m_x m_y E_1 l\left(\frac{A_v}{H}\left(\left(\partial_z u\right)^2+\left(\partial_z v\right)^2\right)+gK_v\partial_z b+\eta_p c_p D_p\left(u^2+v^2\right)^{3/2}\right)+Q_l$$

where (E_1, E_2, E_3) = (1.8, 1.33, 0.25). The third term on the last line of these two equations represents net turbulent energy production by vegetation drag where η_p is a production efficiency factor that has a value less than one. The terms Q_q and Q_l may represent additional source-sink terms such as subgrid scale horizontal turbulent diffusion.

Mellor and Yamada (1982) classified the simplified Reynolds stress equations as the Level 3 Model when all terms in the model equations are scaled. The Level 3 model was further simplified and called the Level 2 model when all derivative and diffusion terms are neglected. However, in situations where the neglected advective and diffusion terms are not small, i.e., in convective entrainment at a density interface in stably stratified environments, an alternative model, Level 2-1/2 Model, was suggested)Mellor and Yamada, 1982). In the Level 2-1/2 Model, derivatives and diffusion terms are neglected in temperature equations so that differential equations for the temperature

variance and water vapor variance are not solved.

In addition, in the 2-1/2 turbulence closure scheme, turbulent energy is calculated from the transport equation and the Reynolds stress equations are solved using the local equilibrium to estimate the turbulent length scale and turbulent intensity algebraically near the bed. Galperin et al. (1988) modified the scheme so that the turbulent exchange coefficients, ϕ_A and ϕ_K, were simplified to be non-dimensional functions of the vertical buoyancy gradient. The near bed balance assumes equilibrium between production of turbulence by shear stresses, vegetation drag, and unstable density stratification, the suppression of turbulence by stable stratification, and dissipation. In the absence of vegetation and stratification, and assuming stresses are obtained from a quadratic law, the turbulent kinetic energy equation can be written as:

$$q^4 - B_1\left(gH\frac{l}{H}\frac{K_v}{H}\partial_z b + \eta_p c_p D_p \frac{l}{H}\left(u^2+v^2\right)^{3/2}\right)q - \frac{B_1}{\phi_A}\left(\tau_{xz}^2+\tau_{yz}^2\right)=0 \tag{14}$$

Near the bed, for three-dimensional model applications, and over the depth of flow, for two-dimensional, vertically integrated applications, the turbulent length scale can be specified by the algebraic relationship:

$$\frac{l}{H} = \kappa z(1-z)^{\lambda} \tag{15}$$

The turbulent intensity, q at any level in the hydrodynamic and sediment boundary layers is specified algebraically as follows:

$$q^4 - B_1\left(\alpha g H \frac{l}{H}\frac{K_v}{H}\partial_z S + \eta_p c_p D_p \frac{l}{H}\left(u^2+v^2\right)^{3/2}\right)q - \frac{B_1}{\phi_A}\left(\tau_c^2 + \frac{1}{2}\tau_{wm}^2 + \frac{4}{\pi}\tau_c\tau_{wm}\cos\left(\psi_c - \psi_{wm}\right)\right) = 0 \quad (16)$$

where τ_c and τ_w are the current and wave shear stress magnitudes, respectively, and the wave shear stress is assumed to be periodic as follows:

$$\tau_w = \tau_{wm}\sin(\omega t)$$
$$\psi_w = \psi_{wm}\mathrm{sgn}\left(\sin(\omega t)\right)$$

For the solution of the momentum equations, the kinematic shear stresses are specified at the sediment bed and the free surface. At the free surface, the *x* and *y* components of the stress are specified by the water surface wind stress.

$$\left(\tau_{xz}, \tau_{yz}\right) = \left(\tau_{sx}, \tau_{sy}\right) = c_s\sqrt{U_w^2 + V_w^2}\left(U_w, V_w\right) \quad (17)$$

where

U_w, V_w = *x* and *y* components of the wind velocity 10 meters above the water surface;

c_s = wind stress coefficient defined by Wu (1982) as representing the best fit to a large number of available data sets:

$$c_s = 0.001\frac{\rho_a}{\rho_w}\left(0.8 + 0.065\sqrt{U_w^2 + V_w^2}\right) \quad (18)$$

ρ_a, ρ_w = Air and water densities.

Specification of the kinematic shear stresses highly depends on the correct approximation of the wind stress coefficient. Wu (1982) used a large number of data sets from different studies in the derivation of equation (18): all the studies estimated wind

stress coefficients based on data collected in open oceans. Effects of surrounding topography might be significant in a reservoir. Equation (18) holds best for wind velocities in the range of 8-20 m/s. Using this equation for very high and low wind conditions might introduce errors.

At the bed, the bed shear stress components are related to the bottom layer velocity components by the quadratic resistance formulation

$$(\tau_{xz}, \tau_{yz}) = (\tau_{bx}, \tau_{by}) = c_b \sqrt{u_1^2 + v_1^2}\,(u_1, v_1) \tag{19}$$

where the subscript 1 denotes a value from the bottom layer. Under the assumption that the near-bottom velocity profile is always logarithmic, the bottom stress coefficient is given by

$$c_b = \left(\frac{\kappa}{\ln(\Delta_1 / 2 z_o)} \right)^2 \tag{20}$$

where

κ = von Karman constant;

Δ_1 = dimensionless thickness of the bottom layer;

$z_0 = z_0^* / H$ = dimensionless roughness height.

Specification of the bottom stress coefficient highly depends on the correct approximation of the dimensionless roughness height and the thickness of the bottom layer defined by the stretched coordinate system in the vertical used by the EFDC. This assumption might introduce errors when associated with either or both high near bottom sediment concentrations and high frequency surface wave activity. The formulation of

hydrodynamic and sediment boundary layer parameterization for representing the bottom stress and the water column-bed exchange of sediment depends on the near bed turbulent kinetic energy balance. As stated previously, the near bed balance assumes an equilibrium between production of turbulence by shear stresses, vegetation drag, and unstable density stratification, the suppression of turbulence by stable stratification, and due to the dissipation.

3.2 Sediment Transport

The ideal advective transport scheme would control the dissipation of the scheme. The EFDC model uses the anti-diffusive MPDATA scheme (Smolarkiewicz et al., 1986) for the advective terms in the transport equation. The sources of dissipation and damping in the forward in time and upwind in space scheme are determined and a significant portion of the dissipation is eliminated by averaging between different time levels, providing a scheme that is second-order accurate in time. The physical horizontal diffusion terms are omitted, yielding the following equations (Tetra Tech, 1999):

$$\partial_t\left(m_x m_y H S_j\right)+\partial_x\left(m_y H u S_j\right)+\partial_y\left(m_x H v S_j\right)+\partial_z\left(m_x m_y w S_j\right)$$
$$-\partial_z\left(m_x m_y w_{sj} S_j\right)=\partial_z\left(m_x m_y \frac{K_V}{H}\partial_z S_j\right)+Q_{sj}^E+Q_{sj}^I \qquad (21)$$

where,

S_j = concentration of the j[th] sediment class;

Q_{sj}^E, Q_{sj}^I = external and internal source-sink terms. The external source-sink term includes point and non-point source loads, and the internal source-sink term includes reactive decay of organic sediments or the exchange of mass between sediment classes, if floc

formation and destruction were simulated.

Vertical boundary conditions for Equation (21) are:

$$-\frac{K_V}{H}\partial_z S_j - w_s S = J_{jo} : z \approx 0$$
$$-\frac{K_V}{H}\partial_z S_j - w_{sj} S_j = 0 : z = 1 \qquad (22)$$

where

J_0 = net water column-bed exchange flux defined as positive into the water column;

z = non-dimensional water depth, which is measured from the bottom and equal to one at the surface.

EFDC simulates the transport of non-cohesive sediment as bed load and suspended load. In both cases, erosion or resuspension of sediment begins when the bed stress exceeds the critical stress (Shields stress). According to the approach by Van Rijn (1984), no erosion or resuspension of sediment occurs when the bed velocity is less than the critical shear velocity. When the bed shear velocity exceeds the critical shear velocity, but is less than the settling velocity, sediment erodes from the bed and is transported as bed load. Sediment is transported as suspended load when the bed shear velocity exceeds the settling velocity.

The shear stress exerted by the near-bed flow, and the size and density of the non-cohesive material at the bed surface control the net flux of non-cohesive sediments at the water column-sediment bed interface. Under steady, uniform flow and sediment loading conditions, an equilibrium distribution of sediment in the water column tends to form, which is expressed analytically in terms of the near bed reference or equilibrium concentration, the settling velocity and the vertical turbulent diffusivity. Equilibrium

concentration assumes one-dimensional (vertical) transport, steady state without any sources and sinks. For unsteady or spatially varying flow conditions, the water column sediment concentration distribution varies as sediment load varies. The net flux is defined by:

$$J_o = w_s\left(S_{eq} - S_{ne}\right) \tag{23}$$

where

S_{ne} = actual concentration at the reference equilibrium level;

S_{eq} = equilibrium concentration;

w_s = settling velocity.

The above equation suggests that a net flux from the bed into the water column occurs when the near bed sediment concentration is less than the equilibrium value and a net flux to the bed occurs when the concentration exceeds the equilibrium concentration.

The water column-bed flux of non-cohesive sediments is specified as a function of the near bed equilibrium concentration and its corresponding reference distance above the bed. EFDC gives four different options for specification of equilibrium concentration. Users can either specify a constant value or choose between the formulations provided by Garcia and Parker (1991), Smith and McLean (1977) and Van Rijn (1984).

In order to use Smith and McLean's formulation, the critical Shields stress must be specified for each sediment size class. If the critical stress is not known, one can choose Van Rijn's formula since the critical Shields stress is calculated internally using a dimensional reference height, which is set to three grain diameters. Garcia and Parker's formulation accounts for armoring effects when multiple sediment classes are simulated,

and the EFDC model has the option to simulate armoring with this formulation. For armoring simulation, the current surface layer of the sediment bed defined by the dimensional reference height. In this study, only transport of cohesive sediments was of interest, since they have the potential to travel greater distances and carry PCBs.

Settling of cohesive sediments is more complicated than that for the non-cohesive sediments, since in addition to gravitational settling, cohesive sediments flocculate - forming larger groups of particles (called flocs or aggregates), the settling characteristics of which are significantly altered. Settling velocities are affected by gravitational forces, degree of flocculation, viscous drag on the particles and interactions among the particles. Settling velocities of cohesive sediments depend on the suspension properties (Mehta et al., 1990).

In the literature, the settling velocity of flocs is parameterized in terms of cohesive and organic material fundamental particle size, suspension concentration, and flow characteristics such as vertical shear of the horizontal velocity, shear stress, or turbulence intensity in the water column or near the sediment bed. In the EFDC model, several formulations are available:

i) Ariathurai and Krone (1976), which relates the effective settling velocity to the sediment concentration,

ii) Hwang and Mehta (1989), which relates the settling velocity to concentration in a parabolic form,

iii) Ziegler and Nisbet, (1994, 1995), which expresses the effective settling velocity as a function of the floc diameter,

iv) Shrestha and Orlob (1996), which relates the settling velocity to the magnitude

of the vertical shear of the horizontal velocity and sediment concentration.

The formulation proposed by Hwang and Mehta (1989) is based on observations of settling at six sites in Lake Okeechobee. When formulation parameters are validated with measurements, this is an appropriate formulation for a reservoir like Hartwell Lake, since it does not depend on flow characteristics, but is based on data from an energetic field condition having both currents and high frequency surface waves.

Fine sediments form flocs of various sizes and densities. The flocculation process is dynamic and complex, but as an approximation, Ziegler and Nisbet (1995) related settling velocity to median floc diameter. The formulation depends on parameters determined in lab experiments for fresh water. Settling velocity is approximated as:

$$w_s = a d_f^b \tag{24}$$

with the floc diameter given by:

$$d_f = \left(\frac{\alpha_f}{S\sqrt{\tau_{xz}^2 + \tau_{yz}^2}} \right)^{1/2} \tag{25}$$

where S is the sediment concentration, α_f is an experimentally determined constant and τ_{xz} and τ_{yz} are the x and y components of the turbulent shear stresses at a given position in the water column. Other constants have been experimentally determined:

$$a = B_1 \left(S\sqrt{\tau_{xz}^2 + \tau_{yz}^2} \right)^{-0.85} \tag{26}$$

$$b = -0.8 - 0.5 \log\left(S\sqrt{\tau_{xz}^2 + \tau_{yz}^2} - B_2 \right) \tag{27}$$

where $B_1 = 9.6 \times 10^{-4}$ and $B_2 = 7.5 \times 10^{-6}$.Water column-sediment bed exchange of cohesive sediments is controlled by the near-bed flow field and the bed shear strength of the surficial bed layer. The EFDC model uses the following formulation for the depositional flux:

$$J_o^d = \begin{cases} -w_s S_d \left(\dfrac{\tau_{cd} - \tau_b}{\tau_{cd}} \right) & : \tau_b \le \tau_{cd} \\ 0 & : \tau_b \ge \tau_{cd} \end{cases} \tag{28}$$

where

τ_b = stress exerted by the flow on the bed;

τ_{cd} = critical stress for deposition, which depends on the type of sediment material and floc physiochemical properties (Mehta et al., 1989);

S_d = near bed sediment concentration.

The above equation suggests that the net deposition to the bed occurs as the flow-induced bed surface stress decreases. The critical deposition stress is generally determined from laboratory or in-situ field observations. The depositional stress is an input parameter in the EFDC model. It is treated as a calibration parameter when no measurement is available. The depositional flux equation requires the specification of the near bed sediment concentration that is taken to be the suspension concentration in the bottom layer.

EFDC models the erosion of a cohesive bed in two distinct modes, mass erosion and surface erosion. When the bed stress exerted by the flow exceeds the depth varying

shear strength, mass erosion occurs. Transport into the water column by mass erosion can be formulated as:

$$J_o^r = w_r S_r = \frac{m_{me}(\tau_s \le \tau_b)}{T_{me}} \tag{29}$$

where

J_0 = erosion flux;

$w_r S_r$ = represents the boundary condition;

m_{me} = dry sediment mass per unit area of the bed having a shear strength, τ_s, less than the flow-induced bed stress, τ_b;

T_{me} = arbitrary time scale for the bulk mass transfer that can be taken as the numerical integration time step (Shrestha and Orlob, 1996).

Surface erosion occurs gradually when the bed shear stress is slightly greater than a critical erosion or resuspension stress, which is dependent on the shear strength and density of the bed. The shear strength of the cohesive sediment bed has been found to be linearly related to the bed bulk density by the formulation proposed by Hwang and Mehta (1989).

EFDC simulates the surface erosion by the following relationship:

$$J_o^r = w_r S_r = \frac{dm_e}{dt}\left(\frac{\tau_b - \tau_{ce}}{\tau_{ce}}\right)^{\alpha} \quad : \quad \tau_b \ge \tau_{ce} \tag{30}$$

where

dm_e / dt = surface erosion rate per unit surface area of the bed ($mg/hr - cm^2$);

τ_{ce} = critical stress for surface erosion or resuspension.

The critical erosion stress depends upon the sediment type and the state of consolidation of the bed, and is assumed to be equal to the surficial bed shear strength. The EFDC model allows for a user defined constant surface erosion rate, dm_e/dt, or predicts the rate using an equation provided by Hwang and Mehta (1989).

$$\log_{10}\left(\frac{dm_e}{dt}\right) = 0.23\exp\left(\frac{0.198}{\rho_b - 1.0023}\right) \tag{31}$$

where the bulk density, ρ_b is in gm/cm^3.

In the model, the sediment bed is represented by discrete layers of thickness B_k, which can vary in time. The following equations describing conservation of mass for sediment and water mass per unit horizontal area in layer *k* are given for the bed layer adjacent to the water column (illustrated by B_a in Figure 4);

$$\partial_t\left(\frac{\rho_s B_{ka}}{1+\varepsilon_{ka}}\right) = J_{s:ka-} - J_{sb} \tag{32}$$

$$\partial_t\left(\frac{\rho_w \varepsilon_{ka} B_{ka}}{1+\varepsilon_{ka}}\right) = \rho_w\left(q_{ka-} - q_{ka+}\right) - \frac{\rho_w}{\rho_s}\left(\varepsilon_{ka}\max\left(J_{sb},0\right) + \varepsilon_b \min\left(J_{sb},0\right)\right) \tag{33}$$

and for the layers not adjacent to the water column,

$$\partial_t\left(\frac{\rho_s B_k}{1+\varepsilon_k}\right) = J_{s:k-} - J_{s:k+} \tag{34}$$

$$\partial_t\left(\frac{\rho_w \varepsilon_k B_k}{1+\varepsilon_k}\right) = \rho_w (q_{k-} - q_{k+}) \tag{35}$$

where ε is the void ratio, ρ_s and ρ_w are the sediment and water density, respectively, and J_s and J_w are the vertical sediment and water mass fluxes with *k*- and *k*+ defining the bottom and top boundaries, respectively of layer *k*.

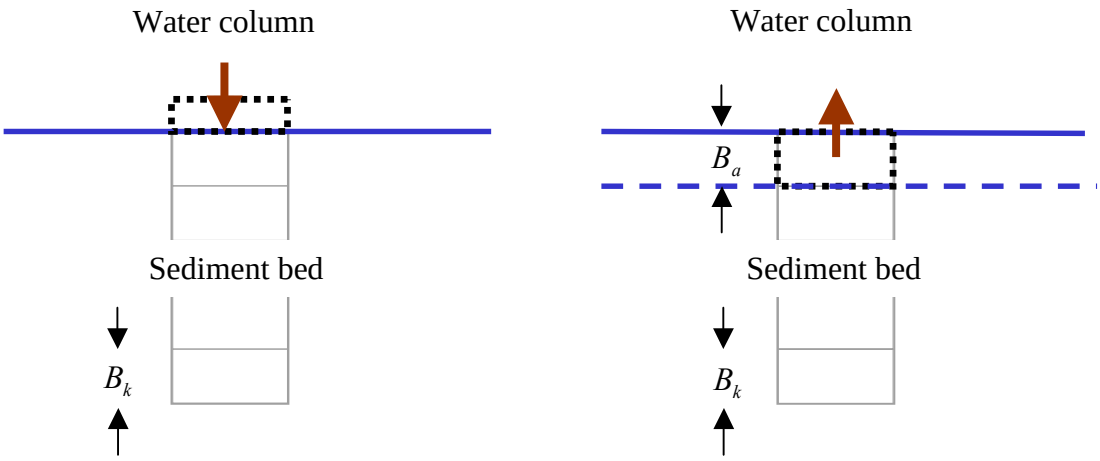

Figure 4 Illustration of sediment bed geomechanical processes a) under continued deposition, b) under continued resuspension.

For the solution of the mass conservation equations, the internal sediment fluxes are set to zero and the change in thickness of the water column adjacent layer, B_a, is determined while the underlying layers have time invariant thicknesses.

The EFDC model is configured to have a user specified maximum number of sediment bed layers. At the start of a simulation, the user specifies the number of layers containing sediment at a specific horizontal location. Under continued deposition, a new surficial sediment bed layer is created when the thickness of the current layer exceeds a

user specified value (Figure 4). If the current water column adjacent layer's index is equal to the maximum number of layers, the bottom two layers are combined and the remaining layers are renumbered before addition of the new layer. Under continued resuspension, the layer underlying the current water column becomes the new adjacent layer when all sediment is resuspended from the current layer.

Solution of the mass conservation equations requires specification of either the specific discharge at the bottom of the deepest layer, q_{k-} or the specific discharge at the top of the uppermost layer, q_{kb+} and the number of layers containing sediment at a specific horizontal location.

For the representation of bed consolidation, three options are available within EFDC. The first approach specifies the void ratio in terms of depositional and ultimate void ratios and is labeled as EFDC's constant porosity option. The second semi-empirical approach assumes that the vertical distribution of the bed bulk density and the void ratio at any time is given by a self-similar function of vertical position, bed thickness, and fixed surface and bottom bulk densities or void ratios. The third approach dynamically simulates the consolidation of the bed.

3.3 Comparison of Numerical Model Results with the Analytical Solutions

Prior to application of EFDC for simulation of hydrodynamics and sediment transport in Hartwell Lake, the numerical model was evaluated with simple forcing and geometry for which analytical solutions are available. These test cases assumed a closed, rectangular water body with a horizontal bottom. Two test cases were considered: 1) constant water surface elevation with wind forcing only (wind setup test), and 2) varying water surface elevation with no external forcing (seiching test).

3.3.1 Wind Setup Test:

In this test, the effect of wind on a closed, flat-bottomed, rectangular water body is simulated (Figure 5). Calculated velocities and calculated wind setup are compared with analytical solutions.

The long wave equations can be used to describe the change in water level induced by wind blowing over bodies of water (Dean and Dalrymple, 2001). The wind setup (η) due to a constant and uniform wind can be calculated using the following equation:

$$\frac{\eta(x)}{h_0} = \sqrt{1 + \frac{2Ax}{L}} - 1 \tag{36}$$

where h_0 is the initial water depth, x is the distance measured from the middle of the domain increasing in the wind direction, L is the basin length and A is the ratio of shear to hydrostatic forces defined as:

$$A = \frac{n\tau_w L}{\rho g h_0^2} \tag{37}$$

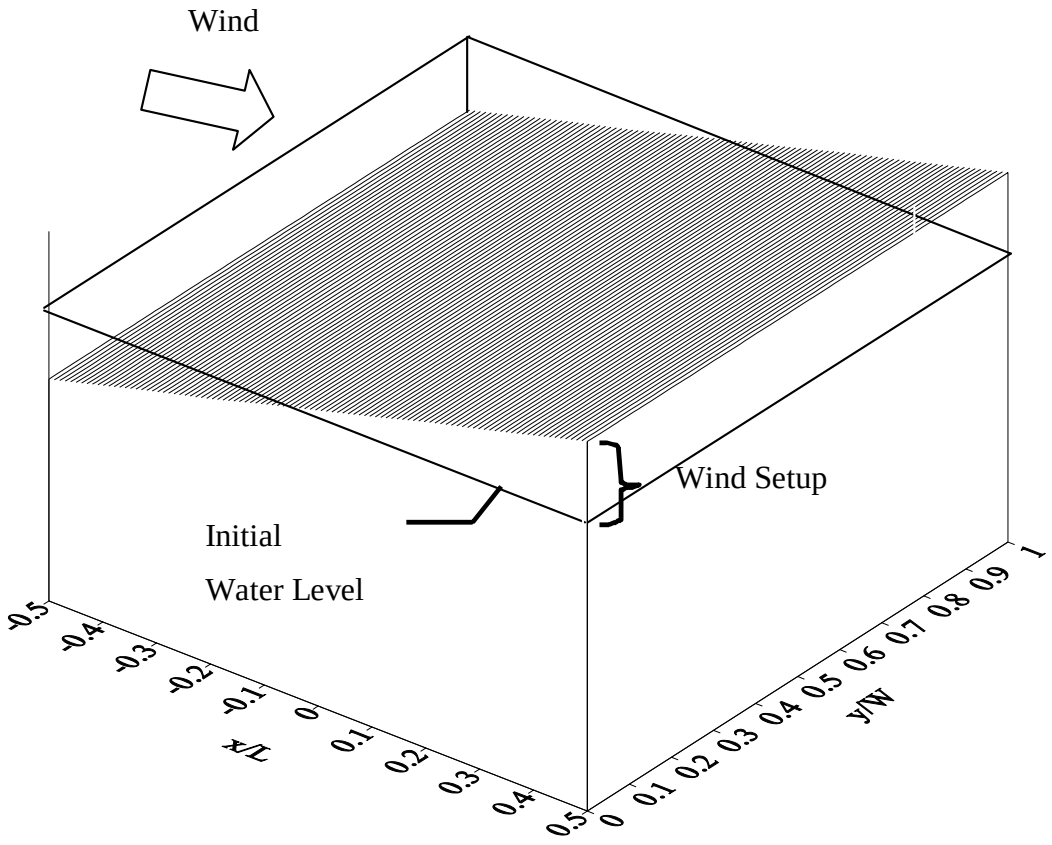

Figure 5 Illustration of model domain for wind forcing.

where n is a factor that lumps the effect of the bottom friction in with the wind shear stress and typical values for n are 1.15 to 1.3 (Dean and Dalrymple, 2001). τ_w is the wind shear stress acting on the water surface, defined as:

$$\tau_w = \rho k W |W| \tag{38}$$

where ρ is the mass density of water, k is a friction factor of order 10^{-6}, and W is the wind speed at a reference elevation of 10 m.

The analytical solution for the velocity profile can be calculated using the

empirical formulation proposed by Wu and Tsanis (1995):

$$u(z) = Au_{*s} \ln\left[1 + \left(z / z_s\right)\right] + Bu_{*s} \ln\left\{1 - \left[z / \left(z_b + h\right)\right]\right\} \tag{39}$$

where; $u(z)$ is velocity at any depth z, and the values of coefficients A and B:

$$A = q_2 / \left(p_1 q_2 - q_1 p_2\right) \tag{40}$$

$$B = -q_1 / \left(p_1 q_2 - q_1 p_2\right) \tag{41}$$

in which;

$$p_1 = \lambda z_{sh} \tag{42}$$

$$p_2 = \lambda z_{sh} / z_{bh} \tag{43}$$

$$q_1 = \left(1 + z_{sh}\right) \ln\left(1 + 1 / z_{sh}\right) - 1 \tag{44}$$

$$q_2 = z_{sh} \ln\left(1 + 1 / z_{bh}\right) - 1 \tag{45}$$

$u_{*s} = \sqrt{\frac{\tau_s}{\rho}}$ is surface shear velocity, λ is a constant to characterize the intensity of turbulence (λ varies from 0.2 to 0.5). The characteristic lengths for z_s and z_b are given as $2.2 \times 10^{-4} h$ and $0.6 \times 10^{-4} h$, respectively. The wind setup and velocities were calculated using the analytical solutions described above. The parameters used in the analytical solution were: initial water depth, $h_0 = 10$ m; domain width, $l = 2000$ m; constant to characterize the intensity of turbulence, $\lambda = 0.2$; mass density of water, $\rho = 1000$ kg/m^3; friction factor $k = 10^{-6}$; constant, $n = 1.2$.

Velocities and water depths resulting from a constant and uniform wind of $W = 10$ m/s in the x-direction were simulated with the numerical model. Simulated wind setup was compared to the analytical solution summarized above (Figure 6). The analytical solution has a parameter n, which lumps the effect of bottom friction with the wind shear stress. In order to get a good match of the two results n was set to 1.2, which is in the given range of values for this parameter.

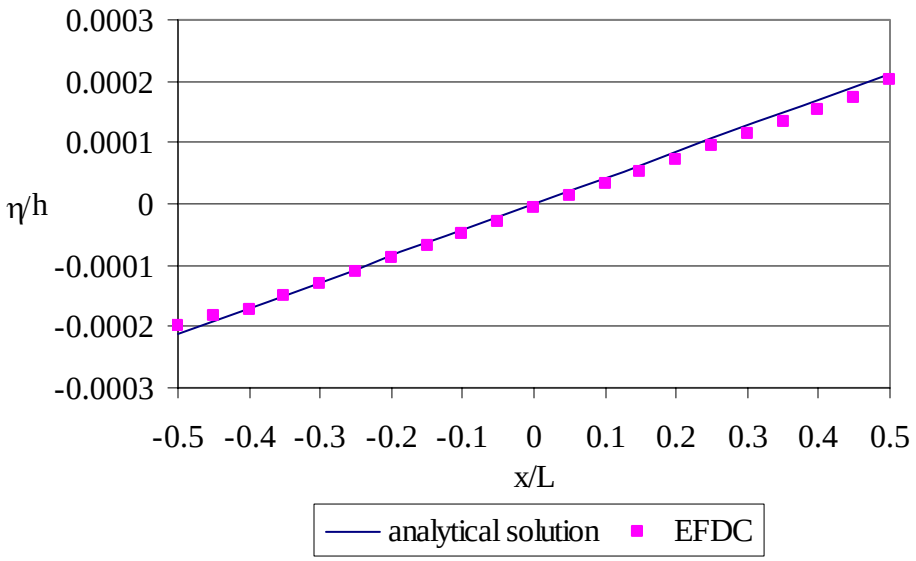

Figure 6 Comparison of numerical model results with the analytical solution for wind setup (η) in a rectangular, flat-bottomed basin subjected to a constant and uniform wind of 10 m/s.

If more than one vertical computational layer is introduced into the numerical model, the model gives a nonlinear velocity profile over depth. The comparison of simulated velocity profiles with the analytical solution is given in Figure 7. Visual comparison indicated that model results matched the analytical solutions of velocity well.

The vertical layer discretization (# of layers) has a significant effect on the prediction of surface velocity in the numerical model. It was observed that the difference between the two velocities at the surface is a function of the number of vertical layers selected to a point. As the number of vertical layers in the numerical model were increased, a higher surface velocity was obtained, since the model calculates a layer averaged value. Thus, as the number of layers was increased and, the thickness of the top layer decreased, the model predicted surface velocity increased and better matched that given by the analytical solution.

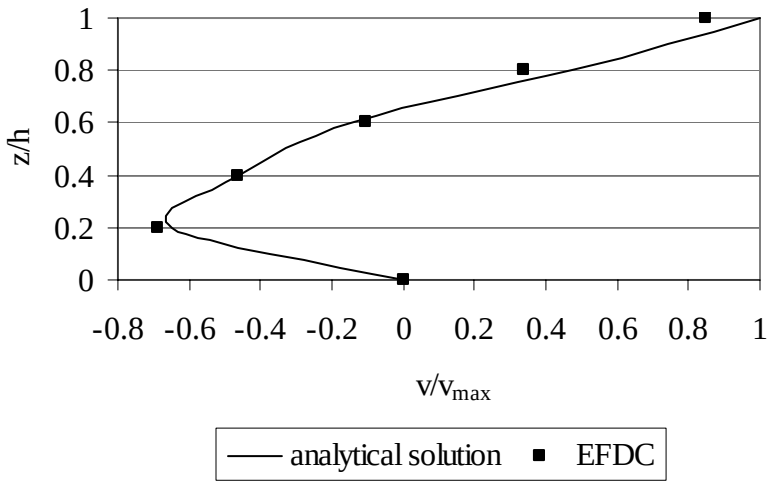

Figure 7 Comparison of numerical model results with the analytical solution of velocity for a rectangular, flat-bottomed basin, subjected to a constant and uniform wind of 10 m/s.

3.3.2 Seiche Test

The numerical model was run to calculate the oscillations of water in a closed basin (Figure 8). Any natural basin, closed or open to a larger body of water, has a natural

oscillation frequency. The analytical solution for the surface profile and depth-averaged velocity of the resulting standing waves for shallow water (based on linear water wave theory) can be written as:

$$\eta = \frac{H}{2}\cos(kx)\cos(\sigma t) \tag{46}$$

$$u = \frac{H}{2}\frac{gk}{\sigma}\sin(kx)\sin(\sigma t) \tag{47}$$

Several assumptions are incorporated in the analytical solution of standing waves for shallow water; these include: homogeneous, inviscid, and incompressible fluid; uniform and constant pressure at the sea surface; and a horizontal, fixed, impermeable sea bed which implies that the vertical velocity at the sea bed is zero. It also assumes that the surface tension and the Coriolis effect are negligible, and the wave height is small compared with both the wavelength and water depth.

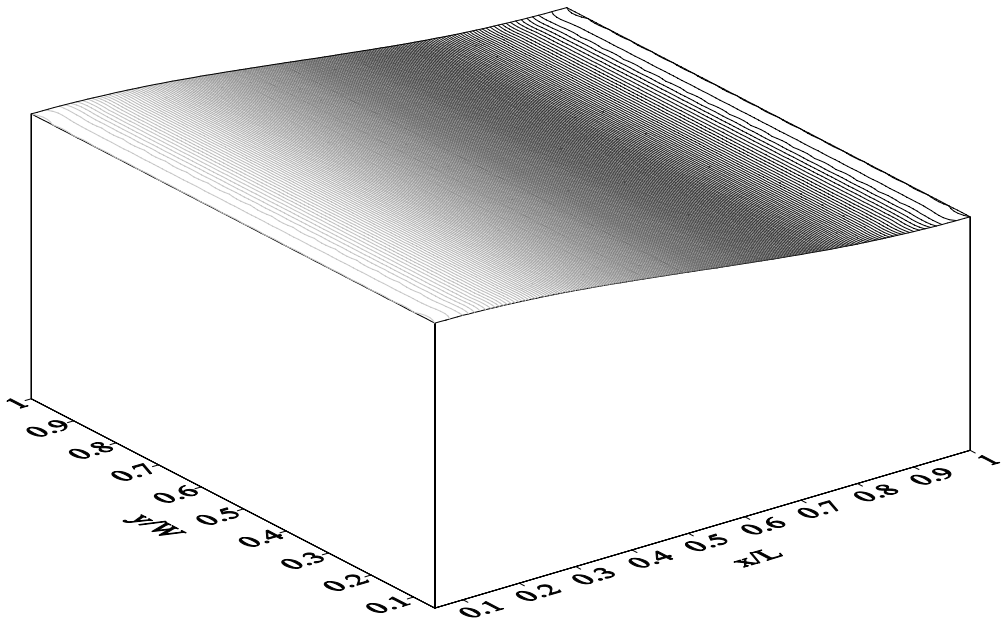

Figure 8 Illustration of model domain for seiche test in rectangular basin with horizontal bottom.

The initial water depth, η_i in the model domain was decreased in *x* direction using the following equation:

$$\eta_i = \eta_i - H \sin\left(\frac{\pi}{2}\frac{x}{L}\right) \tag{48}$$

The parameters used in the analytical solution were: wave height, H=0.2 m; wavelength, L=2000 m; and wave period, T=143 seconds.

The model was run for five days with a time step of 60 seconds. Bottom roughness was set to zero to be consistent with the analytical solution. Without friction, the water surface elevation should fluctuate sinusoidally with constant amplitude,

however a 30% decrease was observed after 150 wave periods of simulation, a result of artificial damping in the model. The comparisons of the numerical model results with the analytical solution are given for the surface profile and velocity in Figures 9, and 10 respectively, after 150.1 periods of simulation.

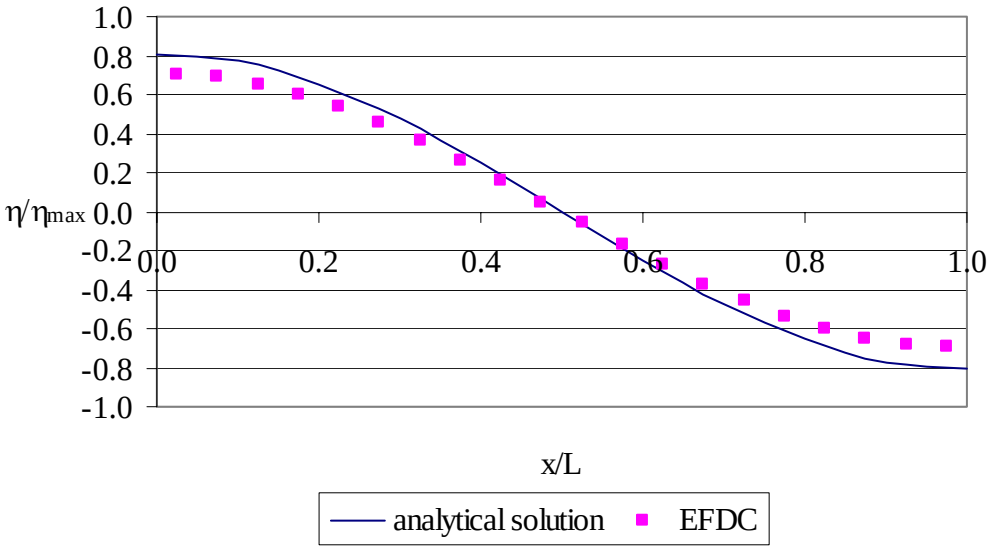

Figure 9 Comparison of numerical model results with the analytical solution for instantaneous depth at the center of the model domain (y/W=0.5).

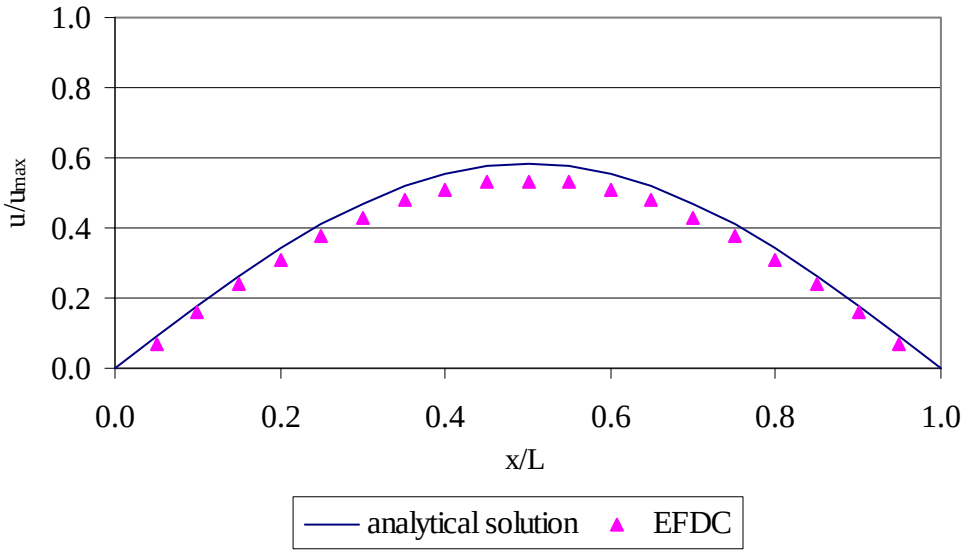

Figure 10 Comparison of numerical model results with the analytical solution for velocity at the center of the model domain (y/W=0.5).

Testing of the EFDC model with simple forcing and geometry indicated that the model performed well for the idealized test cases for which analytical solutions are available in the literature. However, it is important to recognize that significant dissipation (artificial damping) was observed in model simulations because of the numerical dispersion introduced by the approximation of the partial differential equations and the spatial and temporal discretization used in the model.

3.4 Comparison of Numerical Model Results with the Laboratory Experiments for Stratified Flows

The performance of the model under stratified conditions was evaluated by simulating the transient response exhibited by a stratified body subjected to wind shear stress. Monismith (1986) performed lab experiments on the response of a two layer and a

continuously stratified fluid to various surface stresses. The experiments were performed in a rectangular tank 4 m long, 30 cm wide, with water depths ranging from 10 cm to 20 cm. A moving belt was used to apply a shear stress to the fluid since it could be easily controlled. The belt was mounted on the bottom of the flume to allow conductivity probes to enter the fluid from above. Salt was used to obtain density variations. Vertical density profiles were measured using two-electrode conductivity probes placed every 5 mm in the vertical, and every 50 cm in the horizontal direction.

Since the shear stress was applied at the bottom surface of the fluid rather than the free surface, upwelling was defined as vertical flow downwards, towards the belt. Thus the experimental coordinate system was such that the z-axis was positive downwards with the free surface being the origin. To facilitate comparison of the model simulations with the experiments, the vertical axis of the density profiles simulated by the numerical model was reversed.

The density variation in the numerical model was obtained by simulating thermal stratification, while the density variation in the experiments was due to salt. Although the experiments showed the changes in density profiles immediately after the initiation of the surface stress, the spin-up time for the numerical model had to be considered for a realistic comparison. Thermal transport in the numerical model was activated after the model reached a steady state velocity field so that the results could be compared with the experiments at the specified times.

Three cases were considered for the comparison of the numerical model simulations to the experiments. In the first two cases, two layers of fluid were separated by a thin thermocline, and in the third case a linear density variation was considered. The

parameters used in the experiments are listed in Table 2.

In Table 2, U_b is the belt speed, H is the water depth, u_* is the shear velocity generated by the belt, and $\varepsilon_{12}g$ is the reduced gravity and equals to:

$$\varepsilon_{12}g = \frac{(\rho_1 - \rho_2)}{\rho_0} g \tag{49}$$

Table 2 The parameters used in the experiments by Monismith (1986).

Case	H *(cm)*	$\varepsilon_{12}g$ (cm/s^2)	U_b (cm/s)	u_*^2 (cm^2/s^2)	W
1	20	11	20.3	0.8	3.9
2	10	10	22.5	1.6	0.4
3	16.4	8.1	17.6	0.9	6.9

where ρ_0 is the average density of the water column.

The Wedderburn number (W) was defined by the seiche/set-up amplitude non-dimensionalized by the mixed layer depth. A large value of W (W>1) implies slow mixing due to strong stratification and weak wind conditions, whereas low values of W imply intense mixing due to strong wind conditions and/or weak stratification. The Wedderburn number can be written as:

$$W = \frac{\varepsilon_{12} g h_1}{u_*^2} \frac{L}{h_2} \tag{50}$$

where $h_2 = \frac{H}{2}$ for two layer stratification experiments and $h_2 = H$ for the linear

stratification experiments.

In the lab experiments, the shear stresses were calculated from the measurements of the perturbation density field. At steady state, the hydrostatic pressure gradient due to the perturbation density field, measured by the conductivity probes, balances the shear stress gradient in the mixed layer. The pressure was assumed hydrostatic, and sidewall stresses, advective and unsteady accelerations were neglected. Monismith (1986) quantifies the errors introduced by the neglect of these terms as approximately 5%. The shear stress estimated for each case was used to calculate the wind velocity used as an input to the numerical model. Through back calculation, the wind stress acting on the water body was calculated from the shear velocity first, then using the wind stress coefficient used in the numerical model, the wind velocity was calculated.

Several figures below, convey the comparison of model simulations with the experimental results for the three cases listed in Table 2. In the figures, lines of constant density excess ($\rho - \rho_{\min}$) are plotted where $\rho_{\min}$ represents the fresh water density in the experimental results, or the water density corresponding to maximum water temperature in the numerical model results.

In Figure 11, the tilting of the interface is evident. The interface transformed significantly as time passed (Figure 12), while expanding to fill most of the water column at x/L =0.1, the thickness was decreased at x/L=0.9. The numerical model predicted the shape of thermocline transformation well. In Figure 11, the tilting of the thermocline was observed, and in Figure 12, the vertical diffusion of the thermocline at the upwind end of the model domain and the sharpening at the downwind end was predicted, in agreement with the experiments. Differences in the density field contours can be due to several

reasons, including: errors within the lab experiments resulting in use of erroneous wind shear in the numerical simulations, application of the stress at the bottom surface of the fluid in experiments rather than at the free surface as applied in the numerical simulations, and simulation of salinity in the experiments and temperature in the model.

The differences in experiment and model results could also be due to the fact that at time zero, initial velocities of the model and experiments were different. Although the model had already reached the steady state solution for velocities to avoid the long spin-up time of the model in the subsequent thermal simulations, the velocities were zero initially in the experiments.

Figures 13 and 14 compare simulated density fields with the measured values by Monismith (1986) for the two layer stratified conditions. When W<1, mixing rapidly took place as seen in Figure 14.

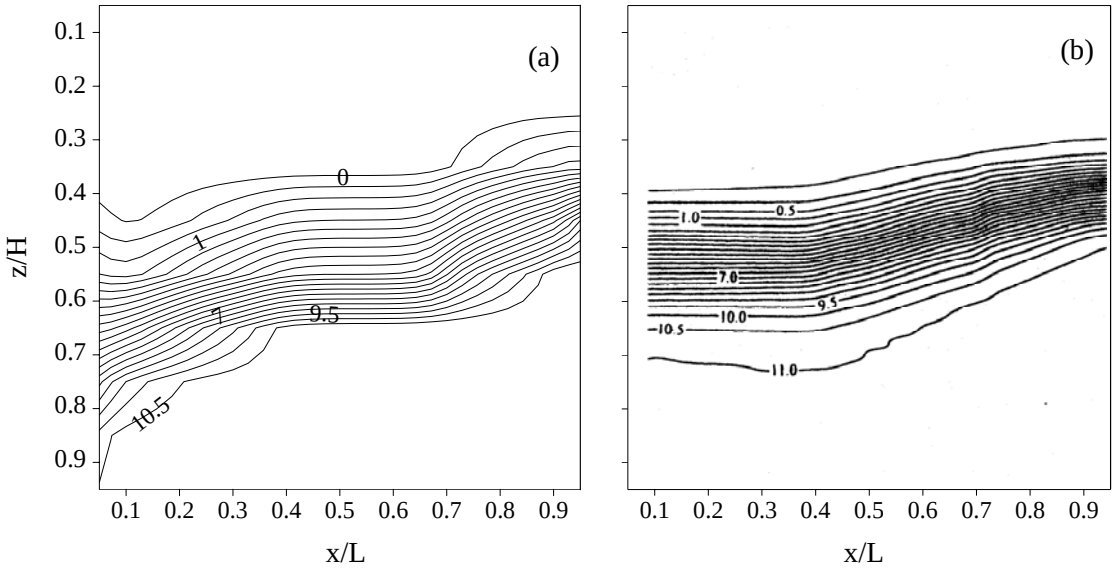

Figure 11 Contour plots of a) simulated, and b) measured density field for case 1 in Table 2 at time 0.3×T.

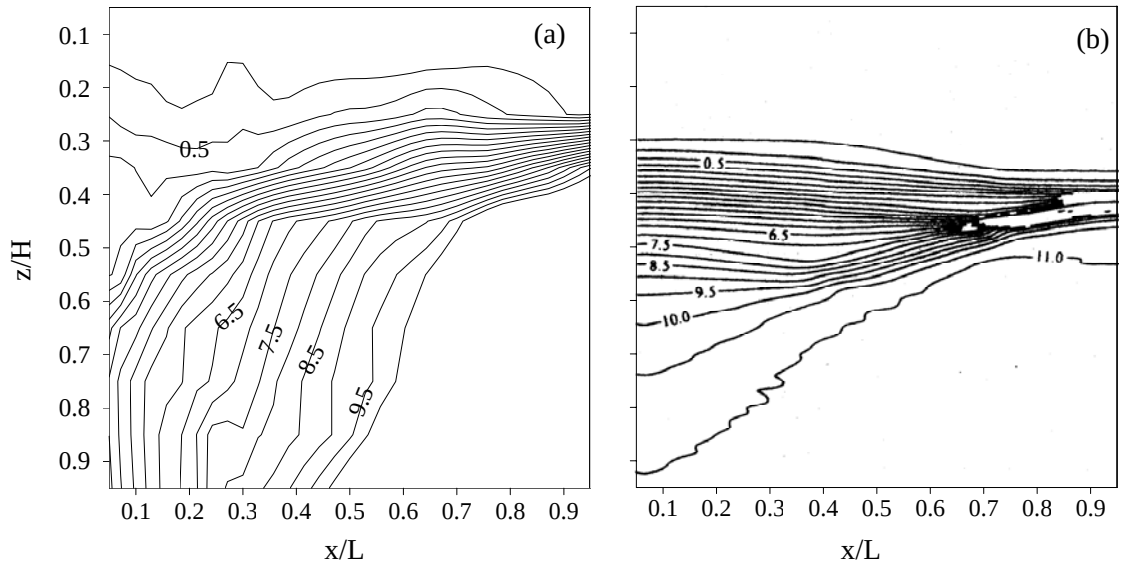

Figure 12 Contour plots of a) simulated, and b) measured density field for case 1 in Table 2 at time T.

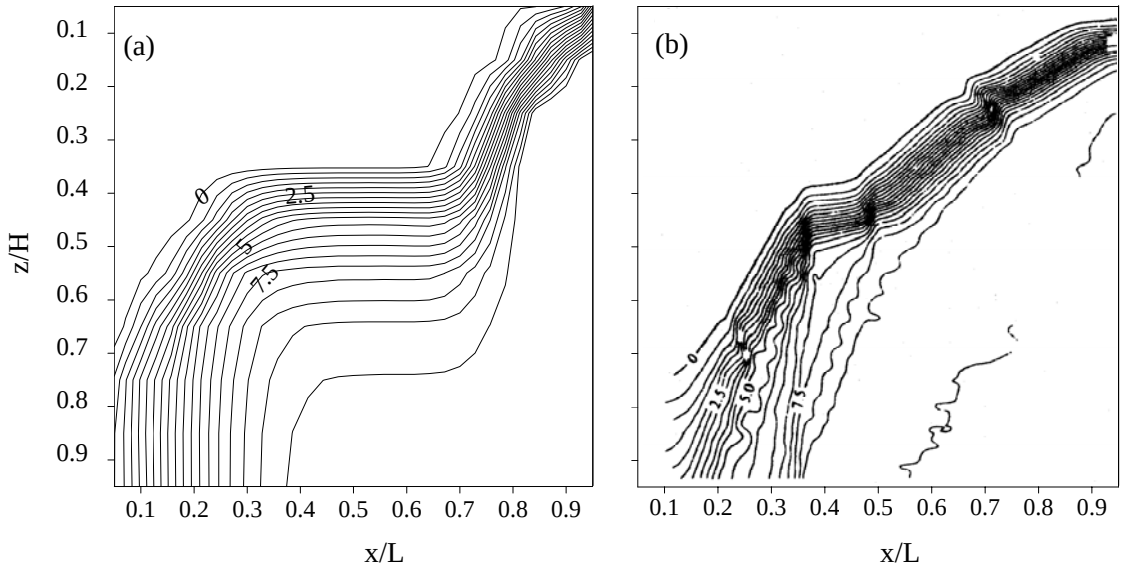

Figure 13 Contour plots of a) simulated, and b) measured density field for case 2 in Table 2 at time 0.5×T.

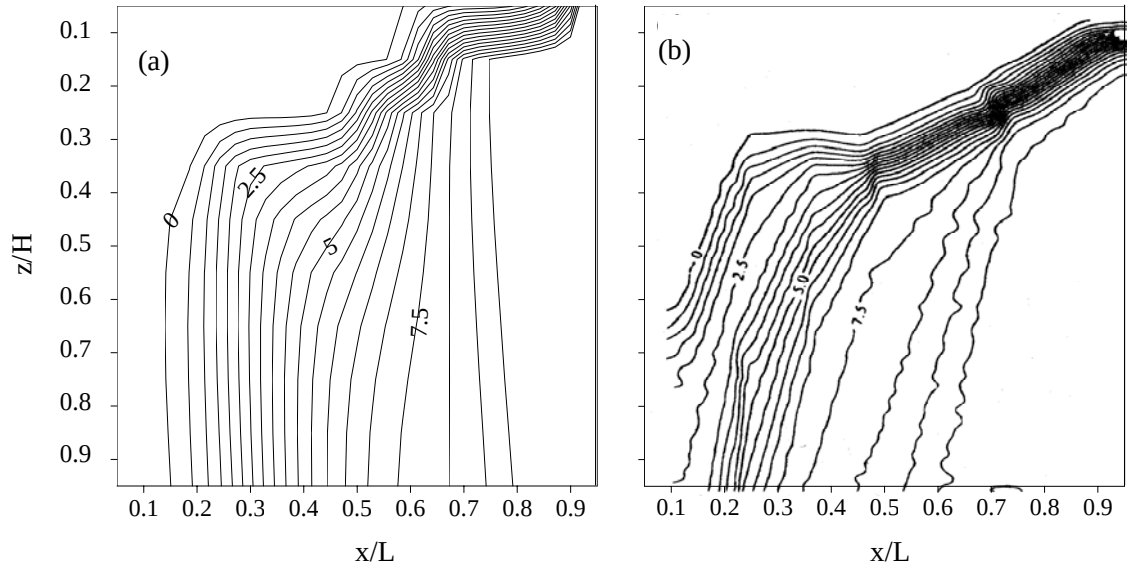

Figure 14 Contour plots of a) simulated, and b) measured density field for case 2 in Table 2 at time T.

Figures 15 and 16 show the evolution of the density field under linear stratification conditions. Since W=6.9 for this last case (see Table 2), slow mixing was observed. At time $6\times T$, tilting of the thermocline was observed in both simulations and measurements.

Comparison of numerical model results with the experiments conducted by Monismith (1986) indicated that the major characteristics of the stratified flow under shear stress were captured well in the model simulations. In particular, for W>1 in the two layered-system, the tilting of the thermocline was simulated, as well as the diffusion of the thermocline at the upwind end and the sharpening at the downwind end was predicted, in agreement with the experiments. For W<1 in the two layered-system, the rapid mixing due to the high applied shear was also observed. With linearly varying density, for W>1, slow mixing was evident in the numerical simulations, in agreement with the lab measurements.

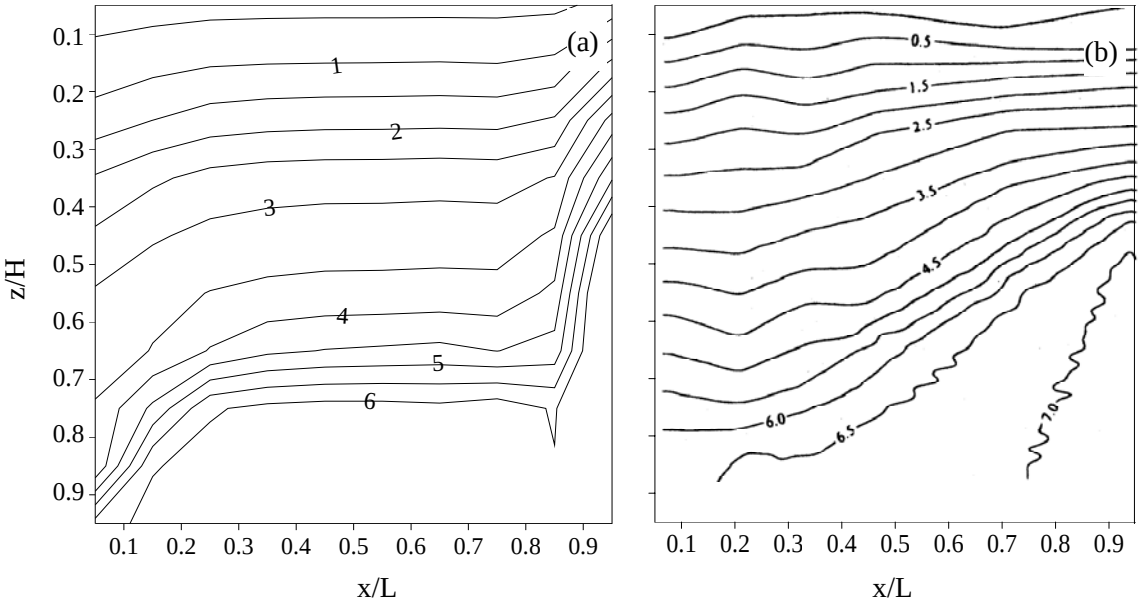

Figure 15 Contour plots of a) simulated, and b) measured density field for case 3 in Table 2 at time $0.3 \times T$.

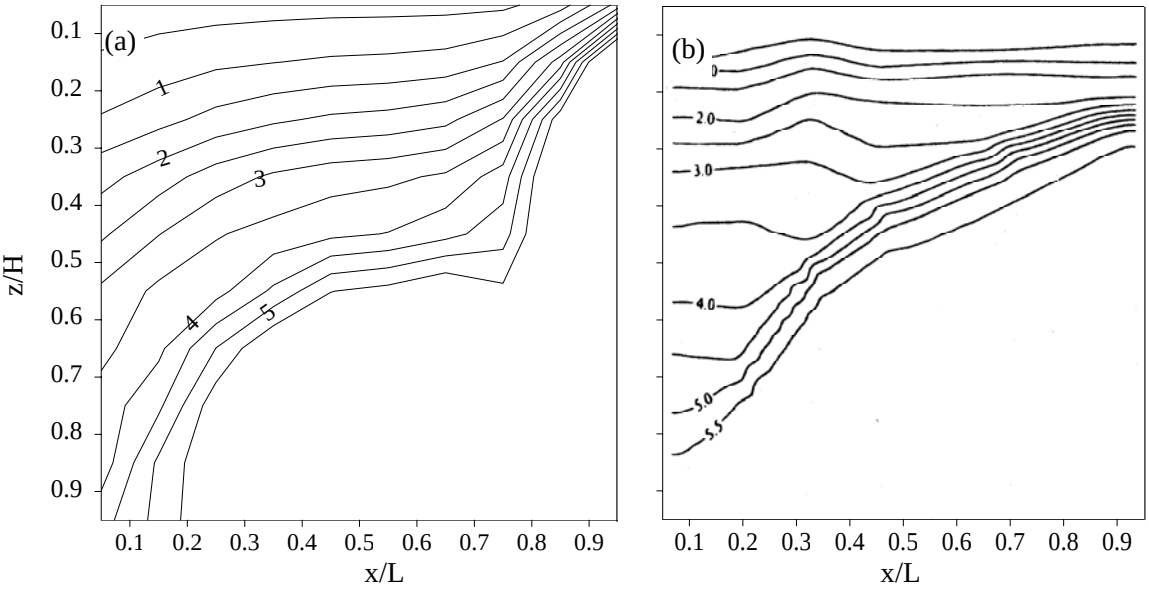

Figure 16 Contour plots of a) simulated, and b) measured density field for case 3 in Table 2 at time T.

3.5 Sensitivity Analysis

Hydrodynamic circulation patterns in the main pool of Hartwell Lake are mainly controlled by wind, inflows and outflows. Daily average inflow and outflow data for Hartwell Lake were obtained from the U.S. Army Corps of Engineers. The USACE derives inflow values from a volume balance of the reservoir and calculates outflows by converting the power measured at the power plant into discharge. Thus, the published inflow values include the changes in reservoir volume due to rainfall, evaporation, and infiltration.

Hourly wind data were obtained from the National Oceanic and Atmospheric Administration (NOAA) for Anderson County Airport, SC. The station is located 15 km east of the lake and the elevation of the station is 231.6 m (10 m above ground).

Boundary data for the numerical model domain were obtained from Digital Elevation Model (DEM) data. DEM data for Lake Hartwell are composed of 4 different 7.5 Minute (scale : 1:24,000, projection : UTM) Quadrangle maps, and were obtained from the SC Department of Natural Resources. They are derived from scanning National Aerial Photography Program (NAPP) photography and rated accuracy is 7 meters. Bathymetry of the lake was obtained from digitized topographic maps (scale : 1:24,000, revised in 1991). The bathymetry of the lake and the model domain is shown Figure 17.

The model domain was selected so that it would represent only the main pool of the lake. The boundaries of the model domain extend to the dam downstream, and to the intersection of the tributaries upstream. The selected upstream boundaries had the same water elevation as the main pool and the backwater effects of the reservoir extended further upstream than the selected model domain.

The variation of numerical model output with model parameters and forcing was investigated through sensitivity analysis. For this purpose, EFDC was applied to Hartwell Lake and several variables including lake water level, grid size, number and thickness of vertical layers, wind direction, and inflow and outflow magnitudes were systematically altered as part of the sensitivity analysis.

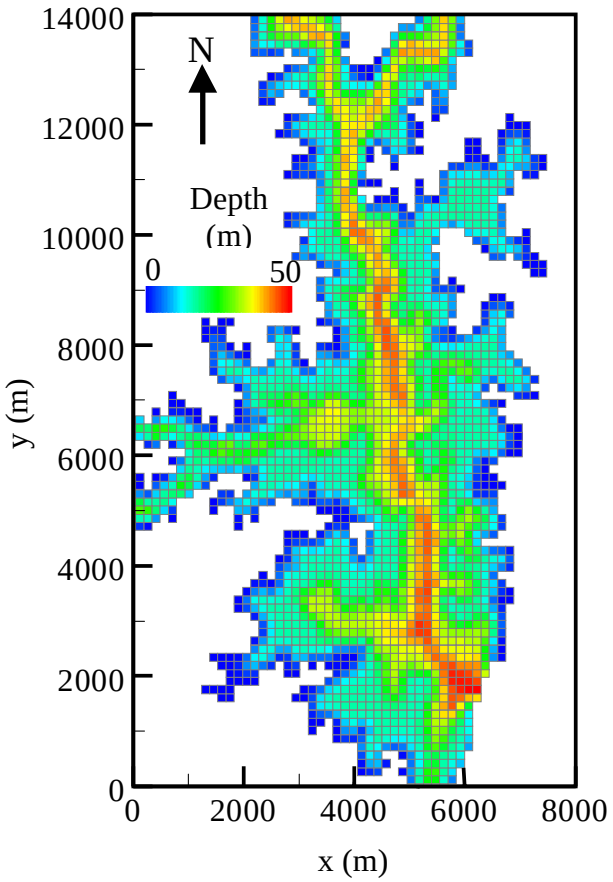

Figure 17 Finite difference computational mesh and bathymetry for Hartwell Lake. Computational cells are 150 m × 150 m. Depth ranges between 0 to 50 meters.

The analysis of monthly water level data from 1964-2001 (Figure 18) showed that minimum and maximum water levels in Hartwell Lake typically vary by up to six meters. During 1990-1999, minimum and maximum water levels varied by three meters. In order to investigate the sensitivity of the model to seasonal changes in the lake level, the model was run using two lake levels initially different from each other by five meters. During this simulation, zero initial velocities were considered in a closed basin. The wind speed used in the simulation was 10 m/s in the northeast direction.

For these two simulations, significant differences in surface layer velocities were observed in shallow parts of the lake, because of drying of cells that were active in the initial run with high water level. The root mean square (RMS) difference was used to compare results:

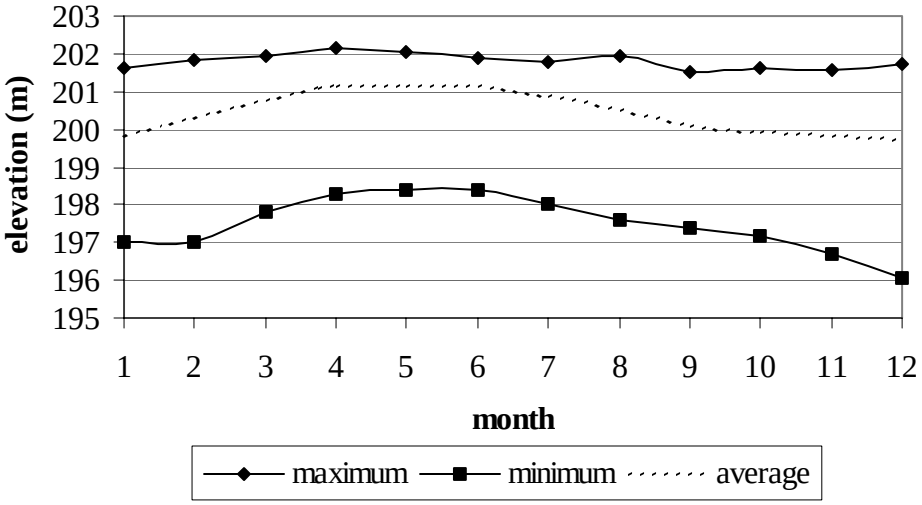

Figure 18 Variation in maximum, minimum and average monthly water levels throughout the year in Hartwell Lake for the years 1964-2001.

$$H_{RMS} = \sqrt{\frac{\sum_{i=1}^{N} \left((H_1)_i - (H_2)_i \right)^2}{N}} \tag{51}$$

where

$(H_1)_i$, $(H_2)_i$= values of the same variable obtained from two different simulations, 1 and 2 at location *i*;

N = number of different locations being compared.

When the cells initially shallower than 5 m were excluded (13% of the cells), the RMS change in flow speed was 0.02 cm/s (about 0.1% of the maximum velocity) which is negligible. The RMS change increased to 2.5 cm/s when all cells were included in the comparison. In the analyses, velocity components were compared separately. Based on the results above, it was concluded that for the deeper parts of the lake (>5 meters), which in fact are of more interest for this study, surface velocities are not sensitive to seasonal changes in water levels.

The sensitivity of model results to horizontal grid cell size was investigated using two different grid configurations as given in Table 3. In the main pool, calculated velocities were almost the same with an RMS change of 0.01 cm/s. Considering other factors such as computer resources and stability of numerical scheme, a 150 m grid resolution was considered reasonable.

Table 3 Computational grids used for sensitivity tests.

Cases	Grid configuration	Cell width (m)	No of vertical cells	Range of vertical layer thickness (m)
1	51 × 94	150	5	0.2~10.58
2	103 × 188	75	5	0.2~10.85

The number of vertical layers was found to strongly influence results. When three vertical layers were simulated and velocities were compared to simulation results with ten vertical layers, RMS differences in velocities increased to 6 cm/s, whereas RMS difference between five and ten-layer simulations was 0.8 cm/s (about 4% of the maximum velocity). Although for the sensitivity analyses presented in this section selection of five vertical layers were satisfactory, in all other simulations described in the following chapters ten layers were used. This was mainly because, the number of vertical layers was found to have a great impact on the predicted velocities. Since the bottom layer velocities are important for sediment transport simulations, and surface layer velocities serve to define the hydrodynamic circulation in a reservoir, using a greater number of layers should result in a more accurate prediction of the velocity profile.

Lakewide circulation patterns are very sensitive to wind direction and magnitude. Wind is typically the major external force driving circulation. Surface currents followed the dominant wind direction in each case. When the wind speed was reduced from 6.8 to 2.8 m/s and inflows and outflows were kept constant, the RMS change in the surface velocities was calculated as 4 cm/s.

Sensitivity of model results to inflows was investigated by comparing results for

three different inflow magnitudes. In all simulations, wind was set to zero. The second and third tests included two times and five times, respectively, the initial inflow in magnitude (mean inflow). Increasing the inflow by a factor of two resulted in a doubling of velocities, while an increase of inflow by a factor of five resulted in an increase in the average of surface layer velocity magnitude by a factor of six. In the presence of typical wind forcing, velocities in the main pool were not particularly sensitive to flow magnitudes.

CHAPTER 4

FIELD OBSERVATIONS OF RESERVOIR HYDRODYNAMICS AND COMPARISON OF MEASUREMENTS TO MODEL SIMULATIONS

This chapter describes field data collected in Hartwell Lake and the analysis of these data. The main objective of the field data collection effort was to document sediment deposition in the main pool of the lake, since the lake was last surveyed in 1973. This effort also yielded velocity data to compare with the results obtained from the hydrodynamic model. Velocity measurements provided a check on the magnitude of the velocities predicted by the numerical model.

The field data were collected February 10-14, 2003. Throughout that week, very strong winds (approximately 4 times the historical average of 3 m/s) from the southwest were observed (Figure 19). The mean water level was 199.33 m. Temperature profile throughout the water column was constant and about 9 ºC.

In this chapter, first the techniques to collect bathymetric data are described, and then topographic surveys conducted by USACE are compared to the new bathymetric survey to quantify 40 years of deposition in the main pool of the lake. Then the velocity data collection techniques are described, and a summary of new velocity data is presented. Finally, the comparison of the velocity measurements to the model simulations is presented.

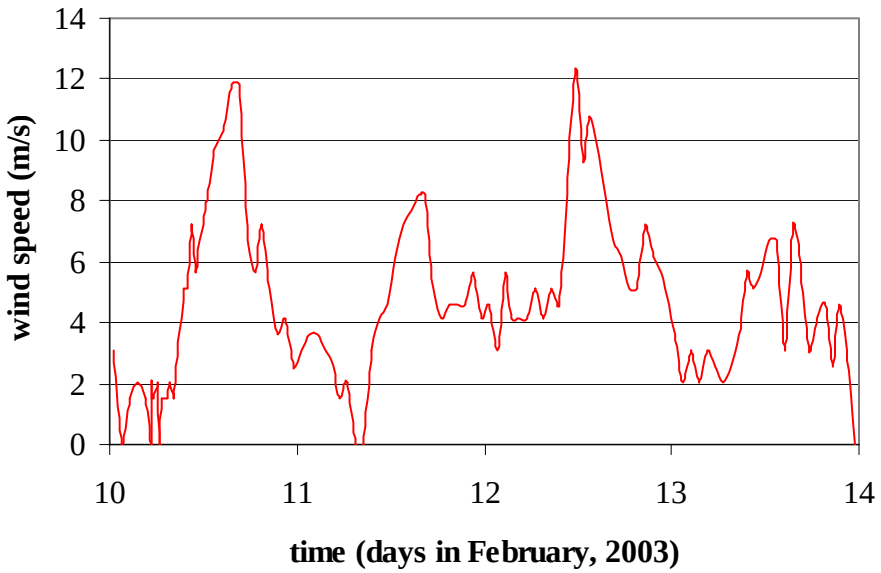

Figure 19 Hourly wind speed data obtained from Anderson County Airport, SC during field measurement campaign. Elevation of the station was 231.6 m.

4.1 Bathymetric Survey Data

Two sources of bathymetric data are available for the lake: data collected by the U.S. Army Corps of Engineers (USACE) in the past, and new data collected in February 2003. Three surveys of different transects across the lake were conducted by the USACE; a topographic survey in 1959 before completion of the dam in 1963, a bathymetric survey in 1963 and another in 1973. Although the 1959 survey included several cross sections within the main pool of the reservoir, surveys from both 1963 and 1973 were available mostly for the upstream region of the main pool on the Tugaloo and Seneca Rivers. The projection, datum and mean water level data for the historical surveys are given in Table 4. A map showing the transects surveyed by USACE is given in Figure 20.

Table 4 Projection, datum and mean water level data for the Corps of Engineers surveys.

Survey year	Mean water level	Vertical Datum	Projection
1959	-	1927 North American Datum	Plane Coordinate System based on Georgia East Zone and South Carolina North Zone
1963	200.59		
1973	201.06		

The historical surveys used the method of triangulation from known benchmarks. Concrete monuments at locations along the future shoreline were established and land was surveyed by creating a loop with level lines and turning points. The stated accuracy of the surveys was ±1.2 cm in the vertical (Jason Ward, USACE, Savannah District, pers. comm.).

The USACE provided the survey data in an analog, graphical format for each transect, with elevations plotted versus horizontal distance from the starting point of the transect. Transect 74 is shown in Figure 21 as an example. The coordinates of the two end points of the transects were not provided, but instead a map (in paper format, digitized) showing the transects was available. Since the locations of benchmarks and thus the starting and the ending coordinates of the transects were not precisely known, the transects were surveyed using approximate coordinates obtained from the map.

A geographical data analysis program (ArcView's Digitize extension) was used for conversion of graphs to digital format. Digitizing errors were estimated as ±15 cm in the vertical and ±1 m in the horizontal, at prototype scale.

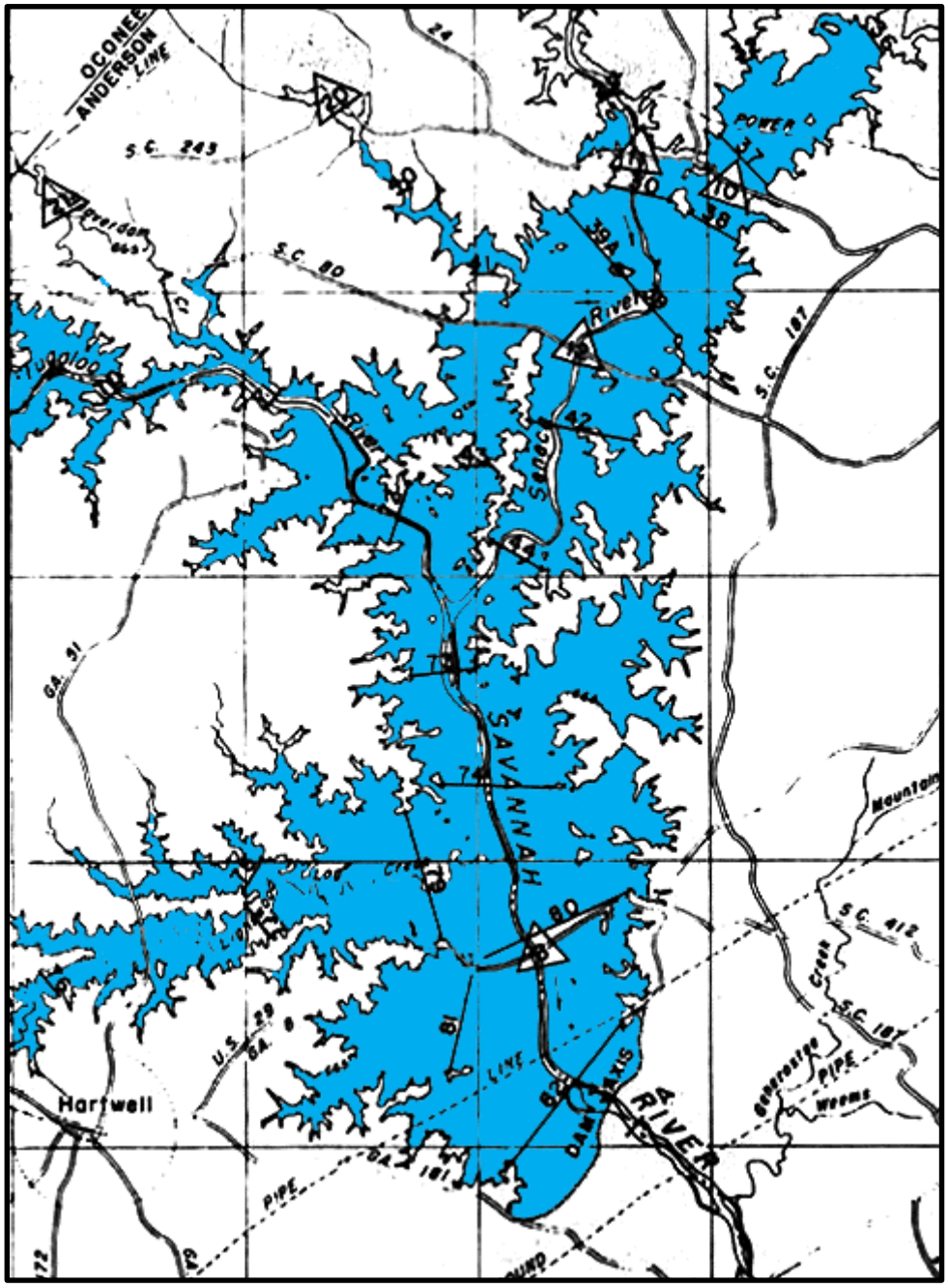

Figure 20 A map showing the transects surveyed by USACE in 1959 (source: USACE, Savannah District).

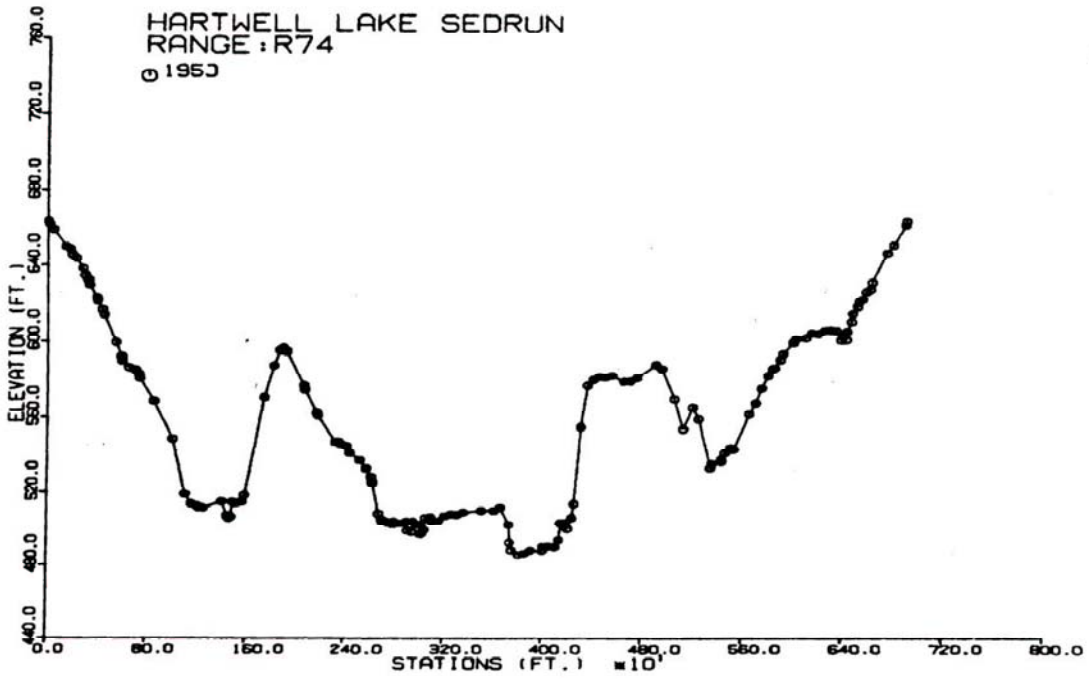

Figure 21 Bathymetric survey data from 1959 provided by USACE for transect 74. Horizontal distance is measured from the east end of the transect.

A survey system shown in Figure 22 was used to collect hydrographic survey data. The survey system was mounted on a fiberglass boat. Depth data were provided by a dual frequency depth measuring system (high frequency 200 kHz, low frequency 30kHz), manufactured by Bruttour Intl. Figure 23 shows the mounting of the depth sounder. Digital depth data were directly logged to a laptop computer equipped with Coastal Oceanographic's HYPACK Hydrographic Survey Software. Data were output and stored at a rate of 6 soundings / sec.

Figure 22 Boat used for data collection.

Figure 23 Over the side mounting for dual frequency depth sounder.

Echo sounders in general determine the distance between a transducer, which converts electrical energy to sound, and dense objects such as fish or a seabed. An ultrasonic wave is transmitted through water, and as the sound wave strikes an object, it is reflected back toward the source and received by the transducer. User specifies the environment (fresh or salt water), and the speed of sound is determined accordingly, after the water temperature is measured by the depth sounder. The speed of the ultrasonic wave varies with density and is 1447 m/s for 10 °C fresh water. The depth of the object is then calculated using the time difference between the transmission of sound wave and the reception of the reflected sound.

Dual frequency echo sounders are commonly employed in areas where soft bottom sediments are present. High frequency transducers often have a smaller beam angle (Figure 24). Low frequency transducers transmit a signal that penetrates to a greater depth in the bottom sediments with a wider beam angle covering a greater sea bottom area. However, a sharper focus of the transmitted energy is achieved at higher frequencies. Low frequency depth measurement can be used only if the slope of the bottom is low and there are no structures nearby.

The transects previously surveyed by USACE in the main pool of the reservoir were marked on the digital lake map within the Mapsource software sold by Garmin (Figure 25). The coordinates of the two ends of the transects were uploaded to a GPS as waypoints that were used to navigate during the surveys.

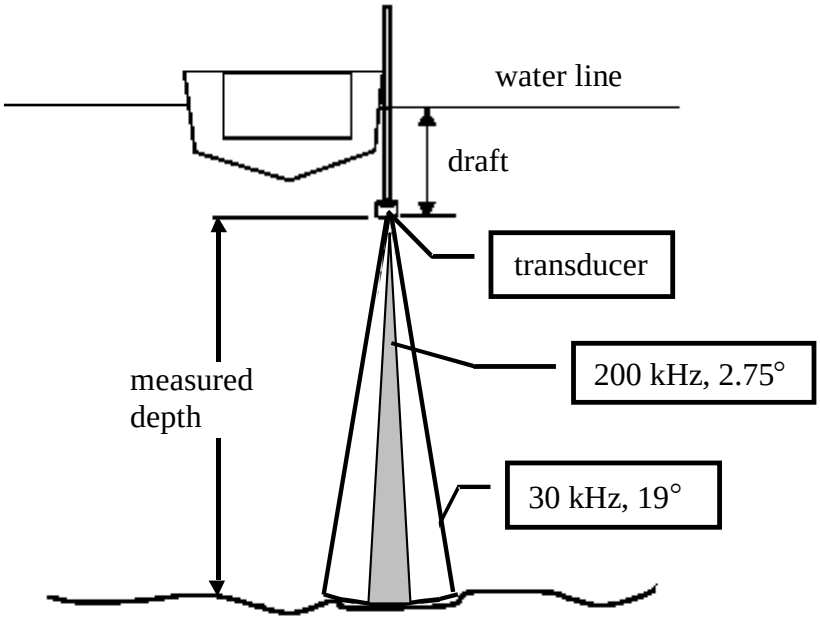

Figure 24 Representation of high and low frequency transducers (adapted from Bruttour, 2003).

The horizontal errors associated with the handheld differential (WAAS) GPS were quantified with a simple test. The GPS was left to record coordinates at a fixed location for 20 minutes, and the recorded coordinates were plotted. The average horizontal error was ± 1 m.

While surveying the transects shown in Figure 25, the drafts for the high and low frequency transducers were 28 ± 1 cm and 20 ± 1 cm respectively. The measurements were corrected to account for the draft. Another correction was made because the projection and datum used in the historical surveys were different from the current survey. Conversion of depth data measured using 1927 North American Datum (NAD 27) projected by the Plane Coordinate System to 1983 North American Datum (NAD 83) projected by the Universal Transverse Mercator (UTM) were made using the Corpscon

software program provided by USACE.

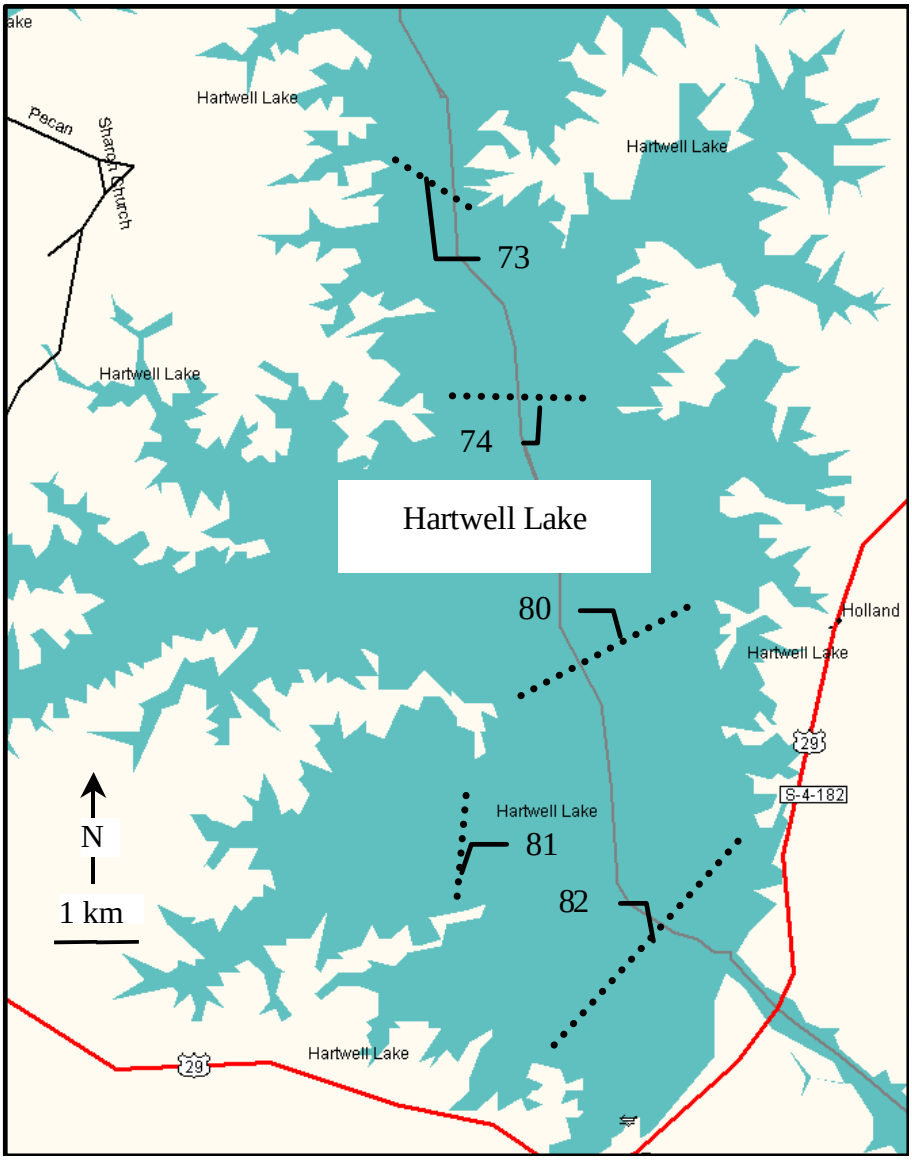

Figure 25 Transects surveyed in Hartwell Lake during February 10-14, 2003. Transects are numbered consistently with the old surveys.

The manufacturer's rated accuracy for the depth sounder is 0.01 meter, however the testing of the equipment indicated 0.10 meter accuracy. The sources of errors in the old and current surveys add up to ± 27 cm and are summarized in Table 5.

Table 5 Error sources in surveys.

	Source	Magnitude
Surveys conducted in February, 2003	Depth measurement errors	± 10 cm
	Draft measurement errors	± 1 cm
Surveys conducted by the Corps of Engineers	Errors in old survey	± 1.2 cm
	Digitizing errors	± 15 cm
		total : ± 27 cm

4.2 Comparison of Bathymetric Data to Historical Surveys

The new survey data were compared with the historical surveys after the old data were adjusted so that both data sets have the same datum and projection. When the data from the high and low frequency transducers were compared, the two results were generally in agreement, except in regions where steep slopes were present. In those regions, data received from the two transducers differed up to 40 cm and the data from the high frequency transducer was selected since its narrow beam angle (2.75º) resolves depths along slopes better. All of the data presented in this section use the 1983 North American Datum (NAD 83) and Universal Transverse Mercator (UTM) projection. The 2003 depth data are from the higher frequency transducer unless stated otherwise.

Figure 26 compares the survey results at transect 73 shown in Figure 25. Unless

otherwise stated, all horizontal distances are measured from the east end of the transects, as looking downstream. Focusing on the thalweg, up to 1.80 ± 0.27 m of deposition were observed at transect 73 (Figure 27). The estimated uncertainty (± 0.27 m) includes potential errors due to digitizing, draft measurement, errors in the old survey, and depth measurement as discussed in the previous section. A topographic map of transect 73 is shown in Figure 28. Since the detailed coordinates of the ends of transects surveyed in 1959 were not provided, the exact same routes of the historical surveys could not be followed at all transects. This was tolerable, since the purpose of this bathymetric survey was to determine, where and at what rate deposition has occurred in the thalweg of the main pool.

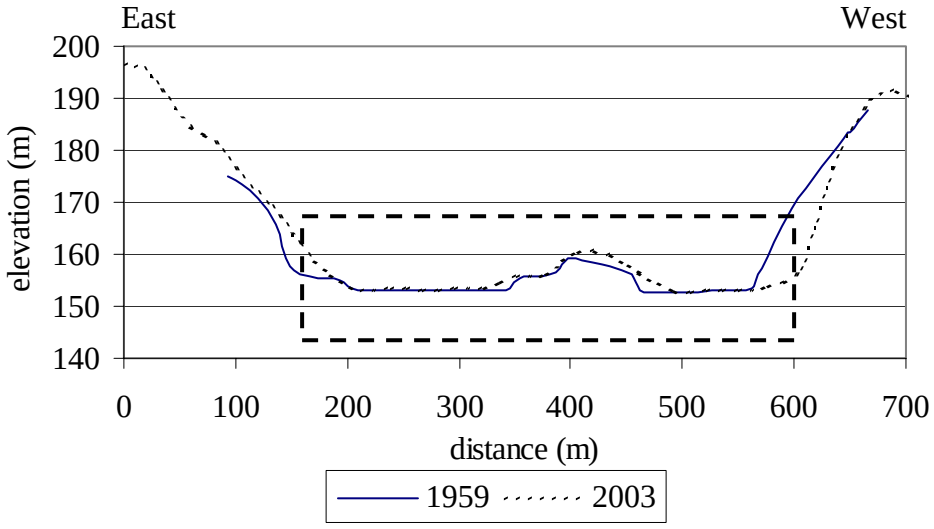

Figure 26 Comparison of survey results at transect 73 shown in Figure 25. Distance is measured from the east end of the transect. Box shows the thalweg of the lake.

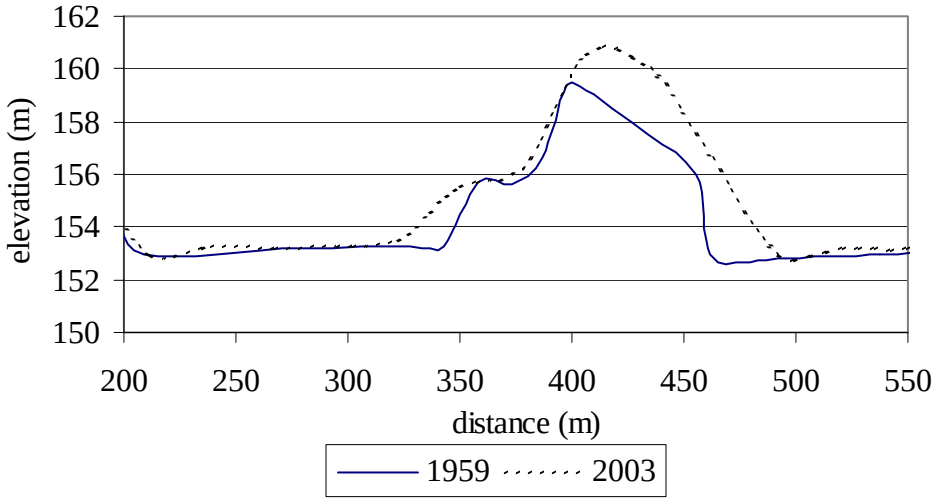

Figure 27 Comparison of survey results within the region shown by the box in Figure 26 with the results of the historical survey conducted in 1959.

A resurvey of transect 73 with a different route (shown by 73b in Figure 28) indicated that deviating from the route did not introduce significant errors to the old river bed (thalweg) elevation estimates at this location. The survey results from the two different routes are compared in Figure 29. It can be inferred from the figure that although the distance between the two routes was more than 100 m, the measured elevations were the same at the thalweg. This observation also justifies the assumption that the horizontal accuracy is not as critical as vertical accuracy in bathymetric surveying of a reservoir.

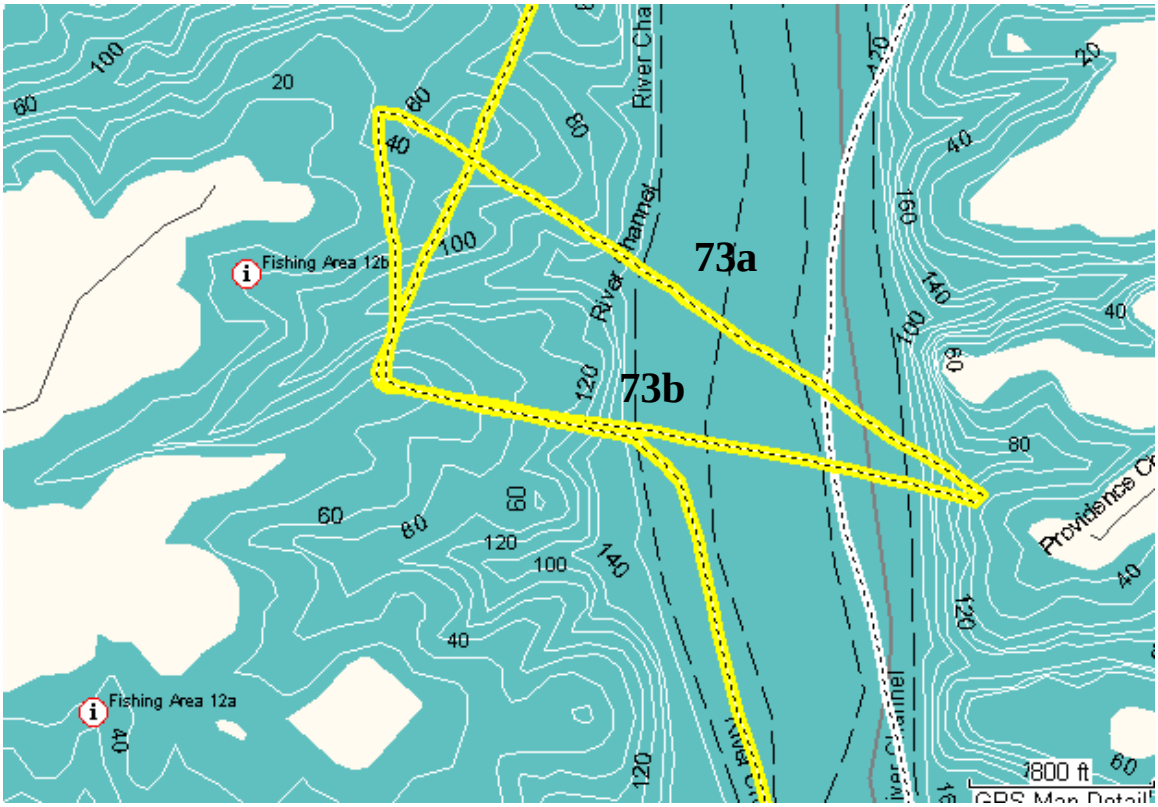

Figure 28 Topography map for transect 73.

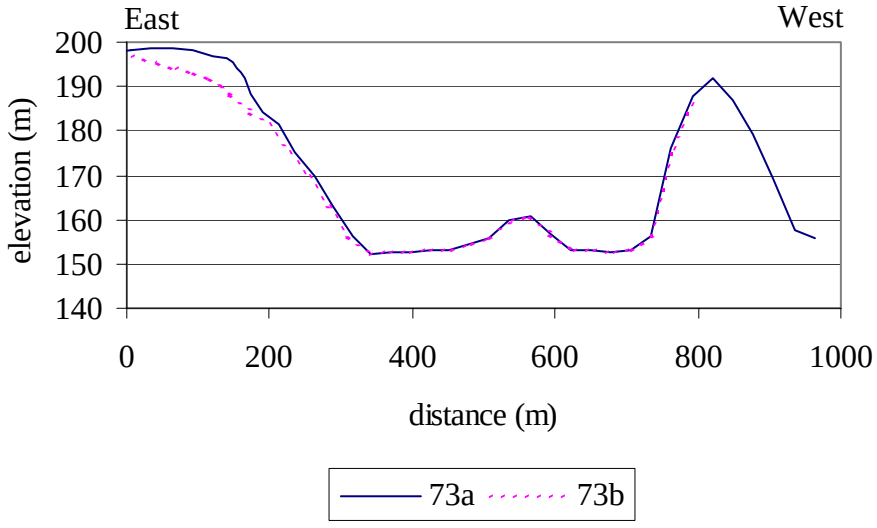

Figure 29 Comparison of surveying results from two different routes shown in Figure 28. Distance is measured from the west end of the transect.

Figure 30 compares survey results at transect 74. Within the thalweg, 2.00 ± 0.27 m of deposition are observed in the deeper regions (Figure 31a). A line is drawn on the topographic map to represent the probable route taken by the surveyors in 1959 based on the comparison of survey results at this transect (Figure 31b). The distance between the actual survey route taken in 2003 and the theoretical route is approximately 100 m. As shown for transect 73, this distance is tolerable for the comparisons of bottom elevations at the thalweg.

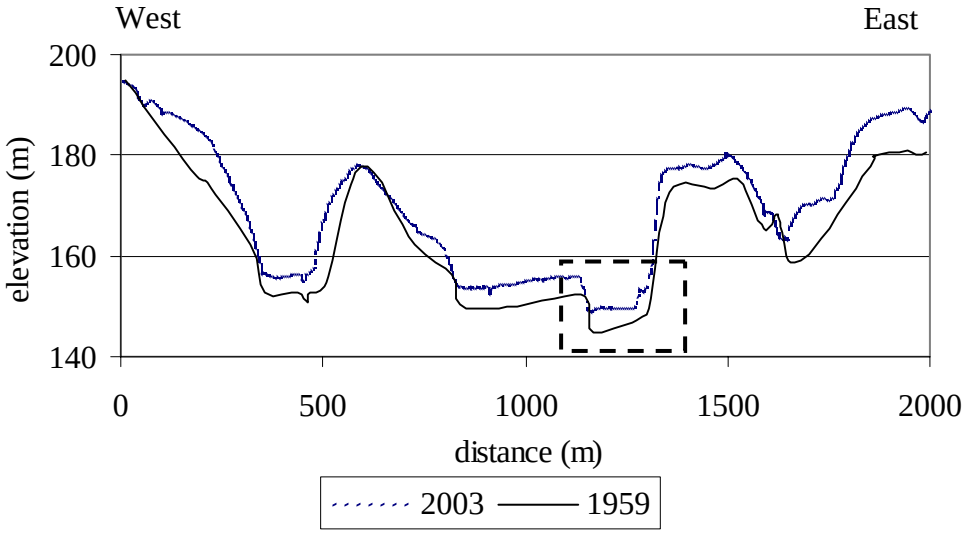

Figure 30 Comparison of survey results at transect 74 shown in Figure 25. Distance is measured from the west end of the transect. Box shows the thalweg of the lake.

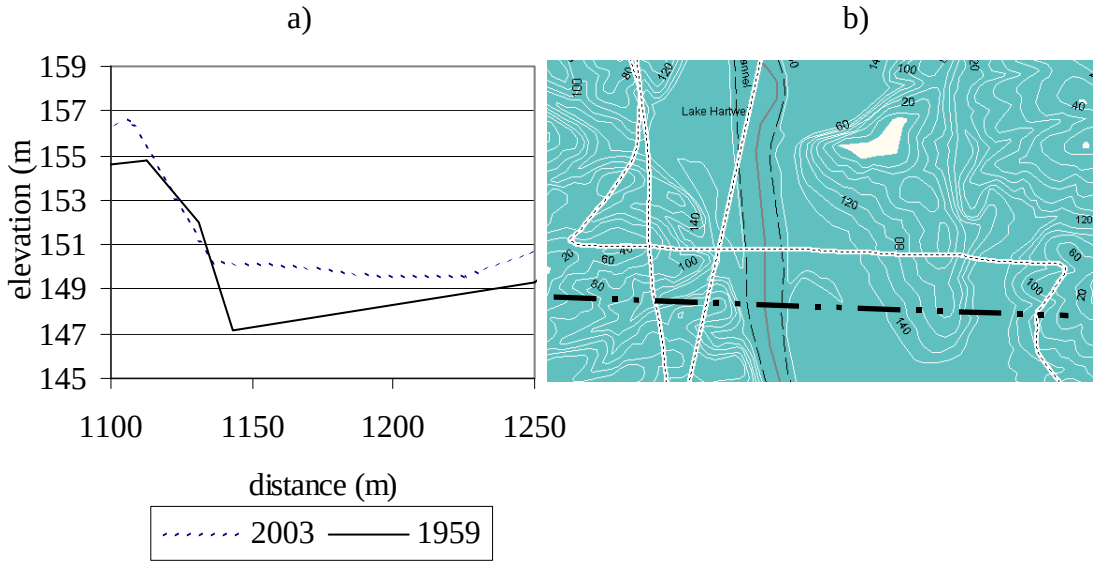

Figure 31 a) Details of survey results shown by box at Figure 30. b) Topography map at transect 74. Solid line represents the possible route taken in 1959.

Transect 81 is the only resurveyed transect that does not pass over the thalweg. The comparison of results with the previous surveys indicated no significant deposition (Figure 32). Details of the deepest region are given in Figure 33a. The differences in the shallow region of the transect ($x \leq$ 1000 m) can be explained by a slight deviation from the route followed by the old survey (see Figure 33b).

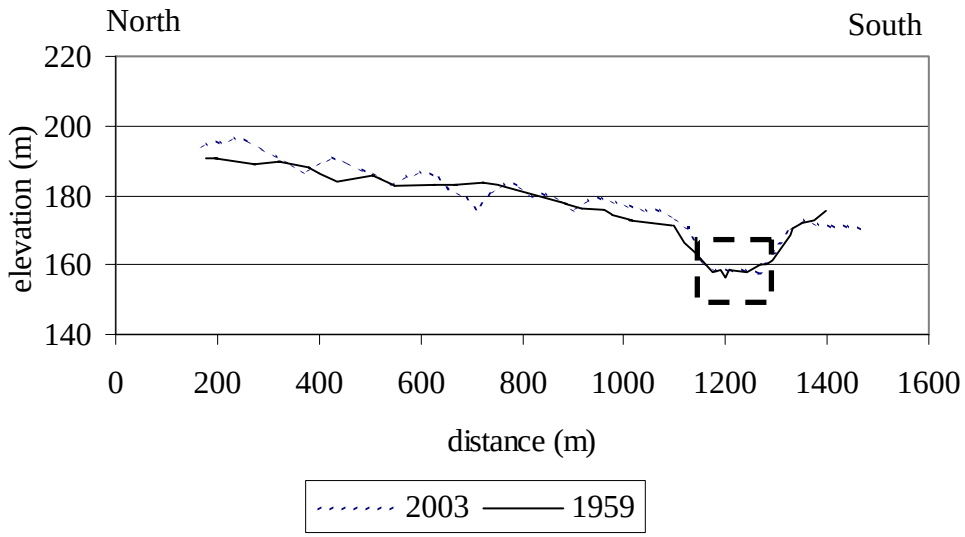

Figure 32 Comparison of survey results at transect 81 shown in Figure 25. Distance is measured from the north end of the transect. Box shows the deepest region of the transect.

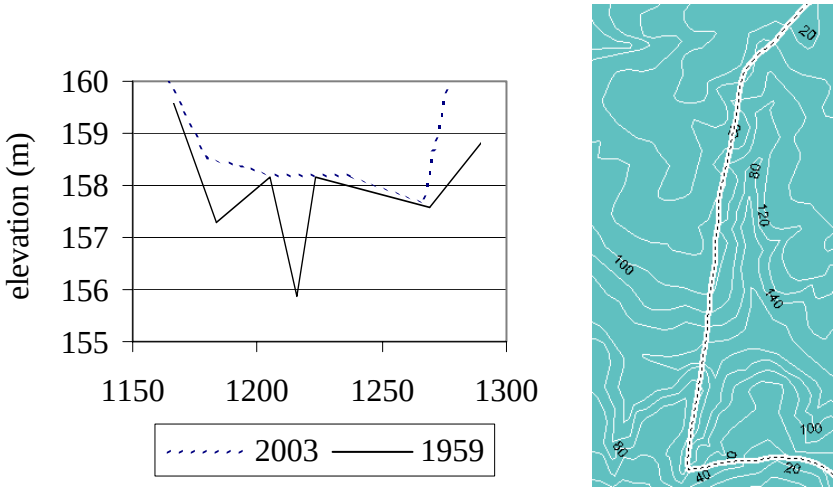

Figure 33 a) Details of survey results shown by box at Figure 32. b) Topography map at transect 81.

Figure 34 shows the comparison of survey results with the previous survey for transect 82. Deposition of 2.00 ± 0.27 m is observed in the thalweg. Details of the thalweg are given in Figure 35.

Results of the bathymetric surveying of different transects at Hartwell Lake indicated that in 40 years approximately 2 meters of deposition occurred in the thalweg of the reservoir. The reservoir had an initial capacity of about 1.75×10^9 m^3 (USACE, 1996b). Although significant amounts of sedimentation appear to be occurring in the old Savannah River bed, a rough estimate of the conservation storage lost is 3×10^7 m^3, which is less than 1.6% of the total storage. The actual volume of storage lost due to incoming sediments should not significantly impact the purposes of the reservoir. For all transects, only the differences inside the thalweg were quantified since the exact routes of the historical surveys could not be followed due to the lack of information in the old surveys.

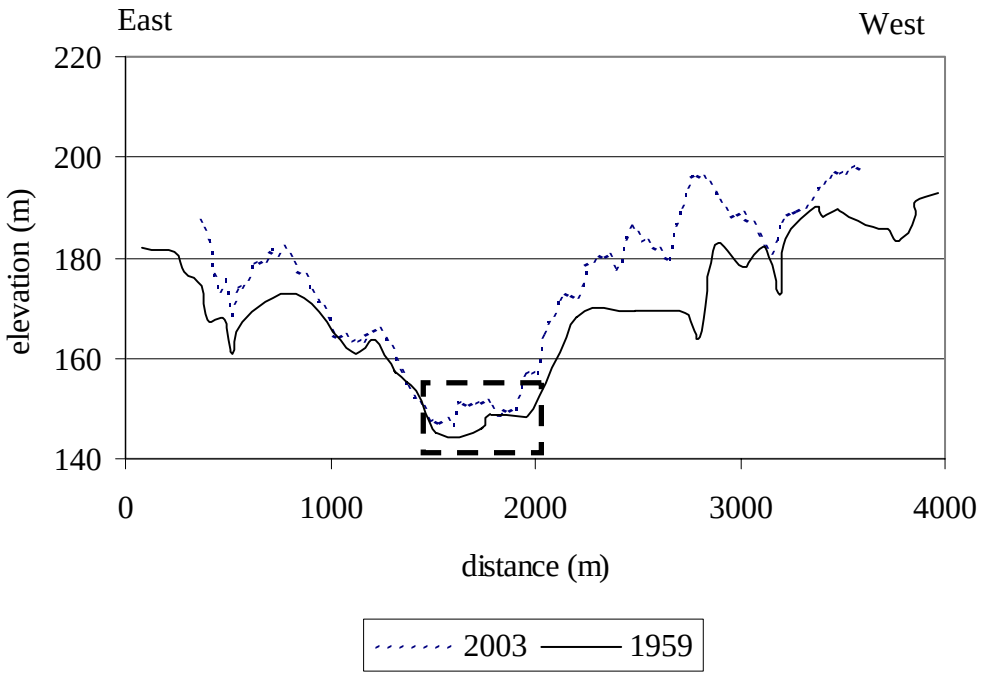

Figure 34 Comparison of survey results at transect 82 shown in Figure 25. Distance is measured from the east end of the transect. Box shows the thalweg of the lake.

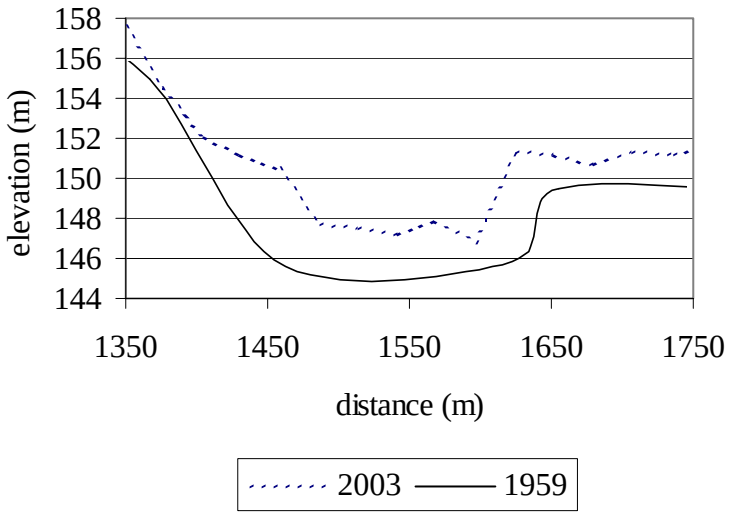

Figure 35 Details of survey results shown by box in Figure 36.

4.3 Velocity Data

Velocity measurements were made using a 1200 kHz Workhorse Sentinel Acoustic Doppler Current Profiler (ADCP) developed by RD Instruments (Figure 36). It is designed for measuring real time current profiles in the ocean, near shore, harbor and lake regions. An ADCP estimates horizontal and vertical velocities as a function of depth by using the Doppler effect: a change in the observed sound frequency that results from relative motion toward or away from the sound source. An ADCP utilizes the Doppler effect by transmitting sound at a fixed frequency and listening to echoes returning from sound scatterers in the water so that the relative velocity between the instrument and scatterers in the ocean is measured. Velocity profiles are produced by dividing the echo into depth bins. Data are averaged vertically in each depth bin, the height of which is defined by the operator. For specifics of the instrument capabilities and configuration options the reader is referred to the user's manual (RD Instruments, 2001).

Figure 36 Over the side mounting for ADCP.

There are two options to provide position data to the ADCP: i) bottom-track, ii) GPS options. The primary function of bottom-track is to measure the ADCP's speed-over-bottom and detected range-to-bottom. The absolute water velocity is calculated by subtracting the boat's velocity vector from the measured velocity vector. However, when the bottom is out of range or if there is a very heavy layer of suspended sediment moving along with the flow, the ADCP can falsely detect the bottom in the moving suspended sediment layer, resulting in biased measurements. Since Hartwell Lake is 50 m deep, the bottom was out of range, and therefore the navigation information provided by a Global Positioning System (GPS) receiver is integrated and used to obtain the relative velocities to the earth's reference frame.

Data are averaged in time to reduce the measurement uncertainty. Velocity uncertainty includes two kinds of errors: random error and bias. Averaging reduces random error. The size of the random error depends on ADCP frequency, depth cell size, number of pings averaged, and beam geometry. External factors such as turbulence,

density gradients and ADCP motion also influence error. Bias error depends on temperature, mean current speed, signal/noise ratio, and beam geometry.

For quantification of this bias error, several tests were performed in a 2.5 meter deep swimming pool prior to the field trip. The ADCP was placed in the middle of the pool bottom looking upwards. The pump of the pool was turned on and off so that the velocity magnitude and direction uncertainty could be investigated. Data were averaged every 10 minutes. The depth of each cell (bin) was selected as 10 cm. The pump was turned off after 30 minutes and turned on again after 460 minutes. When the water was turned off the average noise levels observed varied in the range of 1.4 cm/s. Thus the noise level of the ADCP was determined to be ± 1.4 cm/s for the conditions encountered in the pool tests.

In Hartwell Lake, data were collected and stored internally and averaged every 30 seconds with a bin size of 1 meter. The blanking distance of the instrument, where bad data close to the transducer are blanked out, was 0.44 m. The velocities had to be corrected for the boat speed since the measurements were made while the boat was moving. It is necessary to have an external means for estimating the boat's velocity. A GPS receiver was used to estimate the boat's velocity while underway. Since ADCP data were averaged every 30 seconds, an average of ± 1 m of typical error between two position data readings resulted in ± 6 cm/s error in boat and water current speed when the boat was moving at a typical speed of 2.5 m/s.

A correction is also required to account for the discrepancy between true north and magnetic north. True north is defined by the axis of rotation of the earth. Magnetic north is defined by the earth's magnetism, caused by the flow of electrons in its fluid

metallic core in motion. The earth's magnetic poles are mobile and therefore magnetic north varies over time, as well as from place to place, on the earth. The ADCP uses an internal electromagnetic compass to determine the magnetic heading, and the GPS uses true north. For the duration of the field trip, and for the location of Hartwell Lake, this difference was - 5 degrees and 22 minutes. The velocities were corrected by adding this difference to the direction.

Due to the rough weather conditions during the field trip, successful measurements were mostly made on the west side of the lake. The transects where the velocities were measured are shown in Figure 37.

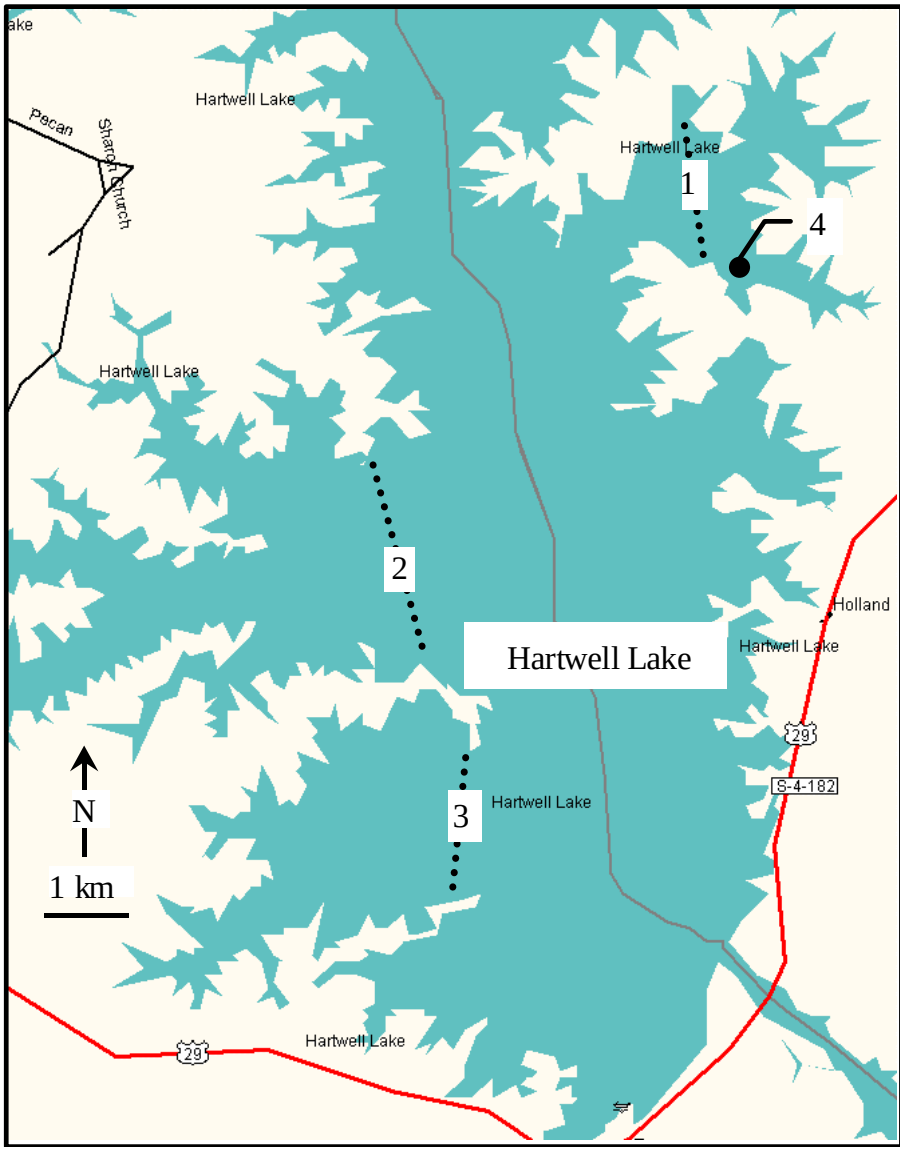

Figure 37 Transects (1, 2, and 3) where the velocity vectors were measured by ADCP. Velocities were also measured at one location (4) when the boat was anchored.

4.4 Analysis of Velocity Data

Velocities at the selected transects in Hartwell Lake shown in Figure 37 were measured using the ADCP with GPS speed corrections. During the measurement period strong winds from the southwest were observed. Boat speed was maintained near 2.5 m/s.

Figure 38 shows the near-surface velocity vectors measured at transect 1 after correction for the boat velocity. At this transect, maximum surface velocities were measured as 25 cm/s. In all cases, reported surface velocities represent velocities averaged over the top bin thickness of 1 m below the instrument's blanking distance of 0.44 m. The measured velocities were filtered to discard measurements for which the error velocities exceeded 5 cm/s (20% of the average velocity). The velocity vectors shown here were also filtered for large changes in the boat heading. The vectors were omitted when abrupt direction changes (more than 10^{o}) in consecutive ensembles provided by the GPS were observed. Without filtering, some of the velocity vectors along the transects pointed in the opposite direction as compared to the rest of the vectors. Comparison of these measurements to the navigation data obtained from the GPS indicated that measurement errors in the navigation data resulted in velocity measurement errors. Figure 39 shows the measured velocity profile for the same transect before the filtering process. The figure shows that without the filtering, very abrupt changes in neighboring ensemble velocities were measured in some locations.

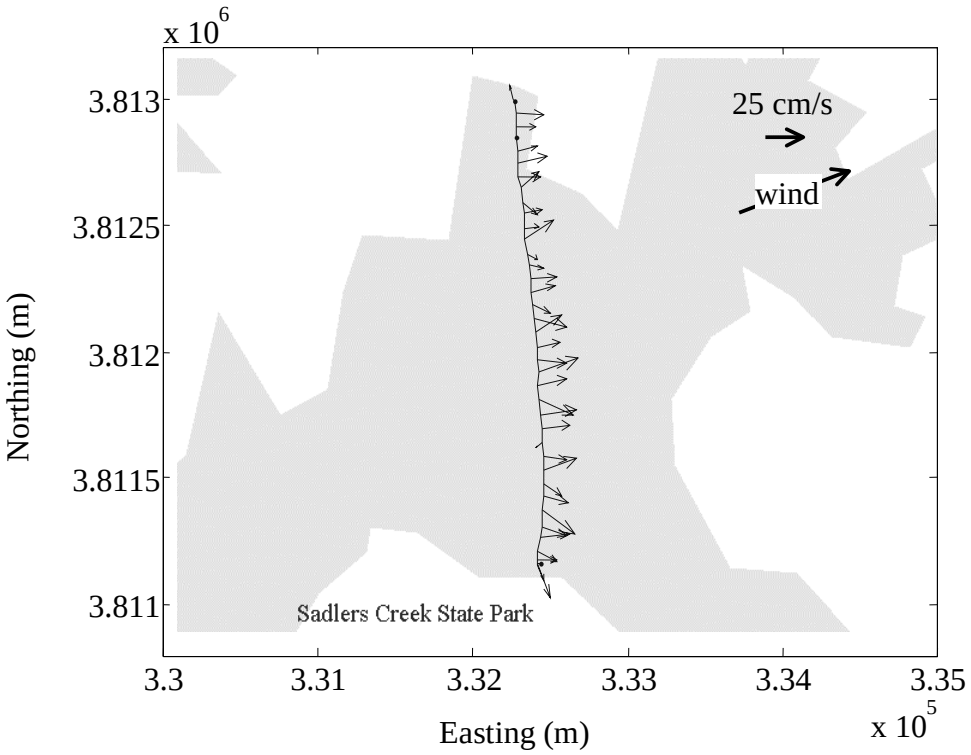

Figure 38 Near-surface velocity vectors measured at transect #1 shown in Figure 37.

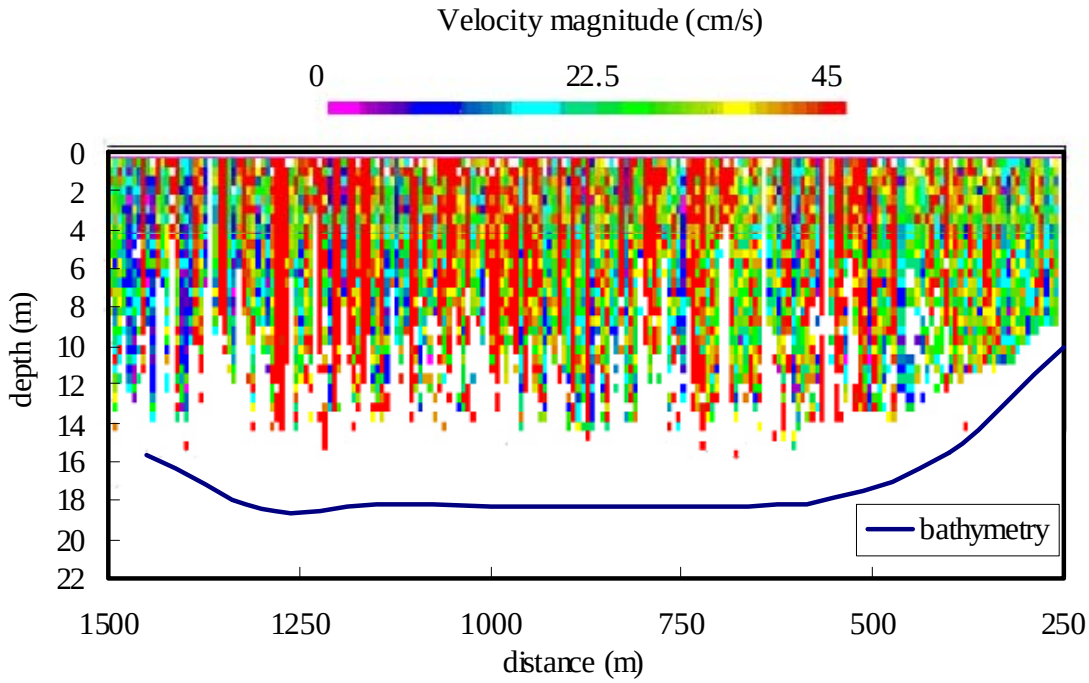

Figure 39 Measured velocity profiles for transect #1 before any filtering was applied.

Measured near-surface velocities at the other two transects (#2 and #3) are shown in Figures 40 and 41, respectively. In both cases, maximum measured velocities are ~50 cm/s and average velocities are ~25 cm/s. One rule of thumb for wind-driven currents in open water is that mean currents are 3% of wind speed. During the field measurement period wind was blowing from the southwest at ~10 m/s magnitude. This simple rule of thumb gives roughly 30 cm/s of surface currents, in agreement with the measurements.

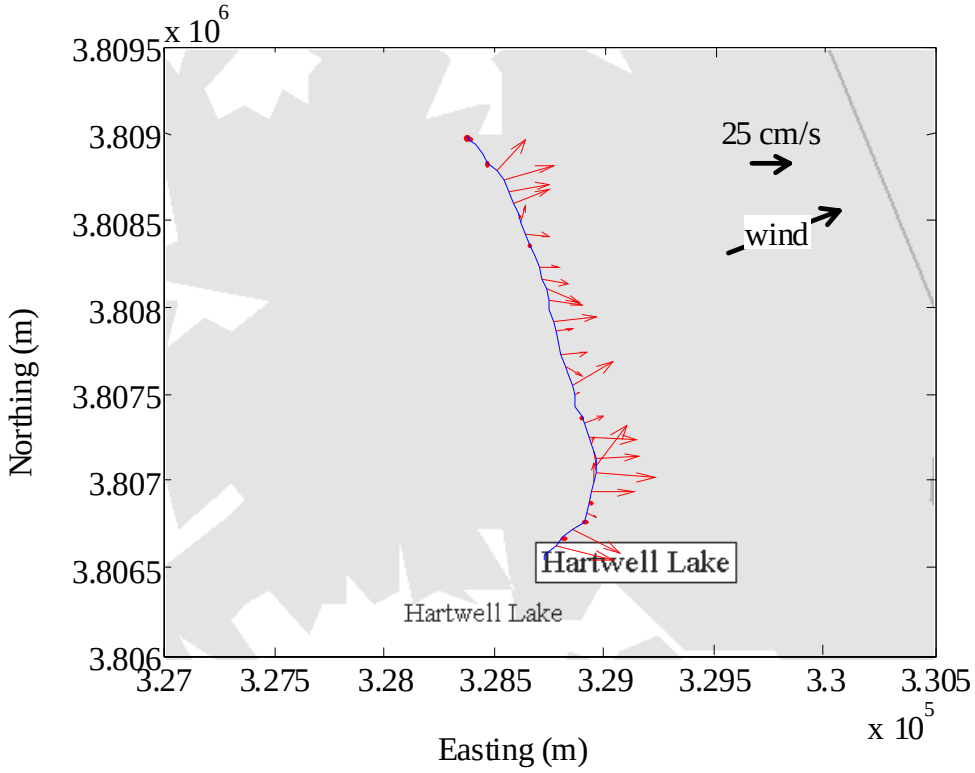

Figure 40 Near-surface velocity vectors measured at transect #2 shown in Figure 37.

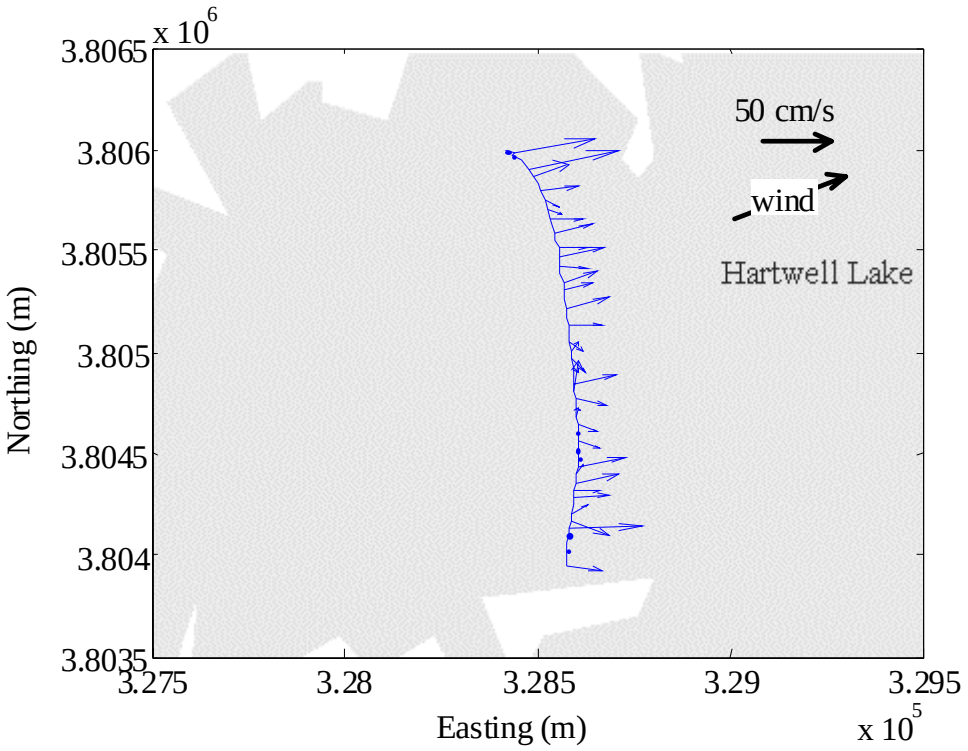

Figure 41 Near-surface velocity vectors measured at transect #3 shown in Figure 37.

4.5 Hydrodynamic Model Simulations

The EFDC hydrodynamic model was applied to Hartwell Lake to simulate lake response to wind forcing and inflows/outflows. The results were compared to the velocity measurements to provide a check on the accuracy of model simulations.

The effects of wind, inflows and outflows on lake circulation patterns were simulated. A 13-day simulation of hydrodynamic processes starting on February 1st and ending on February 13th was conducted using the wind direction and speed data shown in Figures 42 and 43, and flows given in Figure 44. Velocity data were mostly measured on February 12nd and 13th, therefore simulations were conducted long enough to match the measurements. During the field trip, strong winds mostly from the west and southwest directions were observed. The mean water level was constant at 199.4 m.

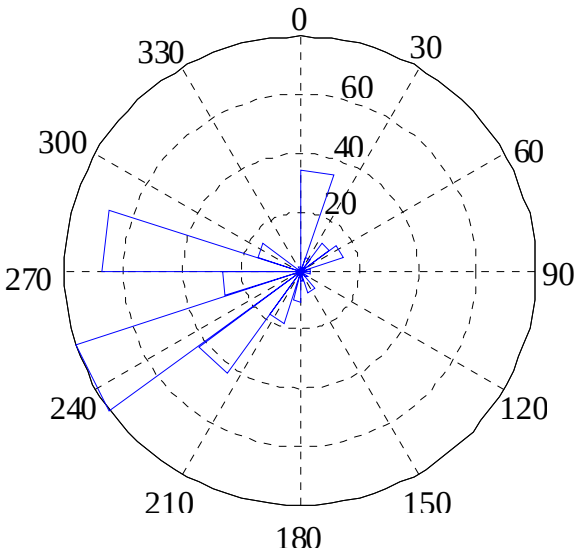

Figure 42 Frequencies of the hourly wind direction data obtained from Anderson County Airport, SC for the period of February 1st to 13th. A direction of 0 refers to winds from the north direction. Radial axis represents the frequency of observations.

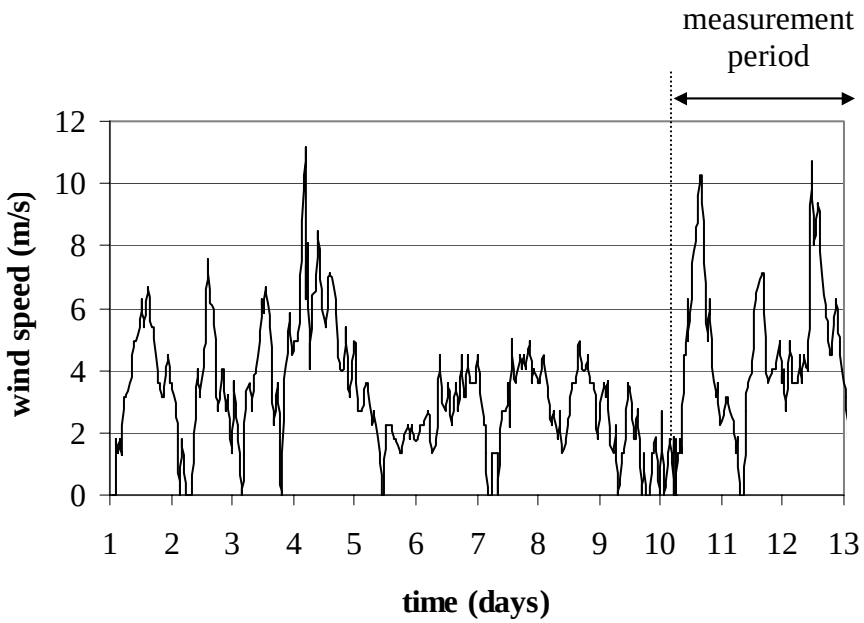

Figure 43 Hourly wind speed data obtained at Anderson County Airport, SC for the period of February 1st to 13th. Data were averaged over one hour period.

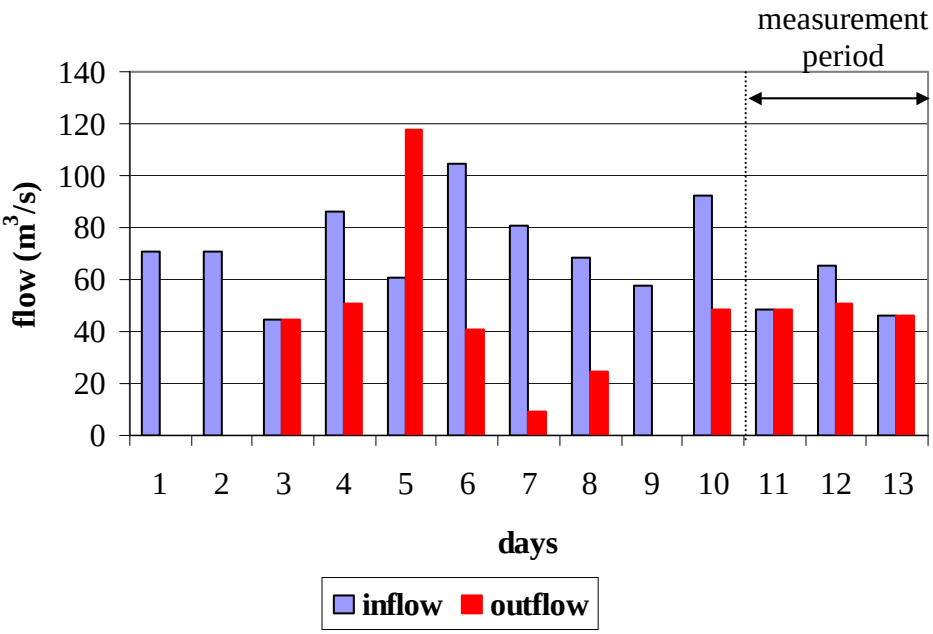

Figure 44 Flow data obtained from USACE for the period of February 1st to 13th.

The computational Cartesian grid used in this simulation was chosen based on sensitivity tests and had 51 × 94 horizontal cells and ten vertically stretched cells, totaling 47,940 cells (Figure 45). 24,210 of these cells were active water cells. Horizontal discretization of each computational cell was 150 m on a side. A 60-second time step was used in the simulations to insure numerical stability.

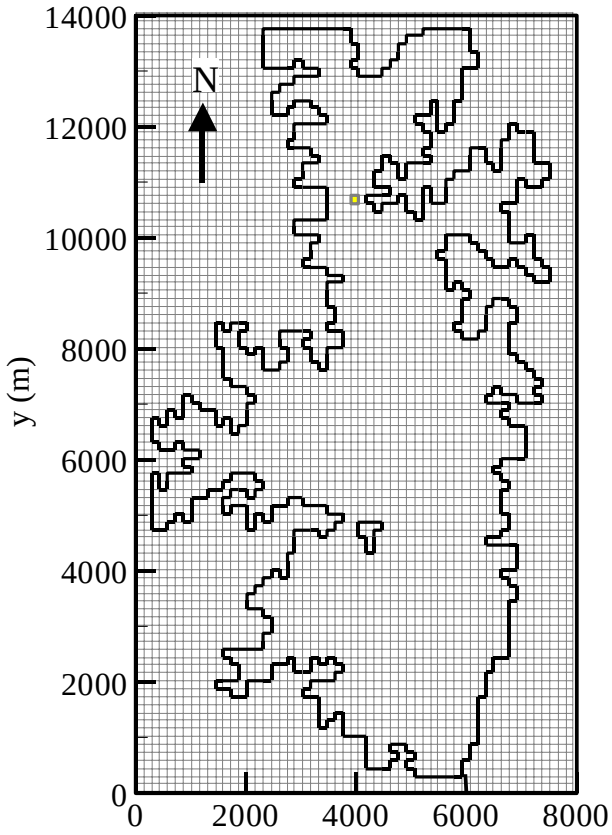

Figure 45 The Cartesian grid used in the simulations. Horizontal discretization was 150 m on a side for each cell.

Initial conditions were set for water depths, flow velocities and water column temperatures. Initial water depths were set to match the data obtained from digitized topo maps. Initial velocities were set to zero. Water column temperatures were initialized at 10 °C (constant in space). The spin-up time period (the time it takes to reach a steady state solution under constant forcings) of the model was about one day. The model was warmed up for 20 days, since initial conditions (i.e. velocities) were approximated.

The bottom drag coefficient used in the simulations was 0.02, appropriate for a mud bottom as suggested by Smith (1997) and Rueda et al. (2003). Other model parameters used in the simulations are given in Table 6.

Table 6 Model parameters used in the simulations.

Parameter	Value
Dimensionless roughness height	0.003
Horizontal momentum diffusivity	0 m^2/s
Kinematic eddy viscosity	0 m^2/s
Kinematic eddy diffusivity	1 E-08 m^2/s
Minimum turbulent intensity	1 E-08 m^2/s^2

The sensitivity of the computed velocities to model input parameters was investigated. When the bottom drag coefficient was increased to 0.06, the simulated bottom velocities were changed by 4% (RMS change: 2 mm/s). Surface velocities were not sensitive to the values of the bottom drag coefficient. When the horizontal momentum diffusivity was increased to 1 E-08 m^2/s, the simulated surface velocities were changed by 1% (RMS change: 0.6 mm/s). Therefore, neither the bottom drag coefficient nor the horizontal momentum diffusivity had a significant effect on the model results. Sensitivity runs demonstrated small differences in velocities for different values of minimum kinematic eddy viscosity, and minimum kinematic eddy diffusivities. Default values for the horizontal momentum diffusivity, minimum kinematic eddy viscosity, and minimum kinematic eddy diffusivities were used in the model, since sensitivity analysis of these parameters did not present any significant effects. The wind stress coefficient was calculated directly from the specified wind velocity in the model as explained previously.

4.6 Comparison of the Velocity Measurements to the Hydrodynamic Model Results

The top and bottom layer velocity distributions within Hartwell Lake after 11.5

days of simulation with the measured flow and wind data are shown in Figures 46 (a) and (b). The model produced velocity vectors indicating that water flows downwind at the surface and returns upwind at the bottom. Although in high wind conditions the velocity vectors followed the wind direction at the surface, when the intensity of the wind decreased, the formation of gyres were observed at several locations in the main pool. Under uniform wind conditions of low intensity, the flow followed the wind in the shallow regions and was directed against the wind in the central deep parts of the reservoir.

Velocities at the selected transects in Hartwell Lake shown in Figure 47 were measured using the ADCP with GPS boat speed corrections. Overlaying the simulated velocities, the measured velocities are plotted for each transect in Figures 48-50.

The simulated top layer velocities were first compared with those measured along transect 1 (Figure 48). At this transect, average surface velocities were measured as 10 cm/s. The difference between simulated and measured average velocities along this transect was 3.6 cm/s, within the measurement error (the model typically under predicted the measured velocities). The depth along the transect cross section was approximately 18 m in the deepest parts, so that the modeled surface velocities are averaged over the top 1.8 m of the water column. Measured velocities were also averaged over each 1 m bin and the blank distance of the ADCP was 0.44 m. Therefore, the figures show the comparison of velocities averaged over the one meter bin measured below the blanking distance, while the modeled velocities are averaged over the top layer thickness whose thickness varied along the transect.

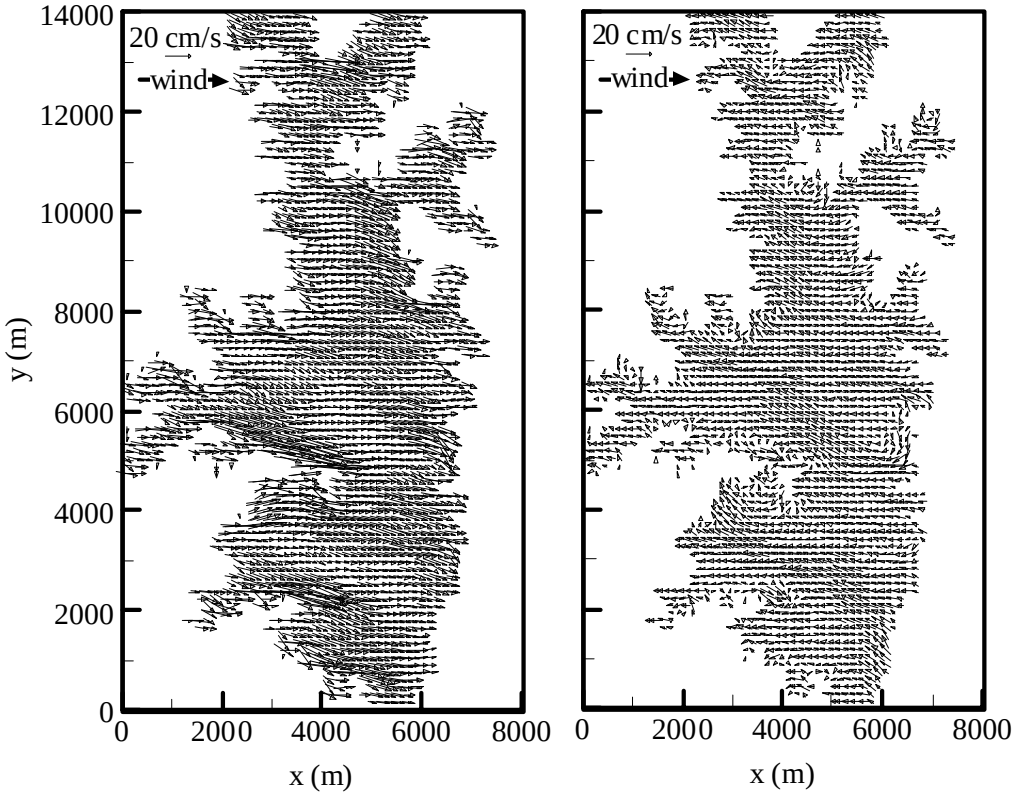

Figure 46 Simulated (a) top layer and (b) bottom layer cell velocity distributions for day 11.5 with the measured flow and wind data.

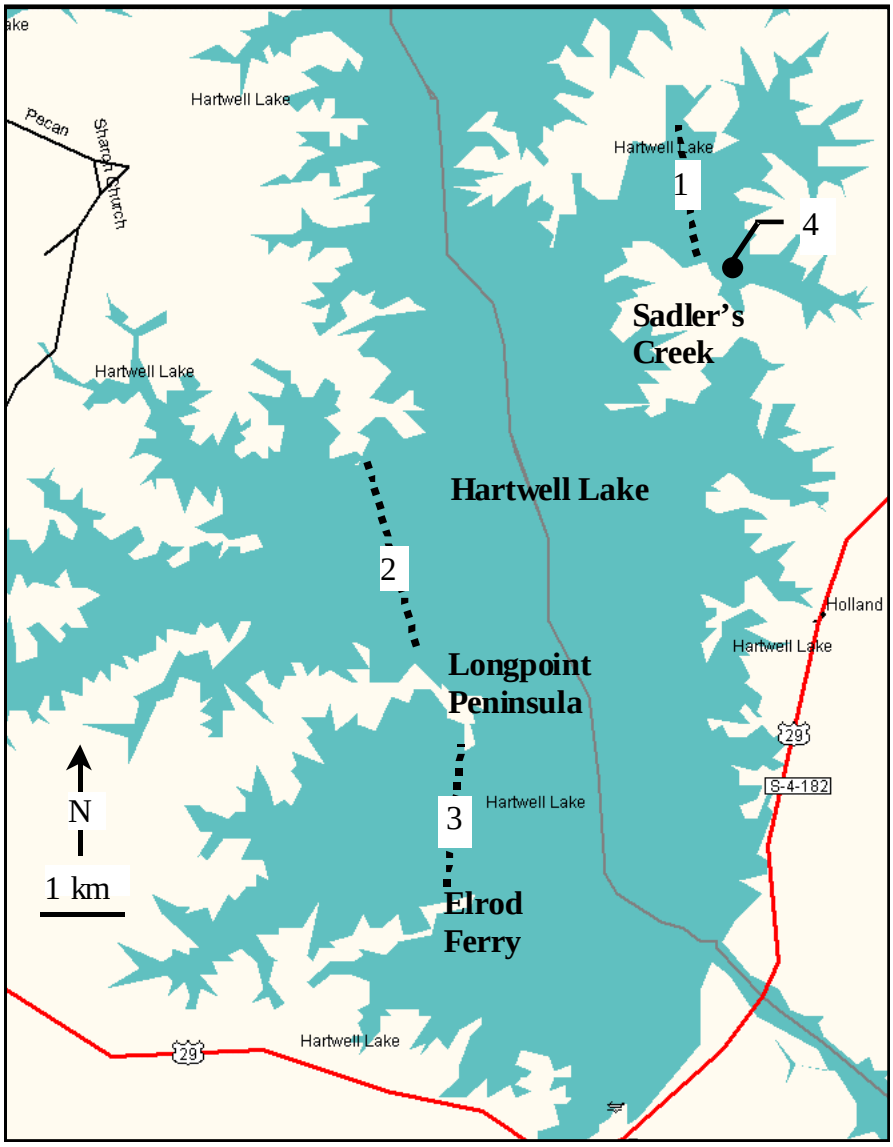

Figure 47 Transects (1, 2, and 3) where the velocity vectors were measured by ADCP. Velocities were also measured at one location (4) when the boat was anchored.

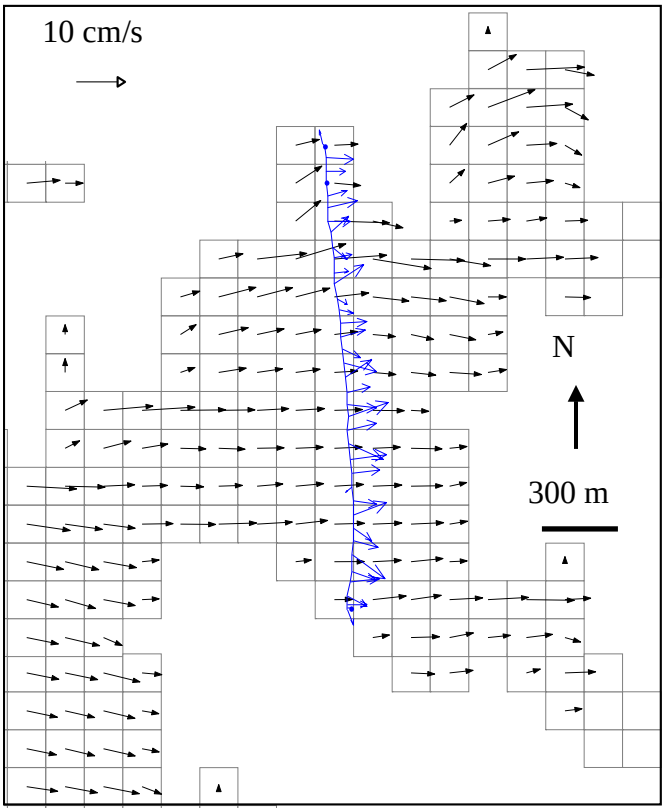

Figure 48 Comparison of measured surface layer velocities with the simulated velocities on day 11.5 at transect 1 shown in Figure 47. The measured velocities are plotted over the simulated velocities.

Figure 49 shows the comparison of simulated top layer velocities with the measured values along transect 2 (Figure 47). At this transect, average surface velocities were measured as 25 cm/s. The measured velocities averaged along the transect were 6 cm/s more then the simulated velocities averaged along the transect. Depth along this transect varied from 5 m to 35 m in the deepest parts.

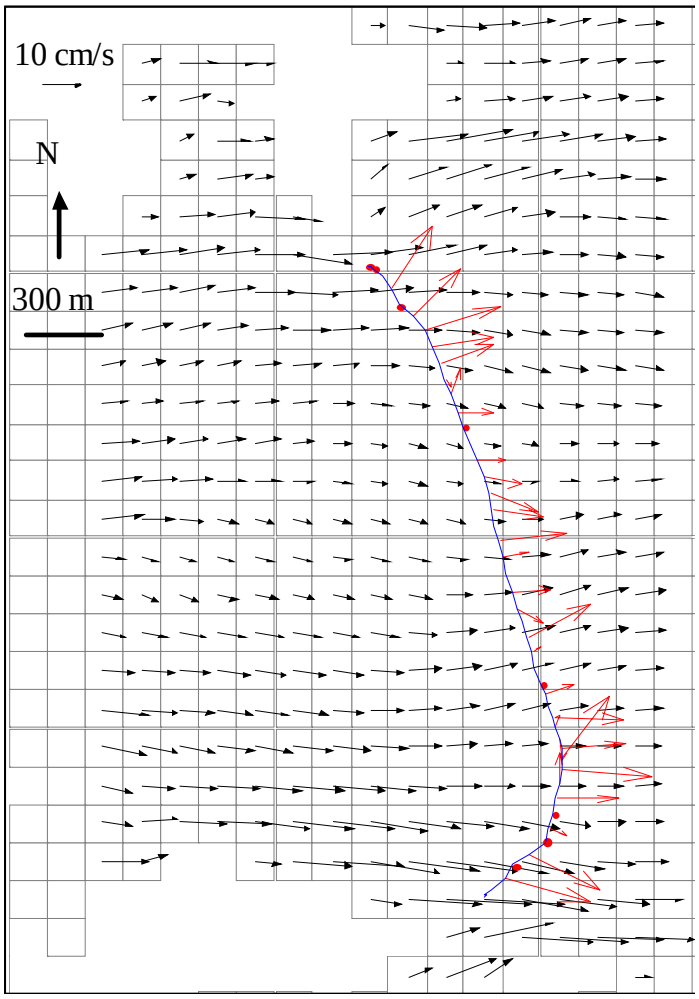

Figure 49 Comparison of measured velocities with the simulated velocities on day 11.5 at transect 2 shown in Figure 47.

Discrepancies in velocity magnitudes would be expected, since the averaging depths for the modeled and measured velocities were not the same at every location along the transect. Similarly, the simulated near surface velocities were compared with the measured values along transect 3 (Figure 50). At this transect maximum depths were approximately 35 m, and average surface velocities were measured as 10 cm/s. The difference between simulated and measured averaged velocities along transect 3 was 5.6 cm/s, where the model underpredicted the measured velocities.

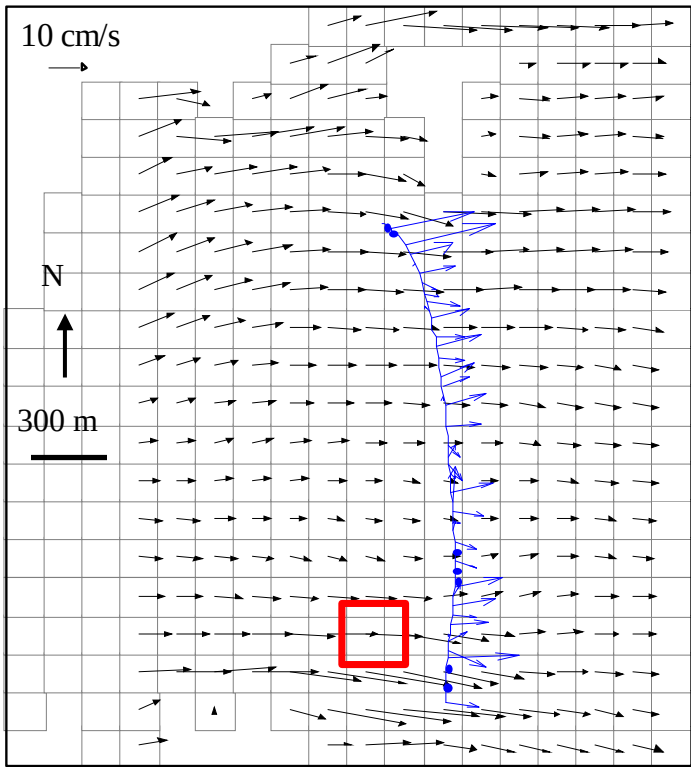

Figure 50 Comparison of measured velocities with the simulated velocities on day 11.5 at transect 3 located between Long Point and Elrod Ferry shown in Figure 47. Square shows a computational cell selected to be used in sensitivity analysis.

Comparison of simulated velocities with the measured values indicated velocity errors ranging from 3.6 to 6 cm/s along the four transects. These values are comparable with other reported values where velocities were measured using similar techniques. Jin et al (2000) reported velocity errors up to 4.56 cm/s, Rueda et al (2003) reported velocity errors up to 5 cm/s. The simulated values were lower than the measured values but still in agreement even without any parameter calibration.

During the field trip, point measurements were made while the boat was anchored at a location near Sadler's Creek shown in Figure 47 (Point 4) where the water depth was 15 m. Point 4 is located behind Sadler's Creek peninsula and has a small fetch of ~ 500 meters (one tenth of the others). The measured east and north velocities are thus much

smaller (about 30 % of the average) than the measured velocities at the three other transects. Comparison of measured and simulated velocities is given in Figure 51.

Since simulated velocities were lower than the measured values, the possible reasons were investigated. Hodges et al. (2000) discusses the importance of using multiple wind stations around the lake for monitoring wind data for a realistic representation. Near Hartwell Lake hourly wind data are monitored at three stations, Anderson, Greenville – Spartanburg, and Athens Airports as shown in Figure 52. Table 7 provides the elevation of each station and their distances from the lake. Data from Anderson Airport were used in simulations since it was the closest station to the lake.

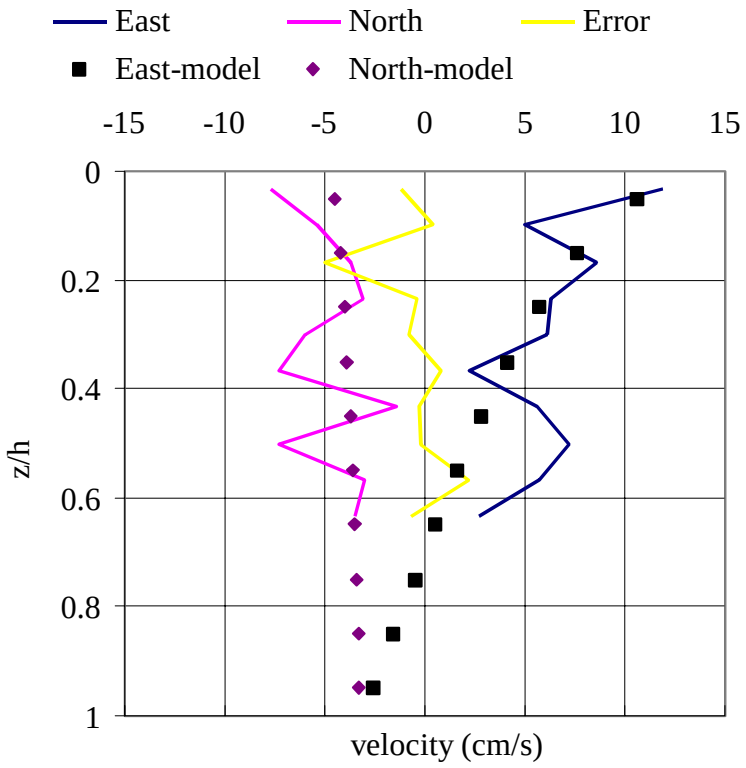

Figure 51 Comparison of measured velocities with the simulated velocities on day 11.5 at point #4 shown in Figure 47. *z/h* is the dimensionless depth and represents surface when equal to 0.

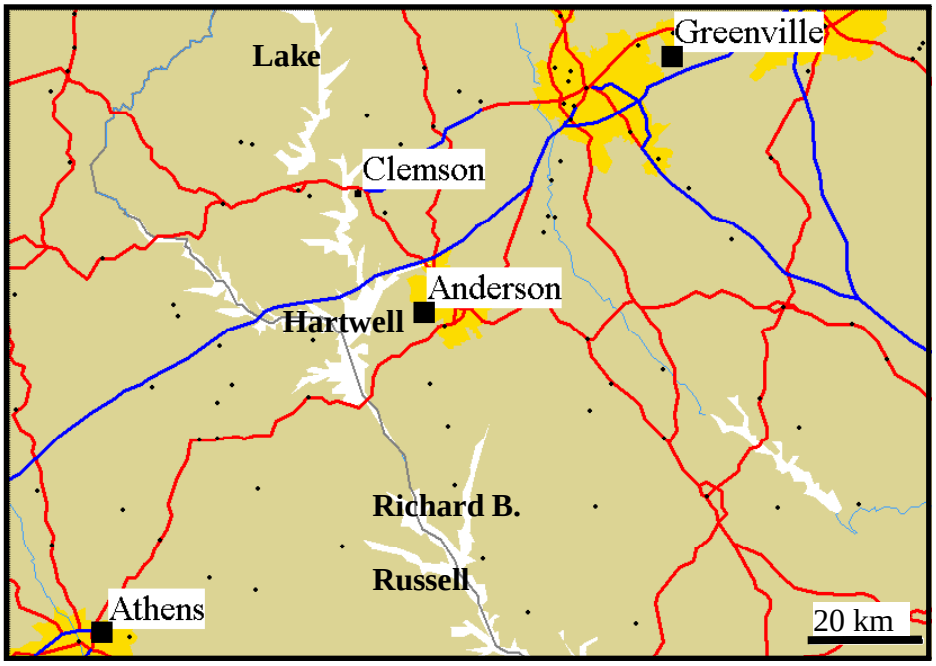

Figure 52 Anderson , Greenville – Spartanburg, and Athens Stations where hourly wind data are monitored near Hartwell Lake.

Table 7 Elevations and distances of wind measurement stations from Hartwell Lake.

Station name	Anderson	Greenville	Athens
Elevation above sea level (m)	231.6	286.6	239.3
Antenna height (m)	10	30	10
Distance from the lake (km)	15	58	60

Measured wind speed and direction data from Anderson and Athens Airports matched closely as seen in Figures 53 and 54. The reason that data from Greenville Airport differed slightly from the other stations may be that the elevation of the Greenville station was approximately 50 m higher than the other two stations. Although data from Anderson and Athens were in good agreement, differences were observed. To account for the possible errors in wind measurements, a sensitivity analysis was performed. The sensitivity tests explained in the following pages present the sensitivity of the predicted east velocities to different parameters. East velocities were used since the dominant wind direction is from the west and southwest. Wind speeds were increased by 20% and the model responded to this increase with an average 21% increase in the surface layer velocities. Figure 55 shows the time series of east velocities at one cell shown by a box in Figure 50.

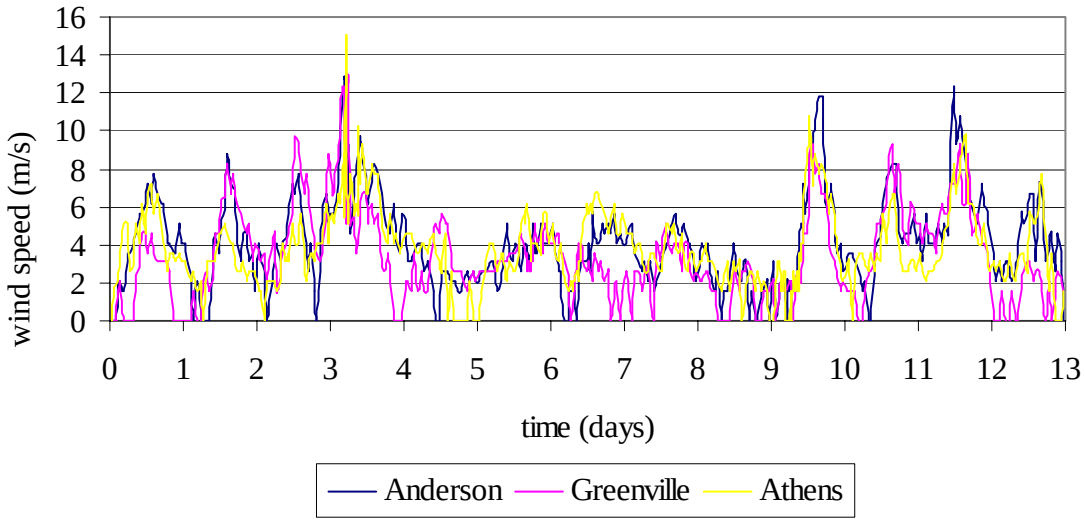

Figure 53 Time series of hourly wind speed data monitored at Anderson, Greenville, and Athens stations. Data were averaged over a one-hour period.

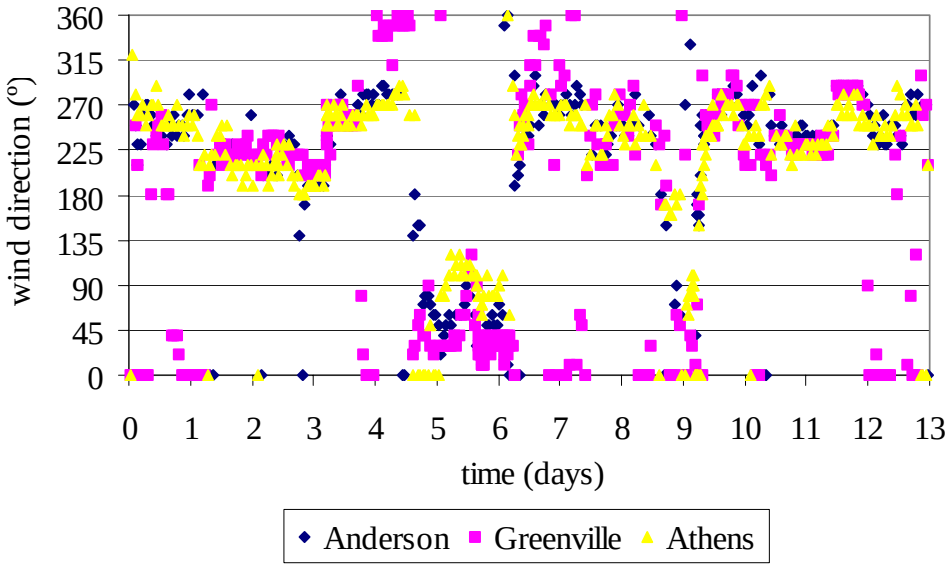

Figure 54 Time series of hourly wind direction data monitored at Anderson, Greenville, and Athens Stations.

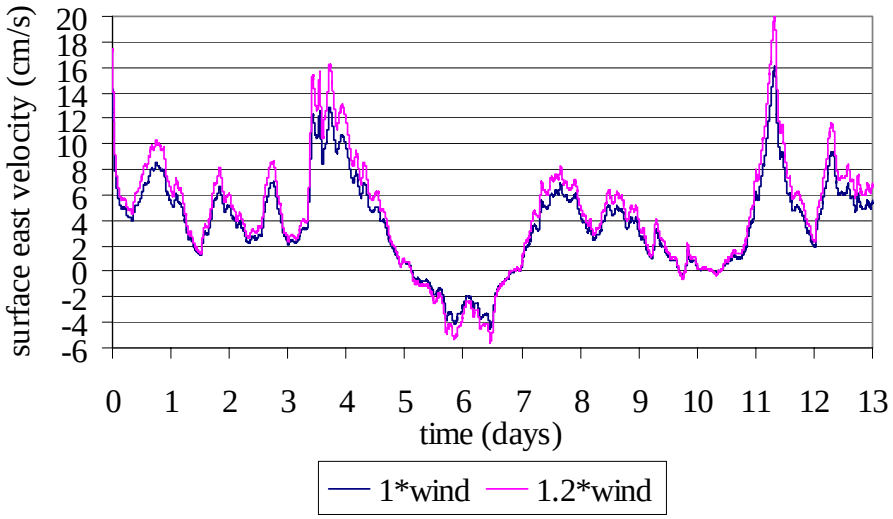

Figure 55 Comparison of simulated surface layer east velocities forced by observed wind conditions with the simulated velocities forced by the enhanced wind speeds at a selected computational cell shown by the square in Figure 50.

When time series of top layer and bottom layer velocities are plotted together with the wind time series (Figure 56), the following observations were made, consistent with Jin et al. (2002): i) During continuous wind conditions, both near surface and bottom layer velocities followed a similar trend with the wind, i.e., flow speed increased as the wind speed increased (see days 1-3). ii) As the wind speed increased from calm conditions, the response of horizontal velocities was changed to a strong surface current, with a weaker current near the bottom (compare days 3 and 11). iii) The response time of horizontal velocities increased when a heavy wind developed from calm conditions (see days 12-13).

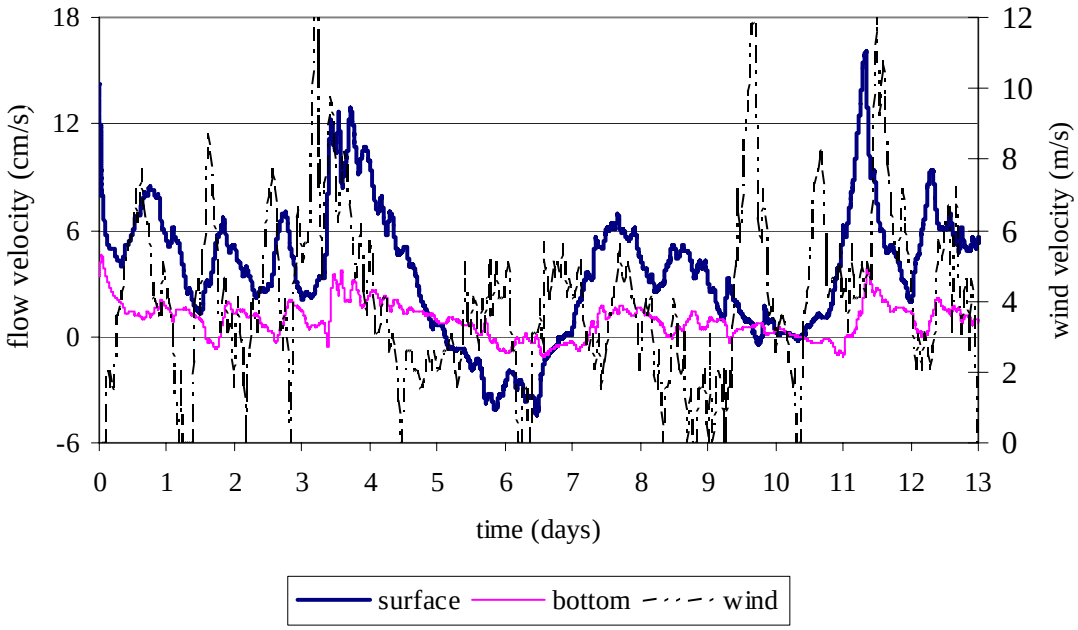

Figure 56 Comparison of simulated surface layer and bottom layer east velocities with wind time series at a computational cell shown by a square in Figure 50.

Total inflow (~ 7×10^7 m^3) and outflow (~ 4×10^7 m^3) volumes were much less than the simulated main pool storage (~ 1×10^9 m^3); therefore, one would expect little impact on the circulation. In order to quantify the influence of possible measurement errors in the flow data, sensitivity of the simulated velocities to the flow data was investigated. The model was run without any flows coming into or leaving the model domain, and the simulated velocities were compared with those obtained when flows were simulated. Comparison of results indicated that wind is the dominant controlling factor, and the inflows and outflows do not have a significant influence. RMS changes for this location were insignificant: 0.089 cm/s and 0.067 cm/s for the surface and bottom velocities corresponding to 2% and 8% of the maximum velocities respectively.

A review of similar modeling studies revealed that other numerical models underpredicted the measured velocities as well. In the studies by Blumberg et al. (1999) (where the Estuarine, Coastal and Ocean Model (ECOM) was applied to simulate estuarine circulation in a harbor), Rueda and Schladow (2003) (where SI3D-L was applied to simulate hydrodynamics of a lake), and Jin et al. (2000) (where EFDC was applied to simulate hydrodynamics in a lake), velocities were simulated and compared to measured values. These comparisons indicated an under prediction of velocities in high wind conditions. A possible reason for this finding might be the tendency of numerical models to dissipate velocities faster than the natural processes.

Another possible reason for the under prediction of measurements is the under estimation of wind stress exerted on the lake surface due to the surrounding topography. Wind data used in the model simulations were monitored at a single station near the lake, but measurement of the wind at different locations along the shores of the lake, might

lead to a better agreement with the measurements.

CHAPTER 5

MODELING OF HYDRODYNAMICS IN A THERMALLY STRATIFIED RESERVOIR: HARTWELL LAKE

Hartwell Lake is an example of a warm monomictic lake, which is vertically mixed during the months from December to March and thermally stratified to varying degrees between April and November. Stratification is strong in summer, and typically a 14ºC difference over a depth of 10 m is measured. Figure 57 shows the temperature profile at a measurement station near the dam during the year 2001.

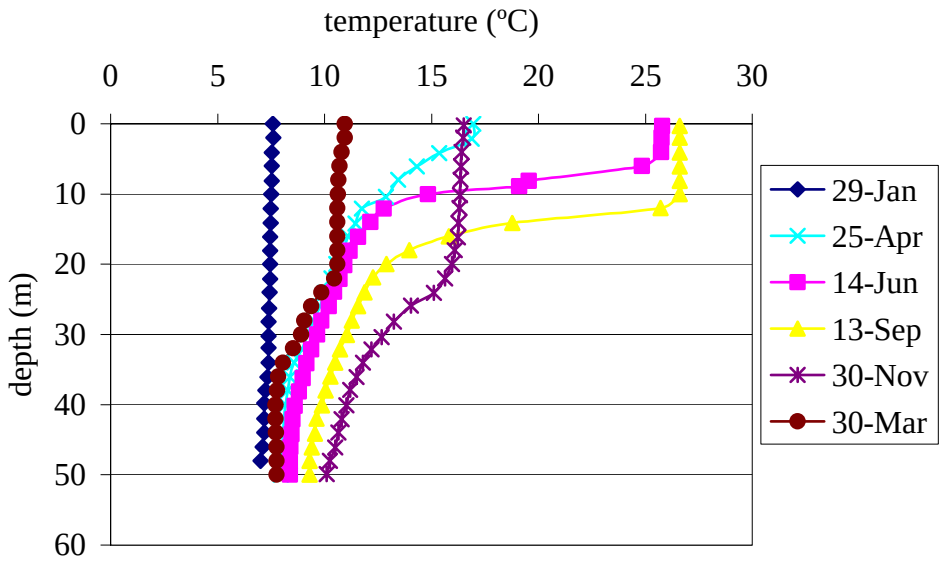

Figure 57 Measured temperature profile near Hartwell dam during 2001. Data were obtained from USACE.

In this chapter, the impact of stratification on hydrodynamics is investigated. The hydrodynamics of a thermally stratified reservoir must be characterized and simulated with good accuracy to avoid large-scale errors in prediction of sediment deposition. Water temperature in lakes and reservoirs varies with diurnal and seasonal changes, mainly due to solar effects and inflows of water. In many cases, inflows are strongly seasonal and they are usually colder than the lake mean water temperature.

Reservoirs have, in general, shorter residence times than natural lakes, meaning that a parcel of fluid remains within the reservoir for a shorter period of time than natural lakes, and therefore they display more significant fluctuations in water temperature than lakes. The stability of a lake's stratification depends on many factors, most importantly the lake's depth, shape, and size. Climate, orientation of the lake to the wind, inflow and outflow also play a role. Lakes or reservoirs with relatively large volumes of water flowing through them (i.e., a residence time less than a month) tend not to develop persistent thermal stratification.

Fischer et al. (1979) classified the mixing regime for a strongly stratified reservoir that is under the influence of wind. He used a non-dimensional ratio of the stability due to stratification compared to the instability caused by the wind stirring (Richardson number). The velocity gradient in the surface water is proportional to the shear velocity induced by the wind, defined by:

$$u_* = \left(0.0013 \frac{\rho_a}{\rho_w} U_{10}^2 \right)^{1/2} \tag{52}$$

where ρ_a is the density of the air, ρ_w is the density of the water and U_{10} is the wind

speed at an elevation of 10 m above the water surface.

The Richardson number, *Ri,* is defined in terms of the shear velocity, u_*, the reduced gravity between the epilimnion and hypolimnion, g', and the depth of mean density, $\bar{h}$ as follows:

$$Ri = \frac{g'\bar{h}}{u_*^2} \tag{53}$$

where the reduced gravity, g', is defined in terms of the acceleration of gravity, hypolimnion density, ρ_h, epilimnion density, ρ_e, and average density, $\bar{\rho}$:

$$g' = \frac{g(\rho_h - \rho_e)}{\bar{\rho}} \tag{54}$$

Fischer et al. (1979) suggested four mixing regimes for different ranges of the Richardson number. Defining the length of the wind fetch across the lake, *L,* and the lake mean depth, *h*, the four regimes defined by Fischer et al. (1979) are as follows (Figure 58):

i) Regime A: $Ri > L^2/(2h)^2$. This regime represents a strongly stratified lake under weak wind conditions. Deepening of the thermocline proceeds very slowly by turbulent erosion.

ii) Regime B: $L/2h < Ri < L^2/(2h)^2$. Internal waves are the predominant feature of this regime.

iii) Regime C: $1 < Ri < L/2h$. Throughout this regime the thermocline will diffuse and incline steeply.

iv) Regime D: $Ri > 1$. This regime represents a weakly stratified lake with strong winds. Deepening of the thermocline is now so rapid and chaotic that the interface will not be well defined.

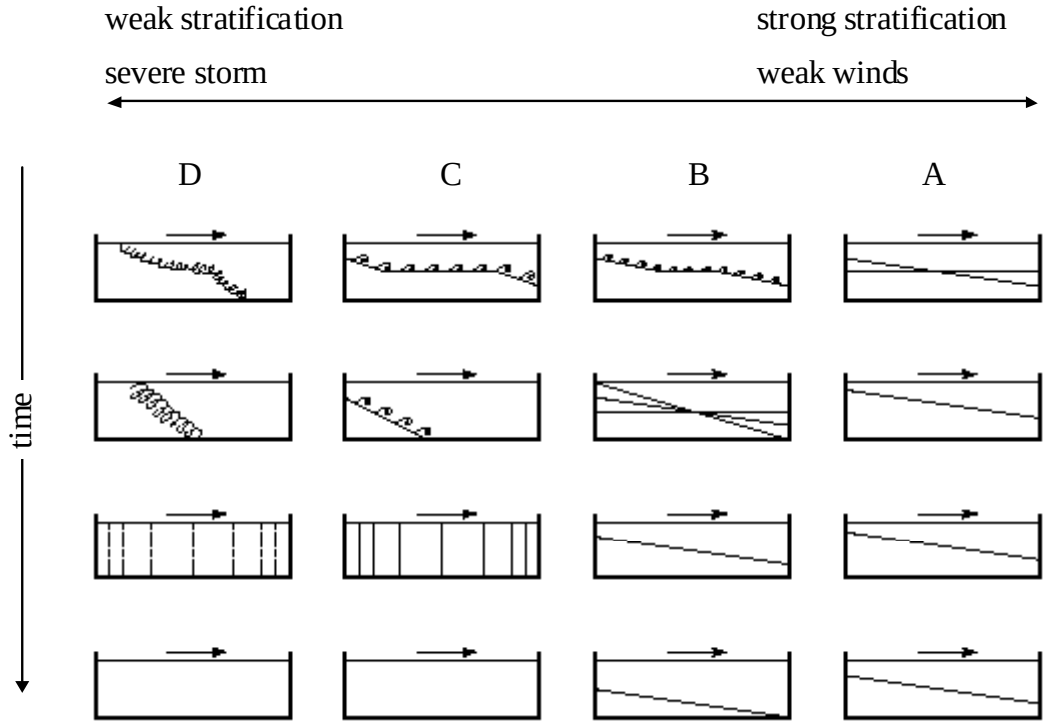

Figure 58 Schematic representation of the mixing sequence for different regimes adapted from Fischer et al. (1979).

A typical Richardson number was calculated for Hartwell Lake. When winds are lower than 6 m/s, Regime A results, and when winds are higher than 6 m/s, Regime B is expected, according to the mixing sequence stated by Fischer (1979). In both regimes, the thermocline would move vertically downward slowly.

Imberger (1998) also characterizes the hydrodynamic regimes operating in a lake

through dimensional analysis. He defined a non-dimensional lake number, L_N, in terms of the total depth of the lake H, the height from the bottom of the lake to the seasonal thermocline h_T, the height to the center of volume of the lake, h_V, the surface area of the lake A_s, the shear velocity u_*, and the stability S_t, as follows:

$$L_N = \frac{S_t\left(H - h_T\right)}{u_*^2 A_s^{3/2}\left(H - h_V\right)} \tag{55}$$

where

$$S_t = \frac{1}{\rho_0}\int_0^H g\left(h_V - z\right)\rho(z)A(z)dz \cong \frac{1}{2}\left(\frac{\Delta\rho}{\rho}g\right)\frac{A_1 A_2 h_1 h_2\left(h_1 + h_2\right)}{\left(A_1 h_1 + A_2 h_2\right)} \tag{56}$$

where h_1 is the depth, and A_1 is the surface area of the upper layer, h_2 and A_2 are the height and the surface area of bottom layer, respectively.

When $L_N > 1$, there is no deep upwelling, and when $L_N < 1$ the deep, cold and often nutrient rich water from the hypolimnion will reach the surface layer during the wind episode. Investigation of the Lake Number for a typical cross section in Hartwell Lake (Figure 59) indicated that for winds < 18 m/s there is no deep upwelling, the momentum induced by the wind is not enough to upwell the water within the hypolimnion. This indicates that except for a severe storm (only 15 hourly measurements for winds >18 m/s were recorded in ten years), deep cold water stays within the hypolimnion. The parameters used in the analysis are given in Table 8.

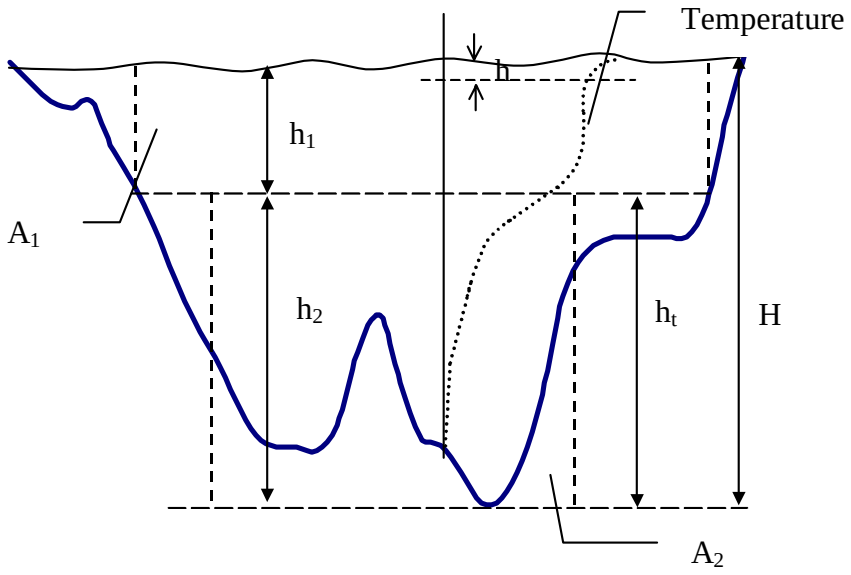

Figure 59 A typical cross section in Hartwell Lake. The parameters used to calculate Lake Number are illustrated. H is the total depth of the lake, h_T is the height from the bottom of the lake to the seasonal thermocline, h_V is the height to the center of volume of the lake, h_1 is the height of the upper layer, A_1 is the surface area of the upper layer, h_2 is the height of the bottom layer, and A_2 is the surface area of the bottom layer.

Table 8 Parameters used to calculate Lake Number for Hartwell Lake.

h_1 (m)	h_2 (m)	A_1 (m^2)	A_2 (m^2)	$\Delta\rho$ (kg/m^3)	H (m)	A_s (m^2)	h_V (m)	h_T (m)	S_t	u_* (m/s)	L_N
10	38.5	6.8E+07	6.1E+07	3	48.5	6.8E+07	35	38.5	3.8E+08	0.022	1.0

When modeling a reservoir numerically, one can choose between a sigma stretched coordinate system (as used by the EFDC model), where vertical layer thicknesses vary spatially, or a coordinate system with constant vertical layer thickness (Figure 60). The effects of using a sigma stretched coordinate system were analyzed by comparing velocities produced by the EFDC model with the velocities produced by a numerical model that uses a coordinate system with constant vertical layer thickness for a stratified fluid over sloping bottom boundary.

For this purpose, and for a better understanding of processes underlying hydrodynamics in thermally stratified reservoirs like Hartwell Lake, a new, 2-D (in vertical plane) simplified numerical model was developed. For the 2-D hydrodynamic model, the governing equations of the EFDC model were used as a basis, with the following assumptions: 2-D (in vertical plane), incompressible flow, and hydrostatic pressure in the vertical (i.e., vertical accelerations are negligible). In addition, the turbulent eddy viscosity and diffusivity were assumed to be constants. The 2-D model used a mesh centered, first order, backward finite differencing scheme on a Cartesian grid to solve the governing hydrodynamic equations. The details of the equations and boundary equations used in the 2-D model are given in Appendix A. The testing of the 2-D model with simple forcing and geometry for which analytical solutions are available in the literature is described in Appendix B.

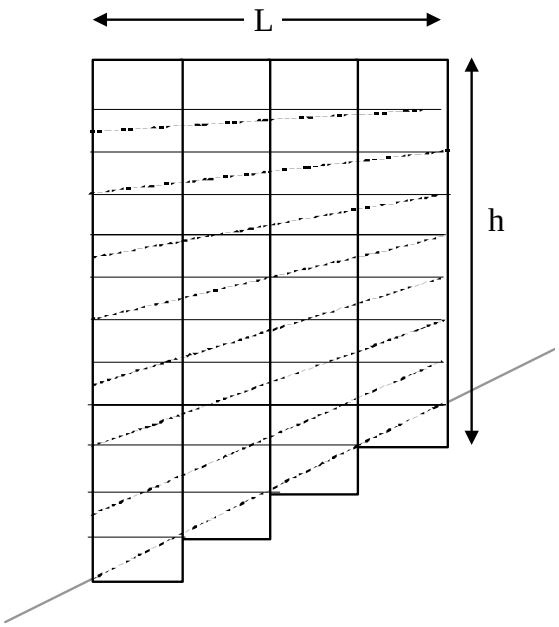

Figure 60 Illustration of two different coordinate systems in the vertical: sigma stretched coordinate system (in dashed lines), and constant vertical layer thickness coordinates sytem (in solid lines).

5.1 Simulation of Stratified Flows

A constant wind of 10 m/s in the (+) *x* direction was simulated by the 2-D model in a 10 m deep, 2000 m wide rectangular model domain for the initial temperature distribution given in Figure 61. A constant heat flux was applied to the surface.

When the velocity vectors simulated for stratified flow are compared to the vectors obtained from the unstratified wind setup case (Figure 62), the major difference is that the depth where the flow reverses moves from the mid-depth to the metalimnion (transition zone) depth. Consistent with other studies, it was evident that the vertical temperature gradient due to the stratification served as a barrier and mixing is confined to the upper layers of the reservoir.

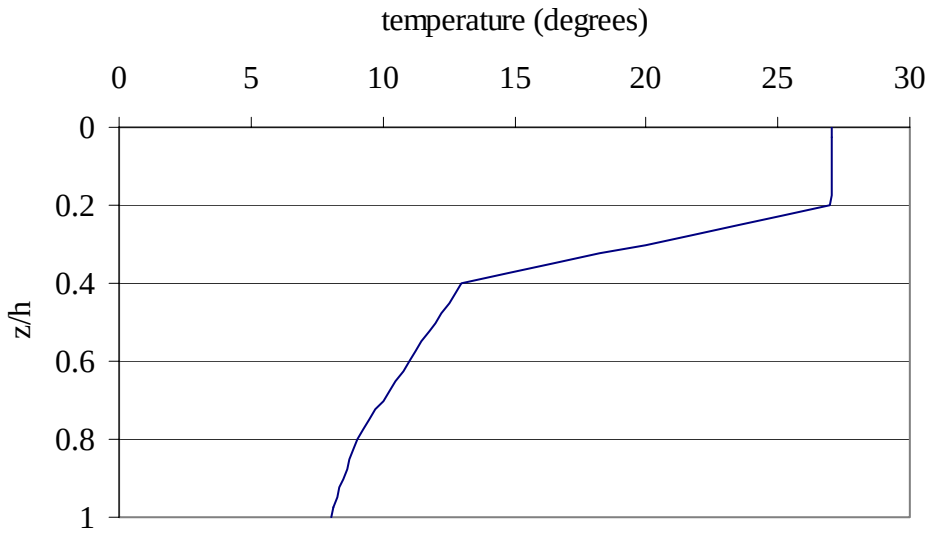

Figure 61 Initial temperature profile of the water column used in model simulations.

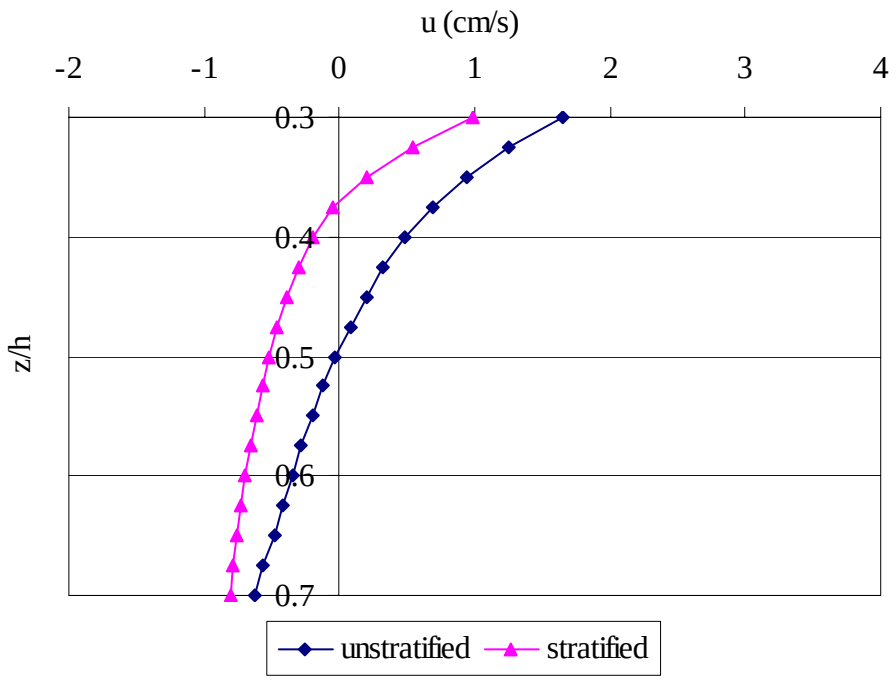

Figure 62 Comparison of the velocity vectors in an initially stratified reservoir with velocity vectors in an unstratified reservoir when wind setup is simulated.

When velocities simulated by the 2-D model from both initially stratified and unstratified cases were compared, the RMS difference was estimated as 3 mm/s (~15% of average velocity) for horizontal velocities and 0.028 mm/s (~6% of maximum velocity) for vertical velocities. Based on this observation, it is concluded that stratification has an effect on horizontal velocities. The magnitudes of vertical velocities were too small to make a realistic comparison.

An assessment of mixing regimes using Richardson number indicated that when a 10 m deep, 2000 m wide, rectangular, initially stratified reservoir was subjected to a constant 10 m/s wind in the east direction, the Richardson number was 785, coinciding into Regime B as described by Fischer et al. (1979). In regime B, a sharp interface energized by surface stirring keeps its position and the thermocline moves towards the surface at one end and deepens to the bottom at the downwind end, consistent with the model results. Figure 63 shows the deepening of the depth at which the flow reverses, an indicator for the thermocline, after 150 seconds. Consistent with this figure the deepening of the thermocline was observed in Figure 64.

In fact this deepening takes place as a result of a sequence of events: i) wind stress moves the water in the epilimnion in the direction of wind, ii) continuity causes the flow in the hypolimnion to flow in the reverse direction, iii) shear develops across the thermocline and increases until the thermocline is tilted to setup a hydrostatic pressure gradient that balances the surface stress (Fischer et al., 1979).

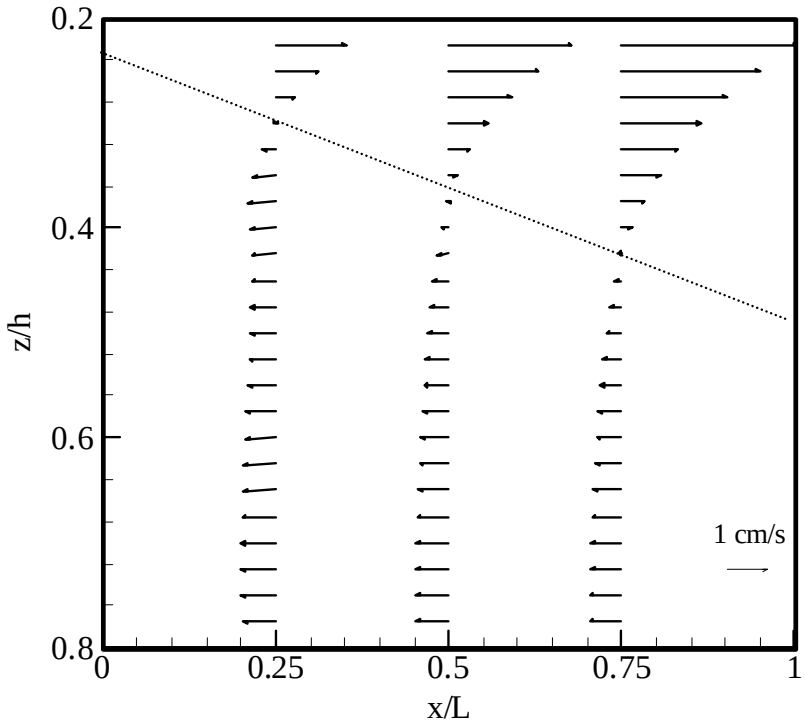

Figure 63 Deepening of the depth of reversal along the axis aligned with the wind. Arrows show the velocity vectors of simulated wind setup in an initially stratified reservoir.

The velocities simulated by the 2-D hydrodynamic model were also compared to the velocities simulated by the EFDC model for a 200 m wide, trapezoidal basin with a sloped bottom boundary that is 10 m deep at the right wall and 8 m deep at the left wall. The reservoir was initially stratified and subjected to a constant 10 m/s wind in the east direction. Figure 65 shows that both models predicted the depth of reversal almost at the same depth, but the velocities differed by an average of 1 cm/s. Differences in velocity magnitudes would be expected for numerous reasons, including the differences in the approximation of turbulence and boundary conditions.

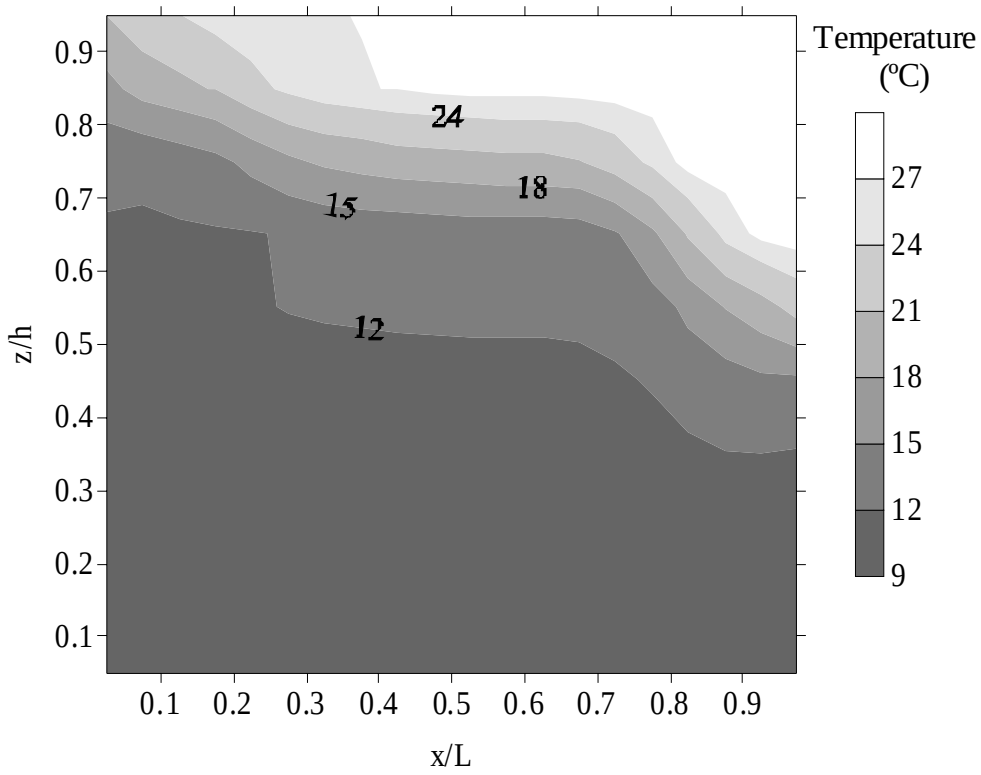

Figure 64 Deepening of the thermocline along the axis aligned with the wind.

Comparisons of velocity profiles produced by the 2-D model and the EFDC model under the same conditions indicated that using sigma stretched coordinates instead of constant vertical layer thickness did not introduce significant differences for the stratified reservoir with a sloping bottom of 1%. The application of both models to a reservoir with a simplified geometry indicated that stratification can, under some scenarios, alter velocity profiles significantly.

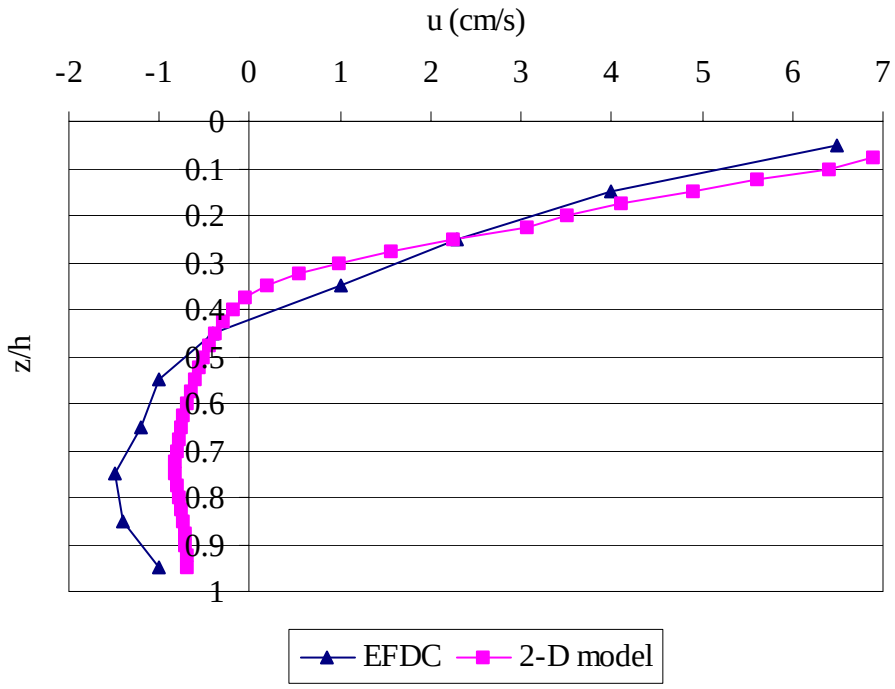

Figure 65 Comparison of the velocity profile in an initially stratified reservoir simulated by the 2-D model with the velocity profile simulated by the EFDC model.

5.2 Simulation of Stratified Flows in Hartwell Lake

Velocities in Hartwell Lake were simulated using the EFDC model, and the sensitivity of model results to initial temperature conditions was investigated by comparing results for stratified and unstratified cases. In both runs, the wind was kept constant at 10 m/s from the southwest. Ten vertical layers with equal thickness were used in the simulations. Results are presented for three different locations (Figure 66): cell A (33.3. m deep), cell B (17.4 m deep) and cell C (21.7 m deep).

For the first case, initial temperature profiles mimic February observations and were kept constant at 9°C throughout the model domain. For the second simulation, a strongly stratified lake is considered, where initial temperature profiles mimic September observations. Figure 67 shows the temperature profiles at locations A, B and C. Since A,

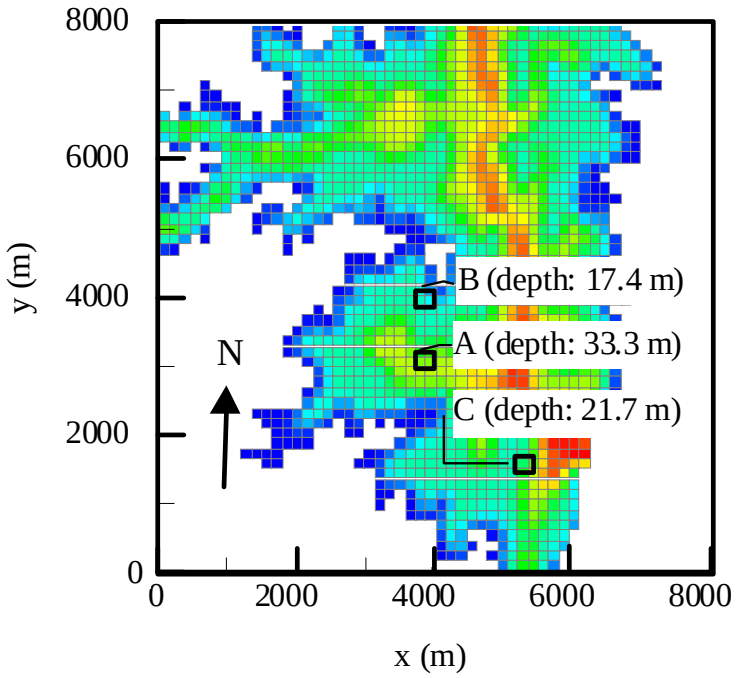

Figure 66 Detail of south end of main pool in Hartwell Lake. Sensitivity analysis results are presented at the computational cells marked A, B and C.

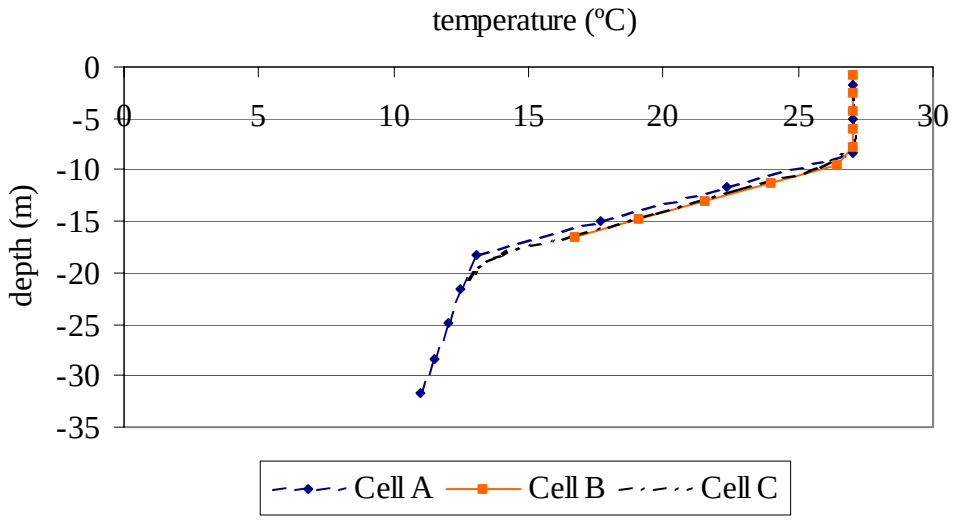

Figure 67 Initial temperature profiles at cells A, B and C for the stratified case.

B and C have different depths, their temperature profiles are also different. Due to this difference in stratification structures, and for other reasons, one would expect variations in velocity profiles.

Comparison of surface velocities at cell A for the initially stratified and unstratified cases indicated that simulated velocities for the unstratified case were higher than the stratified case (Figure 68). Steady-state conditions were reached in less than a day for the unstratified case, but the effect of initial stratification continued throughout the simulation possibly due to the deepening of the thermocline. The evolution of temperature profiles in time for the computational cell A is shown in Figure 69

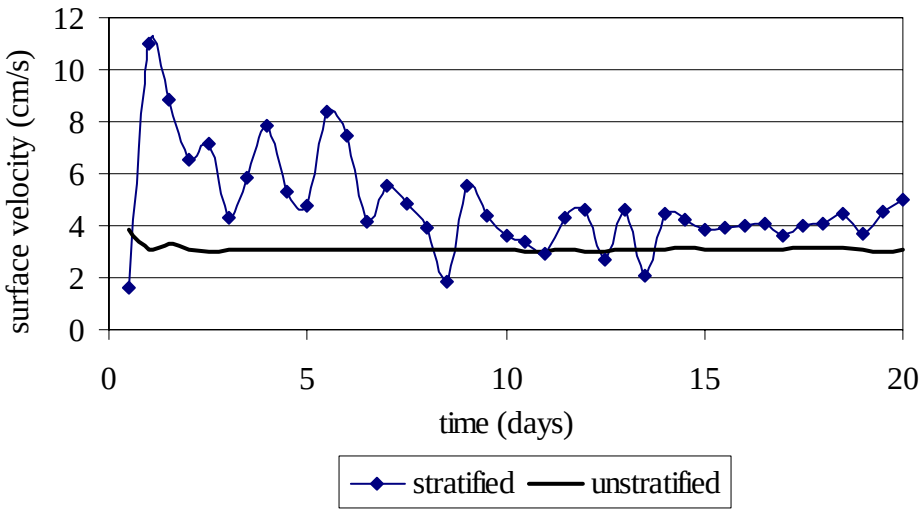

Figure 68 Comparison of surface velocities time series at cell A for initially stratified and unstratified cases.

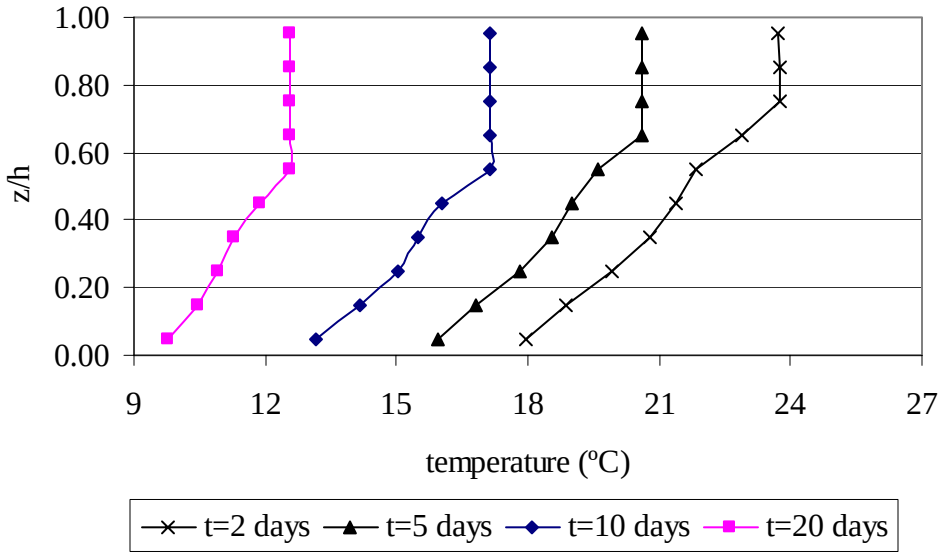

Figure 69 Comparison of temperature profiles at cell A at different times for stratified initial conditions.

Comparison of surface velocities for initially stratified and unstratified cases indicated that the circulation patterns were significantly different for these cases. In fact, when surface velocities were plotted after four days of simulation, differences were observed in both direction and magnitudes of velocity vectors (Figure 70).

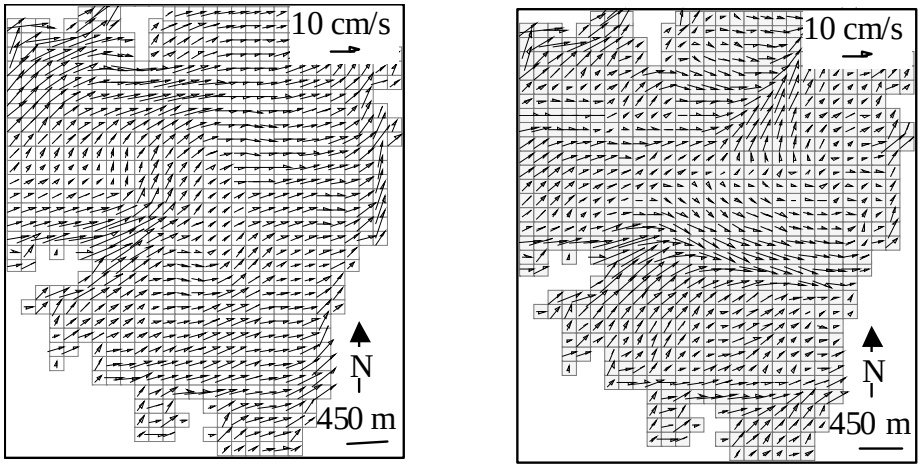

a) b)

Figure 70 Surface velocity distribution at the south end of main pool in Hartwell Lake after four days of simulation for initially (a) unstratified, (b) stratified conditions. Wind was at 10 m/s from the southwest.

When the east velocity profiles at cell A were plotted after 4 days of simulation with constant forcing for both the stratified and unstratified initial conditions (Figure 71), it was observed that the depth at which the reversal of flow begins was located at 30% of the depth below the surface for the stratified flow, where this depth migrated to the mid-depth for the initially unstratified conditions. Figure 72 shows comparison of the mid-depth velocities for both cases, in which the modified circulation pattern due to the stratification was evident. In a stratified flow, most of the kinetic energy imparted by the wind is dissipated by the steep temperature gradient, while the rest is used for the vertical mixing of the fluid in the upper layer.

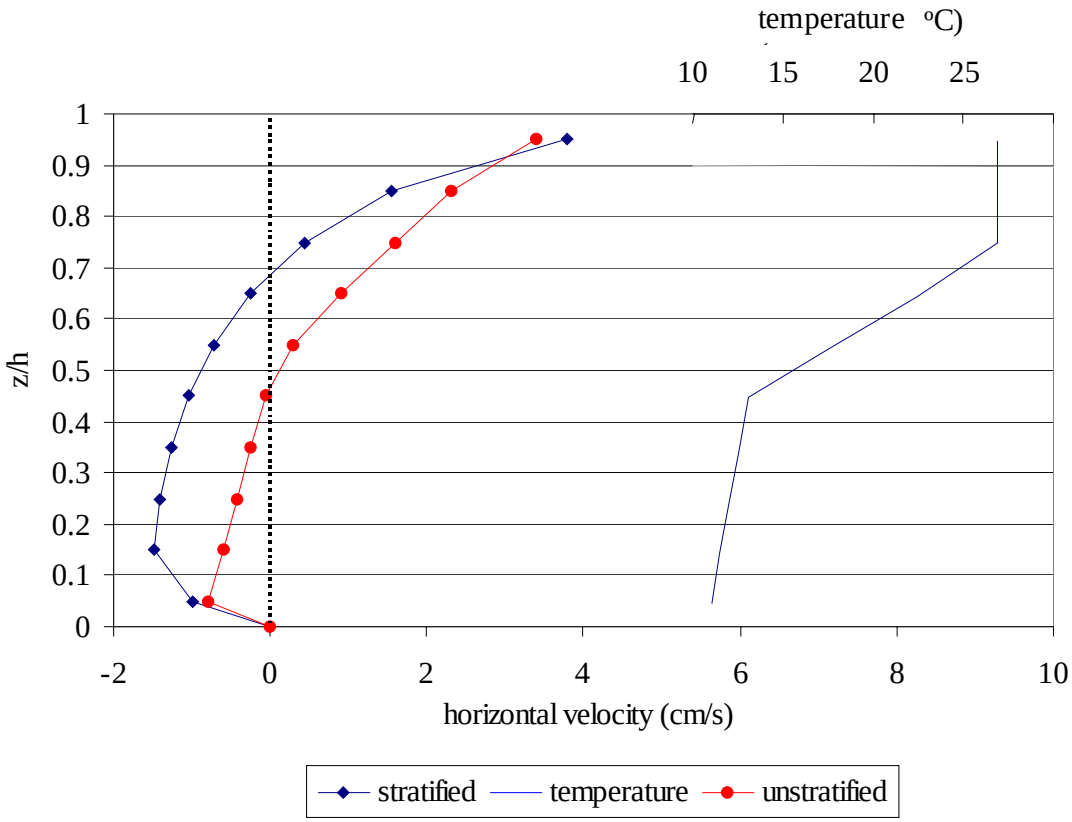

Figure 71 Comparison of east velocity profiles at cell A after 4 days of simulation for stratified and unstratified initial conditions.

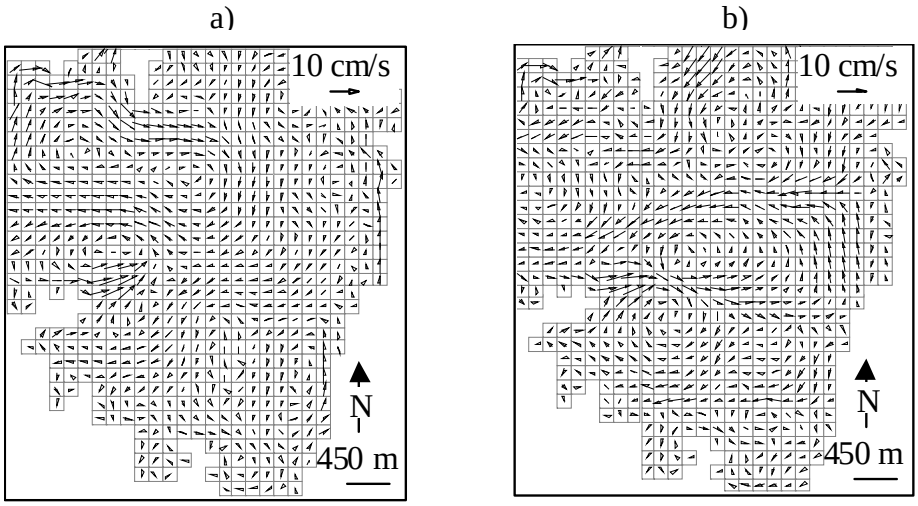

Figure 72 Mid-depth layer velocity distribution at the south end of main pool in Hartwell Lake after four days of simulation for initially (a) unstratified, (b) stratified conditions. Wind was at 10 m/s from the southwest.

Figure 73 shows the comparison of east velocity profiles at cell C after 4 days of simulation with constant forcing for the stratified and unstratified initial conditions. The depth at which the flow reverses was located at 45% of the depth below the surface for the case with unstratified initial conditions, this depth moved upwards to 20% of the depth when the case with the initially stratified conditions was simulated. Also, a decrease in velocity magnitudes was observed with the stratified initial conditions partly due to the energy spent at the thermocline. The differences observed at the bottom velocities are significant and can have implications for sedimentation.

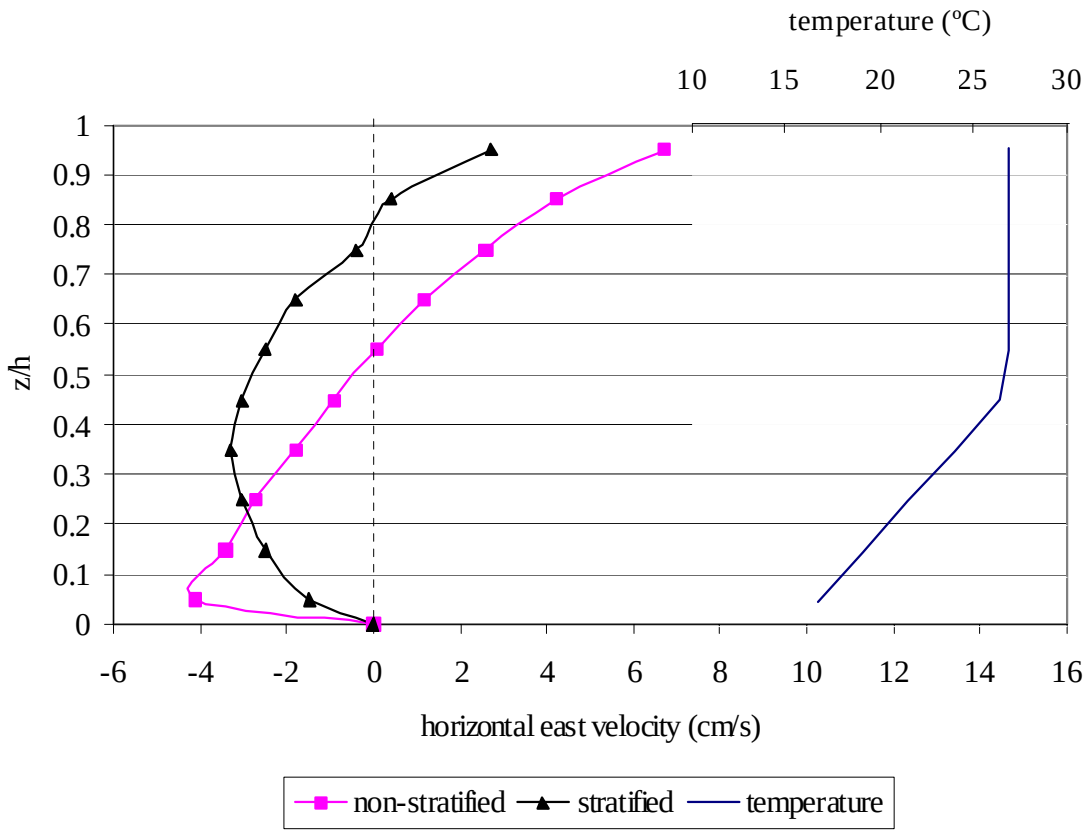

Figure 73 Comparison of east velocity profiles at cell C after 4 days of simulation for stratified and unstratified initial conditions.

Figure 74 shows the velocity profiles at cell B for the initially stratified conditions. It can be inferred from the figure that the depth at which the flow reversal is located migrates downward as time passes and stratification weakens. The evolution of temperature profiles in time for this location is given in Figure 75.

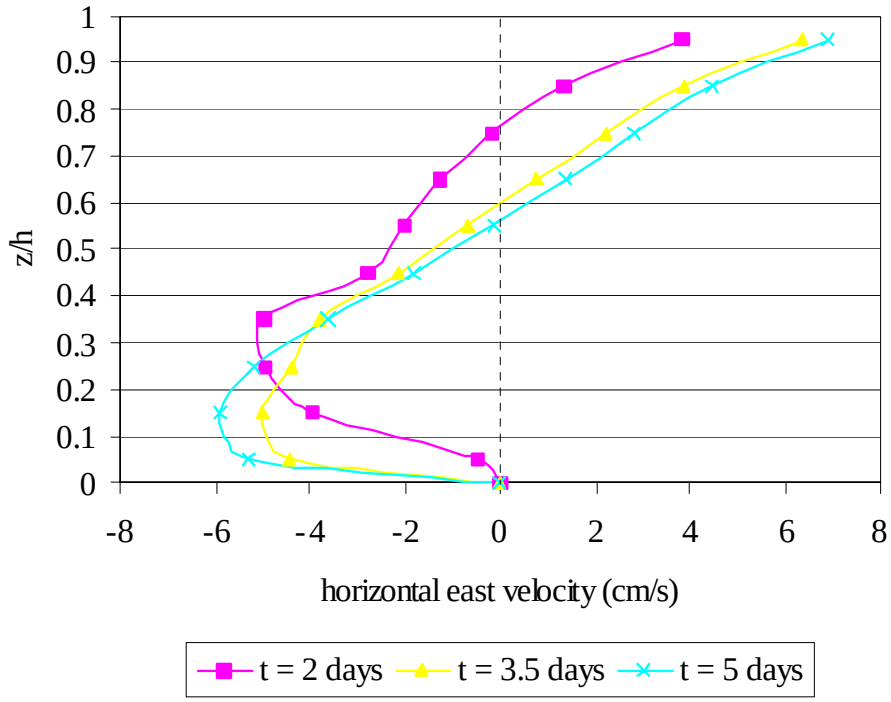

Figure 74 Comparison of velocity profiles at cell B at different times for stratified initial conditions.

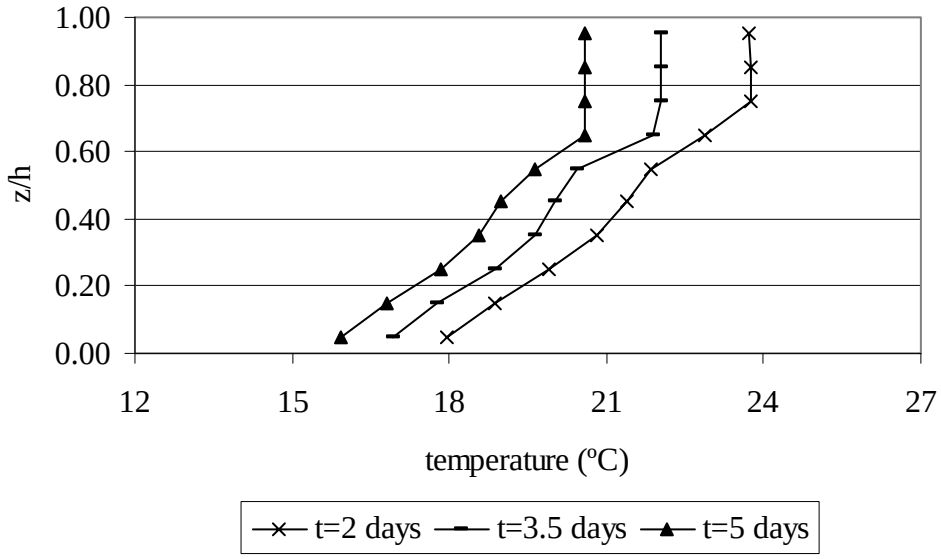

Figure 75 Comparison of temperature profiles at cell B at different times for stratified initial conditions.

Several conclusions can be drawn from the analysis of the effects of thermal stratification on velocities:

- Results obtained from the new 2-D hydrodynamic model and the EFDC model matched the analytical solutions for the simplified cases.
- Using a sigma stretched coordinate system does not have a significant effect on model results if the reservoir is ~1% sloped (typical in Hartwell Lake).
- Results obtained from the 2-D hydrodynamic model and the EFDC model for the simplified model domain were consistent with the mixing regimes derived through non-dimensional analysis, as suggested by Fischer and Imberger.
- The depth at which the flow reverses was typically located at mid-depth for the unstratified initial conditions, while this depth moved upwards when the case with the initially stratified conditions, suggesting more mixing above the thermocline

in the warm surface layer.

- It was concluded that stratification does significantly alter the velocity profile near the bottom, in particular bottom layer velocities, and thus, the impacts on sediment deposition patterns need to be investigated.

CHAPTER 6

MODELING OF SEDIMENT TRANSPORT WITHIN THE MAIN POOL OF HARTWELL LAKE

The concentrations of PCBs within tributaries of the Hartwell Lake are well described (Elzerman et al, 1994; EPA, 1991), but the major question “where would they deposit in the main pool of the lake” remains unanswered. The fine sediments suspended in the water column can behave as a contaminant carrier, since PCBs and other hydrophobic organic chemicals preferentially adsorb to fine-grained sediments suspended in the water column. The cohesive sediments can be advected over large distances before settling, due to their low settling velocities, in particular in freshwater environments.

This chapter describes the prediction of depositional zones for cohesive sediments transported within the main pool of Hartwell Lake. The EFDC model is used to describe lake hydrodynamics and sediment fate. Historical records of wind and flow data were used to determine frequencies of occurrence and representative conditions for prediction of deposition zones for sediment transported by the flow entering from upstream tributaries.

6.1 Input Data

In order to simulate hydrodynamic processes in Hartwell Lake using EFDC, a series of input files describing model domain, bathymetry, initial conditions, climate forcings, inflows and outflows, and sediment properties are required. A careful examination of available data is necessary to determine which forcing combinations should be simulated to represent long-term deposition patterns since modeling every

single climate condition observed in the past is not feasible. For this purpose, a statistical analysis of daily mean values of inflow, outflow and wind data for ten years (1990-1999) was performed, and representative cases were selected for simulation.

Outflows from Hartwell Lake are controlled at the dam. A histogram of flows based on 10 years of flow data (Figure 76) shows that for 20% of the time no water was released at the dam, and for about 40% of the time outflows were in the range of 75-150 m^3/s. The histogram also shows that for about 30% of the time inflows in the range of 25-75 m^3/s were observed. Mean outflow and inflow values were, as expected, the same: 120 m^3/s. A histogram of daily mean water levels is shown in Figure 77, where the observed elevations are between 200 m and 202 m more than 80% of the time.

A histogram of hourly mean wind speeds is shown in Figure 78, indicating that 46% of the time observed wind speeds were in the range of 2-3.5 m/s. Two dominant wind directions were observed in the study area, northeast and southwest (Figure 79). Winds from the southwest dominate in the winter, and winds from the northeast dominate in the summer.

The joint probabilities of the inflow, outflow and wind speed data were also investigated. The cumulative probability distributions for each parameter, calculated independently, were defined in 10% intervals as given in Table 9.

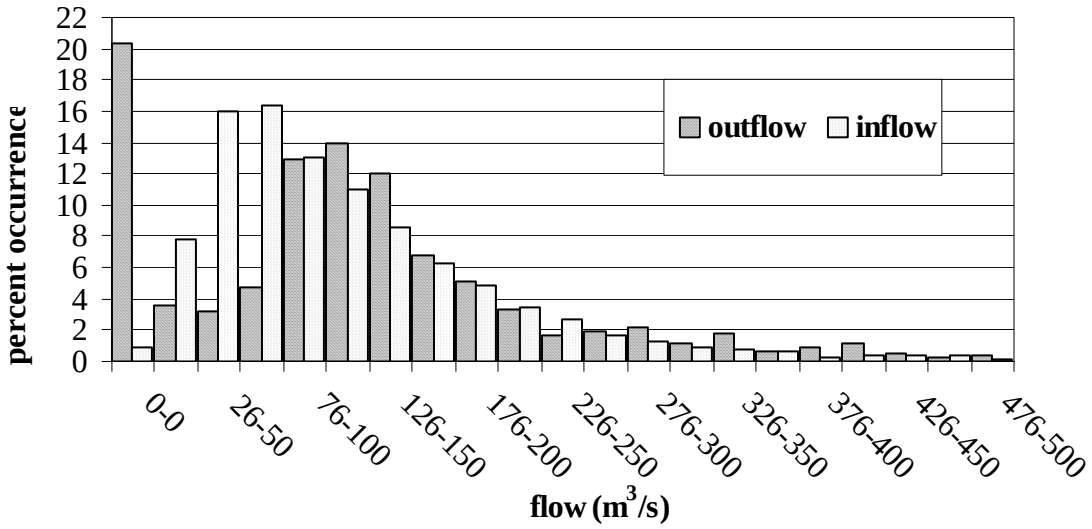

Figure 76 Histogram of inflows and outflows based on daily data for ten years (1990-1999). Mean outflow and inflow values were the same and equal to 120 m^3/s (Source: USACE).

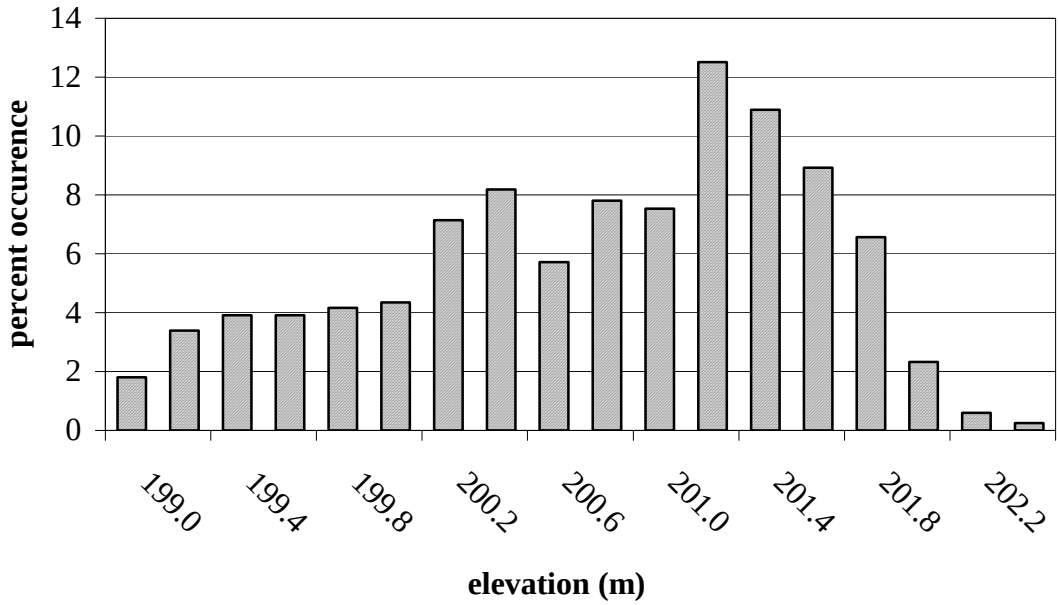

Figure 77 Histogram of water levels (elevation of mean lake surface level measured above mean sea level) based on daily data for ten years (1990-1999) (Source: USACE).

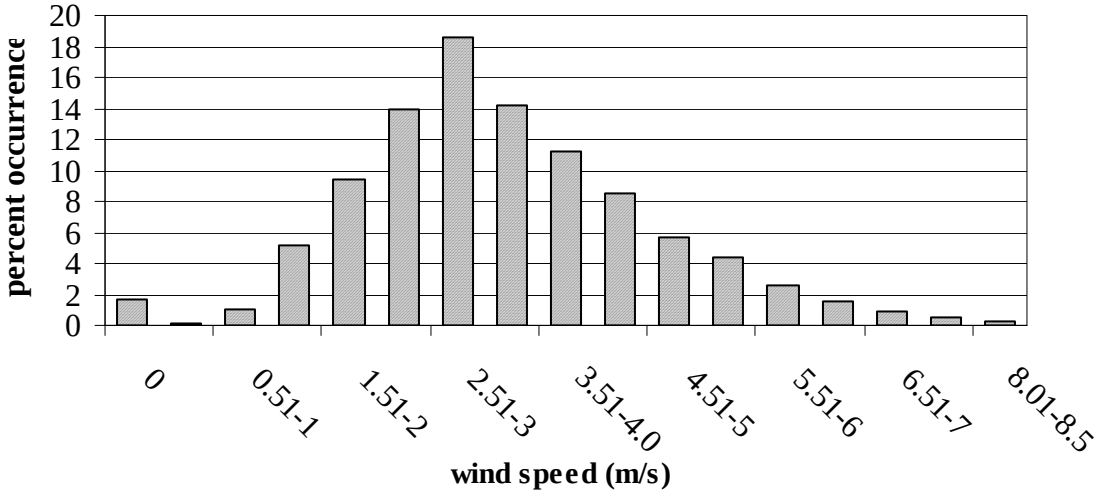

Figure 78 Histogram of wind speeds for Anderson Airport, SC based on hourly data, for ten years (1990-1999) (Source: NOAA). Mean wind speed was 3 m/s.

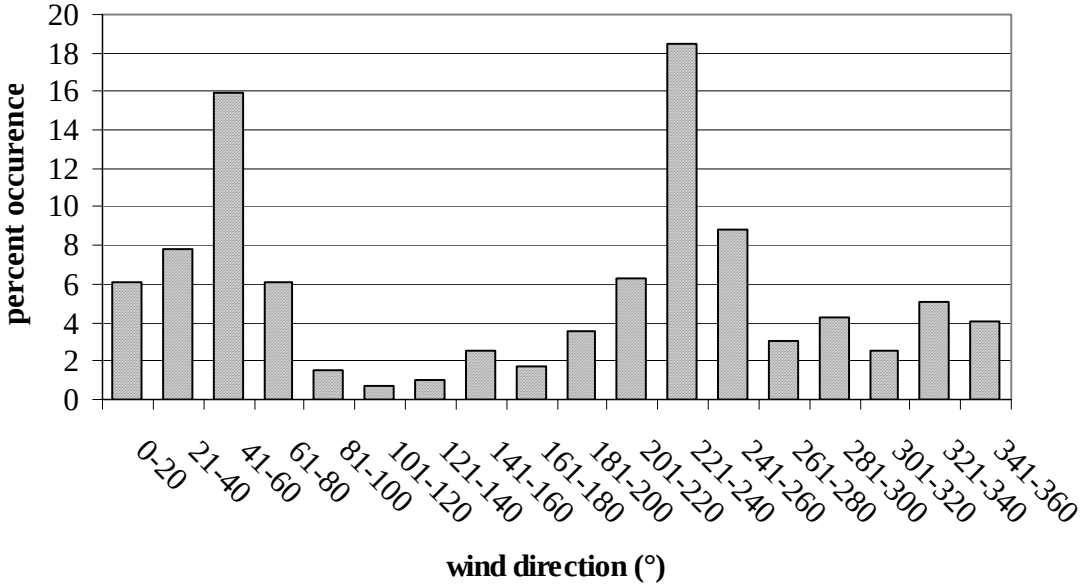

Figure 79 Histogram of wind direction for Anderson Airport, SC based on hourly data, for ten years (1990-1999) (Source: NOAA).

Table 9 Cumulative probabilities of inflow, outflow and wind speed values obtained independently for each parameter.

Cumulative Probability (%)	Inflow (m^3/s)	Outflow (m^3/s)	Wind Speed (m/s)
10	24.3	0.0	1.65
20	39.5	0.0	2.15
30	53.7	59.8	2.50
40	69.7	87.0	2.77
50	86.2	105.6	3.08
60	107.4	122.8	3.40
70	132.8	145.1	3.80
80	170.4	177.8	4.29
90	230.6	267.6	5.14
100	2870	1117	6.84

When the joint probability for inflow and outflow was investigated, it was observed that inflows and outflows were weakly correlated, with a correlation coefficient of 7%. Most of the time outflow values ranged between 40-70 m^3/s, independent of the inflow. In fact, this is expected because the flow in Lake Hartwell is controlled at the dam. For high inflow values (> 230 m^3/s), high outflow values (>268 m^3/s) were observed. This was expected since for flood control purposes, in the event of high inflows, substantial quantities of water were released from the reservoir through the turbines and the spillway.

Although inflow and wind speed were uncorrelated (correlation coefficient: 2%)

when all of the data were considered, for high inflow values (> 230 m^3/s), high wind speed values (>5 m/s) were most likely. The investigation of the joint probability of outflow and wind speed revealed that outflows and wind speeds were also uncorrelated. The joint probability of all three parameters; inflow, outflow and wind speed, was also investigated. For the case of higher inflows (> 230 m^3/s) and outflows (>268 m^3/s), high wind speed values (>5 m/s) were observed.

Based on the analysis of historical data describing inflow, outflow and wind; representative cases to be simulated in the model runs were determined. The first case represented the most frequently observed set of conditions determined by the individual histograms of flows and wind speed. Histogram analyses indicated that the most frequently observed inflow values were between 50-75 m^3/s, with no outflow at the dam. Similarly, wind speeds were most frequently between 2.5-3 m/s. Northeast winds were simulated.

Investigation of the joint probabilities of inflow, outflow and wind speed indicated that the highest probability case includes high inflows (> 231 m^3/s), outflows (>268 m^3/s) and wind speeds (> 5.1 m/s). Two dominant wind directions: northeast and southwest winds were simulated in the second and third cases, respectively.

The last case simulated in the model runs described here represents the second most frequently observed condition, with inflows between 86 m^3/s and 107 m^3/s, outflows between 0 m^3/s and 60 m^3/s, and wind speeds between 3.4 m/s and 3.8 m/s. Northeast winds were simulated. Table 10 shows the values of parameters used in model simulations. Since model results were not sensitive to the water surface elevation, a constant initial water elevation of 201 m was used in all simulations.

Table 10 Four cases selected for simulation of sediment transport within Hartwell Lake. Wind direction is measured from north and pointing to the direction.

Cases	Inflow (m^3/s)	Outflow (m^3/s)	Wind Speed (m/s)	Wind Direction (°)
1) Average inflow, no outflow, dominant northeast wind with average speed	68	0	2.8	55
2) High inflow, high outflow, dominant northeast wind with high speed	465	447	6.8	55
3) High inflow, high outflow, dominant southwest wind with high speed	465	447	6.8	235
4) Moderate inflow, moderate outflow, dominant northeast wind with moderate speed	96	30	3.6	55

Data describing sediment size and suspended sediment concentration, sediment fall velocity and critical shear stresses for both erosion and deposition were required for simulating sediment transport. Bechtel collected bed sediment samples at 11 transects of Twelve Mile Creek, a tributary to Hartwell Lake (EPA, 2001). They also collected water column samples at five stations along Twelve Mile Creek. The median grain sizes of the sediment samples varied from 0.0075 to 0.145 mm. Over half of the sediment samples had more than 50 percent of the grains in the silt and clay ranges, i.e. grain sizes finer than 0.062 mm. Analysis of the water samples indicated that the total suspended solid concentrations varied from 5.6 mg/L in the furthest downstream station to 46 mg/L in the furthest upstream station. The average suspended sediment concentrations in Twelve Mile Creek were about 40 mg/L. Based on the values specified above, the cohesive

sediment parameters to be used in the model simulations were selected; these are summarized in Table 11.

A constant suspended sediment concentration (10 mg/L) in the tributaries flowing into the main pool was used in the simulations due to the lack of TSS (total suspended solids) measurements in the reservoir's tributaries. The implications of not using actual sediment loadings to the reservoir would be incorrect quantification of sedimentation rates. The presented approach could be improved by applying a sediment-rating curve derived from long-term measurements of sediment concentrations. Bathymetric surveying of the lake revealed that sedimentation in the reservoir was not excessive, being on the order of 5 cm/yr in the thalweg. Therefore, the inaccurate quantification of sedimentation rate was tolerable for the purposes of this study.

Table 11 EFDC Model parameter values used in sediment transport simulations.

Model Parameter	Value
SEDI : cohesive sediment conc. corresponding to inflow (g/m^3)	10
SEDO : constant initial cohesive sediment conc. (g/m^3)	40
SEDBO : constant initial cohesive sediment in bed per area (g/m^2)	1×10^{4}
SDEN : sediment specific volume (m^3/g)	4×10^{-7}
SSG : sediment specific gravity	2.65
WSEDO : constant or reference sediment settling velocity (m/s)	1×10^{-4}
TAUD : boundary stress below which deposition takes place (m^2/s^2)	2×10^{-3}
TAUR : boundary stress above which surface erosion occurs (m^2/s^2)	2×10^{-3}
WRSPO : reference surface erosion rate (g/m^2s)	0.01

6.2 Modeling of Depositional Zones in Hartwell Lake

Based on the representative climate and flow conditions presented in the previous section, cohesive sediment deposition patterns and rates in the main pool of Hartwell Lake were simulated. The computational grid used in the simulations is the same grid that was used for the sensitivity analysis in Chapter 3. A 20-day simulation of sediment transport and deposition in Lake Hartwell was conducted for constant boundary and climate conditions specified as Case 3 in Table 10 (Inflow = 465 m^3/s, Outflow = 447 m^3/s, Wind Speed = 6.8 m/s from the northeast). At least five days of simulation was required because it takes approximately five days for sediments to settle 48 m with the specified settling velocity of 1×10^{-4} m/s, which is a typical value for fine sediments (Ziegler and Nisbet, 1994). Representative conditions presented in Table 10 were used in simulations for each case since the variation of sedimentation zones with respect to different conditions was of interest.

The top and bottom layer velocity distributions within Hartwell Lake after ten days of simulation are shown in Figures 80 (a) and 80 (b). Figure 80 (a) shows that the surface flow directions closely match the wind direction. Maximum surface velocities (approximately 14 cm/s) were about 2% of the wind speed. The bottom layer velocities shown in Figure 80 (b) were much lower in magnitude than the surface velocities and formed a return flow, i.e., were in the opposite direction.

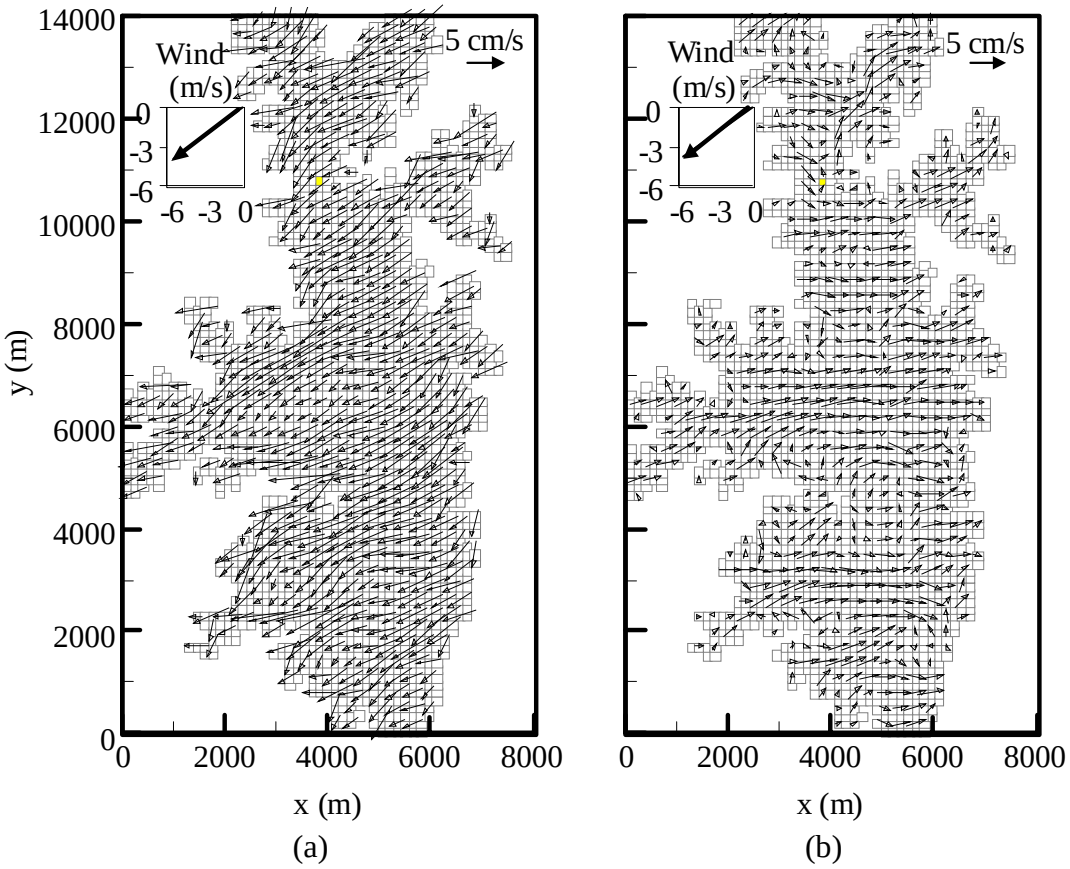

Figure 80 Simulated (a) top layer and (b) bottom layer cell velocity distribution for Case 3 in Table 10 (Inflow = 465 m^3/s, Outflow = 447 m^3/s, Wind Speed = 6.8 m/s).

The settling velocity of sediments estimated by the approach of Ziegler and Nisbet (1995) (where settling velocity is related to median floc diameter) is always less than that for a solid particle of an equal diameter. The impact of implementing different approaches for settling velocities was investigated. Figure 81 shows the comparison of depositional zones simulated for conditions given in Case 3 (Inflow = 465 m^3/s, Outflow = 447 m^3/s, Wind Speed = 6.8 m/s from northeast) with two different settling velocity approaches: the simple approach where the settling velocity is related to the suspended sediment concentration (Ariathurai and Krone, 1976) and the approach by Ziegler and Nisbet (1995). The average thickness of the deposited sediments for both simulations was the same: 8.55 mm after 20 days of simulation. The sediments tended to be deposited in the thalweg at greater rates regardless of the approach used to estimate the settling velocities. However, with the simple approach, more sediments could be advected further distances and deposited close to the dam, suggesting that the estimated settling velocities by the simple approach were less than the velocities estimated by the approach of Ziegler and Nisbet (1995).

Prediction of depositional flux in the EFDC model involves the specification of the critical shear stress for deposition, τ_{cd}, which depends on sediment material and floc physiochemical properties (Mehta et al., 1989). The critical deposition stress is generally determined from laboratory or in-situ field observations and values ranging from 0.01 to 1 N/m^2 have been reported in the literature (Tetra Tech, 1999). The impact of using different critical deposition stress values was investigated in terms of RMS values. When the value of τ_{cd} was increased from 0.002 to 1 N/m^2, RMS difference calculated for the model domain was 2.9×10^{-6} m (0.5% of maximum thickness). Therefore, results were

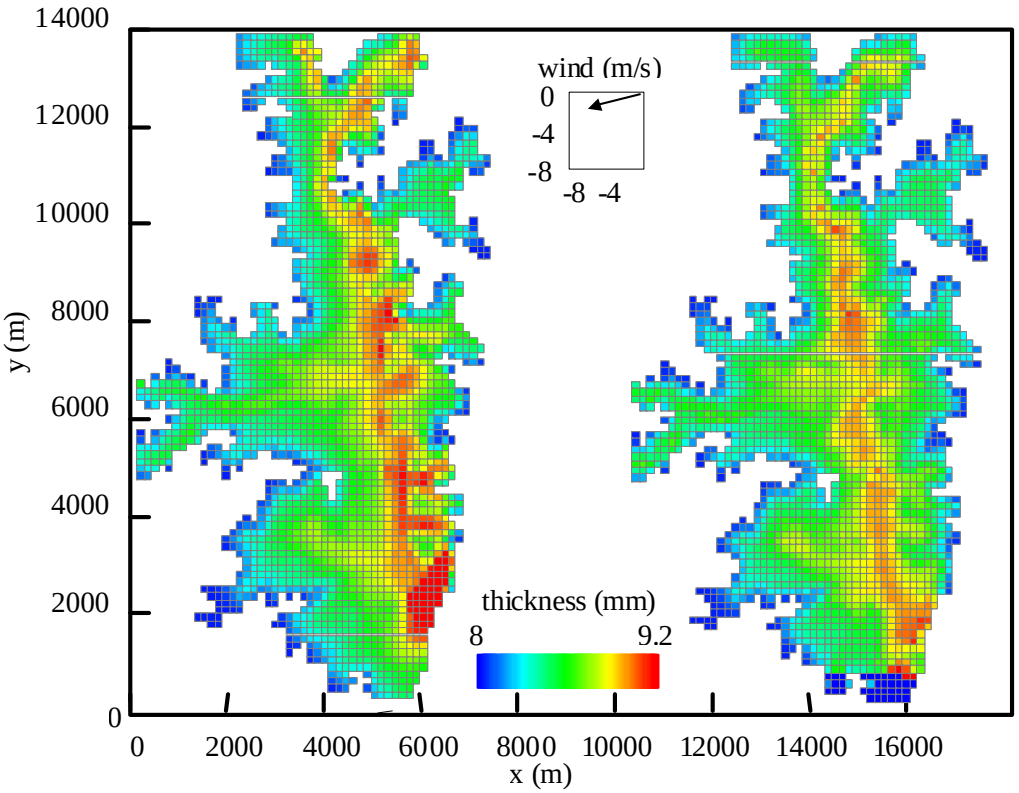

Figure 81 Comparison of sediment deposition in millimeters within Hartwell Lake after 20 days of simulation for Case 3 for two settling velocity approaches: simple approach (Ariathurai and Krone, 1976) on the left and the approach by Ziegler and Nisbet (1995) on the right.

not sensitive to the critical deposition stress value. The critical deposition stress didn't influence results because the bed shear stress ($\sim 1 \times 10^{-4}$ m^2/s^2) was less than the critical shear and full deposition occurred even before the critical shear was increased.

The results for cases with two distinctly different conditions, where lower flows and wind speeds from the southwest (Case 1), and higher flows and wind speeds from the northeast (Case 3) were simulated, deposition of sediments in the thalweg of the lake regardless of the magnitudes of inflows and outflows were observed (Figure 82). When the flow conditions in Case 3 (higher inflows and outflows) were kept same, with wind

conditions corresponding to Case 1 (lower wind speeds from southwest), maximum deposition rates (9.89 mm) were approximately 4% higher than for the case with higher wind speeds (9.51 mm). The average deposited sediment thicknesses for both cases were same: 8.55 mm and the mass was compared to the mass of the incoming sediments for each case. Since sediment mass was conserved in both cases, lower deposition rates observed in the thalweg for high wind conditions can be explained by the shift of depositing sediments from the thalweg to the sides in high wind conditions.

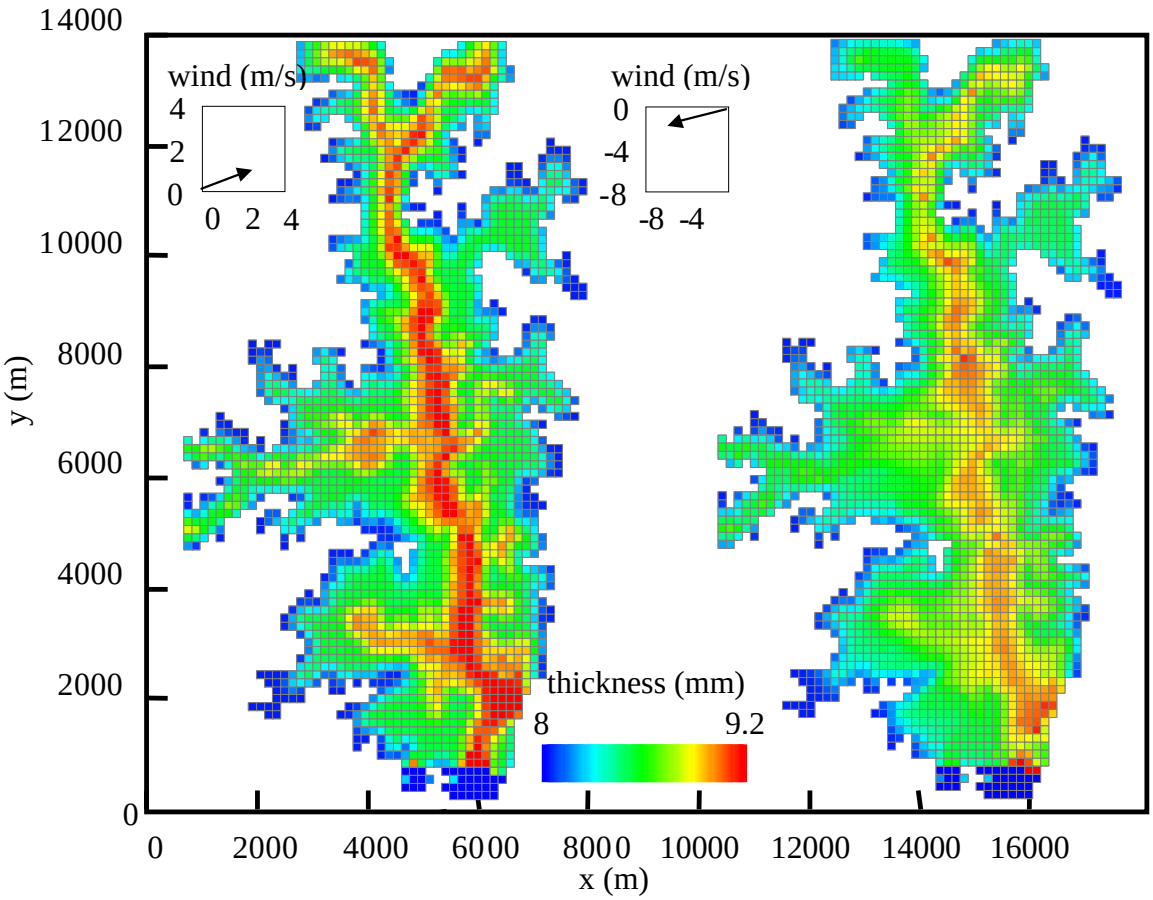

Figure 82 Comparison of deposited sediment thickness in millimeters within Hartwell Lake after 20 days of simulation for Case 1 (left) and for Case 3 (right) in Table 10.

6.3 Potential Significance of Density Currents Arising from Cold Inflows

When a river enters a reservoir, due to its different temperature, and thus density, it will either flow over the colder water in the reservoir, if it is warmer, or submerge, i.e., plunge to the old river bed if it is colder. When the turbulent kinetic energy of the inflow is not sufficient to mix the lake water, the inflow can still have a strong impact on circulation and dominate transport. The inflow currents flow to a layer with equivalent density and move along that layer. When density differences result from temperature gradients, these currents are called density currents and their effects on sediment deposition patterns were investigated in this section.

For this analysis, temperatures of the inflows at the upstream boundary were specified as cold (4 ºC) and warm (27 ºC) temperatures, which is an extreme case. The sediment deposition thicknesses resulting from 10 days of simulation were compared when the lake was initially stratified at two transects shown in Figure 83. The thickness after ten days of simulation along the transects which are 3 km and 10 km from the upstream boundary and are shown in Figures 84 and 85 respectively. As illustrated in the figures, significant differences in inflow temperatures did not have a significant impact on deposition patterns (RMS differences of sediment deposition thickness were less than 1.6% of the average thickness values).

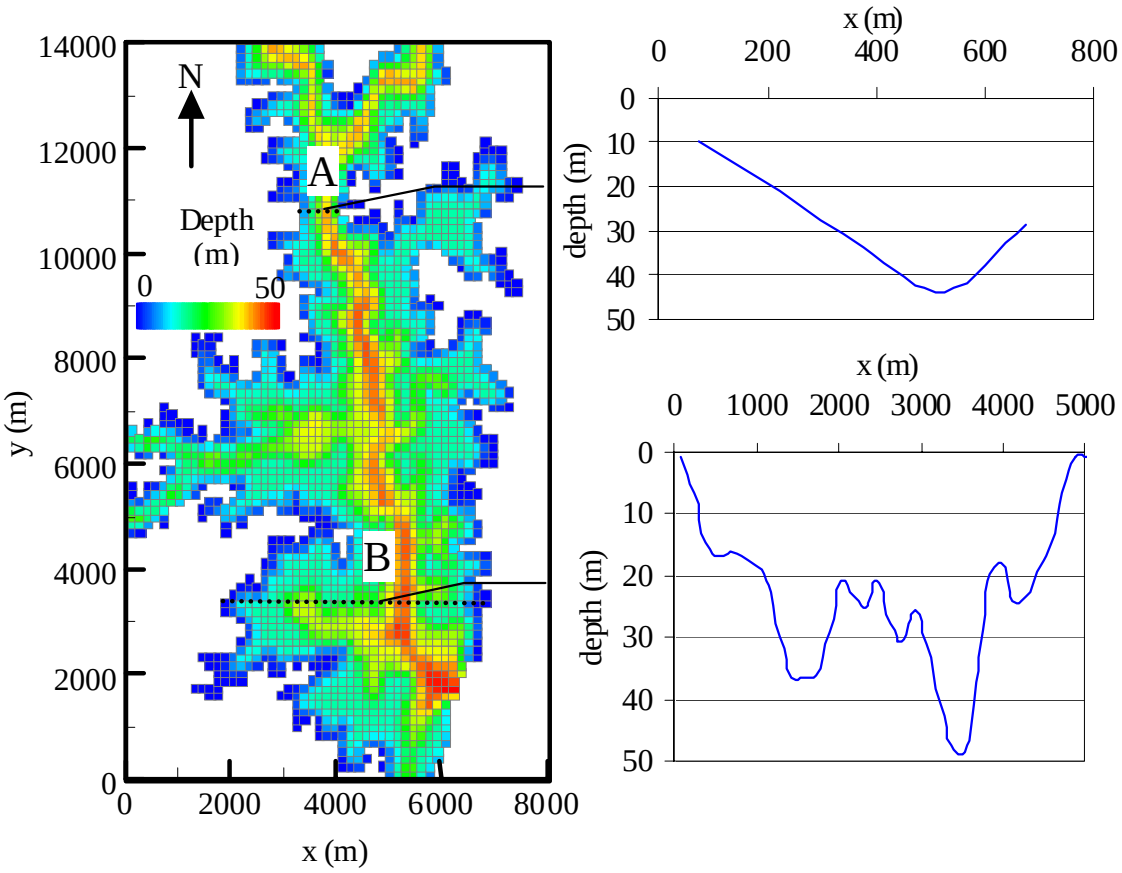

Figure 83 The two transects in the model domain where sediment deposition results are shown.

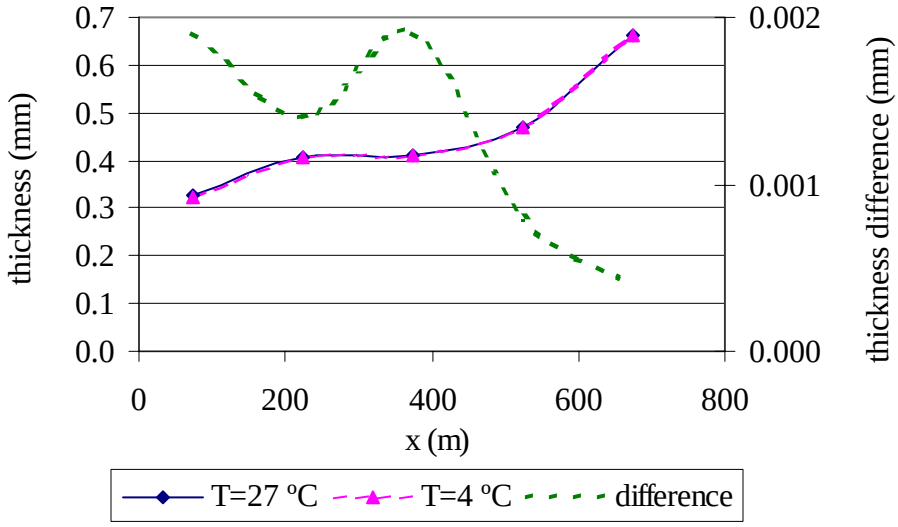

Figure 84 Sediment deposition thicknesses at transect A (see Figure 83) for two different inflow temperatures after ten days of simulation.

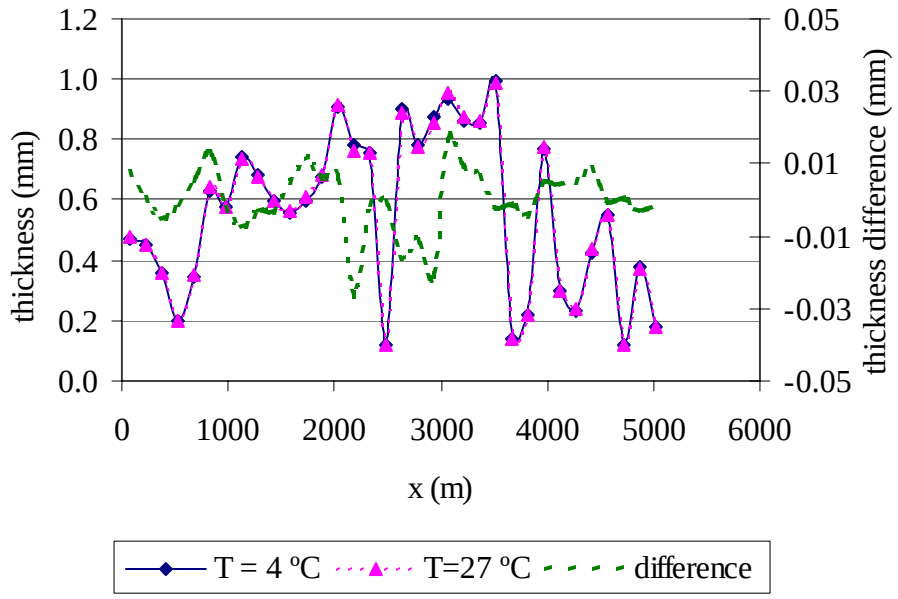

Figure 85 Sediment deposition thicknesses at transect B (see Figure 83) for two different inflow temperatures after ten days of simulation.

A contour plot of the variation of temperatures with time, along the thalweg, measured from the upstream boundary, is shown in Figure 86. The movement of the cold inflow is evident from this figure, where the top figure shows the temperature profiles after 0.5 days and the bottom figure shows the temperature profiles after 3 days. Since the upstream boundaries of the model domain are located downstream of the tributaries within the main pool, therefore, a significant elevation difference along the thalweg was not observed in the model domain.

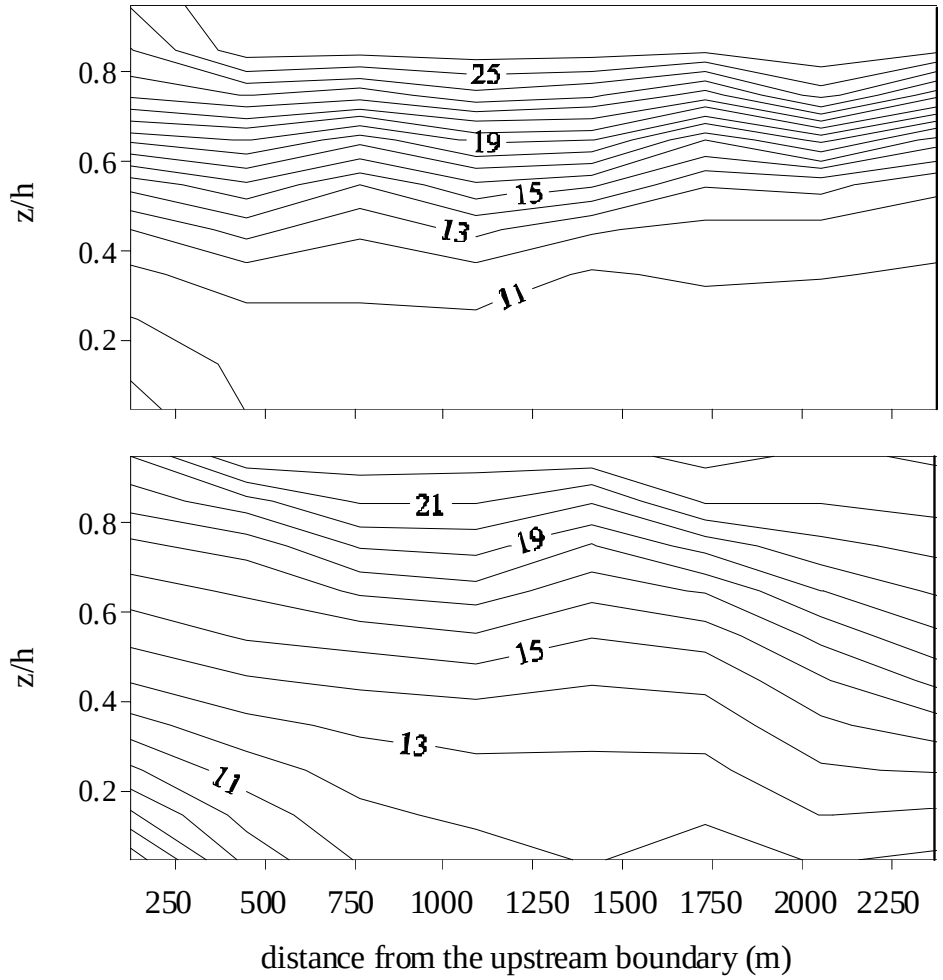

Figure 86 The variation of temperatures along the thalweg after a) 0.5 days and b) 3 days of simulation.

6.4 Modeling of Depositional Zones in Hartwell Lake for Stratified Conditions

Sediment deposition of the incoming sediments from the tributaries was modeled when Hartwell Lake was thermally stratified. The temperature profile representing the typical temperature profile in September was used for the tests. Sediment deposition was modeled for the conditions given in Case 3 (Inflow = 465 m^3/s, Outflow = 447 m^3/s, Wind Speed = 6.8 m/s from the northeast) where settling velocities were calculated using the approach by Ziegler and Nisbet (1995).

The comparison of vertical profiles of velocities at computational cell A (shown in Figure 87) for initially unstratified and stratified temperature profiles indicated that:

- The depth at which the direction of flow reverses is close to mid-depth when the flow is not stratified. This depth moves upward in the stratified flow, suggesting that near surface velocities in the direction of the wind are confined to the epilimnion (warm surface layer). When the flow is stratified, motion changes from whole basin circulation to two closed gyres, one in the epilimnion and the other in the hypolimnion.
- The near surface velocities increase when the flow is stratified due to the enhanced momentum at the surface.
- It takes a lot of energy to disrupt the thermocline, which reduces the vertical turbulent transfer in the stratified case. As a result, velocities near the bottom are decreased.

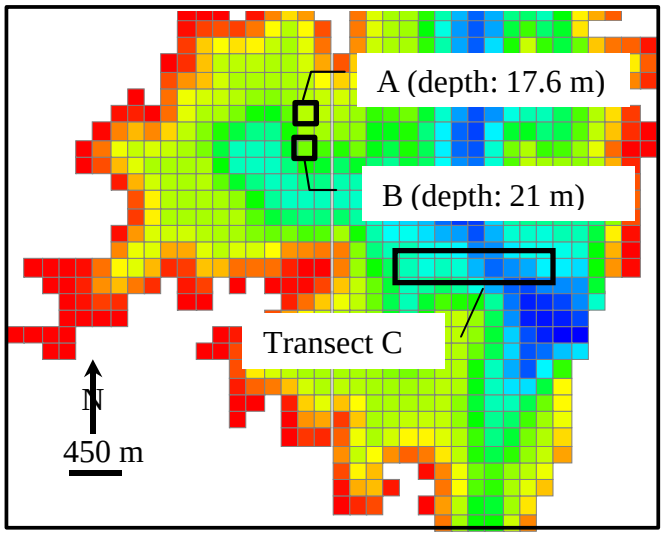

Figure 87 Bathymetry of southern end of main pool of Hartwell Lake. Marked computational cells A and B show the cells at which vertical profiles of velocities are compared. Bottom layer velocities are compared along the transect C.

The comparison of velocity profiles at computational cell B (shown in Figure 87) for initially unstratified and stratified temperature profiles is presented in Figure 89. It can be inferred from the figure that the surface velocities were increased due to the enhanced momentum at the surface and velocities near the bottom were decreased due to the reduced vertical turbulent transfer.

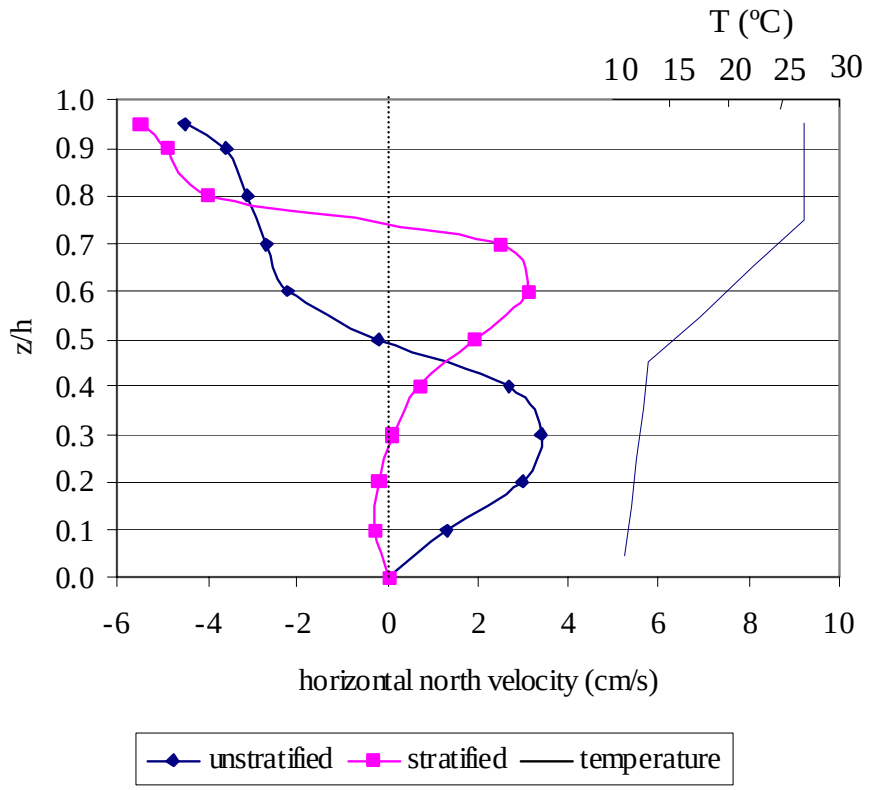

Figure 88 Comparison of velocity profiles at cell A after five days of simulation for stratified and unstratified initial conditions. Wind is from northeast direction.

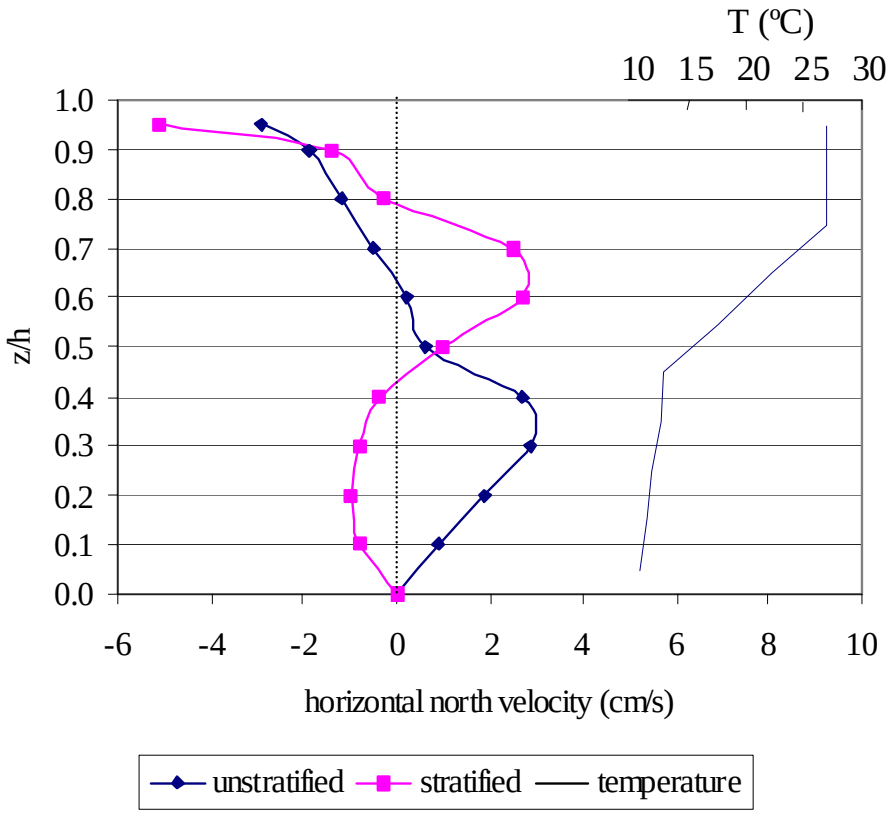

Figure 89 Comparison of velocity profiles at cell B after five days of simulation for stratified and unstratified initial conditions. Wind is from northeast direction.

When the thickness of the deposited layer is plotted for both the stratified and unstratified initial conditions, a decrease (by 6%) in the deposition rate in the thalweg for the stratified case was observed (Figure 90). The average thickness of the deposited sediments was 8.55 mm for the unstratified conditions and 8.34 mm for the stratified conditions after 20 days of simulation. This decrease can be explained by the modified flow patterns due to the stratification. Reduced bottom layer velocities due to the stratification cause sediments to be carried shorter distances and deposit before they reach the thalweg. This was illustrated in Figure 91, which shows the bottom layer velocities and deposited sediment thickness along a selected transect (transect C in Figure 87)

located in the thalweg. In general, sediments deposited at higher rates in the old river bed (thalweg) under both thermally stratified and unstratified conditions, although the stratification caused some of the sediments to settle before reaching the thalweg.

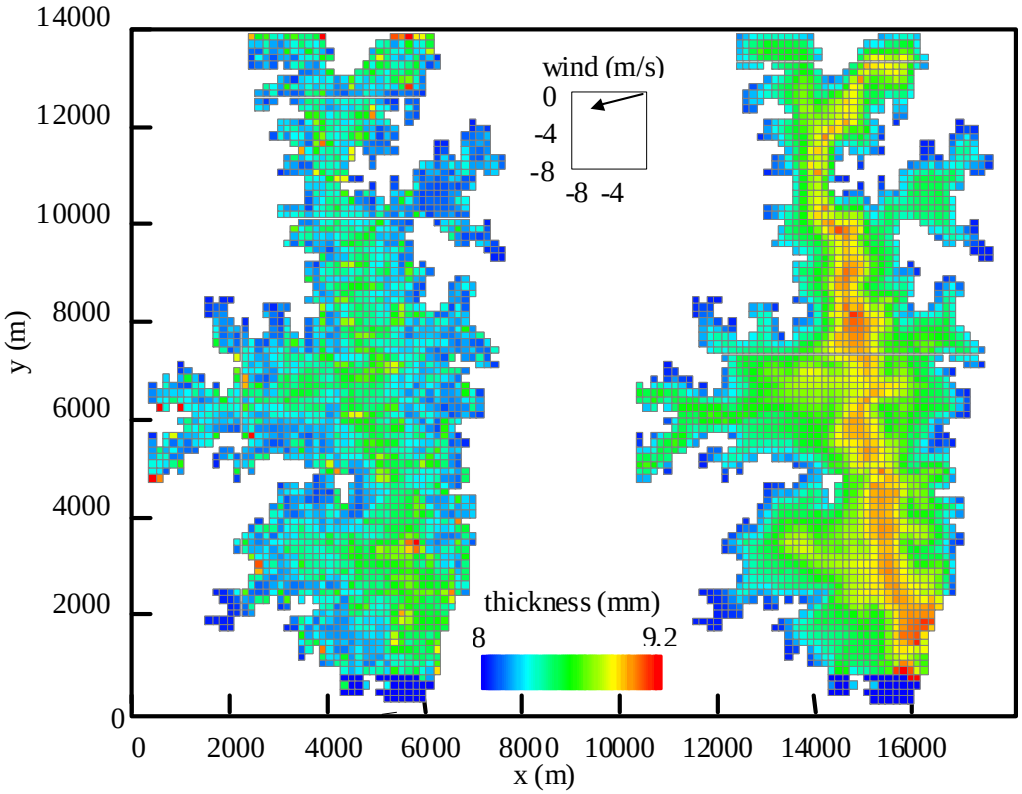

Figure 90 Comparison of thickness of deposited layers after 20 days of simulation of the conditions presented in Case 3 (Inflow = 465 m^3/s, Outflow = 447 m^3/s, Wind Speed = 6.8 m/s from northeast) for the stratified (left) and unstratified (right) initial conditions.

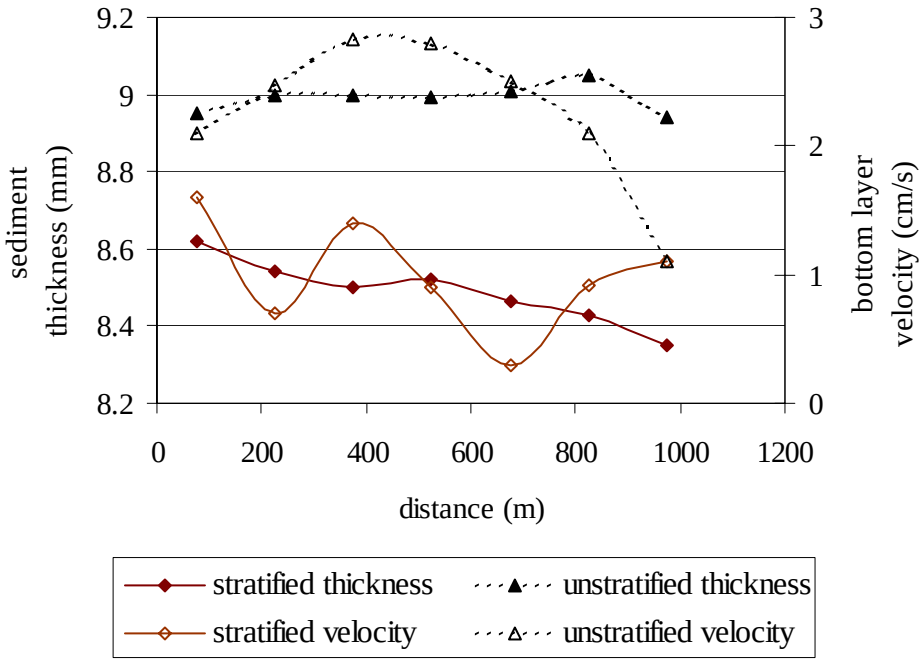

Figure 91 Comparison of thickness of deposited layers and bottom layer velocities along transect C after 20 days of simulation for the stratified and unstratified initial conditions.

CHAPTER 7

SHORELINE EROSION PREDICTION AND QUANTIFICATION

Erosion of Hartwell Lake's shores has been a significant problem for homeowners. For assessment of erosion, a method that predicts erosion rate as a function of shape of the beach profile and climate forcing was developed and applied to a peninsula at Hartwell Lake. For the calibration of the methodology, erosion rates were also estimated using available digital aerial photos. The methodologies used by other researchers to predict erosion rates are also discussed in this chapter. Finally, modeling of the transport and fate of sediments eroded from shores is presented.

7.1 Derivation of Erosion Prediction Method

In lakes and reservoirs there are several physical processes acting on the shore that can influence erosion rates, including surface runoff, groundwater seepage, movement of lake ice, lake currents, wind action, wave action and slumping of the bluff. The Shore Protection Manual (USACE, 1984) states that water waves are the dominant force in determining the geometry and geologic composition of beaches in coastal environments. Surface waves generally derive their energy from the winds. A significant amount of this wave energy is finally dissipated in the nearshore region and on the beaches.

Parameters including offshore bathymetry, beach slope, elevation of toe of the bluff and dynamic factors including incident wave climate and water level affect the amount of wave energy reaching the shore. The incident wave climate depends on winds and fetches and controls wave energy approaching the shore. The water levels in the lake

are affected by meteorological and hydrological conditions and reservoir operation.

A typical bluff profile is shown in Figure 92. The *bluff* is defined as a cliff or headland with a steep face, the *foreshore* is the part of the shore which lies between high and low water levels and is alternately wet or dry as the waves rush up this profile, the *backshore* is the beach that is usually dry, being reached only by the highest water levels, the *nearshore* is the submerged part of the beach (USACE, 2002). SWL represents the still water level, which varies in time.

In a more simplified form applied to a lake, a bluff profile can be divided into the bluff and the foreshore (Figure 93). Wave-based erosional processes and wave breaking mainly affect the foreshore. In some cases, sediments in bluffs and the nearshore bed are dominantly fine-grained, and a large proportion of the material eroded is dispersed offshore in suspension and settles out in deep lake basins (Davidson-Arnott, 1986). The geometry was simplified so that two slopes and two elevations could represent the profile. Each slope is assumed constant. It was also assumed that the lake level would never exceed the height of the bluff.

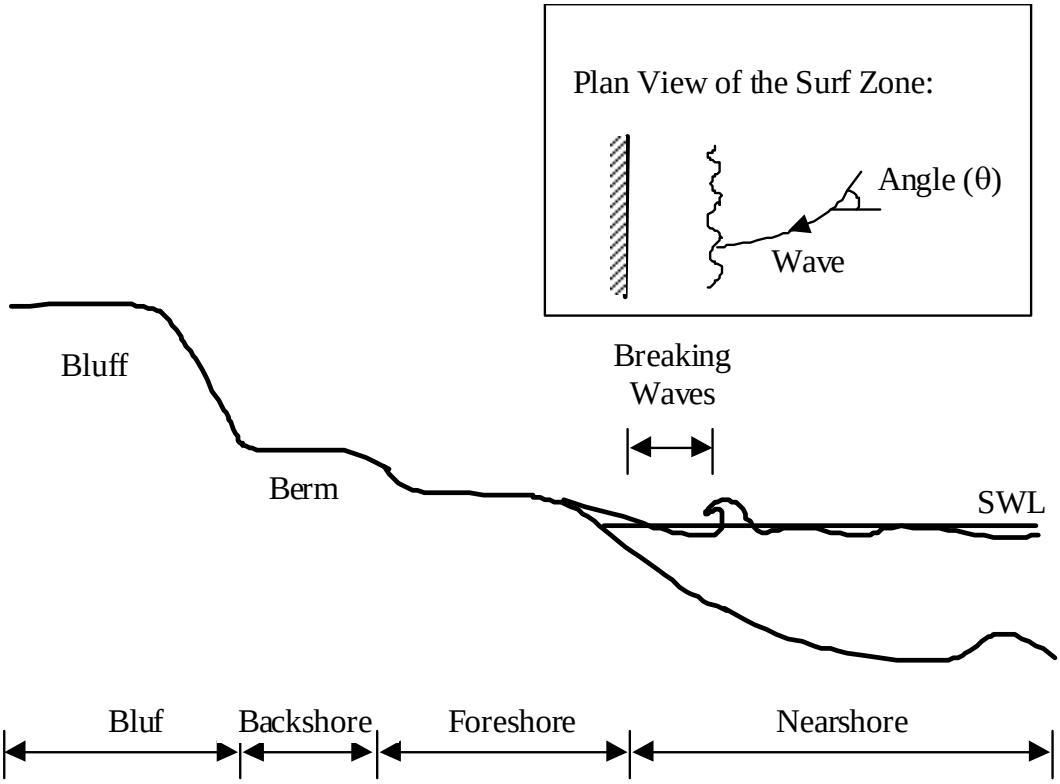

Figure 92 A typical bluff profile (adapted from USACE, 2002).

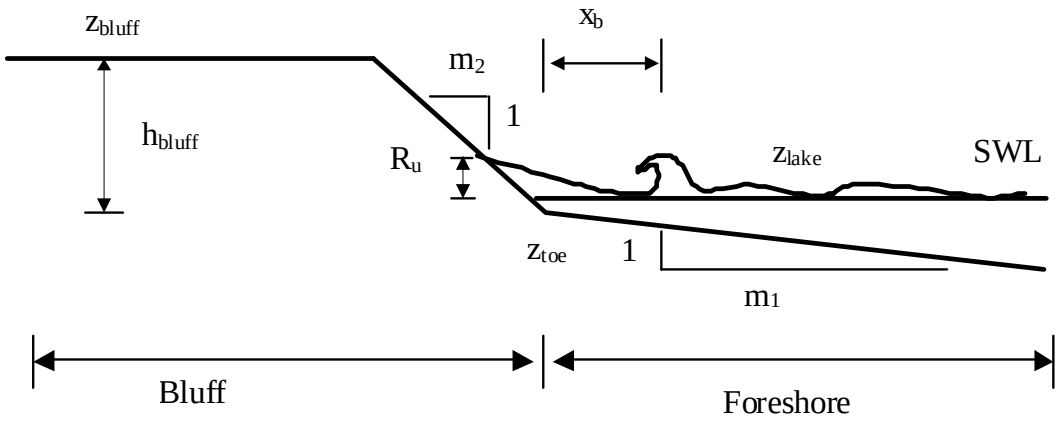

Figure 93 Simplified geometry of shoreline. Parameters defined in Table 12.

Table 12 Definition of parameters used to define simplified beach profile geometry.

Parameter	Definition
z_{bluff}	Elevation of the top of the bluff
z_{toe}	Elevation of the toe of the bluff
z_{lake}	Elevation of the lake water surface
h_{bluff}	Height of the bluff measured between z_{bluff} and z_{toe}
R_u	Wave runup, a local maximum or peak in the instantaneous water elevation at the shoreline
m_1	Slope of the foreshore
m_2	Slope of the bluff
x_b	Distance from the toe of the bluff to the breakpoint
θ	Angle that the wave crest makes with the local bathymetric contours
λ	Wetness (submergence) ratio defined by: $\lambda = \left(z_{lake} + R_u - z_{toe}\right) / \left(z_{bluff} - z_{toe}\right)$

The cohesive behavior of sediments is generally observed at sizes less than 0.074 mm (Dean and Dalrymple, 2001). In most cases, the degree of consolidation, physicochemical conditions (temperature, pH, cation exchange capacity) and the electrochemical bonds between the individual particles control the erodibility of cohesive materials. The cohesive sediments settle to the bed with a low bulk density. In time, as the sediment consolidates, its strength increases. Since the erodibility of cohesive soils is primarily a function of the shear strength of the soil, several models quantifying erosion rate as a function of the shear strength of the soil have been developed. Table 13 summarizes three of these approaches (Dean and Dalrymple, 2001).

Table 13 Equations used in quantifying erosion rates of consolidated cohesive soils.

Equation *	Proposed By
$E = M_1 \frac{(\tau - \tau_c)}{\tau_c}$	Ariathurai and Arulanandan (1978)
$E = M_2(\tau - \tau_c)$	Thorn and Parson (1980)
$E = E_0 e^{\alpha(\tau-\tau_c)^{1/2}}$	Parchure and Mehta (1985)

* where E is the erosion rate (kg/m^2/s), M_1 and M_2 are constants ($M_1 = 0.009$ kg/m^2/s, $M_2 = 9.73\times10^{-8}$ s/m), τ and τ_c are the bottom shear stress and the critical bottom shear stress (N/m^2), $E_0 = 0.5 - 3.2$ gm/cm^2/min, $\alpha = 4.2 - 25.6$ m/N$^{1/2}$

The erosion prediction methodology described in this report is based on the equation by Thorn and Parson (1980) that quantifies the erosion rate for cohesive sediments under water. They used naturally occurring cohesive sediments with quite wide particle size distributions, but median Stokes equivalent diameters of between 0.004 mm and 0.02 mm. The sediments were allowed to settle naturally to form a mud bed that was left to consolidate for 3 days. All three equations listed in Table 13 relate erosion rate to the excess bed shear stress. The chosen equation was selected because of its simplicity.

$$\frac{dm}{dt} = M_2(\tau_c - \tau) \tag{57}$$

where m is the mass of sediment eroded from the bed (kg/m^2), t is time (s), τ and τ_c are the bottom shear stress and the critical erosional shear stress (pascals), M_2 is an empirical coefficient (recommended value: $M_2 = 9.73\times10^{-8}$ s/m).

The erosion prediction methodology described in this section is an improvement

of the methodology described by Work (2001), and accounts for the variability in slopes along the shoreline of a reservoir and spatial variations in sediment characteristics. Erosion is quantified in terms of a recession rate, which is the lateral translation of a particular contour, and is chosen as the contour of the bluff toe for this study.

A schematized beach profile with uniform sediment properties, as shown in Figure 94, is considered. In addition, it was assumed that monochromatic, linear waves approach the beach. A reservoir is likely to feature deepwater waves over much of its surface area, because of the relatively short wave periods resulting from short fetches. Wave runup and recession rate are calculated in terms of influencing parameters such as: simplified profile shape, water level, wind direction and magnitude, and sediment characteristics. Assuming waves will break before reaching the shore, the three cases shown in Figure 94 will be considered.

In the first case, mean water level is below the toe of the bluff, and runup does not rise above the toe of the bluff. Erodibility of the cohesive shore is calculated in terms of excess shear applied to the soil during the wave runup.

In the second case, mean water level is below the toe of the bluff, but the runup rises above the toe of the bluff. Erodibility is calculated as in the first case but modified by an empirical factor based on wetness ratio.

In the third case, mean water level is above the toe of the bluff, and initial wave breaking occurs before waves reach the location of the toe of the bluff. Erodibility is related to wave power.

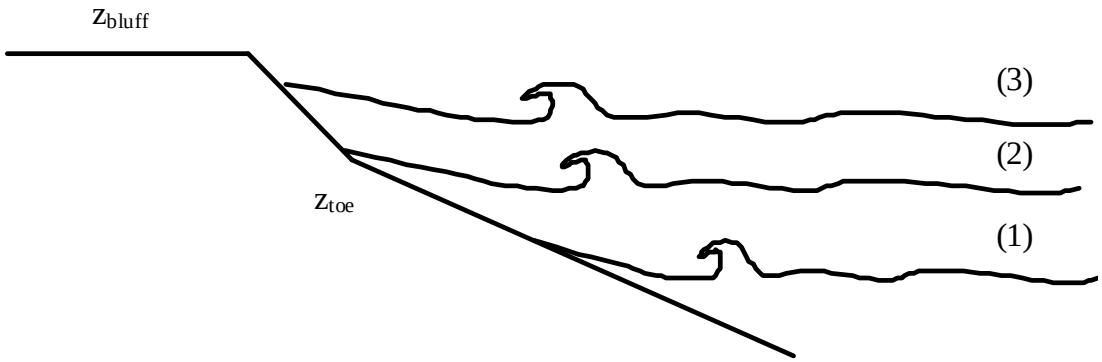

Figure 94 Cases considered for erosion prediction methodology. Case (1): mean water level is below the toe of the bluff, and runup does not rise above the toe of the bluff. Case (2): mean water level is below the toe of the bluff, but the runup rises above the toe of the bluff. Case (3): mean water level is above the toe of the bluff.

For the first two cases where the water level is below the toe (Figure 94), erodibility of the cohesive shore is assumed directly proportional to excess shear applied to the soil. Recession rate of the high mean water level contour, R, is derived from a simple equation for prediction of erosion rates in the case of waves passing over a mud (Whitehouse et al., 2000, Dean and Darlymple, 2001). Recession rate, R (m/s) is assumed proportional to $\frac{dm}{dt}$ the erosion rate (kg/m^2/s). Dividing the erosion rate by sediment density, ρ_s (kg/m^3), recession rate, R (m/s), is then obtained as given below. Details of the derivation are given in Appendix C.

$$R = \frac{M_2}{\rho_s}\left(\frac{1}{6}\rho f_w \kappa^2 \pi^2 m_1^{\ 2} \frac{x_b^{\ 2}}{T^2 \sinh^2(kh)} - \tau_c\right) \tag{58}$$

A and B are defined as:

$$A = \frac{1}{6} M_2 \frac{\rho}{\rho_s} f_w \kappa^2 \pi^2 \tag{59}$$

$$B = \frac{M_2 \tau_c}{\rho_s} \tag{60}$$

A wetness (or submergence) ratio of bluff, λ, will be included as a factor affecting recession rate in the calculations (See Table 12). λ is equal to 0 for Case (1) where mean water level is below the toe of the bluff, and runup does not rise above the toe of the bluff. For the second and third cases it will be included in the calculations. Recession rate (m/s) is obtained in a simple form by inserting A and B into equation 58.

$$R = \left(\frac{A m_1^2 x_b^2}{T^2 \sinh^2(kh)} - B \right) (1 + n\lambda) \tag{61}$$

where *n* is an empirical factor describing the eroding effect of wave runup on the bluff. The upper limit on n is 3 (Penner, 1993), and λ is [0,1]. When λ is equal to 0, Case 1 is represented and runup does not rise above the toe of the bluff. When λ is nonzero, Case 2 is represented and runup rises above the toe of the bluff but mean water level is still below the toe of the bluff. $\lambda = 1$ when the bluff is fully submerged.

Equation (61) states that recession rate is proportional to the wetness ratio, beach slope and wave period. The more the bluff is submerged, the more erosion is expected because the increase of the water level would result in an increase in eroding wave power. Steepness of the beach slope affects the dissipation of the wave energy. The steeper the beach is the less wave energy will be dissipated, resulting in higher erosion rates. Wave period is a measure of the time between consecutive waves. As the wave

period gets smaller, more waves would reach the shore, resulting in higher erosion rates.

For the last case where water level is above the toe (Figure 94), the erodibility of the cohesive soil is related to wave power, which can be calculated as a function of wave height. For this case, the recession is derived from the equation for volume transport rate (USACE, 2002):

$$Q = KH_b^{5/2} \tag{62}$$

where K is a parameter function of the wave height, wave period and slope (Kamphuis and Readshaw, 1978):

$$Q = f(H^2, T, m_1) \tag{63}$$

Dividing the equation for volume transport rate by unit area, multiplying by the wetness ratio λ, and the calibration coefficient, C, the equation for recession rate is derived.

$$R = C\lambda H^2 T m_1 \tag{64}$$

A laboratory study by Newe et al. (1999) investigated beach profiles under storm conditions. The profile recession rates were investigated with respect to different beach slopes. They found that 1:15 is the critical slope. For slopes steeper than the critical value, recession rate was proportional to the slope. For flatter slopes such a dependence was not observed. For slopes steeper than 1:15 Equation (64) is modified to account for the bluff slope m_2.

$$R = C\lambda H^2 T m_1 m_2 \tag{65}$$

The following list summarizes the steps for the erosion rate prediction methodology.

1) Wind speed of interest and potential wind direction and water level data are obtained. Fetches are measured on a map for each location.
2) Geometry of the shoreline of interest is surveyed or estimated from a topographic map and values of $z_{bluff,}$ $z_{toe,}$ $z_{lake,}$ $h_{bluff,}$ $m_{1,}$ and m_2 are measured or estimated.
3) Wave runup (R_u) is calculated as a function of beach slope, wave height, and wave period (see Appendix C).
4) The time, t (in seconds), required for waves crossing a fetch of length, X, for a wind speed, u, (USACE, 1998) is calculated:

$$t = 77.23 \frac{X^{0.67}}{u^{0.34} g^{0.33}} \tag{66}$$

5) If the calculated time, t, is less than or equal to 1 hr, then waves are assumed fetch limited. Use the measured fetch for calculation of wave height, H, and wave period, T. If calculated time is greater than 1 hr, waves are duration limited. Use the new fetch (Equation 67) to compute wave height, H, and wave period, T.

$$X_{new} = 1.523 * 10^{-3} \left(u_* t^3 g \right)^{1/2} \tag{67}$$

6) Wave runup is added to the water level and compared with the elevation of the toe of the bluff:

a) If the water level + wave runup is below the toe ($z_{lake} + R_u < z_{toe}$), then the wetness ratio, λ, is set equal to 0 and recession rate, R (m/s), is calculated using equation 61.

b) If the water level is below the toe ($z_{lake} < z_{toe}$) but the water level + wave runup is

above the toe ($z_{lake} + R_u > z_{toe}$), then the recession rate, R (m/s), is calculated using Equation 61 (λ is nonzero).

c) If the water level is above the toe ($z_{lake} > z_{toe}$), then the recession rate, R (m/s), is calculated using Equation 65.

7) Recession rates (in meters) are integrated in time for the given period and a final recession distance is calculated.

7.2 Other Approaches for Prediction of Shoreline Erosion

This section describes two of many other approaches used in the past for erosion prediction. The similarities and differences between the new approach and the existing approaches are also discussed.

Penner (1993) quantified shoreline erosion in volumetric terms. The annual volumetric erosion rate is calculated as the product of effective wave energy (E_e) and a material erodibility coefficient (K_e) as shown below:

$$V = K_e \times E_e \tag{68}$$

The effective wave energy, E_e (tonne-metre/metre of shoreline/year) is the portion of the total offshore wave energy dissipated and is determined as a function of foreshore slope. For a slope of 1:2, 95% of wave energy is assumed dissipated, whereas for slopes of 1:4, 1:10, 1:15, 1:30 the percentages are 70%, 45%, 30% and 10% respectively. Total wave energy is calculated as follows:

$$E = \frac{\rho g^2}{32\pi} H^2 T t \cos^2 \phi \tag{69}$$

E : average annual wave energy in foot-pounds/foot of shoreline

ρ : mass density of water in lbs/ft^3

ϕ : angle between the wind direction and a line normal to the shoreline

H : equivalent wave height in feet

T : wave period in seconds

t : wind duration in seconds for the selected wind direction.

Wave energy is calculated for each wind direction and integrated to calculate total wave energy at a specific shoreline.

Penner's method depends on the erodibility coefficient K_e (cubic meters/tonne-metre), which is an empirical value, based on correlation of material properties and wave energy conditions. Erodibility coefficients are calibrated and verified based on a known profile retreat rate.

For the calculation of erosion rate, Kamphius (1986) considered two portions of the foreshore, the breaking zone and the zone offshore of the breakers. For the breaking zone, he assumes that the driving mechanisms for erosion are wave power, P_b. Outside the breaking zone, erosion is related to shear stresses.

Recession rate, R, is related to wave power, P_b, with the following equation.

$$R = KP_b^{1.4} \tag{70}$$

where K is a calibration constant and P_b is given by:

$$P_b = \frac{\rho g^{\frac{3}{2}} H_b^2 h_b^{\frac{1}{2}} \cos\alpha_b}{8} \tag{71}$$

where h_b is depth of water, α_b is the angle of wave breaking. Since α_b is small, $\cos\alpha_b$ is assumed to be 1.

Outside the breaking zone, Kamphius (1986) assumed that the erosion rate is directly related to shear stress applied to the soil, τ, and by simple geometry, recession rate is related to erosion rate.

Both methods rely on coefficients that must be calibrated using known shoreline recession rate data. Recession rates are related to wave energy by Penner and to wave power by Kamphius. Penner's method uses slopes to estimate reduction in energy dissipation, but beach profiles are not used in the calculations. When the method described in section 7.1 is compared to these methods the following similarities and differences are observed:

- Both the shoreline erosion prediction methodology described in section 7.1 and the approaches by Kamphius and Penner quantify erosion rates in terms of water levels, wind direction and magnitude, and fetch values.
- In each method, the calibration and verification of the approach were conducted through analysis of aerial photos.
- The shoreline erosion prediction methodology accounts for the shape of the beach profile; therefore the erosion rate calculated by this method for two different sites may differ even if they have the same climate conditions and exposure. The approaches of Kamphius and Penner would give the same erosion rates for two different sites with the same climate conditions.
- The shoreline erosion prediction methodology calculates erosion rates at

preselected time intervals, which allows the modification of beach profile shape if intended.

7.3 Erosion Rates Inferred from Digital Aerial Photos

It is usually difficult to precisely locate the shoreline in aerial photos. Various definitions of shoreline exist, but for the purposes of this report, “mean high-water line identifiable by a distinct line on the beach” (Crowell et al., 1991), is utilized. Shoreline rates of change are defined by at least two instantaneous shoreline positions on different dates. Therefore, results should be presented with a percent error based on different interpretations of the water line, and should account for water level changes and errors due to other factors as well.

Aerial photos of Hartwell Lake are available in different years. The 1994 images were extracted from a Color Infra-Red (CIR) digital orthophoto quadrangle provided by the USGS. The images were photographed on 25 Feb 1994 by the National Aerial Photography Program and digitized by the USGS DOQ Program on 02 Dec 1998. Size, projection and datum information for the images are given in Table 14. The images photographed on 26 Mar 1975 and on 01 Apr 1987 are available at several locations in the lake.

Topographic maps were extracted from a digitized USGS topographic map known as a Digital Raster Graphic (DRG) provided by the USGS. Size, projection and datum information for the images are given in Table 14. The maps were produced in 1980 by the USGS National Mapping Division. The USGS Digital Raster Graphic image is projected in UTM Zone 17 NAD 83 datum.

Shoreline photos should be adjusted to a common datum and should be rectified

so that the scales, projections and coordinate systems match. The 1994 aerial photos of Lake Hartwell (source: USGS) were used as a basis and other images of the lake were rectified accordingly. For this purpose, the ImageWarp extension of ArcView was used. ImageWarp 2.0 is an extension that allows one to geo-reference any image that ArcView can display to a feature theme, grid theme, or image theme. Using this method, images are rectified so that the photo registers with another image, grid, or vector theme, which is in a known projection.

In the shoreline erosion analysis discussed here, islands and peninsulas were selected for analysis, because the rate of erosion can accelerate at places exposed to waves from many directions.

Table 14 Image and topographic map information for Hartwell Lake aerial photos.

	Image	Topographic Map
Size	800 pixels×600 pixels	800 pixels×600 pixels
Pixel to earth conversion	1 pixel : 1meter×1meter	1 pixel : 2 meter×2 meter
Projection	Universal Transverse Mercator (UTM) Zone 17	Universal Transverse Mercator (UTM) Zone 17
Datum	North American Datum of 1983.	North American Datum of 1927.
Scale	1 : 12000	1 : 24000

7.4 Shoreline Erosion Predictions for Hartwell Lake

In this section, the application of the erosion prediction methodology to the Western Carolina Sailing Club located in Anderson County, SC (Figure 95) is described. The topography of the island is shown in Figure 96. This island was chosen for this analysis because of two reasons; a noticeable erosion problem and availability of survey data. Personal interviews with the people at the sailing club indicated that the island shores have severely eroded in the past years. In 1997, Dr.Work and his coastal engineering class in the Civil Engineering Department at Clemson University surveyed the island.

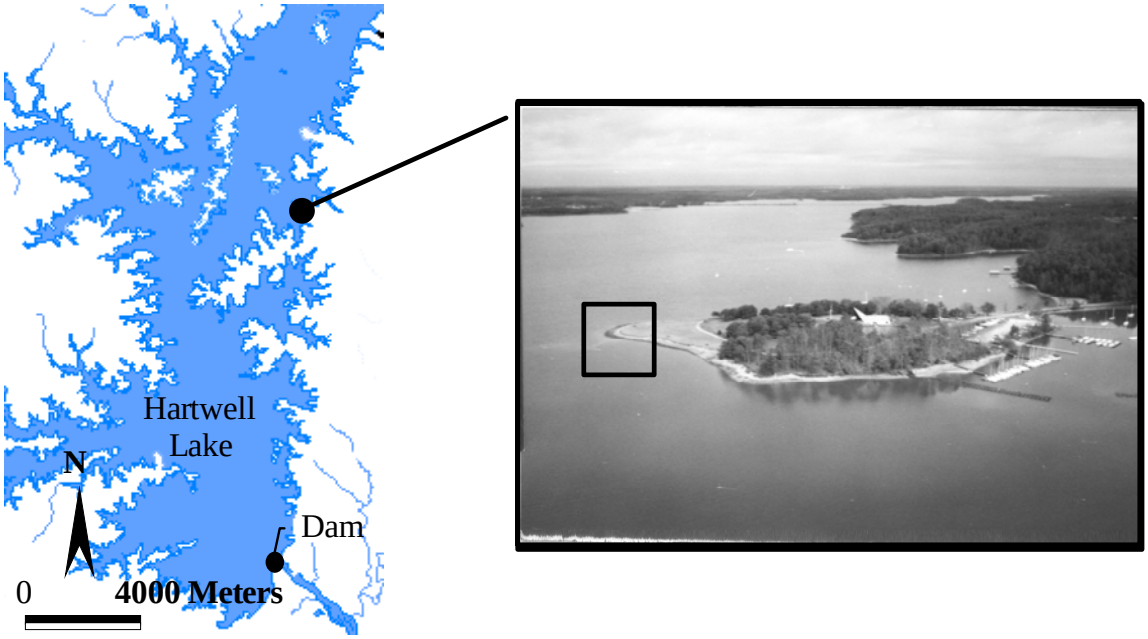

Figure 95 Location of the Western Carolina Sailing Club in Anderson County, SC. The square shows the tip of the island where calculations for erosion prediction are made.

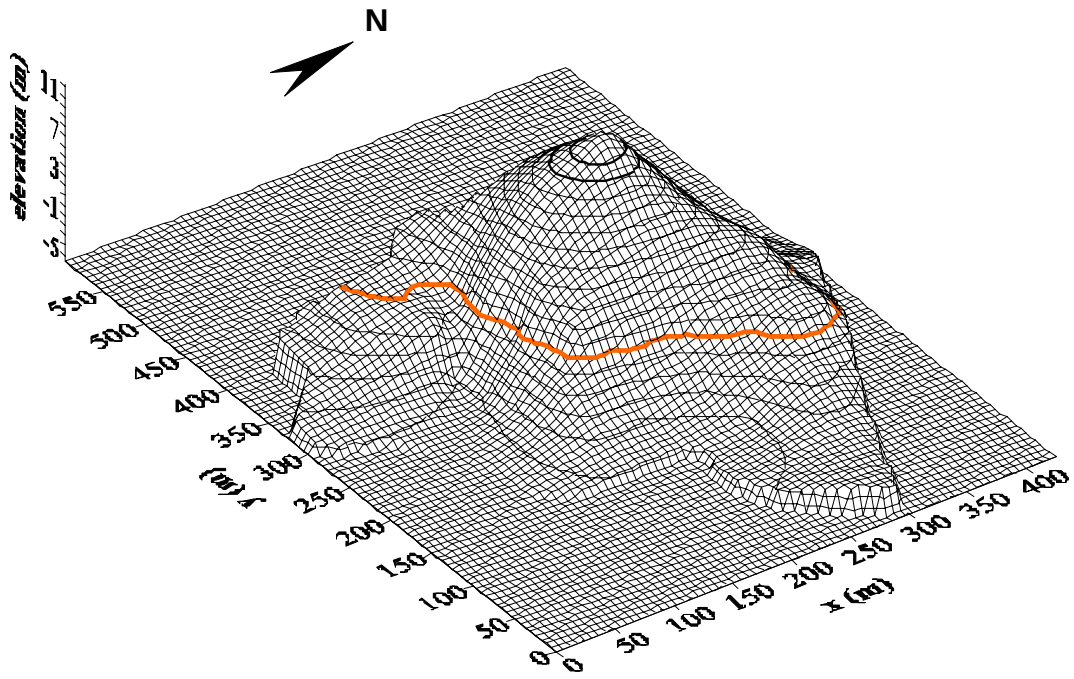

Figure 96 Topography of Western Carolina Sailing Club as surveyed in 1997. Contours are spaced every one-meter and bold line shows zero contour (elevation : 201 m).

The aerial photos from 8 Mar 1981 and 1 Apr 1987 of the Western Carolina Sailing Club, located in Anderson County, were chosen for shoreline erosion analysis. Both images had to be rectified by comparison to an image from 1994, which is in a known projection. This was done using the ImageWarp extension of ArcView. Using the topographic map in Figure 96 the slopes are calculated in the range of 0.06 - 0.12 m/m in 50 m distance from the shore (offshore direction), defined by the mean high-water line identifiable on the beach. Since the water levels on different dates differ, the erosion rates inferred from digital photos were modified accordingly using the slopes. The shoreline change rates were calculated from the two images using ArcView. Figure 97 shows the average shoreline change rates (erosion) per year of the island. The image shown is from

1987 and the polygon is drawn based on the image from 1981. A maximum erosion rate of 1.8 m/year was calculated. The erosion rate at the tip of the island was 0.6 m/year. Each pixel in the digital aerial images, represents 1 meter × 1 meter of earth. Therefore, erosion rates obtained from aerial photo analysis may present 1 meter per analysis duration (6 years in this analysis) error, corresponding to ± 16 cm of error. Considering this possible error, and neglecting other potential sources of error, such as water level, and slope, the erosion rate at the tip of the island can be rewritten as 60 ± 16 cm/year.

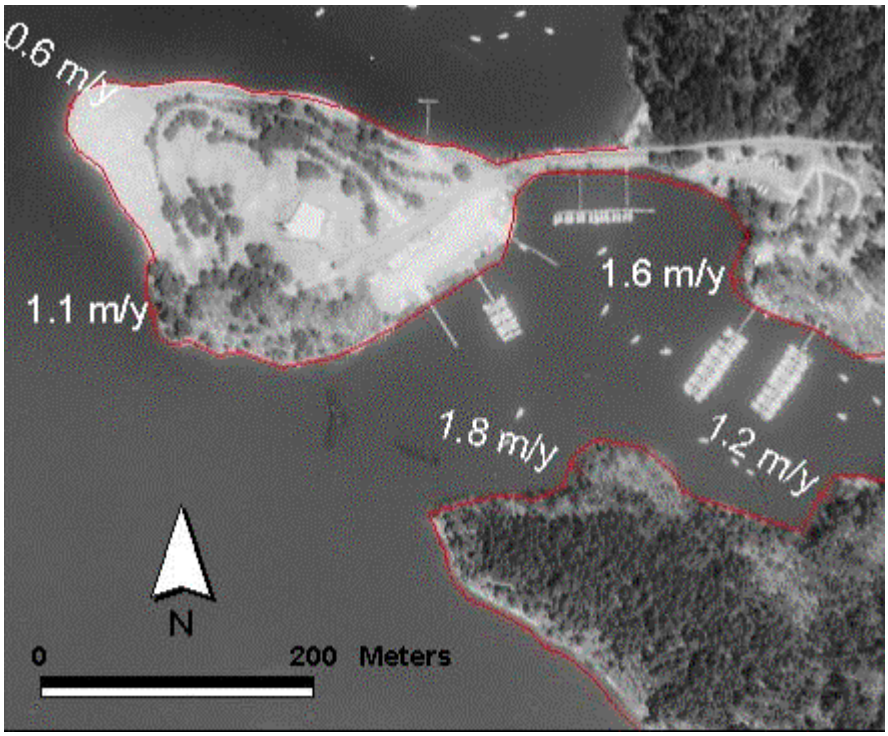

Figure 97 Average shoreline change rates (erosion) per year at the sailing club. The image shown is from 1987 and the polygon is drawn based on the image from 1981.

The erosion prediction methodology was applied to the Western Carolina Sailing Club located in Anderson County, SC. Application of the erosion prediction methodology requires knowledge of beach profile slopes, wind speed and direction, lake levels and fetches. Values of the beach profile parameters obtained from the survey were used in this application (Table 15). The fetches were measured in 10 degrees bands (measured from North). The lake level data (daily) were obtained from the USACE and the National Oceanic and Atmospheric Administration (NOAA) provided the wind data (hourly).

Table 15 Parameters describing the beach profile at the northern and southern tips of the Western Carolina Sailing Club peninsula (see Figure 97).

Parameter	z_{bluff}	z_{toe}	h_{bluff}	m_1	M_2	C
Northern	203.65 m	201.70 m	2 m	0.06	0.08	0.00022
Southern	203.65 m	201.70 m	2 m	0.12	0.10	0.00022

A FORTRAN code developed to predict shoreline erosion at the tip of the island was run from 1981 to 1987 using a time step of one hour, to match the sampling rate of the wind data. These two dates were selected based on the availability of the aerial photos that were used to calibrate the numerical model. The model predicted 0.6 meters / year of erosion at the north tip of the island.

The methodology described in section 7.1, has a calibration coefficient (See Equation 65) that was determined to be 0.00022 by comparing calculated erosion rates to the rates obtained from the digital aerial photo analysis. The new methodology was validated by applying it to the south part of the island. The bathymetric survey of the

island revealed different beach shape profiles at these two locations. When the south beach profile was modeled, the erosion rate was predicted to be 100 cm/year which agreed well with the rate of 110 ± 16 cm/year obtained from aerial photo analysis. The approaches of Kamphius (1986) and Penner (1993) were also applied to the Western Carolina Sailing Club. In both methods, erosion rates were calculated in hourly time steps. Kamphius (1986) has related wave power to erosion rate (see Equation 70). Recession rate of 0.6 meters/year on the northern tip of the island was obtained when $K = 0.46$ and $a = 1.15$ were used.

The method proposed by Penner (1993) relates the effective wave energy to volumetric erosion rate via the erodibility coefficient (see Equation 68). The erodibility coefficient is an empirical value based on correlation of material properties and wave energy conditions and given for different soil types. For clay an average value of K_e = 0.00035 m^2/tonne was suggested. The erosion rate is then calculated by dividing the volumetric erosion rate by the unit area of the beach profile. Penner's method also led to overestimation of the erosion rate when the suggested value of K_e was used. This was expected because both methods were calibrated for the soils on The Great Lakes. Recession rate of 0.6 meters/year on the northern tip of the island was obtained when K_e = 0.0001 m^2/tonne was used.

Using the approaches by Kamphius (1986) and Penner (1993), the erosion rate at the southern part of the island could not be estimated correctly (estimated as 0.6 meters/year), in part because the variability of the beach profile slopes are not included in these methods. Since erosion rates may differ from one location to another even if the climate conditions are the same, it was concluded that specification of the beach shape

profile is essential for an accurate estimation of shoreline erosion.

Comparison of digital aerial photos of Longpoint Peninsula located on the west coast of Hartwell Lake is shown in Figure 97. Application of the methodology to the southeast tip of the Longpoint Peninsula indicated 180 cm/year erosion rate in agreement with the erosion rate inferred from the digital aerial photos. The beach profile was obtained from the shoreline survey conducted in February 2003. Values of the beach profile are given in Tables 16.

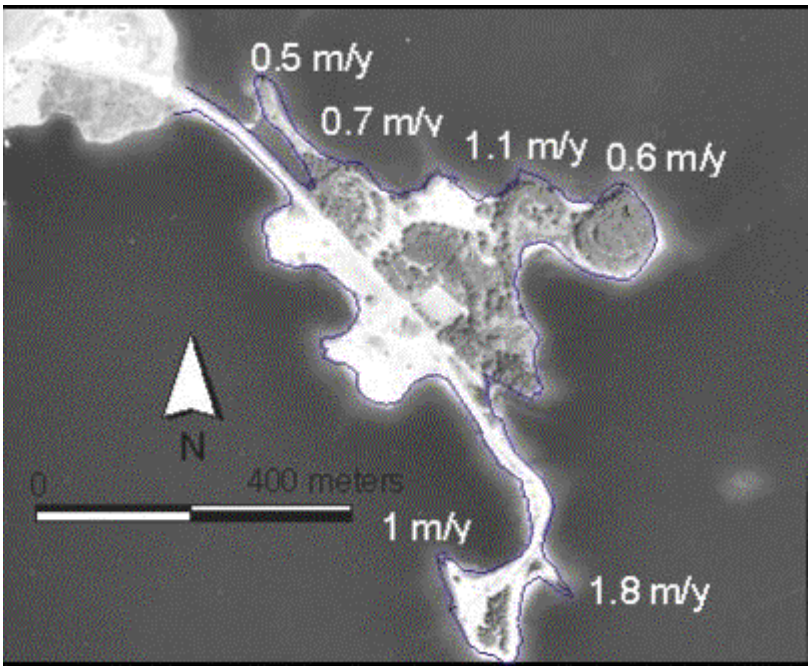

Figure 98 Average shoreline change rates (erosion) per year at the Longpoint Peninsula. The image shown is from 1987 and the polygon is drawn based on the image from 1975.

Table 16 Parameters describing the beach profile at the southeast tip of the Longpoint Peninsula

Parameter	z_{bluff}	z_{toe}	h_{bluff}	m_1	m_2	C
Southeast tip	203.65 m	201.70 m	2 m	0.06	0.2	0.00022

Surveying the shorelines also revealed that, the sites exposed to great fetches were protected with erosion control structures. Peninsulas surveyed were mostly covered with ripraps and wooden bulkheads in order to prevent the downcutting of the nearshore lakebed. Therefore, shoreline erosion analysis was limited by the historical data prior to the building of the erosion control structures.

7.5 Fate of Sediments Eroding from the Shorelines

When high concentrations of PCBs were found in the lake resulting from the operation of a capacitor manufacturing facility, near Twelve-Mile Creek, the U.S. EPA performed and sponsored research on PCBs in Hartwell Lake as part of their “Superfund” program. EPA’s selected remedy (Monitored Natural Recovery) was to rely on burial by natural sedimentation processes (natural attenuation). Over time, “clean” sediments should bury the contaminated sediments, providing a clean sediment cap on top, and gradually reducing the health risks. Besides the new incoming sediments from the tributaries, there is another source of clean sediments: sediments eroding from the shores. In this section, modeling of the transport and fate of sediments eroded from shores is presented.

The erosion prediction analysis presented in the previous section indicated relatively high erosion rates at the peninsulas exposed to the greatest fetches. Two peninsulas, Longpoint Peninsula, located in the southwest, and Sadler Creek Peninsula,

located in the northeast of the model domain, were selected for the shoreline erosion prediction analysis (Figure 99).

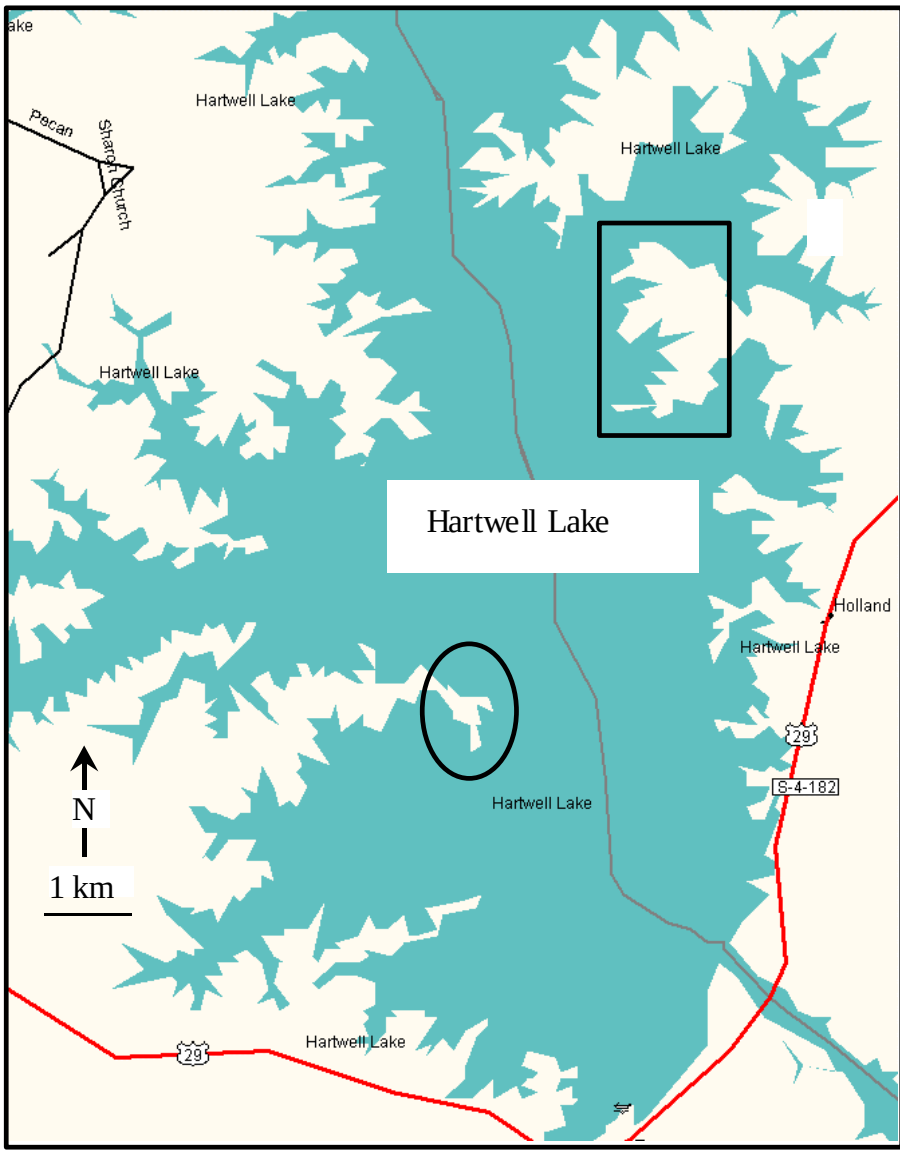

Figure 99 Peninsulas, at which deposition of eroding sediments was modeled. Sadler Creek Peninsula is shown by the rectangle, while the ellipse shows Longpoint Peninsula.

For the simulation of the transport and fate of the sediments eroding from the shores of Longpoint Peninsula, eroding sediment concentrations at neighboring cells of the peninsula need to be specified. For the determination of the sediment concentration in each neighboring cell, based on their depths, the following steps were followed:

1) The recession distance, d (m) during the simulation time is calculated by multiplying the average recession rate, R (m/year) estimated in the previous chapter with the simulation time, t (year).

$$d = R \times t \tag{72}$$

2) The eroding sediment volume, V_s, per unit width (m^3/m) was calculated by multiplying the recession distance, d (m) by the average bluff height, h_{bluff} (m).

$$V_s = d \times h_{bluff} \tag{73}$$

3) The eroding sediment mass per unit width, M_s (kg/m) was calculated by multiplying dry bed density, ρ_{ds} (kg/m^3) by the eroding sediment volume, V_s per unit width (m^3/m).

$$M_s = V_s \times \rho_{ds} \tag{74}$$

4) The eroding sediment concentration, C_s (kg/m^3) was calculated by dividing the sediment mass per unit width, M_s (kg/m) by the cross section of the computational cell, A (m^2) in the model. The cross section of the computational cell, A (m^2) is calculated by multiplying cell length, L (m) with depth of each cell, d (m).

$$C_s = \frac{M_s}{L \times d} \tag{75}$$

Based on the calculations described above, the suspended sediment concentration values at the neighboring cells were specified as a time series at the surface layer, and the bottom layer concentrations were set to the initial concentration as the remaining cells in the model domain. In the EFDC model, concentrations are linearly interpolated between the vertical layers.

The fate of eroding sediments from the Longpoint Peninsula was investigated by a simple case where wind from the south was simulated without any flows entering or exiting the model domain. The sediment bed thickness simulated for this case was then compared with the sediment bed thickness simulated for the same wind and flow conditions when no eroding sediments from the shoreline were considered.

Deposition thicknesses for the sediments eroding from the Longpoint Peninsula are compared for two different wind forcings. When wind from the south with a magnitude of 4 m/s was simulated (Figure 100) it was observed that sediments deposited at slightly higher rates (average thickness increased by 2%) to the northeast of the peninsula. The sediments were carried and deposited at slightly higher rates (average thickness increased by 3%) to the southwest of the peninsula when winds were blowing from the north. The deposition patterns in the other parts of the model domain were not affected.

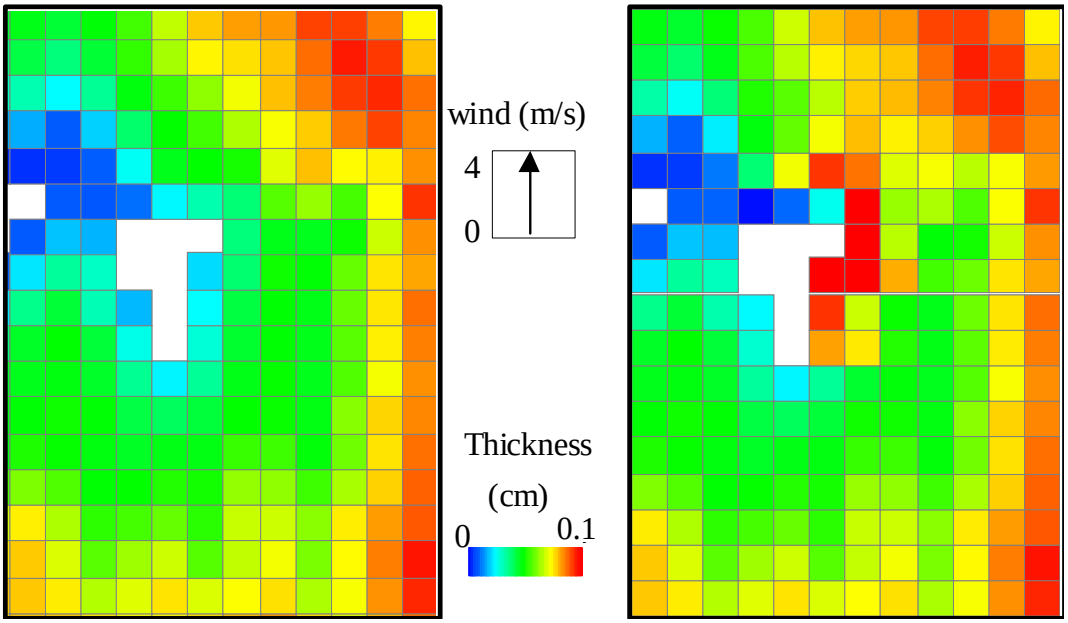

Figure 100 Comparison of depositional zones near Longpoint Peninsula after ten days of simulation with eroding sediments (right) and without eroding sediments (left) modeled. Cell width is 150 meters.

In order to illustrate the differences in deposition patterns when the eroding sediments are introduced, two transects near the Longpoint Peninsula were selected (Figure 101). The comparison of the sediment deposition thickness for these transects are given in Figures 102 and 103 for transects A and B, respectively. As seen in Figure 102, when the eroding sediments were introduced, the deposition thicknesses at the neighboring cells of the peninsula were extremely high as compared with the case where no eroded shoreline sediments were considered. This difference was reduced significantly (2% of the thickness) along the transect further from the peninsula. When the thickness along transect B was plotted, maximum differences were observed in the thalweg region, and were about 4% of the thickness.

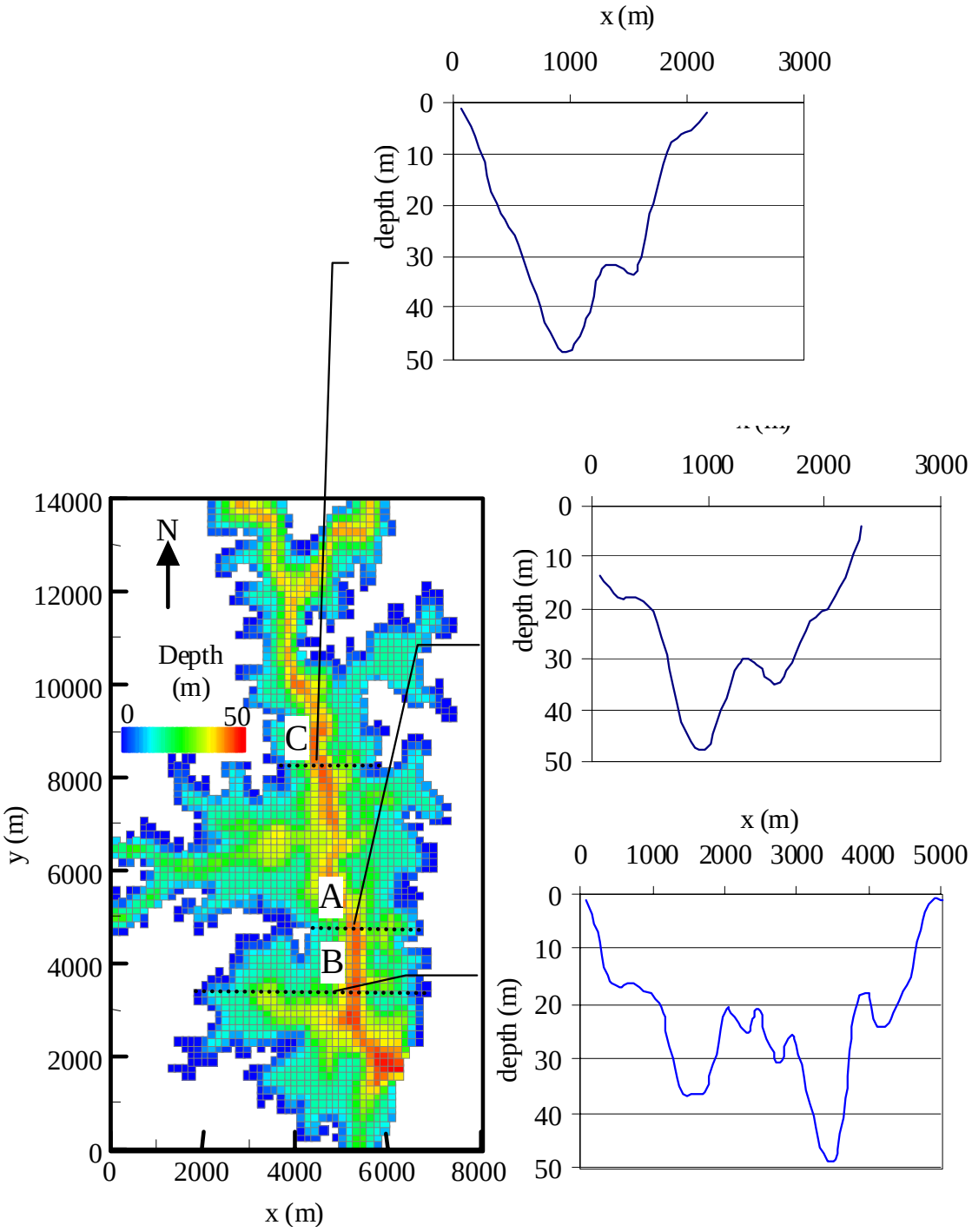

Figure 101 The three transects in the model domain where the sediment deposition results were shown. The Sadler Creek Peninsula is shown by the rectangle, while the ellipse shows the Longpoint Peninsula.

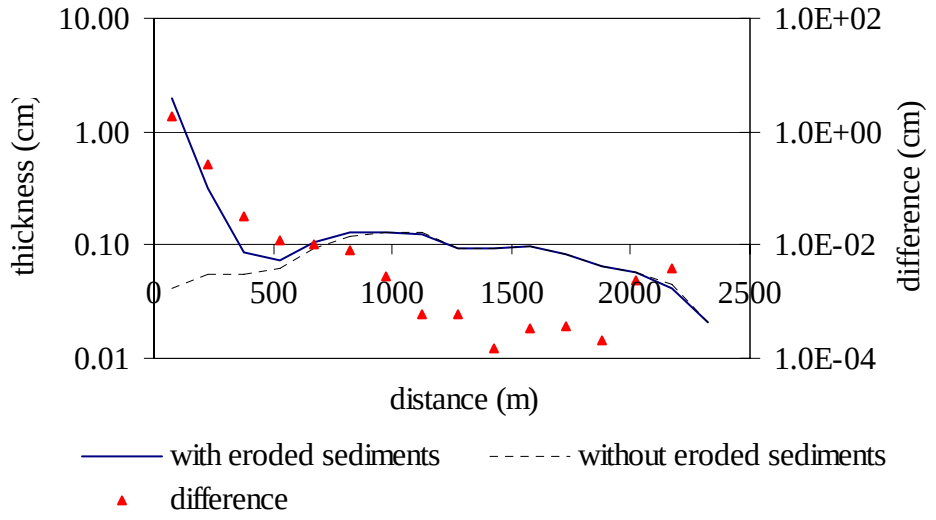

Figure 102 The sediment deposition thicknesses at transect A with and without eroding shoreline sediments after ten days of simulation.

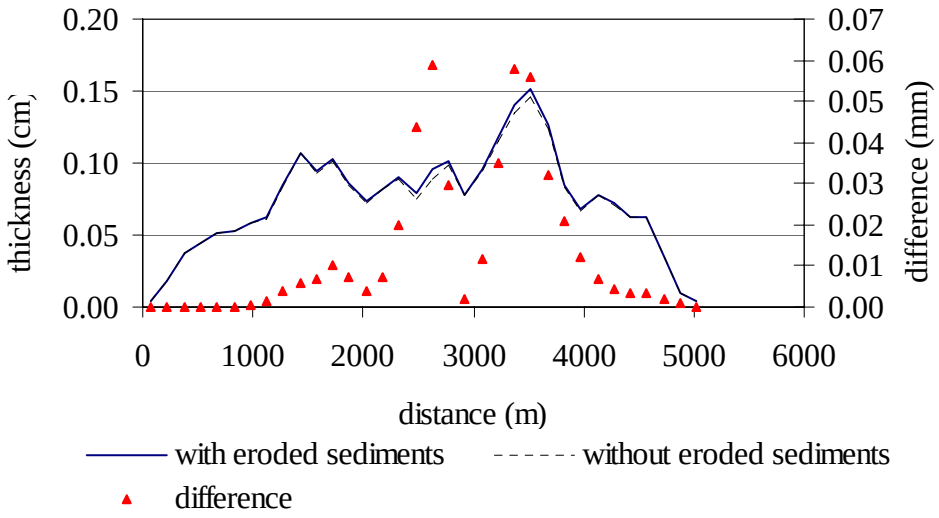

Figure 103 The sediment deposition thicknesses at transect B with and without shoreline eroding sediments after ten days of simulation.

Comparison of deposition rates near the Sadler Creek Peninsula is presented in Figure 104. Higher rates of deposition were observed due to the increased sediment concentration near the peninsula. RMS difference of deposition thickness for the selected region was 4%. Similar to the transects near the Longpoint Peninsula, the comparison of the sediment deposition thickness for transect C (Figure 105) near the Sadler Creek Peninsula revealed that when the eroding sediments were introduced, the deposition thickness at the neighboring cells of the peninsula were extremely high as compared with the case where no eroding sediments were considered. In conclusion, modeling of the deposition of sediments eroding from the shores revealed that the eroding sediments have a localized and small impact on overall deposition patterns in the main pool.

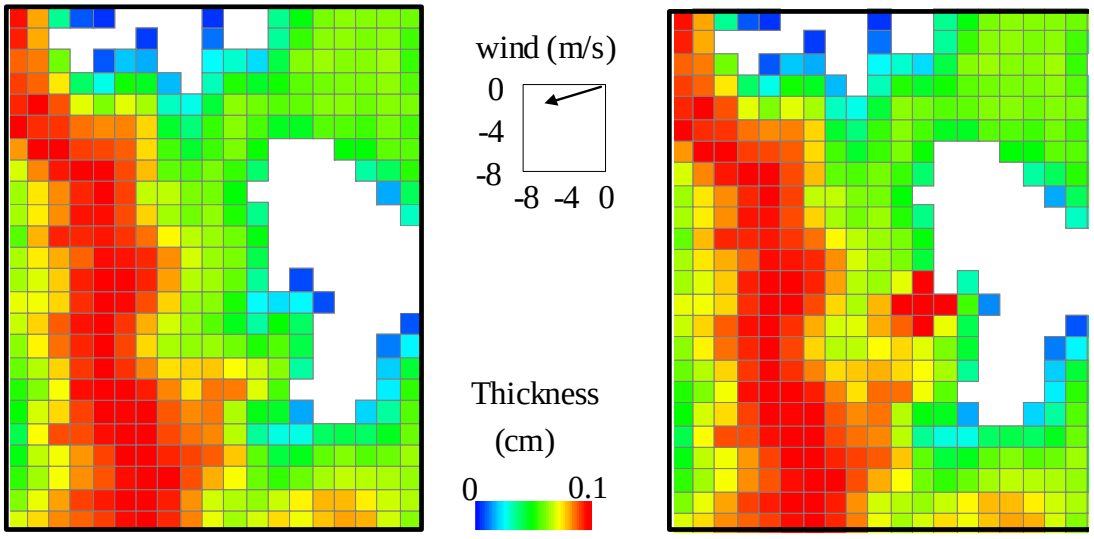

Figure 104 Comparison of depositional zones near Sadler Creek Peninsula after ten days of simulation when the conditions presented in Case 3 with eroding sediments (right) and without eroding sediments (left) were modeled. Cell width is 150 meters.

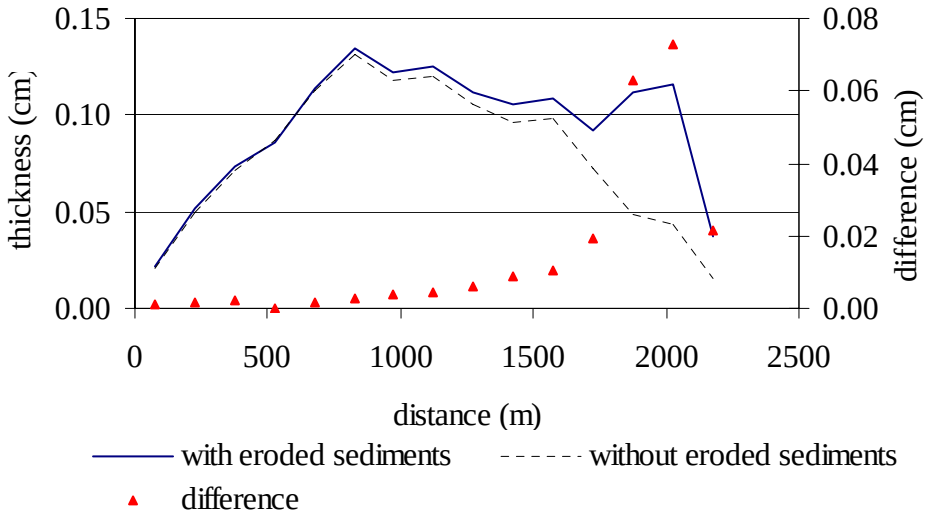

Figure 105 The sediment deposition thicknesses at transect C with and without eroding shoreline sediments after ten days of simulation.

CHAPTER 8

CONCLUSIONS

This study investigated hydrodynamics, sediment transport and shoreline erosion in a deep, periodically stratified reservoir. The primary goal was to document, through field measurements, and model, using a 3-D numerical model of flow and sediment transport, the fate of sediments, those coming from the tributaries and eroding from the shorelines, within the main pool of Hartwell Lake. The study was motivated by two environmental problems:

1) A U.S. Environmental Protection Agency (EPA) Superfund site is located on a tributary to Hartwell Lake because of high concentrations of polychlorinated biphenyls (PCBs) in the lake sediments.
2) A total of 1516 erosion control structures indicated that erosion is a widespread problem along the shorelines of the lake.

Hydrodynamic circulation patterns in the main pool of Hartwell Lake are mainly controlled by wind, and tributaries inflows and outflows at the dam, and were modeled using the EFDC (Environmental Fluid Dynamics Code) model. Prior to application of EFDC for simulation of hydrodynamics and sediment transport in Hartwell Lake, the numerical model was evaluated with simple forcing and geometry for which analytical solutions are available in the literature. Testing of the EFDC model indicated that the model performed well for these idealized test cases. However, it is important to recognize that significant dissipation (artificial damping) was observed in model simulations because of the numerical dispersion introduced by the discretization and solution of the governing partial differential equations in the model.

The performance of the model under stratified conditions was also evaluated by comparing the simulated response of a stratified body to wind shear stresses with the laboratory experiments documented by Monismith (1986). Comparison of numerical model results with the experiments indicated that the major characteristics of the stratified flow under the applied shear stress were captured well in the model simulations.

The variation of numerical model output with model parameters and forcings was investigated through sensitivity analysis. For this purpose, EFDC was applied to the main pool of Hartwell Lake and several variables including lake water level, grid size, number and thickness of vertical grid layers, wind speed and direction, and inflow and outflow magnitudes were systematically altered as part of the sensitivity analysis. The number of vertical layers was found to strongly influence results up to the selection of five layers. Lakewide circulation patterns were very sensitive to wind direction and magnitude. Wind was typically the major force driving the circulation. In high wind conditions, the model produced velocity vectors indicating that water flowed in the downwind direction at the surface and returned upwind at the bottom. Sensitivity of model results to inflows was investigated by comparing results for different inflow magnitudes. In the presence of typical wind forcing, velocities in the main pool were not particularly sensitive to typical inflow magnitudes.

Hartwell Lake is an example of a warm monomictic lake, which is vertically mixed during the months from December to March, and thermally stratified, to varying degrees, between April and November. Sensitivity of model results to initial temperature conditions was investigated by comparing results for typical stratified and unstratified cases. Findings of this analysis were: 1) Horizontal velocities in the direction of the wind

were enhanced at the epilimnion for the stratified conditions. 2) The depth at which the reversal of flow begins differed for stratified and unstratified conditions. 3) The depth at which the reversal flow begins migrates downward as time passes and stratification weakens. Since the stratification altered the velocity profile, the impacts of stratification on sediment deposition patterns were investigated.

Field data were collected in Hartwell Lake during the period of February 10-14, 2003 to quantify 40 years of deposition since construction of the dam. During the field campaign, velocity measurements were made primarily to provide a check on the magnitude of the velocities reported by the numerical model used in the study. Depth data were collected using a dual frequency, acoustic depth measuring system. Velocity data were obtained using a 1200 kHz Acoustic Doppler Current Profiler (ADCP). During the bathymetric surveys and velocity measurements, a handheld differential (WAAS) GPS was also integrated with the devices for navigation.

Comparison of bathymetric surveys to previous surveys provided by USACE indicated approximately 2 meters of deposition have occurred over 40 years within the old Savannah River bed. A rough estimate of the conservation storage lost is 27.4×10^6 m^3 that is less than 1.6% of the total conservation storage. The actual volume of storage lost to date due to deposited sediments should not significantly impact the operational goals of the reservoir.

Strong winds (more than 4 times the historical average) from the southwest were observed during the measurement period. Maximum measured surface velocities at several transects were ~50 cm/s and average velocities were ~25 cm/s over the measurement period. Comparison of simulated velocities with the measured values

indicated velocity magnitude errors ranging from 3.6 to 6 cm/s along the four transects. The simulated values were typically lower than the measured values but still in good agreement even without any parameter calibration.

The locations of depositional zones for cohesive sediments transported within the main pool of Hartwell Lake were predicted via the numerical model. The EFDC model was used to describe lake hydrodynamics and sediment fate. Historical records of wind and flow data were used to determine frequencies of occurrence and representative conditions for prediction of depositional zones for sediment transported by the flow entering from upstream tributaries. Based on the analysis of historical data describing inflow, outflow and wind, representative cases to be simulated in the model runs were determined. Numerical modeling of the lake in response to different climate forcing combinations indicated likely zones of deposition for cohesive sediments. According to the model results, for lower wind speeds, sediments were deposited in the thalweg of the lake regardless of the magnitudes of inflows and outflows. Higher wind speeds caused deposition zones to shift in the downwind direction.

Potential effects of density currents arising from cold inflows on sediment deposition patterns were investigated. For this analysis, inflows at the upstream boundary were specified as cold and warm flows and the deposition thicknesses were compared when the lake was initially stratified. Even after the temperatures of the inflows at the upstream boundary were specified as cold (4 ºC) and warm (27 ºC) temperatures, which is an extreme case, significant impact on deposition patterns were not observed (RMS differences of sediment deposition thickness were less than 1.6% of the average thickness values).

Investigation of stratification on deposition patterns showed that sediments deposited mainly in the thalweg under both thermally stratified and unstratified conditions, although the stratification caused some of the sediments to settle before reaching the thalweg due to the reduced bottom layer velocities that were predicted for the stratified conditions.

The shoreline erosion prediction methodology described in this dissertation quantifies erosion in terms of shoreline recession rate, which is calculated as a function of lake levels, wind direction and magnitude, fetch, and beach profile slopes, and can account for the variability in slopes along the shoreline of a reservoir and spatial variations in sediment erodibility. The erosion prediction methodology was applied to the Western Carolina Sailing Club located in Anderson County, SC. When the erosion prediction methodology was applied to the northern part of the sailing club peninsula, an erosion rate of 60 cm/year was estimated after calibration. For the southern part of the peninsula, a rate of 90 cm/year was computed. These erosion rates agreed well with values obtained from aerial photo analysis for both the northern and southern parts of the island. Two other approaches by Kamphius (1986) and Penner (1993) were also applied to the northern part of the peninsula, and similar rates were calculated using the appropriate calibration coefficients. However, these two methods failed to estimate the erosion rate at the southern part of the island correctly, in part because these methods do not account for the variability of beach profile slopes.

The shoreline erosion prediction methodology was also applied to other peninsulas in the lake, assuming similar sediments. Eroded sediments were treated as a sediment source to investigate the fate of sediments eroded from the shorelines using the

EFDC model. In this study, new methodologies for predicting both the shoreline erosion rates and a methodology for introducing these sediments as a source into the EFDC model are presented. Model results revealed that the eroding sediments have a localized and small impact on lake-wide deposition patterns.

In summary, there are four primary benefits associated with the project:

1) The research project produced a description of the hydrodynamic processes and sediment transport within a large reservoir, and predicted the depositional zones for sediments within the main pool of Hartwell Lake, SC/GA.

2) The research project yielded a method for making objective, quantitative predictions of shoreline evolution in a reservoir featuring cohesive sediments. The method can be easily applied elsewhere as long as the shape of the beach profile and the wind conditions are known. The fate of these eroded sediments was also described through numerical modeling.

3) Knowledge of the predicted erosion “hot spots” along the shoreline can be used in the development or refinement of shoreline protection regulations, and assessment of setback requirements in similar water bodies.

4) The complex behavior of a thermally stratified reservoir was also investigated through nondimensional analysis and numerical modeling of which the results can be used in other studies.

Results presented in the dissertation depend highly on the input parameters used

to drive the numerical model. Wind data, for instance, strongly influence the results. Using a network of wind stations located along the lake, rather than depending on a single station close to the lake, would improve the realism of the wind input since the effects of the topography and vegetation surrounding the reservoir would be considered. In this study, sediment input to the reservoir specified at the upstream boundaries was based on a single measurement. Measurement of a suspended sediment concentration time series and the use of a rating curve obtained from these measurements would describe the sediment input to the system more precisely, and provide more accurate quantitative predictions of sedimentation rates.

Further improvements to the presented study would include more comprehensive field data measurements for model calibration and validation and for the description of the model forcing. Although the 3-D hydrodynamic model used in this study performed well for the simple cases for which the analytical solutions are known, validation of the model when applied to a water body with complex geometry could be only achieved using spatially and temporally extensive velocity measurements. Measurement of velocity time series, suspended sediment concentrations, and temperature time series would provide sufficient data for the calibration of the model parameters. Comparison of the 3-D hydrodynamic model results with the available laboratory experiments indicated that the major characteristics of the stratified flow under shear stress were captured well in the model simulations. However, the measurement of velocity time series, suspended sediment concentrations, and temperature time series for stratified conditions would lead to a better estimation of sediment deposition patterns in the reservoir.

APPENDICES

Appendix A

GOVERNING EQUATIONS OF THE TWO DIMENSIONAL HYDRODYNAMIC AND HEAT TRANSFER MODEL

The continuity and momentum equations solved in the 2-D hydrodynamic model can be written as:

$$\frac{\partial u}{\partial x}+\frac{\partial w}{\partial z}=0 \tag{76}$$

where

$u, w =$ velocities in horizontal x and vertical z directions

$$\frac{\partial u}{\partial t}+u\frac{\partial u}{\partial x}+w\frac{\partial u}{\partial z}=-\frac{1}{\rho}\frac{\partial P}{\partial x}+\upsilon\left(\frac{\partial^2 u}{\partial x^2}+\frac{\partial^2 u}{\partial z^2}\right) \tag{77}$$

where

$P =$ pressure

$t =$ time

$\rho =$ water density

$\upsilon =$ turbulent eddy viscosity

Assuming hydrostatic pressure (the weight of the fluid balances pressure) in the vertical direction, the vertical momentum equation is written as:

$$\frac{\partial P}{\partial z}=-\rho g \tag{78}$$

where

g = gravitational acceleration

Integrating over the depth results in:

$$P(z) = \int_{z}^{\eta} \rho g dz \tag{79}$$

and applying Leibnitz's rule gives:

$$\frac{1}{\rho}\frac{\partial P}{\partial x} = +g\frac{\partial \eta}{\partial x} + \frac{g}{\rho}\int_{z}^{\eta}\frac{\partial \rho}{\partial x}dz \tag{80}$$

where

η = free surface elevation

Finally, inserting equation (80) into the horizontal momentum equation gives:

$$\begin{aligned}\frac{\partial u}{\partial t} &= -g\frac{\partial \eta}{\partial x} - \frac{g}{\rho}\int_{z}^{\eta}\frac{\partial \rho}{\partial x}dz + \upsilon\left(\frac{\partial^2 u}{\partial x^2} + \frac{\partial^2 u}{\partial z^2}\right) - u\frac{\partial u}{\partial x} - w\frac{\partial u}{\partial z} = \\ &\underbrace{-g\frac{\partial \eta}{\partial x} - \frac{g}{\rho}\int_{z}^{\eta}\frac{\partial \rho}{\partial x}dz + \upsilon\left(\frac{\partial^2 u}{\partial x^2} + \frac{\partial^2 u}{\partial z^2}\right) - u\frac{\partial u}{\partial x} - w\frac{\partial u}{\partial z}}\end{aligned} \tag{81}$$

where

$$F_x = -\frac{g}{\rho}\int_{z}^{\eta}\frac{\partial \rho}{\partial x}dz + \upsilon\left(\frac{\partial^2 u}{\partial x^2} + \frac{\partial^2 u}{\partial z^2}\right) - u\frac{\partial u}{\partial x} - w\frac{\partial u}{\partial z} \tag{82}$$

The equation for the free surface elevation is derived by integrating the continuity equation over the water column and combining it with the kinematic boundary condition at the free surface. The continuity equation states that the sum of all the net fluid flows

into the water column must be balanced by an increase in the height of the fluid in the water column.

$$\frac{\partial \eta}{\partial t} = -\frac{\partial}{\partial x}\int_{-h}^{\eta} u dz \tag{83}$$

The transport equation for temperature is written as:

$$\frac{\partial T}{\partial t} + u\frac{\partial T}{\partial x} + w\frac{\partial T}{\partial z} = \frac{\partial}{\partial x}\left(\varepsilon \frac{\partial T}{\partial x}\right) + \frac{\partial}{\partial z}\left(\varepsilon \frac{\partial T}{\partial z}\right) + \frac{1}{\rho c_p}\frac{\partial I}{\partial z} \tag{84}$$

where

$T =$ temperature

$\varepsilon =$ turbulent eddy diffusivity

$c_p =$ heat capacity of water

$I =$ downward solar irradiance defined as:

$$I(z) = SR * 0.5 * \exp[-nz] \tag{85}$$

where

$n =$ the extinction coefficient

$SR =$ the short wave radiation.

In order to obtain a relationship between density and temperature, published density values at different temperatures were plotted (Gerhart et al. 1992). The least squares fit through measured values was obtained by the following equation:

$$\rho = 999.97 + 0.0219T - 0.006T^2 + 2 * 10^{-5}T^3 \tag{86}$$

For the solution of the momentum equations, boundary conditions at the surface are applied. The horizontal velocity gradient is related to kinematic shear stresses at the water surface by the following equation:

$$\frac{\partial u}{\partial z} = \frac{\tau_w}{\upsilon * \rho_w} \tag{87}$$

where wind shear stress τ_w, can be calculated as a function of wind speed, U_w and surface drag coefficient, c_s as follows:

$$\tau_w = c_s \sqrt{U_w^2} U_w \tag{88}$$

Surface drag coefficient, c_s, is defined by Wu (1982) and represents best fit to a large number of available data sets:

$$c_s = 0.001 \frac{\rho_a}{\rho_w} \left(0.8 + 0.065 \sqrt{U_w^2}\right) \tag{89}$$

where

$\rho_a, \rho_w =$ densities of air and water

The temperature gradient at the surface is related to heat flux at the water surface by the following equation:

$$\frac{\partial T}{\partial z} = \frac{Q_h}{\rho_w c_{pw} D_v} \tag{90}$$

$Q_h =$ the flux of heat through molecular or turbulent transfer between the air and

water surface (J/s/m^2)

c_{pw} = heat capacity of water (J/kg/ºC)

D_v = thermal diffusivity of water (m^2/s)

The vertical velocity at the surface layer is set to the local time rate of change of the free surface ($w = \frac{\partial \eta}{\partial t}$), at the reservoir bottom, vertical velocities are set to zero ($w = 0$) and heat fluxes are set to zero ($\frac{\partial T}{\partial z} = 0$). At lateral walls, horizontal velocities are set to zero ($u = 0$) and no flux of heat is allowed ($\frac{\partial T}{\partial x} = 0$).

Appendix B

TESTING OF THE TWO DIMENSIONAL HYDRODYNAMIC MODEL

In order to evaluate the performance of the code, the 2-D model was evaluated with simple forcing and geometry for which analytical solutions are available in the literature. The analytical solutions for seiche and wind setup tests were discussed previously in Chapter 3.

In the seiche test, the 2-D model was run to calculate the oscillations of water in a closed basin. When variation of the free surface height at the left wall was plotted (Figure 107), free surface heights oscillated while the amplitudes dropped at each oscillation due to numerical damping. The reasons and possible ways to eliminate or minimize the numerical damping were investigated. Hoffmann and Chiang (2000) gave a brief discussion of numerical damping. In summary, first-order accurate methods (where second and higher order derivatives in the Taylors series expansion have been dropped in the approximation process) produce errors that are dissipative. These errors depend on the time step and grid size, and affect the accuracy of the solution. Hoffmann and Chiang (2000) investigated different Courant Numbers for the first order accurate wave equation, and concluded that the maximum Courant Number that satisfied the stability criteria gave the best solution.

The model results for the seiche test were compared with the analytical solutions for a standing wave. Figure 108 and Figure 109 show the comparisons of horizontal velocity and free surface height at time equal to 1.2 seiche periods to the analytical solutions. In order to make a consistent comparison with the analytical solution, the equations used in the model were simplified by omitting convective terms, and setting the

diffusion to zero.

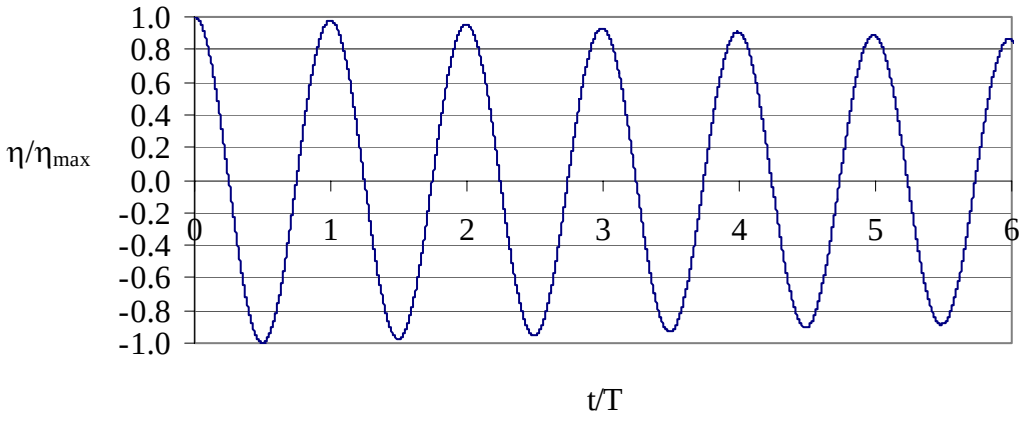

Figure 106 Variation of free surface height at the left wall with time. η_{max} is the maximum free surface height and T is the seiche period.

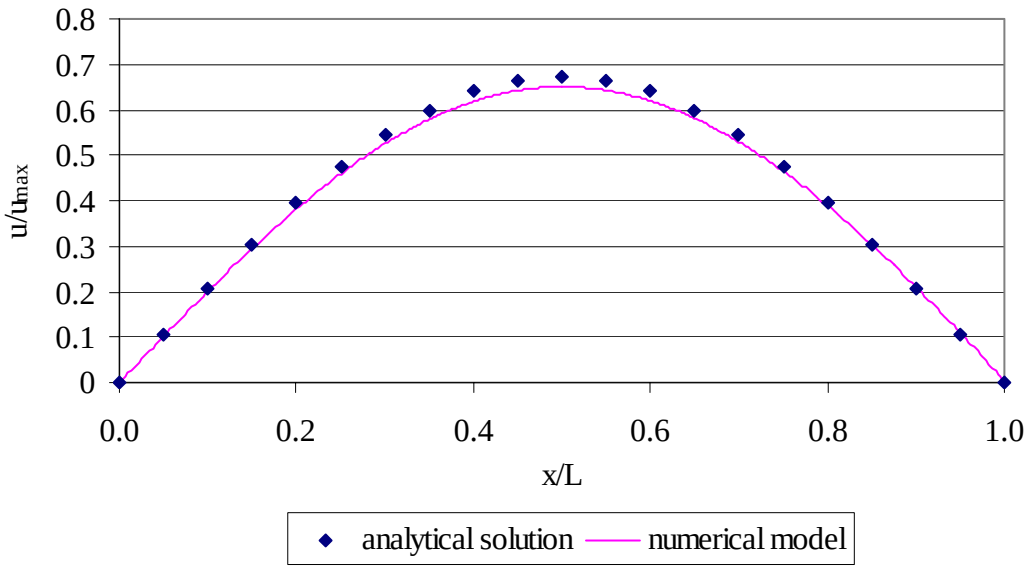

Figure 107 Comparison of numerical model results at mid cross section with the analytical solution for variation of velocity in x direction after 1.2 seiche

periods. u_{max} is the maximum velocity and L is the width of the model domain.

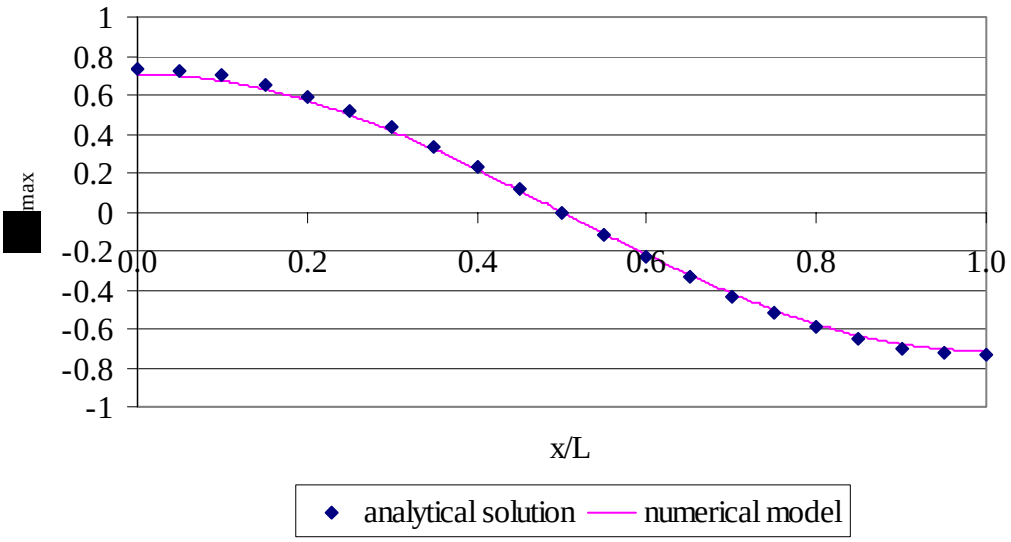

Figure 108 Comparison of numerical model results at mid cross section with the analytical solution for free surface height after 1.2 seiche periods.

In the wind setup test, the effect of constant wind was simulated in a flat-bottomed, rectangular water body. For this test, all convective and diffusion terms in the equations were activated. In order to determine when the steady-state solution was reached, the time series of free surface height at the right wall were plotted. Steady-state conditions were reached after 150 seconds (Figure 110).

Wind setup was compared to the analytical solution (described in Chapter 3) at time = 150 seconds (Figure 111). Mass conservation was checked by integrating the area under the free surface heights in the x-direction. Conservation of mass was not completely satisfied and fractional change of mass was 4×10^{-6}. This is partly due to the

very steep velocity gradients that may occur at the water surface. The spatial gradients for the top boundary conditions are approximated as third order accurate (derived from the Taylor series expansion). An improvement in overall mass balance is observed if third-order accurate derivatives are used as opposed to first-order accurate (results not shown). Besides the higher order accurate approximations for the boundaries, applying a higher order accurate scheme for the simulations, and using a more conservative filtering function could make further improvements. Rueda and Schladow (2002) reported values in the range of $1\times10^{-6} - 1\times10^{-7}$ for fractional change of mass for the same problem. The fractional volume error output for the same problem by EFDC model was 2×10^{-7}. Since the numerical model was not developed as a decision tool in water systems but developed as a tool to investigate the hydrodynamics in a thermally stratified water body, further improvements in the numerical model were not necessary.

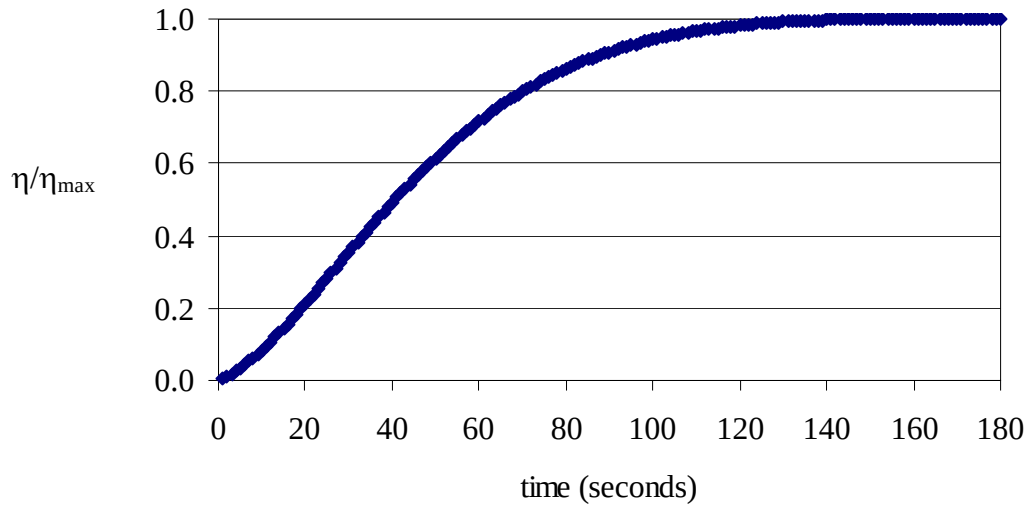

Figure 109 Variation of free surface height at the right wall with time.

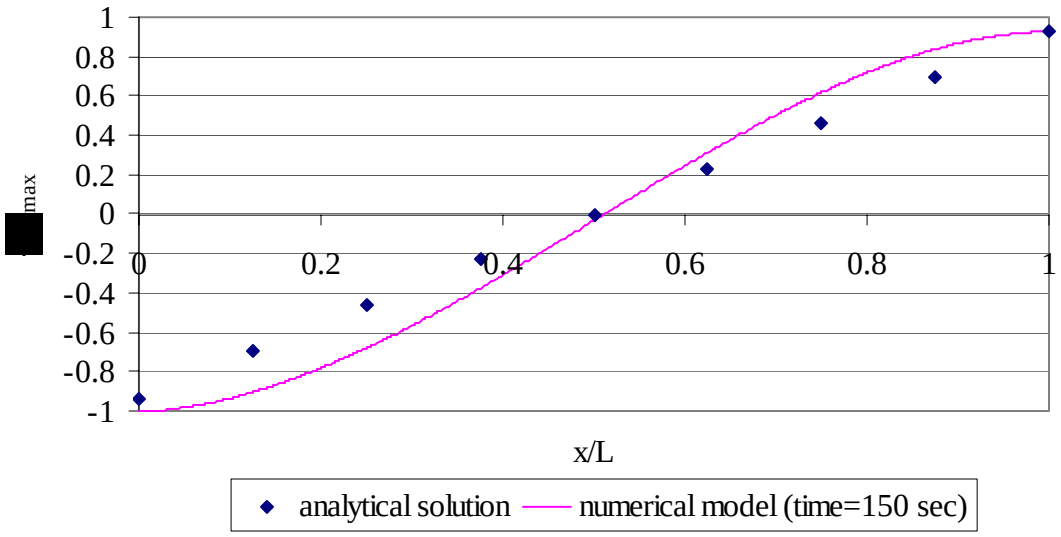

Figure 110 Comparison of free surface height when steady state is reached with the analytical solution.

The thermal transport equation in the model was tested for the following conditions: initially free surface height was set to zero, no wind forcing was allowed, and no sources or sinks in the system were considered. Initial temperature distribution was $20^{\circ}C$ at $0 \le z \le 5$ m, and $10^{\circ}C$ at $5 < z \le 10$ m (Figure 112) where z is the depth measured from the surface.

The analytical solution for this case can be obtained by applying the separation of variables principle to the heat equation with non-insulated boundaries. The analytical solution was derived in Giordano and Weir (1998), and is given below:

$$T(z,t) = \frac{A_0}{2} + \sum_{n=1}^{\infty} A_n e^{-k(n\pi/h)^2 t} \cos\left(\frac{n\pi z}{h}\right) \tag{91}$$

where k is the thermal diffusion coefficient and the constants A_0 and A_n are the

coefficients of the Fourier cosine series for the initial function. When the initial conditions are applied, the final form of Equation 91 can be written as:

$$T(z,t) = \frac{30}{2} + \sum_{n=1}^{\infty} \frac{20}{n\pi} \sin\left(\frac{n\pi}{2}\right) e^{-k(n\pi/h)^2 t} \cos\left(\frac{n\pi z}{h}\right) \tag{92}$$

Figure 108 shows the comparison of the model results for vertical temperature profile with the analytical solution after 500 seconds. Overall, the temperature distribution in the water column matches the analytical solution very closely. The RMS difference is calculated as 0.28 $^{\circ}C$ (1.4% of maximum temperature). Although the same diffusivity coefficient is used in both the analytical and numerical models, the dissipation in the numerical model appears to be more rapid.

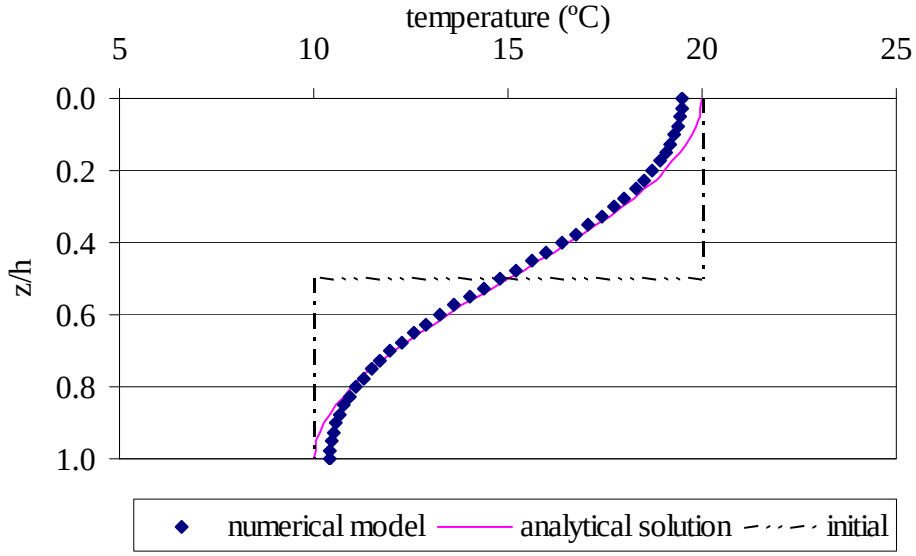

Figure 111 Comparison of vertical temperature profiles in the middle of the domain with the analytical solution, after 500 seconds of simulation. No wind forcing, and no sources or sinks in the system were allowed.

Appendix C

DERIVATION OF SHORELINE EROSION PREDICTION METHODOLOGY

Analytical predictions of wind waves typically involve one of the following assumptions: 1) Fetch-limited waves: wind blows from a constant direction over a fetch for a sufficient time to achieve steady-state values. 2) Duration-limited waves: wind increases very quickly through time in an area removed from any close boundaries 3) Depth-limited, fully developed waves: fully developed wave height will evolve under the action of wind (USACE, 2002). Based on the characteristics of the water body relative water depth conditions are employed. Assuming deep water conditions are valid, the equations governing growth of wave height, H, and period, T with fetch for deep water conditions are given as:

$$H = 4.13 * 10^{-2} u_* \sqrt{\frac{X}{g}} \tag{93}$$

$$T = 2.727 \sqrt[\frac{1}{3}]{\frac{X u_*}{g^2}} \tag{94}$$

where X is the fetch length, g is gravity, u_* is the friction velocity at the water's surface and is a function of wind speed (u) measured at 10 m elevation. Based on Figure II-2-14 of the USACE (1998), the following relation between friction velocity (u_*) and wind speed (u) is defined.

$$u_* = 0.0275u \tag{95}$$

Wave runup (R_u) results from the decreased momentum flux upon breaking. For regular breaking waves, Hunt (1959) empirically determined runup as a function of beach slope, incident wave height and wave steepness based on laboratory data. In non-dimensional form (Battjes, 1974), the equation for runup is given by:

$$\frac{R_u}{H} = \xi \tag{96}$$

ξ is the surf similarity parameter, defined as

$$\xi = m_1 \left(\frac{H}{L_0} \right)^{-\frac{1}{2}} \tag{97}$$

where m_1 is the beach slope, and L_0 is the deep water wave length:

$$L_0 = \frac{gT^2}{2\pi} \tag{98}$$

Therefore, the equation for wave runup (in meters) is simplified and written as a function of beach slope, wave height and wave period:

$$R_u = 1.24 H^{0.5} T m_1 \tag{99}$$

For the first two cases where water level is below the toe, erodibility of the cohesive shore is assumed directly proportional to excess shear applied to the soil. Recession rate, R, is derived from a simple equation for prediction of erosion rates in the case of waves passing over a mud (Whitehouse et al., 2000, Dean and Dalrymple, 2001).

Pathirana (1993) defines the critical shear stress for erosion, τ_c (N/m^2), in terms

of bed dry density T_s, as given below:

$$\tau_c = 7.95 \times 10^{-10} T_s^{3.64} \tag{100}$$

A quadratic relationship between the bed shear stress and the near-bed velocity is assumed:

$$\tau = \frac{1}{2} \rho f_w u_b^2 \tag{101}$$

in which f_w is the friction factor under waves (recommended value by Kamphius (1986): 3.4×10^{-3}), ρ is the density of water, u_b is the orbital wave velocity at the bottom defined based on linear (Airy) wave theory. The main assumptions of this theory are: incompressible, irrotational, inviscid flow, and small amplitude waves.

$$u_b = \frac{H\pi}{T} \frac{\cosh k(h+z)}{\sinh(kh)} \cos(kx - 2\pi t/T) \tag{102}$$

where k is the wave number, equal to

$$k = \frac{2\pi}{L} \tag{103}$$

and where L is the wave length, can be calculated using the following relationship

$$L = \frac{g}{2\pi} T^2 \tanh \frac{2\pi h}{L} \tag{104}$$

At the seabed ($z = -h$) Equation (104) simplifies to (Dean and Dalrymple, 2001):

$$|u_b| = \frac{H\pi}{T\sinh(kh)} \tag{105}$$

Waves are assumed to break when their height becomes equal to a fraction of the water depth (Dean and Dalrymple, 2001):

$$H_b = \kappa h_b \tag{106}$$

where $\kappa = 0.78$ and subscript b denotes the value at breaking. The depth at which wave breaking occurs can be determined by employing shoaling and refraction formulas for shallow water. Assuming shallow water at breaking, deep water offshore, and $\cos\theta_b = 1$, the wave height at breaking is calculated by:

$$H_b = H\left(\frac{L}{2T\sqrt{gh_b}}\right)^{1/2}(\cos\theta)^{1/2} \tag{107}$$

For a plane beach where $h = m_1 x$ and m_1 = beach slope, the distance to the breaker line from shore is:

$$x_b = \frac{h_b}{m_1} \tag{108}$$

inserting Equations (105) and (106) into (108) gives :

$$x_b = \frac{1}{m_1 g^{1/5}\kappa^{4/5}}\left(\frac{H^2 L\cos\theta}{2T}\right)^{2/5} \tag{109}$$

It will be assumed that the erosion rate of the bed is proportional to the excess

shear stress (bed shear stress minus the critical shear stress for erosion). Spatial averaging of the equation by Thorn and Parson (1980) gives:

$$\frac{dm}{dt} = M_2\left(\overline{\tau - \tau_c}\right) \tag{110}$$

The mean value of the bed shear stress within the surf zone, wherever this bed shear stress exceeds the critical value can be calculated as:

$$\overline{\tau - \tau_c} = \frac{1}{x}\int_0^x (\tau - \tau_c)dx = \frac{1}{x}\int_0^x \left(\frac{1}{8}\rho f_w \frac{\pi^2 H^2}{T^2 \sinh^2(kh)} - \tau_c\right)dx \tag{111}$$

Recession rate, R (m/s) is assumed proportional to $\frac{dm}{dt}$ the erosion rate (kg/m^2/s). The upper limit in equation (111) is replaced by x_b, which is the distance to the breakpoint (equation 109). Dividing the erosion rate by sediment density, ρ_s (kg/m^3), recession rate, R (m/s), is then obtained as given below.

$$R = \frac{M_2}{\rho_s}\left(\frac{1}{6}\rho f_w \kappa^2 \pi^2 m_1^{\ 2} \frac{x_b^{\ 2}}{T^2 \sinh^2(kh)} - \tau_c\right) \tag{112}$$

REFERENCES

Anglin, C.D., Nairn, R.B., Baird, W.F., Donnelly, P. and Sawyer, D., 1986. “Shoreline management along the cohesive shorelines of the Great Lakes.” Coastlines of Canada, 73-87.

Ariathurai, R., and R. B. Krone, 1976. “Finite element model for cohesive sediment transport.” J. Hyd. Div. ASCE, 102, 323-338.

Ariathurai, R., and Arulanandan, K. (1978). “Erosion rates of cohesive soils.” J. Hydr. Div. ASCE, 104, 279-283.

Arulanandan, K., Loganathan, P., and Krone, R. B., 1975. “Pore and eroding fluid influences on surface erosion on soil.” J. Geotech. Eng. Div., ASCE, 101(1), 51-66.

Arnold, J.G., Bircket, M.D., Williams, J.R., Smith, W.F., and McGill, H.N., 1987. “Modeling the effects of urbanization on basin water yield and reservoir sedimentation.” Water Resources Bull., 23(6), Amer. Water Resources Assoc., 1101-1107.

Battjes, J.A., 1974. “Computation of setup, longshore currents, runup, and overtopping due to wind generated waves.” Report, 74-2, Civil Eng. Dep., Delft Univ. of Techology.

Beletsky, D., and Schwab, D.J., 1998. “Modeling thermal structure and circulation in Lake Michigan.” Proc. 6th Int. Conf, Estuarine and Coastal Modeling, ASCE, 511-522.

Blumberg, A.F., and Mellor, G.L., 1987. “A description of a three-dimensional coastal ocean circulation model.” In: N.S. Heaps (ed.) Three-dimensional coastal ocean models, American Geophysical Union, Washington, D.C., 1-16.

Blumberg, A.F , Khan, L.A., and St. John, J.P., 1999. “Three-dimensional hydrodynamic model of New York Harbor Region.” J. of Hydraulic Eng., ASCE, 125 (8), 799-815.

Bonnet, M.P., Poulin, M., and Devaux, J., 2000. " Numerical modeling of thermal stratification in a lake reservoir. Methodology and case study." Aquatic Sciences, 62, 105-124.

Bruttour, 2003. Ceestar User Guide for dual frequency digital survey echo sounder, published by Bruttour International.

Clearwater, 1997. PCB Contamination of the Hudson: addressed at http://www.clearwater.org/news/hazard.html.

Coakley, J.P., Rukavina, N.A, and Zeman, A.J., 1986. "Wave induced shear stress and subaqueous erosion of cohesive tills." Proc. Symp. On Cohesive Shores. National Water Res. Ins., Environment Canada, 120-136.

Crowell, M., Leatherman, S.P., and Buckley, M.K., 1993. "Shoreline change rate analysis: Long term versus short term data." Shore and Beach, 4, 13-20.

Davidson-Arnott, R.G.D., 1986. " Erosion of the nearshore profile in till: Rates, controls, and implications for shoreline protection." Proc. Symp. On Cohesive Shores. National Water Res. Ins , Environment Canada, 137-149.

Dean, R.G., and Dalrymple, R.A., 2001. Water Wave Mechanics for Engineers and Scientists. World Scientific.

Deas M. and Lowney, C.L., 2000, " Water temperature modeling review, Cental Valley". California Water Modeling Forum.

De Cesare, G., Schleiss, A., and Hermann, F., 2001. "Impact of turbidity currents on reservoir sedimentation." J. of Hydraulic Eng., 127(1), ASCE, 6-16.

DeGasperi, C., Khangaonkar, T., Yang, Z, and Marshall, K., 2000, "BETTER temperature model of Lake Billy Chinook, Oregon." Available at: http://www.fwc.com/publications/tech_papers/env/pdfs/lakebill.pdf.

Elci, S. and Work, P.A., 2002. Prediction of shoreline erosion and sedimentation in Hartwell Lake, SC/GA. Technical Report No. GTREP-CEE/2002-1.

Elzerman, A.W., Farley, K.J., Dunnivant, F.M., and Cooper, C., 1994. Predicting the future fate of PCBs in Lake Hartwell. Technical Completion Report, G1588-03, submitted to U.S. Department of the Interior, U.S. Geological Survey Reston, VA.

EPA, 1991. Sangamo-Weston Inc./Twelve-Mile Creek/Lake Hartwell PCB Contamination: addressed http://www.epa.gov/oerrpage/superfund/sites/npl/nar486.htm

Falconer, R.A., George, D.G., Hall, P., 1991. "Three-dimensional numerical modeling of wind driven circulation in a shallow homogenous lake." Journal of Hydrology, 124, 59-79.

Ferguson, B.K., and Overend, M., 1998. "Shoreline erosion and its potential control on a multi-purpose reservoir." Shore & Beach, 66(1), 23-30.

Fischer, H. B., List, E. G., Koh, R. C. Y., Imberger, J. & Brooks, N. H., 1979. Mixing in Inland and Coastal Waters, Academic Press, New York, NY.

Fuller, J.A., 1986. "Shore erosion at Maumee Bay State Park, Lake Erie: A two year study." Proc. Symp. On Cohesive Shores. National Water Res. Ins., Environment Canada, 110-119.

Gal, G., Imberger, J., Zohary, T., Antenucci, J. Anis, A., and Rosenberg, T., 2003. "Simulating the thermal dynamics of Lake Kinneret." Ecological Modeling, 162, 69-86.

Galperin, B., L. H. Kantha, S. Hassid, and A. Rosati, 1988. "A quasi-equilibrium turbulent energy model for geophysical flows." J. Atmos. Sci., 45, 55-62.

Garcia, M., and G. Parker, 1991. "Entrainment of bed sediment into suspension." J. Hyd. Engrg., 117, 414-435.

Gerhart P.M., Gross, R. and Hochstein, J., 1992. Fundamentals of Fluid Mechanics. Published by Addison –Wesley Publishing Company.

Giordano and Weir, 1988. Differential equations, a modeling approach. Published by Addison –Wesley Publishing Company.

Hamrick, J.M., 1996. User's Manual for the Environmental Fluid Dynamics Computer Code. Special Rep. No. 331, The College of William and Mary, Gloucester Point, VA.

Hamrick, J. M., and Wu, T. S., 1997. ''Computational design and optimization of the EFDC/HEM3D surface water hydrodynamic and eutrophication models.'' Next generation environmental model and computational methods, G. Delich and M. F. Wheeler, eds., Society of Industrial and Applied Mathematics, Philadelphia, 143–161.Hines, A. and Willmott, A.J., 2001. "Solution of the linear thermocline equations driven by wind stress and thermohaline forcing." Atmosphere-Ocean, 39 (1), 23-34.

Hodges, B.R., Imberger, J., Laval, B., and Appt, J., 2000. "Modeling the hydrodynamics of stratified lakes." Proceedings, Hydroinformatics 2000 Conference, reprint, 14 pages.

Hoffmann and Chiang, 2000. Computational Fluid Dynamics, Volume 1. Published by Engineering Education System.

Hunt, I. A., 1959. "Design of Seawalls and Breakwaters." J. Waterw. Harbors Div., Am. Soc. Civ. Eng., September, 123-152.

Hwang, K.-N, and A. J. Mehta, 1989. Fine sediment erodibility in Lake Okeechobee. Coastal and Oceanographic Engineering Dept., University of Florida, Report UFL/COEL-89/019, Gainesville, FL.

Imberger, J. (1998). Physical Processes in Lakes and Oceans, AGU Coastal and Estuarine Studies Volume 54.

Ji, Z.-G., Morton, M. R., and Hamrick, J. M., 2000. "Modeling hydrodynamic and sediment processes in Morro Bay." Estuarine and coastal modeling: Proc., 6th Int. Conf., M. L. Spaulding and H. L. Butler, eds., ASCE, New York, 1035–1054.

Ji, Z.-G., Morton, M. R., and Hamrick, J. M., 2001a. "Wetting and drying simulation of estuarine processes." Estuarine, Coastal Shelf Sci., 53, 683-700.

Jin, K.-R., Hamrick, J. H., and Tisdale, T., 2000. “Application of a three-dimensional hydrodynamic model for Lake Okeechobee.” J. Hydraul. Eng., ASCE, 126 (10), 758–771.

Jin, K. R., and Ji, Z.-G., 2001. “Calibration and verification of a spectral wind-wave model for Lake Okeechobee.” J. Ocean Eng., 28, 571–584.

Jin, K. R., Ji, Z.-G., and Hamrick, J. M., 2002. “Modeling winter circulation in Lake Okeechobee, Florida.” J. Waterway, Port, Coastal, Ocean Eng., ASCE, 128 (3), 114-125.

Johnson, B. H., K.W. Kim, R. E. Heath, B. B. Hsieh and H. L. Butler, 1993. “Validation of three-dimensional hydrodynamic model of Chesapeake Bay.” J. Hydraul. Eng., ASCE 119: 2–20.

Kamphuis, J.W. and Readshaw, J.S., 1979. “Model study of alongshore sediment transport rate.” Proc. Coastal Eng. Conf. 16th, 2, 1656-1674.

Kamphuis, J.W. and Sayao, O.F.S.J., 1983. “Model tests on littoral sand transport rate.” Proc. Coastal Eng. Conf., ASCE, 2, 1305-1325.

Kamphuis, J.W., Davies, M.H., Nairn, R.B., and Sayao, O.J., 1986. “Calculation of littoral sand transport rate.” Coastal Eng. 10(1), 1-21.

Kamphuis, J.W., 1989. “ Influence of sand and gravel on the erosion of cohesive sediment.” J. Hydraulic Res., 28(1), 43-53.

Krone, R.B., 1962. “Flume studies of the transport of sediment in estuarial shoaling processes.” Hydr. Eng. Lab. And Sanitary Eng. Lab., Univ. of California, Berkeley, CA.

Launder, B. and Sandham, N., 2002. “Closure Strategies for Turbulent and Transitional Flows.” Published by Cambridge University Press.

Leatherman, S.P., 1983. “Historical and projected shoreline mapping.” Coastal Zone, Proc. of the Symp. on Coastal and Ocean Management, 3, 2902-2910.

Lo, K.F.A., 1994. “Quantifying soil erosion for Shihmen Reservoir watershed, Taiwan.” Agricultural Systems, 45, Elsevier, 105-116.

Mehta, A.J., Carey, W.P., Hayter, E.J., Heltzel, S.B., Krone, R.B., McAnally, W.H., Jr., Parker, W.R., Schoellhamer, D., and Teeter, A.M., 1989. “Cohesive sediment transport: Part 1, process description; Part 2, Application.” J. of Hydraulic Eng., 115(8), ASCE, 1076-1112.

Mehta, A.J., R. Ariathurai, P-Y. Maa, and E.J. Hayter, 1990."Sedimentation - Preventive and Removal Measures," Port Engineering, by Per Bruun, 4th Ed., Vol. 2, Gulf Publishing Co., pp 546-553.

Mellor, G. L., and T. Yamada, 1982. “Development of a turbulence closure model for geophysical fluid problems.” Rev. Geophys. Space Phys., 20, 851-875.

Mollard, J.D., 1986. “Shoreline erosion and slumping studies on Prairie Lakes and Reservoirs.” Proc. Symp. On Cohesive Shores.National Water Res. Ins., Environment Canada, 277-291.

Monismith, S., 1986. “An experimental study of the upwelling response of stratified reservoirs to surface shear stress.” J. Fluid Mech. 171, 407-439.

Nairn, R.B., Pinchin, B.M., and Philpott, K.L., 1986. A Cohesive Coast Development Model. Proceed. Symposium on Cohesive Shores, National Research Council Canada, Associate Committee on Shorelines, 246-261.

Newe, J., Peters, K. and Dette, H.H., 1999. “Profile development under storm conditions as a function of beach slope.” Proc. of the 4th Int. Symp. On Coastal Eng., ASCE, 2582-2596.

Paine, J.G. and Morton, R.A., 1986. “Historical shoreline changes in Trinity, Galveston, West, and East Bays, Texas Gulf Coast.” Geological Circular 86-3, Bureau of Economic Geology.

Parchure, T.M., and Mehta, A.J., 1985. “Erosion of soft cohesive sediment deposits.” J. Hydraul. Eng. ASCE, 111(10), 1308-1326.

Penner, L.A., 1993. “Shore erosion and slumping on Western Canadian lakes and reservoirs - a methodology for estimating future bank erosion rates.” Environment Canada, Regina, Saskatchewan.

Philpott, K.L., 1984. “Cohesive coastal progresses.” Proc., Annual Conference - Canadian Society for Civil Eng., 2, 619-629.

Podsetchine, V. and Schernewski, G., 1999. “Influence of spatial wind inhomogeneity on flow patterns in a small lake.” Water Res., Elsevier Science Ltd., 33(15), 3348-3356.

RD Instruments, 2001. WorkHorse Sentinel user's Guide, published by the RD Instruments.

Rubin, H. and Atkinson, J., 2001. Environmental Fluid Mechanics. Publisher: Marcel Dekker, 728 pages.

Rueda, F.J., Schladow, S.G., Monismith, S.G., and Stacey, M.T., 2003. “Dynamics of large polymictic lake. I: Field observations”. J. of Hydraulic Eng., ASCE, 129 (2), 82-91.

Rueda, F.J., and Schladow, S.G., 2003. “Dynamics of large polymictic lake. II: Numerical simulations”. J. of Hydraulic Eng., ASCE, 129 (2), 92-101.

Rueda, F.J., and Schladow, S.G., 2002. “Quantitative comparison of models for barotropic response of homogeneous basins.” J. of Hydraulic Eng., ASCE, 128 (2), 201-212.

Smolarkiewicz, P. K., and T. L. Clark, 1986. “The multidimensional positive definite advection transport algorithm: further development and applications.” J. Comp. Phys., 67, 396-438.

Sheng, Y.P., and Lick, W., 1979. “The transport and resuspension of sediments in a shallow lake.” J. Geophys. Res., 84(C4), 1809-1826.

Sheng, Y.P., 1984. “A turbulent transport model of coastal processes.” Proc. 19th Int. Conf. On Coastal Eng., ASCE, 2380-2396.

Sheng, Y.P., 1991. “Lake Okeechobee phosphorus dynamics study: Hydrodynamics and sediment dynamics – a field and modeling study; vol. VII. Contract No. C-91-2393.” Report to the South Florida Water Management District, West Palm Beach, FL.

Shrestha, P. A., and G. T. Orlob, 1996. “Multiphase distribution of cohesive sediments and heavy metals in estuarine systems.” J. Environ. Eng., 122, 730-740.

Sotiropoulos, F., 2001. Review for Statistical Theory and Modeling for Turbulent Flows, by P. Durbin and B. A. Pettersson (Wiley), AIAA Journal 39(9), pp. 1829-1830.

Smith, J. D., and S. R. McLean , 1977. “Spatially averaged flow over a wavy bed.” J. Geophys. Res., 82, 1735-1746.

Smith, P. E., 1997. “A three-dimensional, finite-difference model for estuarine circulation.” PhD dissertation, Univ. of California, Davis, Calif.

Tetra Tech, 1999. “Theoretical and computational aspects of sediment transport in the EFDC model.” Technical Rep. Prepared for U.S. Environmental Protection Agency, Tetra Tech, Inc., Fairfax, Va.

Thorn, M.F.C. and Parsons, J.G., 1980. “Erosion of cohesive sediments in estuaries: an engineering guide.” Proc. of the Int. Symp. on Dredging Technol., 349-358.

U.S. Army Corps of Engineers, 1984. The Shore Protection Manual. Dept. of the Army, Washington, DC.

U.S. Army Corps of Engineers, 1996. User’s guide for the sigma stretched version of CH3D-WES. Technical report HL-96-21. Waterways Experiment Station.

U.S. Army Corps of Engineers, 1996b. Water Control Manual, Savannah River Basin: Hartwell Dam and Lake, Richard B. Russell Dam and Lake, and J. Strom Thurmond Dam and Lake multiple purpose projects.

U.S. Army Corps of Engineers, 1998. Coastal engineering manual, Part III. Dept. of the Army, Washington, DC.

U.S. Army Corps of Engineers, 2002. Coastal engineering manual, Part III. Dept. of the Army, Washington, DC.

Van Rijin, L. C., 1984."Sediment transport, Part II: Suspended load transport." J. Hyd. Eng., ASCE, 110, 1613-1641.

Whitehouse, R., Soulsby, R., Roberts, W., and Mitchener, H., 2000. "Dynamics of estuarine muds." Thomas Telford, London.

Work, P.A., Hansen, M., and Rogers, W.E., 1998. "Bathymetric surveying with GPS and heave, pitch, and roll compensation." J. Surv. Eng., ASCE , 124(2), 73-90.

Work, P.A., 2001. Plant-based bioengineering to mitigate shoreline erosion along Piedmont reservoirs of South Carolina. Report to Clemson University Enhancement of Research and Technology Transfer Program, September 18, 2001.

Wu, J., 1982. "Wind-stress coefficients over sea surface from breeze to hurricane." J. Geophys. Res., 87, C12, 9704-9706

Wu, J. and Tsanis, I.K., 1995. "Vertical/horizontal integration wind induced circulation model (VHI3D). A method for including surface and bottom logarithmic profiles." Adv. Water Resour., 18(2), Elsevier Science Ltd , p 77.

Yang, Z., Khangaonkar, T., DeGasperi, C., and Marshall, K., 2000. "Three-dimensional modeling of temperature stratification and density-driven circulation in Lake Billy Chinook, Oregon." Proc. 6th Int. Conf, Estuarine and Coastal Modeling, ASCE, 411-425.

Yu, W.S., Lee, H.Y., and Hsu, S.M., 2000. "Experiments on deposition behavior of fine sediment in a reservoir." J. of Hydraulic Eng., ASCE, 126 (12), 912-920.

Ziegler, C. K., and B. Nesbitt, 1994. "Fine-grained sediment transport in Pawtuxet River, Rhode Island." J. Hyd. Eng., ASCE, 120, 561-576.

Ziegler, C. K., and B. Nesbitt, 1995. "Long-term simulation of fine-grained sediment transport in large reservoir." J. Hyd. Eng., ASCE, 121, 773-781.

Zreik, D.A., Krishnappen, B.G., Germaine, J.T., Madsen, O.S. and Ladd, C.C., 1998. "Erosional and mechanical strengths of deposited cohesive sediments." J. Hyd. Eng., ASCE, 124(11), 1076-1085.